Freie Universität Berlin

"Kinetic and X-ray crystallographic studies of glycogen phosphorylase. On the way to structure based drug design for diabetes type 2"

Inaugural-Dissertation
to obtain the academic degree
Doctor rerum naturalium (Dr. rer. nat.)
submitted to the Department of Biology, Chemistry and Pharmacy
of Freie Universität Berlin

by

Kyriaki-Melinda Alexacou, MSc

Athens, Greece

March 2010

April 2006 – April 2009

EU-6th Framework programme MARIE CURIE ACTIONS

« EURODESY: A European research training site for the design and synthesis of novel neuroprotective and hypoglycaemic agents through a multi-disciplinary approach »

Under the supervision of

Dr. Nikos G. Oikonomakos & Dr. Demetres D. Leonidas

National Hellenic Research Foundation

48 Vassileos Constantinou Avenue, 11635, Athens, Greece

1st reviewer:

Associate Professor of Biochemistry

Dr. Demetres D. Leonidas

University of Thessaly, Greece

2nd reviewer:

Professor Dr. Udo Heinemann

Freie Universität Berlin, Germany

Max Delbrück Centre, Berlin, Germany

Date of defence: July 12th 2010

Acknowledgements

First of all, I would like to express my gratitude to Professor Dr. Udo Heinemann at the Freie Universität Berlin, because without him the completion of this PhD would not have been possible. I thank him from the bottom of my heart for the trust he showed in me.

When I started my PhD I had no idea that it would be such a promising experience. I have spent the past four years of my life in lab 409 of the Structural Biology & Chemistry Group at the National Hellenic Research Foundation. During such a long time, the lab quickly becomes your house and your colleagues become your family.

Unfortunately though even during promising times, tragedy can strike. On August 31st 2008, my supervisor Dr. Nikos G. Oikonomakos suddenly and untimely passed away. I consider myself privileged to have been taught X-ray crystallography by him. He accepted me in his lab with the faith that I wouldn't let him down, and I hope I have succeeded in making him proud. He was always here to guide me but at the same time giving me the freedom and responsibility a PhD student undoubtedly needs. I thank him for the opportunities he offered me. He is greatly missed.

Thank you to my supervisor Dr. Demetres D. Leonidas for all his valuable help, and for supporting my PhD after Nikos Oikonomakos' passing. It has been an absolute pleasure working with him.

Many thanks to current and former members of the Structural Biology & Chemistry Group, as well as various researchers and fellow students at the National Hellenic Research Foundation, for their excellent collaboration. Thank you to Robert Csonka for his valuable help. It is a pleasure to thank various collaborators around the world who provided the compounds that were studied.

My parents have been by my side at every step of my life. My mother taught me never to give up and my father to always take risks in life. Their advice has made me the person I am today. Finally, I must say that I owe my PhD firstly to Chloe but most of all to my beloved mother. Thank you from the bottom of my heart for the strength you gave me and for finding solutions when problems seemed impossible to solve. You are my rock. I owe you everything...

Abstract

Diabetes type 2 is a complex disease characterized by altered glucose metabolism and insulin resistance. Almost half of all people with diabetes type 2 are not aware they have this life threatening condition, as they can show symptoms years after the onset of the disease. Glycogen phosphorylase, an allosteric enzyme, plays a pivotal role in controlling the metabolism of glycogen. It catalyzes the first step in the degradation of glycogen by releasing glucose-1-phosphate from a long chain of glucose residues. As an allosteric enzyme, the inactive T state is switched to the active R state by a change in conformation controlled by phosphorylation of a single residue (Ser14) by phosphorylase kinase. Phosphorylation leads to transition between the two forms of the enzyme, called phosphorylase *a* and *b*. Glycogen phosphorylase is a dimer composed of two identical subunits. Each subunit has a molecular weight of 97.444 Da, consists of 842 amino acids and an essential co-factor, pyridoxal-5´-phosphate (PLP). Various binding sites on the enzyme are known, notably the catalytic, allosteric, new allosteric and inhibitor sites. By means of kinetic *in vitro* experiments and X-ray crystallography experiments, these binding sites were targeted by studying a large number of glycogen phosphorylase inhibitors as potential hyperglycaemic drugs. The essential inhibitory and binding properties of specific compounds were analyzed in an effort to provide rationalizations for the affinities of these compounds and to exploit the molecular interactions with the goal to design new better inhibitors. Most of the inhibitors studied were glucose analogues and were found to bind at the catalytic site of the enzyme but interesting results were also found for more binding sites. A novel binding site was also discovered and mapped out. These studies have given new insights into fundamental structural aspects of the enzyme enhancing our understanding of how the enzyme recognizes and specifically binds ligands, which could be of potential therapeutic value in the treatment of diabetes type 2.

Zusammenfassung

Typ-2-Diabetes ist eine komplexe Stoffwechselkrankheit, die sich durch einen veränderten Glucosestoffwechsel sowie Insulinresistenz auszeichnet. Fast die Hälfte aller Menschen mit Typ-2-Diabetes sind sich nicht bewußt, daß sie an dieser lebensgefährlichen Krankheit leiden, da sie oft schleichend beginnt und sich die ersten Symptome erst nach Jahren zeigen. Die Glycogenphosphorylase (PYG), ein allosterisches aktiviertes Enzym, ist das Schlüsselenzym der Glycogenolyse, die den Glycosestoffwechsel steuert. Es katalysiert den ersten Schritt des Glycosestoffwechsels, bei dem freies Phosphat am C-Atom 1 der Glycose angebunden wird, wobei die glykosidische Bindung zwischen den Glycose-Molekülen aufgespalten und Glucose-1-phosphat entsteht. PYG ist die Ursache der Konformationsänderung von der inaktiven T-Form zur aktiven R-Form in der Phosphorylierung eines Serin-Restes (Ser14) durch die Phosphorylase-Kinase. Die Phosphorylierung führt zum Übergang zwischen den zwei Enzymformen, die Phosphorylase a und b genannt werden. Glykogenphosphorylase ist ein Dimer, das aus zwei identischen Monomeren besteht. Jedes Monomer besitzt eine molekulare Masse von 97.444 Da und besteht aus 842 Aminosäuren, sowie dem Kofactor Pyridoxal-5´-Phosphat (PLP). Mehrere Bindungstellen für Inhibitoren an diesem Enzym sind bekannt, insbesondere die sogenannte katalytische, die allosterische, die neue allosterische und die Inhibitor Bindungsstelle. In dieser Arbeit wurden mithilfe von kinetischen *in vitro* Experimenten und kristallographischen Roentgenstruktur-Untersuchungen die Bindungs-and Inhibitor-Eigenschaften der verschiedenen Bindungsstellen des Enzyms gegenüber einer großen Anzahl ausgewählter Inhibitoren ausführlich untersucht. Die Analyse der Ergebnisse dieser Untersuchungen ermöglichen ein besseres Verständnis der molekularen Wechselwirkungen, mit Hinblick auf die gezielte Entwicklung neuer hyperglykämischer Wirkstoffe mit besserem Wirkungsgrad. Die meisten der untersuchten Inhibitoren waren Glykose-Derivate, und die Bindung fand in der Regel an der katalytischen Bindungsstelle des Enzyms statt. Aber auch für die anderen Bindungsstellen wurden interessante Ergebnisse gefunden. Es wurde auch eine neue Bindungstelle im Enzym entdeckt und charakterisiert. Die Ergebnisse dieser Arbeit vermitteln neue Erkenntnisse über die Struktur des Enzyms, sowie über die Mechanismem der Erkennung spezifischer Liganden und ihrer selektiven Bindung, und sind daher von potentiellen therapeuthischem Wert für die Behandlung der Typ 2 Diabetes-Krankheit.

Contents

2. Materials & Methods

3. Results & Discussion

1. Introduction

1.1 Early history of crystals and X-ray crystallography

Crystals have been admired for their symmetry since early on in history, but it wasn't until the 17th century that they were investigated scientifically. In 1611 Johannes Kepler, in his work "*Strena seu de Nive Sexangula*", proposed that the hexagonal symmetry of snowflake crystals was due to a regular packing of spherical water particles [1].
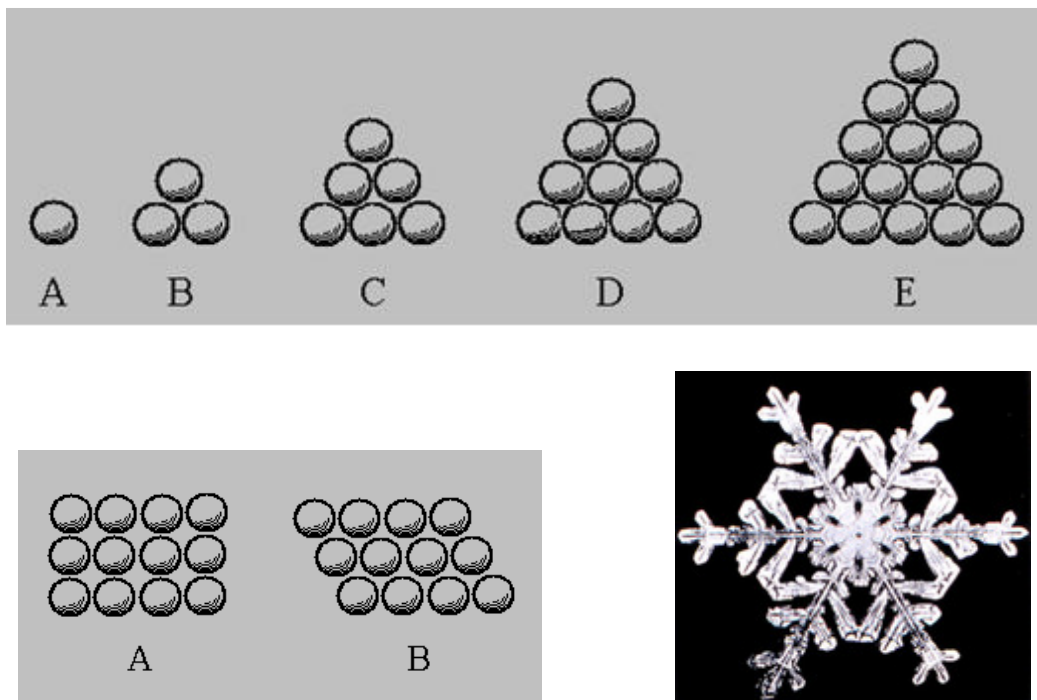
Figure 1. Johannes Kepler's first concept of crystal symmetry [1].

Crystal symmetry was first investigated experimentally by Nicolas Steno in 1669, who demonstrated that the angles between the faces are the same in every type of crystal [2]. In 1784, René Just Haüy discovered that every face of a crystal can be described by simple stacking patterns of blocks of the same shape and size [3]. In 1839 William Hallowes Miller, in his work "*A treatise on crystallography*", gave an interesting description of crystals: "*Many natural substances and many of the results of chemical operations occur in the form of solids which are bounded by plane surfaces, and which commonly exhibit a tendency to separate when broken in the directions of planes, passing through any point between them, either parallel to some of their bounding planes, or else making given angles with them*". He was able to characterize every face of a crystal with three small integers, the Miller indices, which are still used today for identifying crystal faces [4]. In

the 19th century, a complete list of the possible symmetries of crystals was presented by Johann Hessel, Auguste Bravais, Yevgraf Fyodorov, Arthur Schönflies and William Barlow [5-8]. Based on these data, Barlow proposed several crystal structures in the 1880s [9]. On November 8th 1895, Wilhem Conrad Röntgen, a German physicist, produced and detected electromagnetic radiation in a wavelength range known today as X-rays. This achievement earned him the Nobel Prize in Physics in 1901. However, it wasn't until 1912 that the first X-ray diffraction confirmed that X-rays are in fact a form of electromagnetic radiation [10]. X-ray crystallography is the method that uses X-rays and crystals to determine the three dimensional structure of molecules, and it has led to many advances in science and medicine over the years. The first structure of an organic compound, hexamethylenetetramine, was determined in 1923 [11]. However, the recognition of the power of the method came with the discoveries of the three dimensional structures of cholesterol (1937), vitamin B12 (1945) and penicillin (1954) by Dorothy Crowfoot Hodgkin, for which she was awarded the Nobel Prize in Chemistry in 1964.
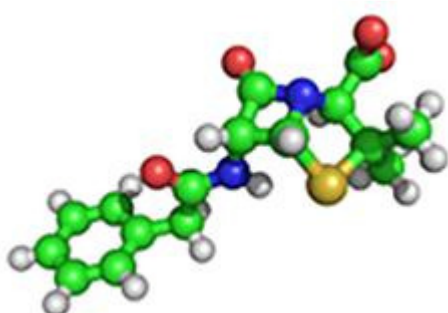
Figure 2. The three dimensional structure of penicillin for which Dorothy Crowfoot Hodgkin was awarded the Nobel Prize in Chemistry in 1964 [12]. The green, red, white, yellow and blue spheres represent carbon, oxygen, hydrogen, sulphur, and nitrogen atoms respectively.

1.2 Structure based drug design

Structure based drug design is a powerful and rapidly growing method for discovering new drug leads against important targets. The first example was reported by the group of Beddell and Goodford in 1973 at Wellcome Laboratories in the United Kingdom [13]. Structure based drug design has contributted over the years to very important drug discoveries, notably the HIV protease inhibitors [14, 15]. The process of structure based drug design comprises many cycles. The first cycle includes the cloning, purification and structure determination of the target protein or nucleic acid by one of the three main

methods for structure determination of macromolecules: X-ray crystallography, NMR or homology modelling. Using computer algorithms, compounds or fragments from a database are positioned into a selected region of the structure. These compounds are scored and ranked based on steric and electrostatic interactions with the target site, and the best compounds are tested with biochemical assays. In the second cycle, structure determination of the target in complex with a promising lead from the first cycle, reveals sites on the compound that can be altered to increase its affinity for the target. Additional cycles include the generation of a 2nd and possibly a 3rd generation of compounds with optimum affinity profile for the target [16]. Enzymes are often excellent drug targets because compounds can be designed to fit within their active site pocket. During the process of drug design, protein flexibility is an important parameter. The constant cycling between a resting and an activated conformation is crucial for protein function. Protein flexibility allows for the binding of structurally diverse inhibitors at the same binding site. Therefore mobility in a protein is crucial in understanding the ways in which potential drugs exert biological effects, as these can be limited by absorption, distribution, metabolism and toxicology considerations [17]. Glycogen phosphorylase, an enzyme implicated in glycogen metabolism, has been a target of structure based design of hypoglycaemic drugs for many years [61].

1.3 Glucose

Glucose is an important and common fuel. In mammals, glucose is the only fuel that the brain uses under non-starvation conditions and the only fuel that red blood cells can use at all. Glucose ($C_6H_{12}O_6$) contains six carbon atoms, one of which is part of an aldehyde group, and is therefore referred to as an aldohexose. In solution, the glucose molecule can exist in an open-chain (acyclic) form and a ring (cyclic) form (in equilibrium). The cyclic form is the result of a covalent bond between the aldehyde C atom and the C5 hydroxyl group to form a six-membered cyclic hemiacetal. At pH 7 the cyclic form is predominant. In the solid phase glucose assumes the cyclic form. Because the ring contains five carbon atoms and one oxygen atom, which resembles the structure of pyran, the cyclic form of glucose is also referred to as glucopyranose. In this ring, each carbon is linked to a hydroxyl side group with the exception of the fifth atom, which is linked to a sixth carbon atom outside the ring, forming a –CH_2OH group. Glucose is commonly available in the

form of a white substance or as a solid crystal [18]. It exists in two stereoisomers, D-glucose and L-glucose, but only D-glucose is active. L-glucose cannot be metabolized by cells during glycolysis. D-glucose cyclizes reversibly in aqueous solution to a 36:64 mixture of two anomers, a process called mutarotation. Mutarotation occurs by a reversible ring opening of each anomer to the open chair aldehyde, followed by reclosure. Although equilibration is slow at neutral pH, it is catalyzed by both acid and base. The minor α anomer has the OH group at C1, trans to the –CH$_2$OH substituent at C5. The major β anomer has the OH group at C1, cis to the –CH$_2$OH substituent at C5. Both anomers of D-glucose can be crystallized and purified. Pure α-D-glucose has a melting point of 146°C and a specific rotation, [α]$_D$, of +112.2°. Pure β-D-glucose has a melting point of 148-155°C and a specific rotation of +18.7° [132].
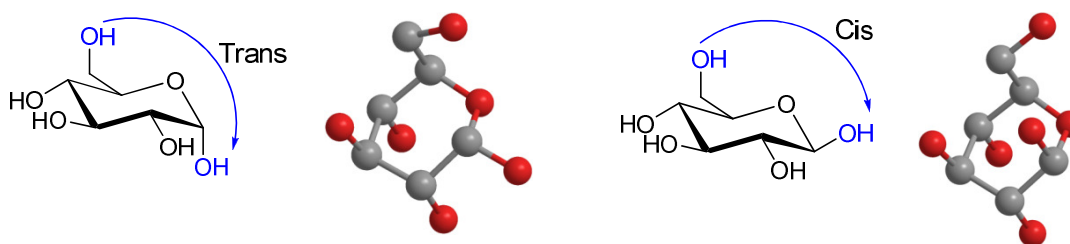
Figure 3. α-D-glucopyranose 36% (left) and β-D-glucopyranose 64% (right).

Glycolysis and gluconeogenesis: two processes reciprocally regulated

Gluconeogenesis and glycolysis are coordinated so that within a cell one pathway is relatively inactive while the other is highly active. The amounts and activities of the distinctive enzymes of each pathway are controlled so that both pathways are not highly active at the same time. The rate of glycolysis is also determined by the concentration of glucose, while the rate of gluconeogenesis is determined by the concentrations of lactate and other precursors of glucose. A high level of AMP indicates that the energy charge is low and signals the need for ATP generation. Conversely, high levels of ATP indicate that the energy charge is high and that biosynthetic intermediates are abundant. Under these conditions, glycolysis is nearly switched off and gluconeogenesis is promoted [18].
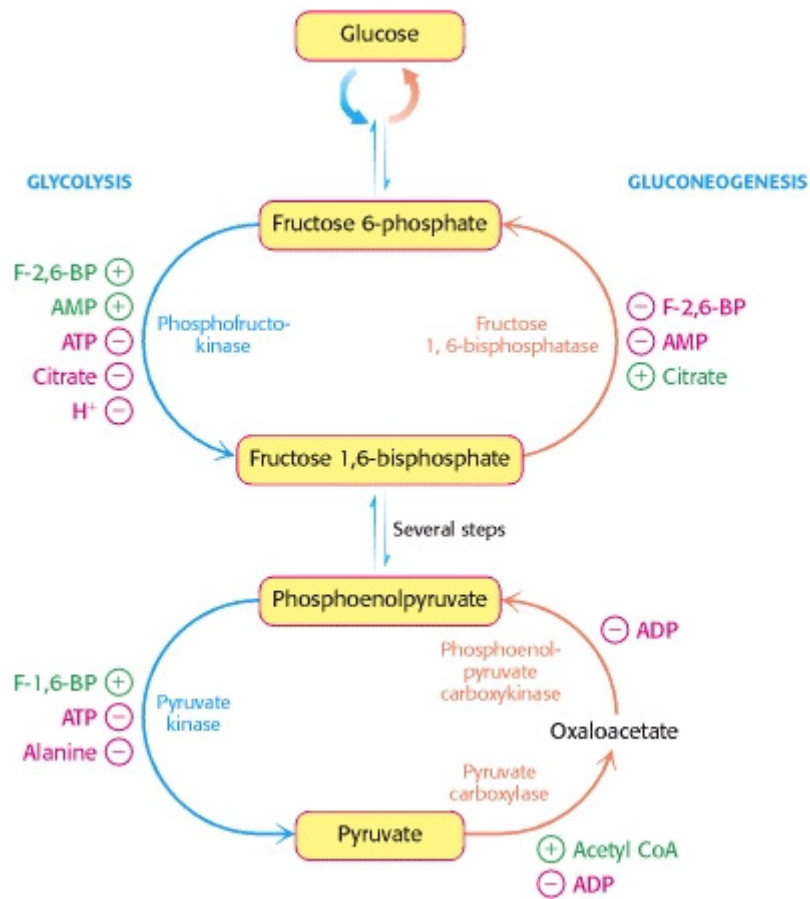
Figure 4. Regulation of glycolysis and gluconeogenesis in the liver [18].

1.4 Glycogen

Glycogen is a readily mobilized storage form of glucose. It is a very large, branched polymer of glucose residues that can be broken down to yield glucose molecules when energy is needed.
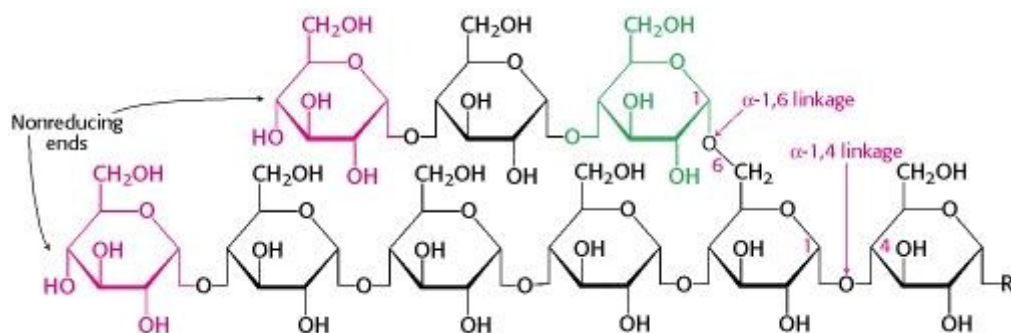
Figure 5. Glycogen structure [18].

Most of the glucose residues in glycogen are linked by α-1,4-glycosidic bonds. Branches at about every tenth residue are created by α-1,6-glycosidic bonds. Glycogen is an important fuel reserve for several reasons. The controlled breakdown of glycogen increases the amount of glucose that is available between meals. Hence, glycogen serves as a buffer to maintain blood glucose levels. Glycogen's role in maintaining blood glucose levels is especially important because glucose is virtually the only fuel used by the brain, except during prolonged starvation. Moreover, the glucose from glycogen is readily mobilized and is therefore a good source of energy for sudden, strenuous activity. Unlike fatty acids, the released glucose can provide energy in the absence of oxygen and can thus supply energy for anaerobic activity. The two major sites of glycogen storage are the liver and skeletal muscle. The concentration of glycogen is higher in the liver than in muscle (10% versus 2% by weight), but more glycogen is stored in skeletal muscle overall because of its much greater mass. Glycogen is present in the cytosol in the form of granules ranging in diameter from 10 to 40 nm. In the liver, glycogen synthesis and degradation are regulated to maintain blood glucose levels as required to meet the needs of the organism as a whole. In contrast, in the muscle these processes are regulated to meet the energy needs of the muscle itself [18].

1.5 Glycogen metabolism

Glycogen synthesis

The first step in the synthesis of glycogen is the autocatalytic attachment of C1 of glucose to a single tyrosine residue of the enzyme glycogenin, using UDP-glucose as a glucosyl donor. Subsequently, glycogenin autocatalytically extends the glucan chain by six to seven α-1,4-linked glucose residues. This 'primed' glycogenin is further and similarly elongated by glycogen synthase, which is initially complexed to glycogenin, but dissociates during the elongation process. Finally, a branching enzyme transfers a terminal oligo-glucan (at least six glucose units) from an elongated external chain and attaches its C1 to a C6 in a neighbouring chain [18].
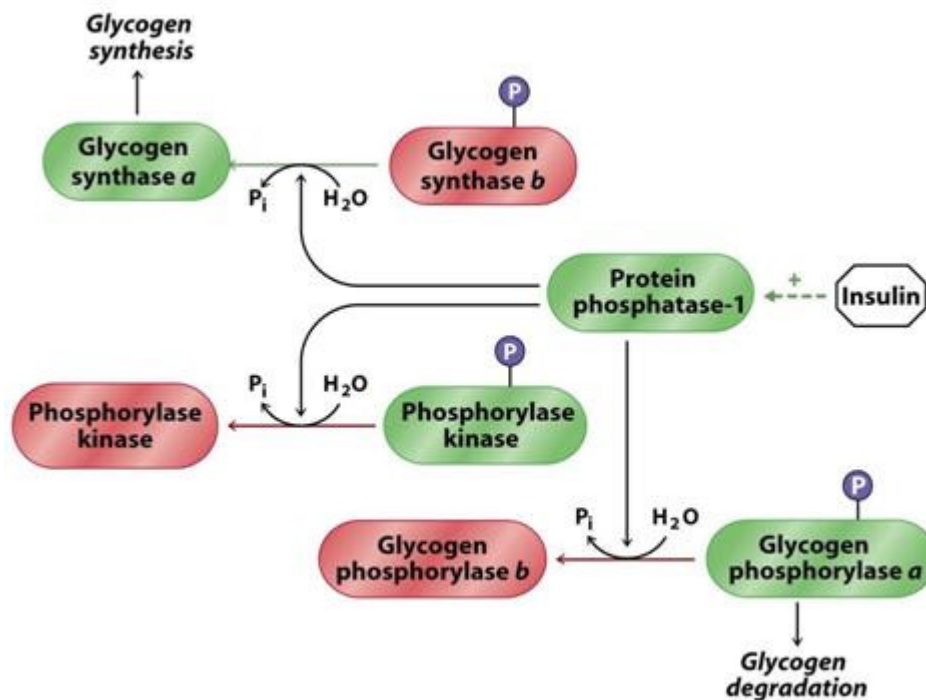
Figure 6. The regulation of glycogen metabolism [18].

Glycogen degradation

Glycogen degradation consists of three steps: (a) the release of glucose-1-phosphate from glycogen, (b) the remodelling of the glycogen substrate to permit further degradation and (c) the conversion of glucose-1-phosphate into glucose-6-phosphate for further metabolism. Glucose-6-phosphate derived from the breakdown of glycogen has three fates: (a) It is the initial substrate for glycolysis, (b) it can be processed by the pentose phosphate pathway to yield NADPH and ribose derivatives and (c) it can be converted into free glucose for release into the bloodstream. This conversion takes place mainly in the liver and to a lesser extent in the intestines and kidneys. The degradation of glycogen requires the concerted action of the enzyme glycogen phosphorylase and the bifunctional debranching enzyme. In the presence of phosphate ions, glycogen phosphorylase releases the terminal glucose residue of an external chain as glucose-1-phosphate and continues to do so until the external chains have been shortened down to four glucose units. Subsequently, a debranching enzyme transfers a maltotriose unit from the α-1,6-linked stub and attaches it through an α-1,4-glucosidic bond to the free C4 of the main chain. The single remaining α-1,6-linked glucose unit is then liberated as glucose by the α-glucosidase activity of the debranching enzyme, while additional α-1,4-linked glucose residues become available for phosphorylase [19]. Glycogen synthesis requires an activated form of

glucose, uridine diphosphate glucose (UDP-glucose), which is formed by the reaction of UTP and glucose-1-phosphate. UDP-glucose is added to the non-reducing end of glycogen molecules. As is the case for glycogen degradation, the glycogen molecule must be remodelled for continued synthesis. The regulation of these processes is quite complex. Several enzymes taking part in glycogen metabolism, allosterically respond to metabolites that signal the energy needs of the cell. These allosteric responses allow the adjustment of enzyme activity to meet the needs of the cell. Glycogen metabolism is also regulated hormonally by cascades that lead to the activation or deactivation of enzymes through mechanisms of phosphorylation. Regulation by hormones allows glycogen metabolism to adjust to the needs of the entire organism. By both these mechanisms, glycogen degradation is integrated with glycogen synthesis. Several hormones greatly affect glycogen metabolism. Glucagon and epinephrine both trigger the breakdown of glycogen.

Epinephrine   Glucagon
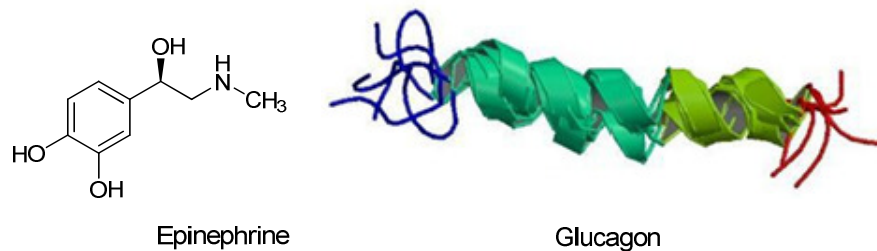
Figure 7. The structures of epinephrine and glucagon [18].

Muscular activity or its anticipation leads to the release of epinephrine, also referred to as adrenaline, a catecholamine derived from tyrosine from the adrenal medulla. Epinephrine markedly stimulates glycogen breakdown in muscle and to a lesser extent in the liver. The liver is more responsive to glucagon, a polypeptide hormone that is secreted by the α-cells of the pancreas when the blood sugar level is low. Physiologically, glucagon signifies the starved state. The effect of insulin is the exact opposite of the effect of glucagon and epinephrine. Insulin binds to a cell surface receptor and triggers a pathway that leads to activation of protein phosphatase-1 [18].

1.6 Diabetes type 1

Diabetes type 1 is caused by a cellular-mediated autoimmune destruction of the insulin producing β-cells of the islets of Langerhans of the pancreas. There are two phases of the disease: insulitis, when a mixed population of leukocytes invades the islets; and diabetes, when most β-cells have been killed off and there is no longer sufficient insulin production

to regulate blood glucose levels, resulting the hyperglycaemia. Diabetes type 1 is primarily a T lymphocyte mediated disease. Immunohistological studies show that most leukocytes in the islet infiltrate are T cells [20]. This form of disease is lethal unless treated. Patients need to inject insulin in order to compensate for the deficiency. The rate of β-cell destruction is quite variable, being rapid in some individuals (mainly infants and children) and slow in others (mainly adults). Some patients, particularly children and adolescents, as the first manifestation of the disease may develop ketoacidosis, a type of metabolic acidosis caused by high concentrations of ketone bodies, formed by the breakdown of fatty acids and the deamination of amino acids. Others have modest fasting hyperglycaemia that can rapidly change to severe hyperglycaemia and/or ketoacidosis in the presence of infection or stress. Other patients particularly adults, may retain residual β-cell function sufficient to prevent ketoacidosis for many years. These individuals eventually become dependent on insulin for survival and are at risk of ketoacidosis. At this latter stage of the disease, there is little or no insulin secretion, as manifested by low or undetectable levels of plasma C-peptide, a peptide which is produced when pro-insulin is split into insulin and C-peptide [21]. Although diabetes type 1 remains predominantly a childhood disease, it is likely that diabetes type 2 will be the predominant form within 10 years in many ethnic groups. It has already been reported in children in a number of countries including Japan, India, Australia, the UK and the USA [22, 23, 24, 25, 26].

1.7 Diabetes type 2

This is the most common form of diabetes and accounts for approximately 90-95% of diabetes cases. Diabetes type 2, also known as diabetes mellitus, is characterized by insulin resistance and/or abnormal insulin secretion, which leads to hyperglycaemia. Insulin resistance occurs when there is target tissue resistant to insulin mediated glucose disposal. It is the condition in which normal amounts of insulin are inadequate to produce a normal insulin response from fat, muscle and liver cells. To maintain normal glucose levels there is compensatory pancreatic β-cell over-secretion resulting in hyperinsulinemia. As a result of this constant overburdening, the pancreatic β-cells become exhausted and cease to function normally. The combination of β-cell dysfunction and insulin resistance on the major target tissues of insulin action, namely skeletal muscle, the liver and fat tissue, gives rise to the increased blood glucose levels. Hyperinsulinemia also causes increased

reabsorption of Na^+ ions in the kidneys, leading to increased blood volume and blood pressure. Insulin resistance is strongly associated with obesity and physical inactivity. Most patients who are diagnosed with diabetes type 2 are obese at the time of diagnosis. A number of circulating hormones, cytokines and metabolic fuels originate in the adipocytes and modulate insulin action [27]. Although lifestyle and overeating seem to be the triggering pathogenic factors, genetic elements are also involved in the pathogenesis of diabetes type 2. Positive family history confers a 2.4 fold increased risk. 15-25% of first degree relatives of patients with the disease develop impaired glucose tolerance or diabetes [28]. Unlike diabetes type 1, there is little tendency towards ketoacidosis in diabetes type 2. Unfortunately, this form of diabetes is often undiagnosed for many years, because usually there are no symptoms or they develop years after the onset of the disease. Insulin resistance may improve with weight reduction and pharmacological treatment but is seldom restored to normal levels [29, 30]. There is also sufficient evidence to support the notion that increased β-cell apoptosis is an important factor contributing to β-cell loss and the onset of diabetes type 2. A recent study found that a key signalling molecule that promotes β-cell growth and survival, the insulin receptor substrate 2, is a member of a family of proteins whose inhibition contributes to the development of insulin resistance in the liver and other insulin responsive tissues. Therefore it was concluded, that this molecule appears to be a vital participant in the fine balance between healthy β-cell function and insulin resistance [31]. The chronic hyperglycaemia of diabetes is associated with long-term damage, dysfunction and failure of various organs, especially the eyes, kidneys, nerves, heart and blood vessels. Symptoms of hyperglycaemia include polyuria (frequent urination), polydipsia (increased thirst), polyphagia (increased appetite) and sometimes blurry vision. If left untreated, this disease can have life-threatening consequences to the patient [32]. Long-term complications of diabetes type 2 include the development of diabetes specific microvascular pathology in the retina, renal glomerulus and peripheral nerve. As a consequence of its microvascular pathology, diabetes is a leading cause of blindness, end-stage renal disease and of a variety of debilitating neuropathies. Diabetes is also associated with accelerated atherosclerotic macrovascular disease affecting arteries that supply the heart, brain and lower extremities. As a result, patients with diabetes have a much higher risk of myocardial infarction, stroke and limb amputation [33]. Until recently, diabetes was regarded as a disease of the middle-aged and the elderly. While it is true that this age group is mostly affected, it is becoming

increasingly evident that younger adults and even children are becoming caught up in the diabetes "epidemic".
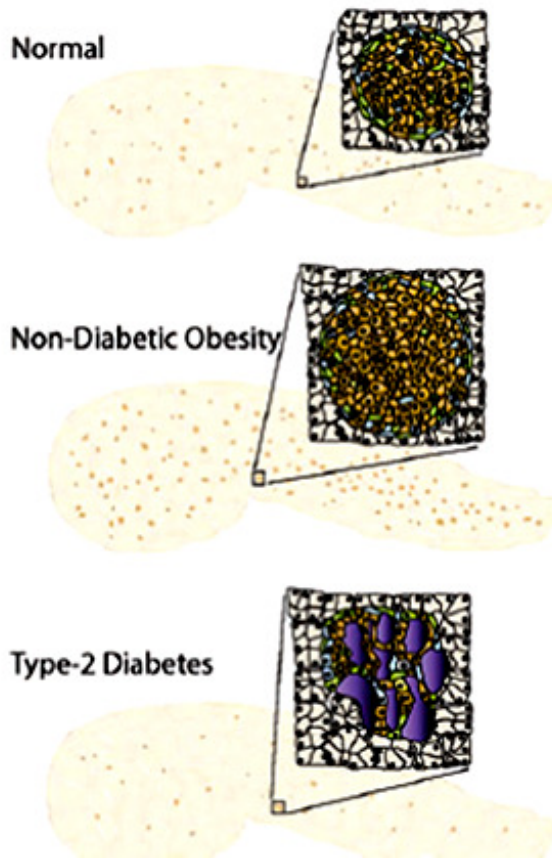
Figure 8. Adult pancreatic morphology in normal, non-diabetic obesity and in diabetes type 2. The whole pancreas which is composed primarily of exocrine cells retains the same shape and size in all three of the above cases. Under normal circumstances the islets are scattered throughout the pancreas and comprise about 1% of the total pancreatic population of cells. In non-diabetic obesity, the number of islets in the pancreas increases and the islets tend to be larger. In diabetes type 2, the number of islets decreases and they tend to be disorganized and misshapen. There is a marked reduction in the number of β-cell per islet and amyloid plaques (purple) can dominate the area [31].

1.8 The key molecule behind diabetes: insulin

Insulin captured the interest of Nobel Prize winner Dorothy Crowfoot Hodgkin in 1934, when British chemist Robert Robinson gave her a small sample of crystalline insulin [34]. She solved the three dimensional structure in 1969.

In 1960, Yalow and Berson studied insulin secretion during the oral glucose tolerance test and showed that patients with diabetes type 2 produced insulin [35].
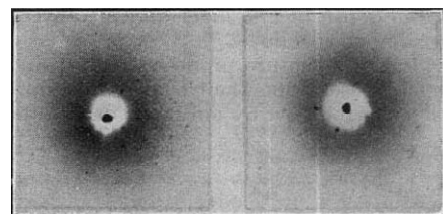
Figure 9. First X-ray photographs of crystalline insulin [34].

Several years later, Bagdade and co-workers demonstrated that the β-cell does not respond normally to a glucose challenge during the oral glucose tolerance test in patients with diabetes type 2 [36].
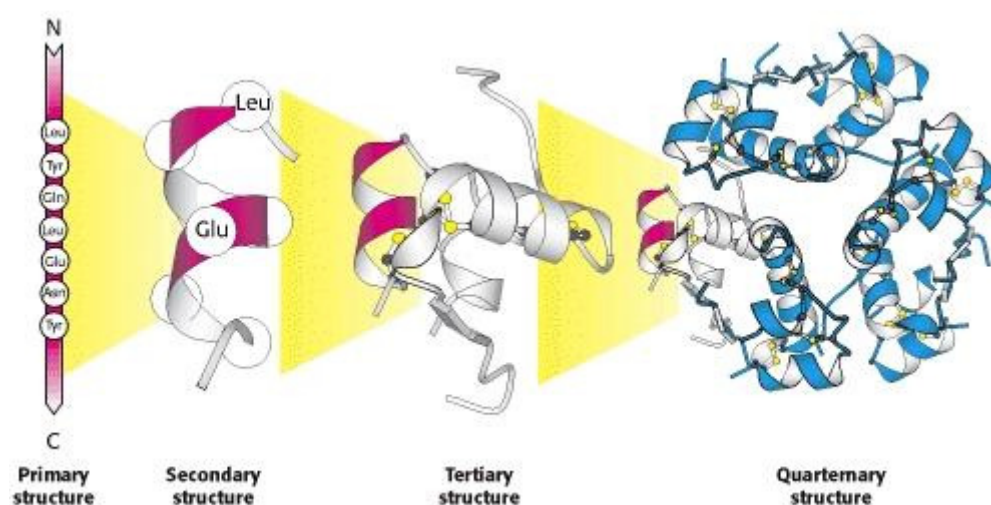
Figure 10. The structure of human insulin [18].

This peptide hormone consists of a 30-amino acid A chain and a 21-amino acid B chain. Two disulfide bridges hold the two chains together [37]. Insulin concentrations are normally determined by a feedback control system that is responsive to the prevailing level of plasma glucose [38]. The overall sensitivity of the pancreatic β-cell to glucose is determined by the sensitivity of peripheral tissues to the action of insulin with insulin resistant subjects having higher insulin levels and insulin secretion rates than insulin sensitive subjects. Insulin is also secreted in response to amino acids and fatty acids and the magnitude of this response is modulated by a variety of neural and hormonal factors [39]. Normally, plasma glucose remains in a narrow range between 4 and 7 mM in most individuals. This control is governed by the tight balance between glucose absorption from the intestine, production by the liver, uptake and metabolism by peripheral tissues. Insulin increases glucose uptake in muscle and fat and inhibits hepatic glucose production, in this way acting as the primary regulator of blood glucose concentration. It also stimulates cell growth and differentiation, and promotes the storage of substrates in fat, liver and muscle, by stimulating lipogenesis, glycogen and protein synthesis and by inhibiting lipolysis, glycogenolysis and protein breakdown [40]. Insulin secretion from the pancreas normally reduces glucose output by the liver, enhances glucose uptake by skeletal muscle and suppresses fatty acid release from fat tissue. The various factors that contribute to the pathogenesis of diabetes type 2 affect both insulin secretion and insulin action. Under

normal conditions, glucose is rapidly taken up by the pancreatic β-cells via the glucose transporter 2 (GLUT2), upon which it is phosphorylated via glucokinase, which is the rate-limiting step of β-cell glucose metabolism.
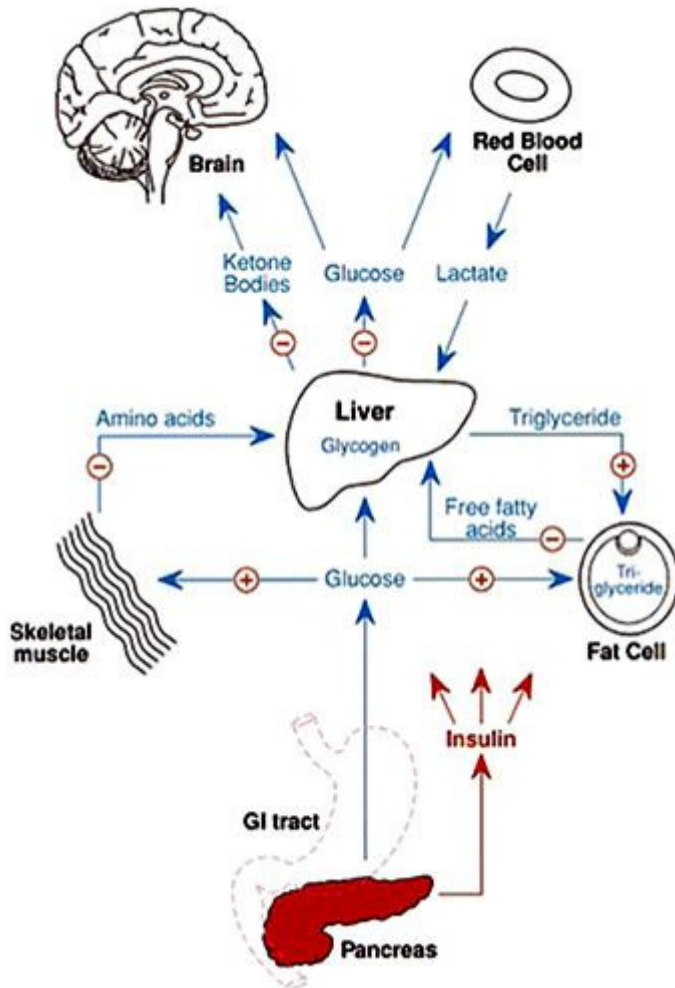
Figure 11. Consumption of food triggers the secretion of insulin by pancreatic β-cells, which directs the body to store fuel. Insulin regulates the metabolism of multiple fuels (blue). It activates transport of glucose into muscle and adipose tissue, and promotes synthesis of glycogen and triglycerides. Insulin inhibits lipolysis in adipose tissue, ketogenesis in liver, and proteolysis in muscle. It also affects hepatic glucose production by inhibiting both glucogenolysis and gluconeogenesis [29].

Further degradation leads to the formation of pyruvate, which is taken up by mitochondria in which further metabolism leads to ATP formation. ATP is necessary for the delivery of energy needed for the release of insulin and is also involved in membrane depolarization. ADP/ATP ratio leads to the activation of the sulphonylurea receptor (SUR1) protein, which leads to the closure of the adjacent potassium channel. The closure of these channels alters the membrane potentials and opens calcium channels, which triggers the release of preformed insulin-containing granules [27]. However, in diabetes type 2 the signal from the binding of insulin to its receptor is lost and the signalling pathway is down-regulated. The body attempts to compensate by producing large amounts of insulin, which eventually leads to the dysfunction of the β-cells of the islets of Langerhans. Decreased insulin secretion will reduce insulin signalling in its target tissues. Insulin resistance pathways

affect the action of insulin in each of the major target tissues, leading to increased circulating fatty acids and the hyperglycaemia of diabetes. In turn, the raised concentrations of glucose and fatty acids in the bloodstream will feed back to worsen both insulin secretion and insulin resistance. It will also give rise to undesirable effects such as stimulation of the synthesis of triglyceride rich very low density lipoproteins.
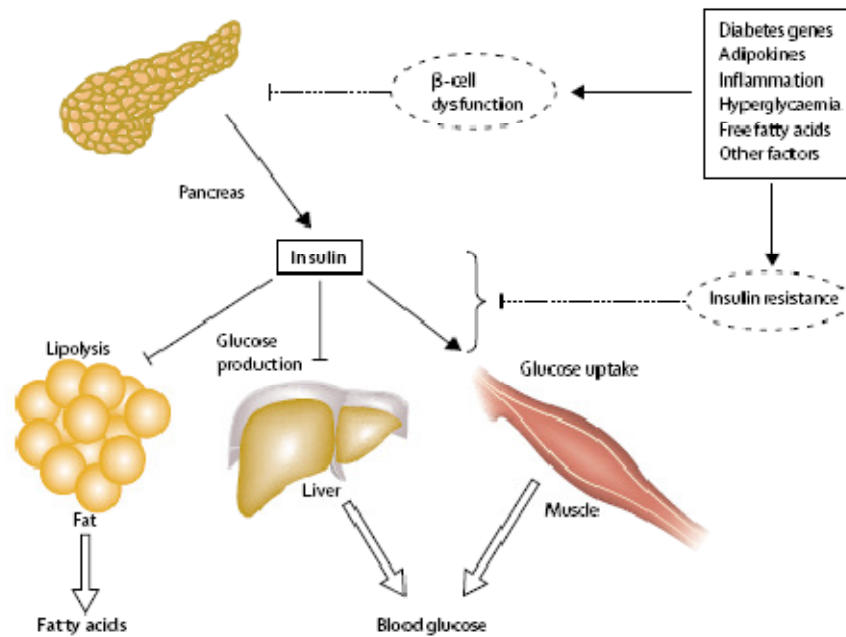
Figure 12. Pathophysiology of hyperglycaemia and increased circulation of fatty acids in diabetes type 2 [27].

Cholesterol is likewise esterified by these free fatty acids and bound to high-density lipoprotein (HDL) or to low-density lipoprotein (LDL). LDL-cholesterol particles play an important role in the formation of atherosclerotic plaques on the internal lining of the blood vessels. This can lead to myocardial infarction and strokes. A recent study showed that insulin resistance in skeletal muscle, due to decreased muscle glycogen synthesis, can promote atherogenic dyslipidemia by changing the pattern of ingested carbohydrate away from skeletal muscle glycogen synthesis into hepatic *de novo* lipogenesis, resulting in an increase in plasma triglyceride concentrations and a reduction in plasma HDL concentrations [41].

1.9 Mitochondrial function and diabetic β-cells

Mitochondria are the main source of energy which is required for vital cellular functions, such as the maintenance of transmembrane ion gradients, protein synthesis and vesicular transport. As already mentioned, in individuals destined to develop diabetes type 2, pancreatic β-cells do not secrete enough insulin to compensate for the increased demand. This β-cell failure is likely caused by inadequate expansion of the β-cell mass and/or failure of the existing β-cell mass to respond to glucose [31]. It is evident that β-cells do not "sense" glucose properly and therefore do not release the appropriate amounts of insulin. Glucose sensing requires oxidative mitochondrial metabolism, leading to the generation of ATP. This increases the ratio of ATP to ADP in the β-cell, which then initiates a cascade of events: inhibition of the cell's ATP/ADP-regulated potassium channel, plasma membrane depolarization, opening of a voltage-gated calcium channel, calcium influx and secretion of insulin. It is therefore clear that oxidative mitochondrial metabolism plays a key role in glucose stimulated insulin secretion [42]. This is also supported by evidence of rare hereditary disorders, in which diabetes with β-cell dysfunction has been traced to specific mutations in the mitochondrial genome [42, 43]. It is also established that blockage of the respiratory chain inhibits glucose stimulated insulin secretion. It is therefore possible that decreased mitochondrial function in β-cells might predispose individuals to develop β-cell dysfunction and diabetes type 2 [44, 45, 46].

1.10 The statistics for diabetes type 2

The number of diabetes cases has been increasing exponentially during the past years, and it is slowly turning into a global "epidemic". It is suggested that by the year 2025 the number of prevalent patients in the world will reach 285.5 million [47, 48]. However, it is suggested that this may be an underestimate due to currently available methods to estimate the future global burden of diabetes type 2. Further modifications and validity tests may be necessary in order to develop a more reliable method to globally monitor the effects of this fast growing problem. From world demography studies and division by socio-economic status, as suggested by Murray and Lopez [49], it is suggested that most patients with diabetes type 2 are found in the Established Market Economies regions, with the smallest number found in Sub-Saharan Africa. In the developed regions (Established Market

Economies and Formerly Socialist Economies of Europe), most diabetes patients are over 65 years of age, while China and India have been set aside in separate categories due to their huge populations. By the year 2025 India alone is estimated to experience an annual increase of almost 2 million patients. By 2030, is it expected that the number of people with diabetes over 64 years of age will be more than 82 million in developing countries and more than 48 million in developed countries [50]. The top three countries with the highest numbers of estimated cases for 2000 and 2030 are India, China and the USA. Although highly unlikely, even if the prevalence of obesity remains stable until 2030, it is anticipated that the number of people with diabetes will double, as a consequence of population ageing and urbanization. Currently, the World Health Organization suggests that approximately 2.9 million deaths per year can be attributed to diabetes and estimates that the prevalence of diabetes worldwide will increase by more than 50% in the next 10 years without urgent action.

1.11 An interesting case of diabetes: Nauru

Nauru is a remote island in the Pacific that was colonized by the Micronesians in the prehistoric times. It was annexed and declared a colony by Germany in 1888, occupied by Australia in 1914 and eventually achieved independence in 1968. It is the world's smallest independent republic without an official capital. However, these facts are not merely as interesting as the fact that this small island has a sticking case of non-insulin dependent diabetes mellitus and impaired glucose tolerance. The traditional lifestyle of the Nauruans was based on agriculture and fishing and involved frequent episodes of starvation because of droughts and the island's poor soil. Early European visitors nevertheless noted that the Nauruans were obese people. In 1906 it was discovered that most of Nauru consists of high quality phosphate rock that could be used as a fertilizer, and in 1922 a mining company extracting the rock began to offer generous amounts of money to the islanders. As a result of this new wealth, average sugar consumption by the Nauruans increased exponentially by 1927 and labourers were imported because the natives disliked working as miners. During the Second World War the island was occupied by Japanese military forces, which reduced daily food intake dramatically. When the survivors returned, they regained their phosphate royalties and resumed eating sugar. They abandoned agriculture almost completely and came to rely on motor vehicles to travel around their small island. Today they are the most

obese of all the people in the Pacific. During the past decade, prevalence of the disease has begun to fall. As there were no changes in the frequency of recognized risk factors, the decline in the number of incidences of glucose intolerance is probably due to the intensity of the epidemic in Nauru. This has already removed a high proportion of the genetically susceptible individuals from the pool with normal glucose tolerance. If this interpretation is correct, then Nauru provides a case of very rapid natural selection in a human population. Coupled with the observations that mortality is higher and fertility lower in diabetic Nauruans across the age range, the observed decline in incidences and the prevalence of non-insulin dependent diabetes mellitus and impaired glucose tolerance, may presage a fail in the population frequency of the diabetic genotype, at least in its more severe form, as might be predicted on the basis of Neel's thrifty genes hypothesis [51, 52, 53].

1.12 James Neel's Thrifty Genes Hypothesis

The leading evolutionary theory for the possible benefits of genes predisposing to diabetes type 2 is James Neel's thrifty genes hypothesis. James Neel put forward a novel hypothesis to explain the growing incidence of diabetes mellitus in the mid-20th century human population. He claimed the existence of metabolically thrifty genes. These permit more efficient food utilization, fat deposition and rapid weight gain at occasional times of food abundance. According to the hypothesis, the thrifty genotype would have been advantageous for hunter-gatherer populations, especially child-bearing women, because it would allow them to gain weight more quickly during times of abundance. Fatter individuals carrying the thrifty genes would thus better survive times of food scarcity. However, in modern societies with a constant abundance of food, this genotype efficiently prepares individuals for a famine that never comes. The result is widespread chronic obesity and related health problems like diabetes. Neel supported his hypothesis using two lines of human evidence and two animal models. Non-diabetic Nauruans and Arizona Pima Indians have postprandial levels of plasma insulin, in response to an oral glucose load, that are triple from that of Europeans. In addition, Neel noticed that diabetes prone populations of Pacific Islanders, Native Americans and Aboriginal Australians were more prone to obesity than Europeans [54]. First they developed weight gain and then diabetes. Concerning the animal models, Neel postulated that laboratory rats that carry genes, predisposing them to diabetes type 2 and obesity, survived starvation better than normal

rats, illustrating the advantage of these genes under occasional conditions of famine [55]. Finally, he noticed that Israeli rats developed high levels of leptin and insulin as well as insulin resistance, obesity and diabetes, when kept on a westernized rat diet with abundant food. However, these symptoms were reversed when the food was restricted [56]. In 1962 James Neel quoted the following: *"The problem of understanding the genetic nature of man is both a philosophical and these days, of rapidly changing environment, a practical challenge. Progress demands both a broad approach on the theoretical level and a very specific approach geared to particular traits presenting favourable analytic opportunities. Diabetes mellitus may be one such trait"* [57].

1.13 Glycogen phosphorylase: phosphorylation and allosteric effectors

Glycogen phosphorylase (GP) is a regulatory allosteric enzyme that catalyzes the first step in the intracellular degradation of glycogen to yield glucose-1-phosphate (G1P).

$$Glycogen_{(n)} + P_i \longleftrightarrow Glycogen_{(n-1)} + Glucose\text{-}1\text{-}P_i$$

The principle of regulation by molecules unrelated to the substrate is the basis of allostery with studies on haemoglobin pioneering the development of this area [131]. Allosteric enzymes change their conformation upon binding of effectors. They have at least two subunits with multiple binding sites. Allosteric modulators bind non-covalently to the enzyme and precipitate changes in either the K_m of the substrate or the V_{max} of the enzyme. Whereas enzymes with single active sites display normal Michaelis-Menten kinetics, allosteric enzymes have multiple active sites and show cooperative binding. As a result, allosteric enzymes display a sigmoidal dependence on the concentration of their substrates [128]. The above reaction is readily reversible *in vitro* and the ratio [G1P]/[P$_i$] concentrations at equilibrium is 0.28 at pH 6.8. However, the enzyme *in vivo* acts only in the direction of glycogen phosphorolysis because in the cell the inorganic phosphate concentration significantly exceeds that of G1P [58]. Glycogen phosphorylase is found in every species from unicellular organisms and bacteria to the complex tissues of higher plants and mammals, where it plays a key role in carbohydrate metabolism. The best studied example of glycogen phosphorylase is the rabbit muscle enzyme, which was first isolated and characterized by G.T. Cori and C.F. Cori in 1943 [59]. Glycogen phosphorylase is a dimer composed of two identical subunits. Each subunit has a molecular

weight of 97.444 Da, consists of 842 amino acids and an essential co-factor, pyridoxal-5´-phosphate (PLP). In the muscle, G1P is utilized via glycolysis to generate metabolic energy. In the liver, it is mostly converted by phosphoglucomutase to glucose-6-phosphate and glucose, which is released for the benefit of other tissues [60]. In the resting state glycogen phosphorylase exists in the inactive b form (GPb-low activity, low substrate affinity, predominantly T state).
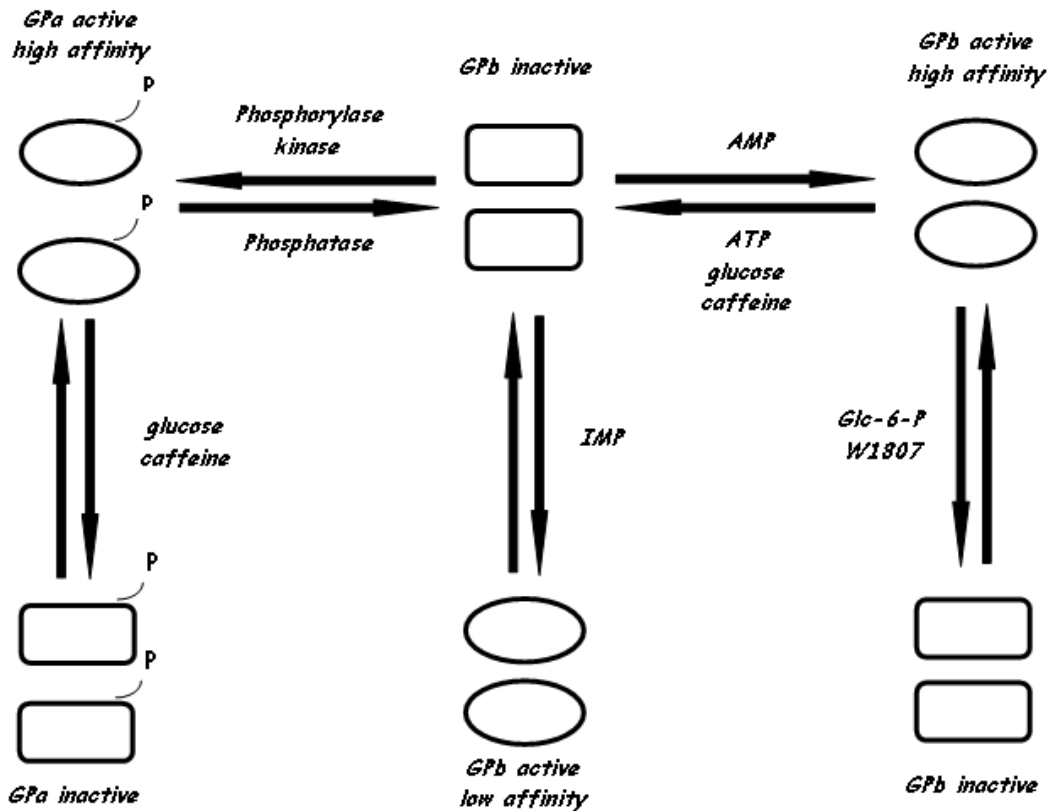
Figure 13. Schematic representation of the allosteric and covalent activation of glycogen phosphorylase [61].

In response to nervous or hormonal stimulation, GPb is converted to the phosphorylated form GPa (high activity, high substrate affinity, predominantly R state) through the phosphorylase kinase catalyzed addition of a phosphoryl group to a hydroxyl group of a specific serine (Ser14), as part of the cascade system initiated by cyclic AMP. The reverse process of dephosphorylation, stimulated by insulin, is catalyzed by protein phosphatase 1 (PP1). Allosteric activators, such as AMP or allosteric inhibitors such as ATP, glucose-6-phosphate, glucose and caffeine can alter the equilibrium between the two states according to the Monod-Wyman-Changeux model for allosteric proteins [62]. The T state is stabilized by the binding of ATP, glucose-6-phosphate, glucose, caffeine and the Bayer compound W1807 [61]. The R state is induced by AMP or IMP, substrates or certain

substrate analogues. The T state is a better substrate than the R state for protein phosphatase 1. GPa is a potent inhibitor of the phosphorylase action on glycogen synthase and it is only when GP has been dephosphorylated that the phosphatase is free to activate glycogen synthase [63], the rate limiting enzyme involved in glycogen synthesis. The phosphorylated form, GPa, is no longer dependent on AMP for activity, although the activity of GPa can be enhanced by AMP by about 10%. The conversion of GPa to GPb relieves the allosteric inhibition that GPa exerts on the glycogen-associated PP1, which converts glycogen synthase D to the I form, thus allowing the phosphatase to stimulate the synthesis of glycogen [18, 61, 64, 65, 66]. On the T to R transition, the quaternary structural change is represented by a 5° rotation of each subunit, around an axis close to the interface between the *cap´* region (residues 36´ to 47´, from the symmetry subunit) and helix *a2*. In the native T state enzyme, there is no access from the surface to the buried catalytic site. Access to this site is partly blocked by the 280s loop (residues 282 to 286). On the transition from the T state to the R state, the 280s loop becomes disordered and displaced, thus opening a channel that allows a crucial amino acid, Arg569, to enter the catalytic site in place of Asp283 and create the phosphate recognition site. This also provides access to glycogen substrate to reach the catalytic site. The shift and disordering of the 280s loop is associated with changes at the intersubunit contacts of the dimer that give rise to the allosteric effects [64, 67, 68].

1.14 Pyridoxal-5´-phosphate

In 1957, in Cori's laboratory, Baranowski and his colleagues discovered pyridoxal-5´-phosphate and proposed its role in glycogen phosphorylase catalysis: the phosphate of the cofactor and the substrate phosphate ions approach each other within a hydrogen bonding distance allowing the transfer of a proton, assigning the phosphate group of the pyridoxal-5´-phosphate molecule the role of a proton shuttle which recharges the substrate phosphate actions [69]. In more detail, the aldehyde group of this co-enzyme forms a Schiff base with the imino group of Lysine 680 in each subunit. The 5´-phosphate group of PLP acts in tandem with the orthophosphate ion by serving as a proton donor and then as a proton acceptor (as a general acid-base catalyst).
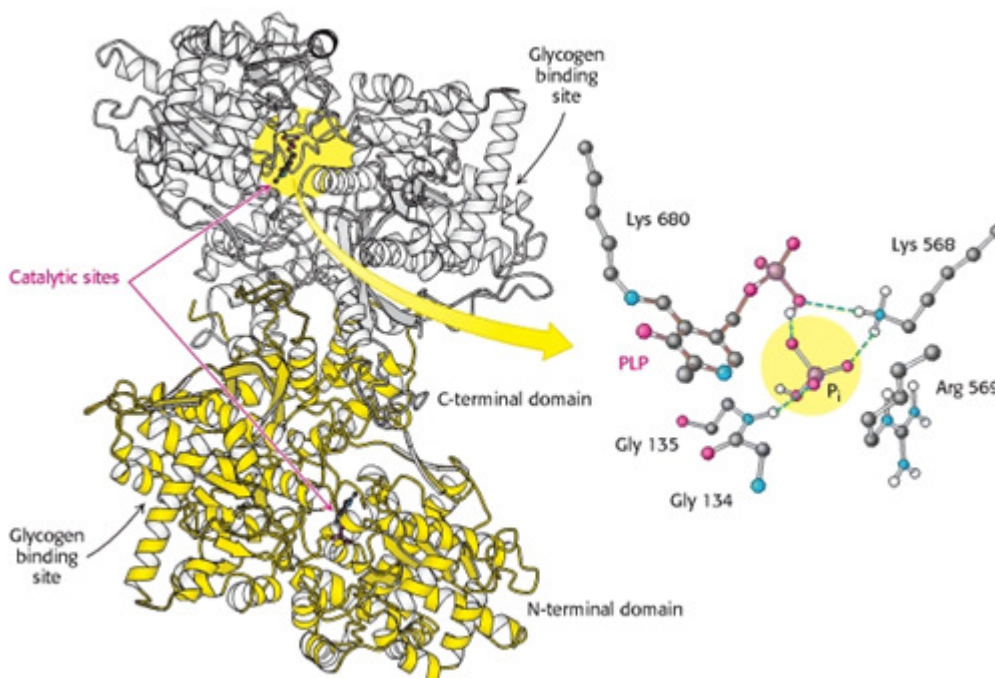
Figure 14. PLP-Schiff base linkage and its location in glycogen phosphorylase [18].

Orthophosphate ion donates a proton to the oxygen atom attached to C4 of the departing glycogen chain and simultaneously acquires a proton from PLP. The intermediate carbonium ion formed in this step is then attacked by the orthophosphate ion to form α-glucose-1-phosphate, with the concomitant return of a proton to pyridoxal phosphate. The direct participation of PLP in catalysis is accompanied by its role as a conformational cofactor of phosphorylase, stabilizing the active dimeric structure of the enzyme and regulating the affinity of the enzyme for substrates and effectors [18, 58].
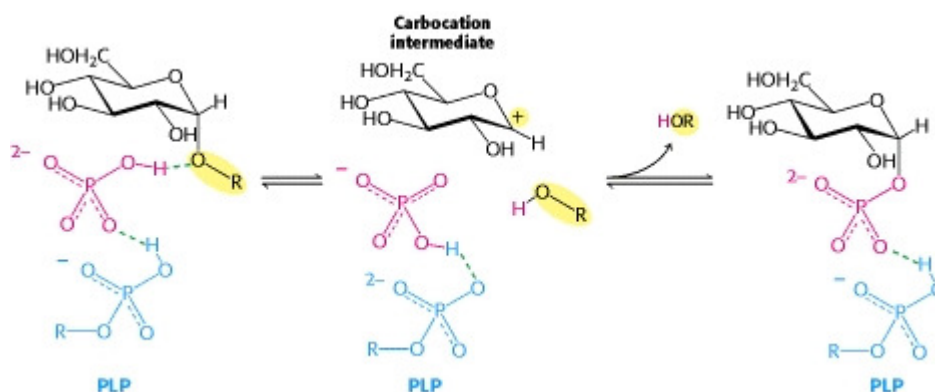
Figure 15. Phosphorylase mechanism. A bound HPO_4^{2-} group (red) favours the cleavage of the glycosidic bond by donating a proton to the departing glucose (black). This reaction results in the formation of a carbocation and is favoured by the transfer of a proton from the protonated phosphate group of the bound pyridoxal phosphate PLP group (blue). The combination of the carbocation and the orthophosphate results in the formation of glucose 1-phosphate [18].

1.15 Glycogen phosphorylase: the binding sites

Several binding sites have been identified on GP: the Ser14-phosphate recognition site; the allosteric site that binds the activator AMP and the inhibitor glucose-6-P; the catalytic site that binds substrates G1P and glycogen, the physiological inhibitor glucose as well as glucose analogues; the inhibitor site, which binds caffeine and related compounds; the glycogen storage site, and a new allosteric site. Because of its central role in the regulation of glycogen metabolism, GP has been a molecular target for the discovery of compounds, inhibitors that might prevent unwanted glycogenolysis under high glucose conditions.

Figure 16. A schematic diagram of the muscle GPb dimeric molecule viewed down the 2-fold axis. The positions are shown for the catalytic, allosteric, inhibitor, storage, and the new allosteric sites. The catalytic site, which includes the essential cofactor pyridoxal-5´-phosphate (PLP, not shown), is buried at the centre of the subunit accessible to the bulk solvent through a 15 Å long channel. Glucose (shown in red), a competitive inhibitor of the enzyme that promotes the less active T state through stabilization of the closed position of the 280s loop (shown in white), binds at this site. The allosteric site, which binds the activator AMP, glucose-6-P and the Bayer

compound W1807 (shown in magenta), is situated at the subunit-subunit interface some 30 Å from the catalytic site. The inhibitor site, which binds purine compounds, such as caffeine, nucleosides or nucleotides at high concentrations, and flavopiridol (shown in green) is located on the surface of the enzyme some 12 Å from the catalytic site and in the T state, obstructs the entrance to the catalytic site tunnel. The glycogen storage site (with bound maltopentaose shown in orange) is on the surface of the molecule ~ 30 Å from the catalytic site, 40 Å from the original allosteric site, and 50 Å from the new allosteric site. The new allosteric inhibitor site, located inside the central cavity formed on association of the two subunits, binds CP320626 molecule (shown in yellow) and is some 15 Å from the allosteric effector site, 33 Å from the catalytic site and 37 Å from the inhibitor site.

The catalytic site

The catalytic site, a deep cavity at the centre of the molecule, 15 Å from the protein surface and close to the essential co-factor pyridoxal-5´-phosphate, has been probed with glucose and glucose analogue inhibitors. The three dimensional structure of T state GPb in complex with α-D-glucose, has been used as the starting point for the design and synthesis of a series of glucose analogues, inhibitors that bind at the catalytic site of the enzyme [70, 71]. During this design, the inhibitors must stabilize the T state of the enzyme and mimic the contacts of glucose that stabilize the closed position of the 280s loop. On binding at the catalytic site glucose promotes the less active T state [61].

The allosteric site

The allosteric site is formed by two α helices (*α2* and *α8*), the short β strand (*β7*), it is closed by the *cap´* region and it is situated at the subunit/subunit interface. The two subunits of the functional dimer associate at two positions located on opposite sides of the enzyme molecule. One contact, the *cap´/α2* interface, is formed by the association of the *cap´* region with the *β7* strand and the *α2* helix. An identical interface is produced by the molecular 2-fold symmetry operation. A second subunit-subunit contact involves the tower interface and consists of the anti-parallel association of two symmetry related helices *α7* (residues 262-276). The Bayer compound W1807 is the most potent inhibitor of GP known to date (K_i: 1.6 nM for GPb and K_i: 10.8 nM for GPa) and was found to bind at the allosteric site [72]. It acts in synergy with glucose and caffeine. The allosteric site shows a great degree of versatility of ligand binding, which underlines great protein conformational flexibility [61].

The inhibitor site

The inhibitor site is a hydrophobic binding pocket located on the surface of the enzyme, near the domain interface at the entrance to the catalytic site (~ 12 Å from it). It comprises residues from both domains 1 (residues 13-484) and 2 (residues 485-842). In the T state, this site obstructs the entrance to the catalytic site tunnel. Binding to this site also shows great diversity: purines (e.g. adenine and caffeine), nucleotides (e.g. AMP, IMP and ATP), nucleosides (e.g. adenosine and inosine), NADH, FAD, riboflavin and flavopiridol [73]. In

the T state, the phenyl ring of Phe285 from the 280s loop, is stacked against the hydroxyl-phenyl group of Tyr613, from the start of the *α19* helix (residues 613-631) and together these two hydrophobic aromatic residues form the inhibitor site. Occupation of this site stabilizes the T state conformation of the enzyme and blocks access to the catalytic site, thereby inhibiting the enzyme. Glucose can bind simultaneously at the catalytic site, and inhibit the enzyme's activity synergistically with caffeine [72]. Part of the effectiveness of both glucose and caffeine as inhibitors arises from the interactions that both make in different ways to residues of the 280s loop that stabilize the T state conformation of the loop. The physiological significance of the inhibitor site has yet to be established [61].

The new allosteric site

In 2000, the late Dr. G. Nikos Oikonomakos and his group at the National Hellenic Research Foundation, determined the crystal structure of a novel potent inhibitor, CP320626 (IC_{50}: 334 nM), in complex with GPb and glucose [74]. The structures revealed a novel binding site located in the region of the central cavity at the subunit interface. This cavity is about 30 Å long and the radius varies from a maximum of ~ 8 Å to a minimum of ~ 4 Å and occupies a volume of about 1300 $Å^3$ in the T state GPb. The cavity is closed at one end by residues from the *cap´* region and *α2* helices (Arg33, His34, Arg60, Asp61 and their symmetry related residues) and at the other end by the tower helices (residues Asn270, Glu273, Ser276 and their symmetry related residues). In the 2.0 Å resolution 100 K native T state GPb structure, the cavity contains 60 located water molecules (30 water molecules from each subunit). These water molecules make a few contacts with the protein and only 4 out of the 30 make more than one hydrogen bond to protein atoms. Nine water molecules present in the native T state GPb structure become displaced on binding of CP320626, five from one subunit and four from the symmetry-related subunit. The CP320626 binding site in the central cavity is some 15 Å from the allosteric site, 33 Å from the catalytic site and 37 Å from the inhibitor site [61, 73, 75]. The inhibitor becomes almost entirely buried on forming the complex with GPb. Both polar and nonpolar groups are buried, but the greatest contribution comes from the nonpolar groups, which contribute 457 $Å^2$ (85%) of the surface that becomes inaccessible.

The glycogen storage site

This binding site is located on the surface of the enzyme that is more than 30 Å from the catalytic and allosteric sites and is formed by a subdomain consisting of residues 397 to 437. In the T state the 280s loop packs against a loop formed by residues 377-384 (380s loop). On transition to the R state, the disordering of the 280s loop is correlated with a displacement of the 380s loop. Glu382 shifts by 4.5 Å and a salt bridge between Glu382 and Arg770 is broken. The 380s loop is connected to the glycogen storage domain through a hydrogen bond network, so that events at the catalytic site have an indirect effect on the glycogen storage site [64].

1.16 Is there a cure for diabetes?

For diabetes type 1 there is no effective cure, as patients are totally dependent on insulin for their survival. Over the years however, several orally administrated antihyperglycaemic agents have been proposed for the treatment of diabetes type 2:

- α-glucosidase inhibitors: delay intestinal carbohydrate absorption
- Biguanide: increases liver and muscle insulin sensitivity
- Sulfonylureas (gliclazide, glimepiride, glyburide): increase insulin secretion
- Non-sulfonylureas (repaglinide, nateglinide): acute increase of insulin secretion
- Insulin sensitizers or thiazolidinediones (rosiglitazone, pioglitazone): increase adipose and muscle insulin sensitivity
- Intenstinal lipase inhibitor (orlistat): decreases intestinal fat absorption (weight loss)

However, many side effects have been noted from acute ones such as hypoglycaemia, weight gain, anaemia and gastrointestinal problems, to more severe ones such as irritable bowel syndrome and severe kidney and liver dysfunction [76].

There are other more radical methods for treating severe cases of diabetes type 2. Pancreas transplant is most commonly performed as a combined pancreas-kidney transplant, and is therefore done mainly in patients with advanced disease with renal complications. This combined transplant generally offers reduced rates of immune rejection as compared to

pancreas-only transplants. The patient survival is now excellent. There has been dramatic improvement in graft survival over the past several years [77].

There is currently a great deal of work being done to make the transplant of the islets of Langerhans a viable cure for the large number of patients with diabetes. The goal is to allow the emission of insulin and access of glucose as the primary insulin secretagogue, but prevent infiltration and destruction by the immune system of the recipient. Although work on this approach continues, there are considerable technical problems, not the least of which is identifying a material that allows the passage of glucose and insulin freely but blocks the access of immune effectors [78].

Another approach which has been tried is that of cell engineering. This involves the development of cells targeted for implantation with a unique gene complement that will produce insulin in response to glucose. An interesting study combining genetic engineering and gene therapy was reported in Korea, describing potential means of replacing insulin in diabetes. The investigators developed a bioactive, single peptide chain form of insulin, generated a gene that would make the isoform in response to glucose, and inserted that gene into hepatocytes of diabetic mice and rats. The investigators report that there was a long-term remission of diabetes in these animals [79].

A recent study investigated new targets within the liver as potential antihyperglycaemic drugs. They include glucokinase, which catalyzes the first step in glucose metabolism, the glucagon receptor and enzymes of gluconeogenesis and glycogenolysis such as glucose-6-phosphate, fructose-1,6-bisphosphatase and glycogen phosphorylase. Preclinical studies with candidate drugs on animal models were very promising. Data from clinical studies are awaited [80].

1.17 The aim

The worldwide "epidemic" of diabetes and the recognition that lifestyle and obesity are major epidemiologic determinants of the disease, call for immediate action in the prevention and treatment of the disease. The goal is to find new drugs that will lower blood glucose levels without the risk of hypoglycaemia and other severe complications. The aim of this project was to extend our knowledge on molecular recognition of small molecules at the catalytic, allosteric, new allosteric and inhibitor sites of glycogen phosphorylase. Research conducted is part of an ongoing project to discover new GP drugs as potential hyperglycaemic agents. Inhibitors of GP have been proposed as a therapeutic strategy for improving glycaemic control in diabetes type 2 and various studies have shown the efficacy of such compounds at lowering blood glucose or inhibiting liver glycogenolysis *in vivo*. Inhibitor design for GP targets mainly the catalytic site. In this project we wished to develop new potent inhibitors by using as scaffolds the inhibitor *N*-acetyl-β-D-glucopyranosylamine and oxadiazole derivatives of glucopyranose. Several groups of compounds were studied including glucosyltriazolylacetamide, pentacyclic triterpenes, hydroquinone derivatives, glucopyranosylidene-spiro-iminothiazolones and aldehyde/ketone glucopyranosyl thiosemicarbazones. Structural comparisons were made with *N*-acetyl-β-D-glucopyranosylamine, *N´*-benzoyl-β-D-glucopyranosylamine and flavopiridol depending on the location of binding. All compounds were tested kinetically in order to determine their IC_{50} value and for those compounds with a strong inhibitory effect against GPb, with IC_{50} less than approximately 100 µM, detailed K_i experiments were performed. To elucidate the mechanism of inhibition for these compounds, the crystal structures of GPb in complex with each one of these inhibitors were determined and refined at high resolution.

2. Materials & Methods

2.1 Extraction and purification of glycogen phosphorylase b from rabbit skeletal muscle

Glycogen phosphorylase b was isolated from rabbit skeletal muscle according to a slight modification (L-cysteine was replaced with 2-mercaptoethanol) of the original protocol developed by Dr. Edmond H. Fischer and Dr. Edwin G. Krebs [81, 82]. They were awarded the Nobel Prize in Physiology or Medicine in 1992 for discovering reversible protein phosphorylation.
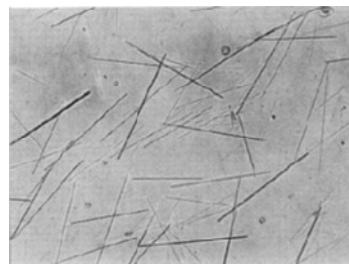
Figure 17. The first pictures of crystalline glycogen phosphorylase b isolated and crystallized by E. H. Fischer and E. G. Krebs in 1958 [81].

Materials

- 4 rabbits
- Cheese cloth
- Glass wool
- Büchner funnel
- Round filter papers 15 cm
- Dialysis tubing
- Cellulose: SIGMA, 25x16 mm
- Large centrifugation tubes
- $(CH_3COO)_2Mg \cdot 4H_2O$: SIGMA, MW 214.45 g/mol
- Adenosine-5-monophosphate (AMP): SIGMA, MW 365.24 g/mol

- Centrifuge: Sorvall Instruments, RC5C
- UV-Visible Spectrophotometer: CARY 100 Conc
- Saturated $KHCO_3$: SIGMA, MW 100.12 g/mol
- Acetic acid (1 N)
- 90% $(NH_3)_2SO_4$: SIGMA, MW 132.14 g/mol
- Tris(hydroxymethyl)aminomethane (Tris): SERVA, MW 121.10 g/mol
- Glycerol (plant): SERVA, MW 92.10 g/mol

- Buffer solution: β-GP (50 mM), 2-mercaptoethanol (50 mM), EDTA (1 mM)
  - ✓ *β-glycerol phosphate disodium salt pentahydrate: FLUKA, MW 306.12 g/mol*
  - ✓ *2-mercaptoethanol: MW 78.30 g/mol*
  - ✓ *Ethylenediaminetetraacetic acid (EDTA): SERVA, MW 372.30 g/mol*

Experimental procedure

Rabbit skeletal muscle extraction

The muscle from the hind legs and back of the rabbits was excised and placed on ice. It was then ground in a meat grinder at room temperature, weighed out and kept on ice until all the muscle had been ground. The enzyme was extracted from the ground muscle by treating the muscle with distilled water three times in less than 30 minutes. More specifically, the ground muscle was stirred with a volume of distilled water equal to the weight of the ground muscle for 8 minutes, filtered through two cheese clothes and the solution was collected in a beaker cooled on ice. During the final round the ground muscle was stirred with a volume of distilled water equal to half of the weight of the ground muscle for 8 minutes, filtered through two cheese clothes, and collected in a beaker cooled on ice. The extract was then combined and filtered through glass wool to remove remaining particles of fat.

Precipitation of unwanted proteins and enzymes in an acidic environment

The pH of the cold extract was adjusted to 5.1-5.2 by addition of acetic acid (1 N) solution while stirring gently. An increase in turbidity was observed as a result of the precipitation of various unwanted proteins. The extract was placed on ice for 5 minutes and then centrifuged at 5500 rpm (5117 g) for 30 minutes at 0-4°C. The supernatant was filtered through a Büchner funnel (on ice) to remove any remaining unwanted material. The pH was adjusted to 6.8 with the addition of saturated $KHCO_3$ solution.

Precipitation of glycogen phosphorylase with ammonium sulphate

The pH of a saturated ammonium sulphate (90% w/v) solution was adjusted to 6.8 with the addition of a few drops of ammonium hydroxide with the use of pH paper. An appropriate amount of the ammonium sulphate solution was added to the protein solution to reach a concentration of 41% w/v. The mixture was then allowed to stand in the cold room (4°C) overnight. The next day the supernatant was discarded with the use of a pump, and the precipitate was collected by centrifugation at 5500 rpm (5117 g), for 30 minutes at 0-4°C. After centrifugation, the supernatant was discarded and the pellet was dissolved in the minimum amount of distilled water (<100 ml for the entire pellet) at room temperature. The solution was then dialyzed overnight at 4°C against 0.001 M Tris at pH 7.5.

Heat treatment at high pH

After dialysis the protein solution was centrifuged at 15000 rpm (27000 g), for 30 minutes at 0-4°C and the following reagents were added to the supernatant solution:

- ✓ *2-mercaptoethanol 0.3 M, pH 7.0, final concentration 0.03 M*
- ✓ *EDTA 0.1 M, pH 7.0 (EDTA volume=(supernatant volume after the addition of 2-mercaptoethanol × 5)/1000)*
- ✓ *Tris 2 M, in order to adjust the pH to 8.8*

The mixture was then incubated at 37°C for 1 hour with continuous stirring, cooled in the cold chamber for 10 minutes and adjusted to pH 7.0 with acetic acid (1 N). The solution was centrifuged at 15000 rpm (27000 g) for 10 minutes and the pellet discarded. The heat treatment at high pH in the presence of EDTA and 2-mercaptoethanol serves to inactivate enzyme contaminants.

Crystallization and re-crystallization of glycogen phosphorylase b

AMP (0.1 M, pH 7.0) and $(CH_3COO)_2Mg \cdot 4H_2O$ (1.0 M, pH 7.0) were added to the supernatant in a ratio of 1:100 with respect to the enzyme solution. The crystallization involves the formation of an Mg^{++}/AMP/enzyme complex. The solution was cooled to 0°C (on ice), and left overnight in the cold room so crystallization of phosphorylase b could

take place (crystallization usually starts within 10 minutes to 2 hours and lasts approximately 6 hours in total). The next day the crystals were collected by centrifugation at 15000 rpm (27000 g) for 10 minutes (0-4°C). Enzyme crystals were dissolved in the minimum amount of freshly prepared buffer solution of β-GP/ 2-mercaptoethanol/ EDTA buffer solution at 30°C. Centrifugation of this solution was performed at 17500 rpm (37000 g) for 10 minutes (25-30°C). AMP (0.1 M, pH 7.0) and $(CH_3COO)_2Mg \cdot 4H_2O$ (1.0 M, pH 7.0) were added to the supernatant at a ratio of 1/100 with respect to the enzyme solution. The final mixture was placed into centrifuge tubes at 0°C for several hours. Re-crystallization of the enzyme in this way was performed 4 more times in 3-4 hour intervals. In the final two re-crystallization procedures, addition of AMP and $(CH_3COO)_2Mg \cdot 4H_2O$ was omitted. At the end, enzyme concentration was determined by measuring the absorption at 260 and 280 nm and using $A^{1\%}_{280nm}$=13.2 for a cell with a path length of 1 cm. The ratio of the optical densities at wavelengths 260 nm and 280 nm is a measure of the nucleotide concentration in the enzyme solution. A value of 0.62 for the A_{260}/A_{280} ratio is usually suitable for the long-term preservation of the enzyme solution. At this value the mol ratio of enzyme:AMP is usually 1:1. Glycerol, a cryoprotectant, was added (50% of the total volume) and the enzyme was kept at -20°C for experimental use.

2.2 Kinetics of glycogen phosphorylase

The aim of a kinetic experiment is to measure the rate of formation of a product or the rate of cleavage of a substrate under specific conditions. The data collected can then be used to determine the kinetic constant (K_m) of the enzyme and characterize its behaviour. Enzymes are very sensitive to the conditions of an experiment and therefore parameters such as temperature (30°C) and pH (6.8) must be closely monitored and kept stable. There are various types of inhibition systems. Glycogen phosphorylase inhibitors usually follow competitive inhibition kinetics.

Competitive inhibition

A competitive inhibitor is a substance that combines with free enzyme in a manner that prevents substrate binding. It diminishes the rate of catalysis by reducing the proportion of

enzyme molecules bound to a substrate. Under these conditions, the substrate outcompetes the inhibitor for the active site. The inhibitor and the substrate are mutually exclusive, because they compete for the same site. The substrate molecule cannot enter the active site while the inhibitor is there, and the inhibitor cannot enter the active site when the substrate is there. At any given moment, competitive inhibitor concentration can be overcome by increasing the substrate concentration, in which case the substrate will outcompete the inhibitor in binding to the enzyme [18, 86].

Non-competitive inhibition

A non-competitive inhibitor has no effect on substrate binding and *vice versa*. It acts by decreasing the turnover number rather than by diminishing the proportion of enzyme molecules that are bound to the substrate. Non-competitive inhibition, in contrast with competitive inhibition, cannot be overcome by increasing the substrate concentration. The inhibitor and the substrate bind reversibly, randomly and independently at different sites. The inhibitor binds to the enzyme and to the enzyme-substrate (ES) complex. The substrate binds to the enzyme and the enzyme-inhibitor (EI) complex. The binding of one ligand has no effect on the dissociation constant of the other. However, the substrate and the inhibitor are not mutually exclusive but the resulting ESI complex is inactive [18, 86].
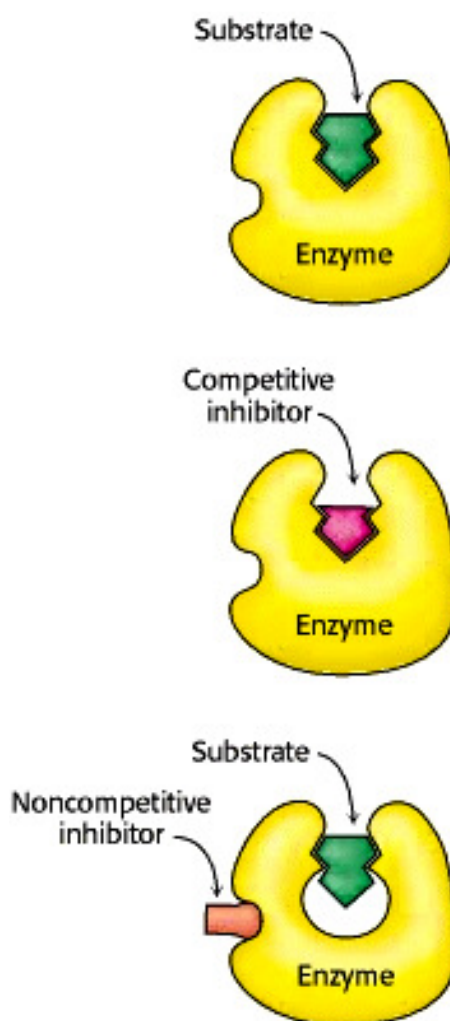
Figure 18. Distinction between competitive and non-competitive inhibition. In competitive inhibition the inhibitor binds to the active site thus preventing the substrate from binding. However, in non-competitive inhibition the inhibitor does not prevent the substrate from binding [18].

Uncompetitive inhibition

An uncompetitive inhibitor binds reversibly only to the enzyme-substrate (ES) complex yielding an inactive ESI complex. The inhibitor does not bind to the free enzyme. Uncompetitive inhibition works best when substrate concentration is high. An uncompetitive inhibitor need not resemble the substrate of the reaction it is inhibiting [86].

2.3 Kinetics: The K_m experiment

Materials

- UV-Visible Spectrophotometer, CARY 100 Conc
- Water bath (30°C)
- α-D-glucose-1-phosphate: SIGMA, MW 336.00 g/mol
- Adenosine-5-monophosphate (AMP): SIGMA, MW 365.24 g/mol
- Glycogen (oyster): SIGMA

- Sodium dodecyl sulphate (SDS): SIGMA, MW 288.38 g/mol
- L-ascorbic acid (vitamin C): FLUKA, MW 176.13 g/mol
- Ammonium molybdate: SDS, MW 1235.68 g/mol
- Zinc acetate: SIGMA, MW 219.49 g/mol
- KH_2PO_4: MERC, MW 136.09 g/mol

- Buffer solution: β-GP (50 mM), 2-mercaptoethanol (50 mM), EDTA (1 mM)
  - ✓ *β-glycerol phosphate disodium salt pentahydrate: FLUKA, MW 306.12 g/mol*
  - ✓ *2-mercaptoethanol: MW 78.30 g/mol*
  - ✓ *EDTA: SERVA, MW 372.30 g/mol*
- Buffer solution: Imidazole (30 mM), KCl (60 mM), EDTA (0.6 mM), DTT (0.6 mM)
  - ✓ *Imidazole: SERVA, MW 68.10 g/mol*
  - ✓ *KCl: SIGMA, MW 74.56 g/mol*
  - ✓ *EDTA: SERVA, MW 372.30 g/mol*
  - ✓ *DL-Dithiothreitol (DTT): SIGMA, MW 154.25 g/mol*

Preparation of glycogen

45 grams of glycogen were dissolved in 900 ml of distilled water. 2 grams of charcoal were added to the homogenous solution and mixed with a glass rod for approximately 10 minutes. The solution was then centrifuged at 5000 rpm (3640 g), for 10 minutes at 8°C. The centrifugation was repeated twice in order to make sure that glycogen was free from any nucleotides e.g. AMP. The final solution was filtered several times in order to remove any remaining charcoal using a Büchner funnel and filter paper. The solution was centrifuged at 5000 rpm (3640 g), for 10 minutes at 8°C. When the charcoal was removed completely, absolute ethanol was added to the solution, at a final concentration of 60%.

Volume of ethanol = 1.5 × volume of glycogen

The final solution was kept at 0°C, for 15 minutes and the precipitate was collected by centrifugation at 5000 rpm (3640 g), for 10 minutes at 8°C. The precipitate was then filtered and washed with ethanol. Finally, the precipitate was lyophilized and the solid glycogen was dissolved in pure water, so that the final concentration of glycogen was 10%.

Experimental procedure

K_m is the concentration of substrate at which half of the active sites are filled. Thus, it provides a measure of the substrate concentration required for significant catalysis to occur. The maximal rate, V_{max}, reveals the turnover number of an enzyme, which is the number of substrate molecules converted into product by an enzyme molecule in a unit time, when the enzyme is fully saturated with substrate [18]. Glycogen phosphorylase catalyzes the first step in the degradation of glycogen:

Glycogen $_{(n)}$ + P$_i$ ⟷ Glycogen $_{(n-1)}$ + G1P

This reaction can be catalyzed by GPb in either direction *in vitro*. However, for purely experimental purposes as it is easier to measure P$_i$ release, the reaction measured *in vitro* was that of glycogen synthesis. The reaction was driven towards glycogen synthesis by adding an excess of G1P in the reaction. During the kinetic experiment, reaction rates were measured at pH 6.8 and 30°C by the release of orthophosphate ions from G1P. The substrate G1P is hydrolyzed by 78% during this reaction.

Preparation of G1P solutions at various concentrations

A stock solution of G1P (400 mM) was diluted with the buffer solution of imidazole (200 mM), KCl (200 mM), EDTA (4 mM), DTT (4 mM) in order to obtain a G1P solution of 90 mM in imidazole (135 mM), KCl (270 mM), EDTA (2.7 mM), DTT (2.7 mM) at pH 6.8. This concentration of G1P was then used in order to obtain the following G1P solutions, all in imidazole (135 mM), KCl (270 mM), EDTA (2.7 mM), DTT (2.7 mM) at pH 6.8: 9 mM, 18 mM, 22.5 mM, 45 mM and 67.5 mM.

Preparation of the various substrate solutions

Six solutions were prepared each containing G1P at various concentrations, AMP (50 mM), which acts as an activator of the reaction, and distilled water. In more detail, the final solutions contained AMP (1mM), H_2O and the following G1P concentrations: 2 mM, 4 mM, 5 mM, 10 mM, 15 mM and 20 mM. The low concentrations of G1P are needed in order to determine the K_m of the enzyme, while the higher concentrations are needed in order to determine the V_{max} of the reaction.

Preparation of the enzyme solution

The original stock solution of GPb was diluted using the buffer solution of β-GP (50 mM), 2-mercaptoethanol (50 mM), EDTA (1 mM). The concentration of this solution was determined by measuring the absorbance at 280 nm (due to the presence of tyrosine and tryptophan) and by converting this into concentration using the Beer-Lambert law: $A=\varepsilon \times c \times l$, where A is the concentration of the protein, ε is the extinction coefficient for the protein (1.32 ml × cm/mg), c is the concentration of the protein and the path length is 1 cm [83]. Once the concentration of the solution was known, an enzyme mixture solution was prepared which contained the following:

- ✓ *GPb 25 μg/ml*
- ✓ *Glycogen 0.2 % w/v*
- ✓ *Buffer solution β-GP (2.5 mM), 2-mercaptoethanol (2.5 mM), EDTA (0.05 mM)*

Preparation of "blanks"

The determination of the K_m value is based on the release of orthophosphate ions from G1P. Therefore any other presence of phosphate ions must be accounted for. Two sets of blanks were prepared from which the average is calculated for greater accuracy. Two series of "blank" solutions were prepared:

- ✓ *G1P blank at the maximum concentration present during the reaction*
- ✓ *Glycogen blank*
- ✓ *Phosphate blank from which the absorbance of each μmol of phosphate ions is calculated*

Inorganic phosphate assay

The determination of inorganic phosphate ions released by the hydrolysis of G1P was carried out according to the protocol by Saheki *et al* [84]. This method is based on the reduction of the phosphomolybdate complex with ascorbic acid. A solution was prepared containing 15 mM ammonium molybdate and 100 mM zinc acetate. The pH was adjusted to 5.0 with concentrated HCl. Another solution was prepared containing 10% w/v ascorbic acid. The pH of this solution was also adjusted to 5.0 with NaOH (1 N). These two solutions were mixed in a ratio of 1:4 with respect to the ascorbic acid solution. The mixture is light sensitive and was therefore kept in an aluminium foil wrapped flask and a minimum incubation time of 15 minutes was required prior to its use. Inorganic phosphate ions form a complex with ammonium molybdate in the presence of Zn^{2+} at pH 5.0, which strongly absorbs ultraviolet light. After the reduction with ascorbic acid, the complex produces a chromophore that shows maximum absorption at wavelength 850 nm. However, the exact role of Zn^{2+} is not exactly known.

Experimental procedure

The enzyme solution was placed in a water bath at 30°C for 10 minutes. After this time period the substrates were also added and the mixture was incubated for an additional period of 5 minutes. The reaction proceeded by adding 180 µl of enzyme solution to each substrate containing tube every 20 seconds. After the reaction was complete, aliquots of

200 µl from each of the assay tubes were removed every 20 seconds and were placed in tubes containing 50 µl of 1% w/v SDS. This way the reaction was stopped. 2.5 ml of the ammonium molybdate/zinc acetate/ascorbic acid mixture were added to each assay tube and placed in the water bath for 20 minutes at 30°C. Finally, the absorbance values were measured at 850 nm.

Processing the data

After deducting the "blank" values from the recorded assay absorbance values, data were processed with the program Grafit [85] using non-linear regression and explicit weighting. Absorbance values were converted to specific activity, which is the amount of product formed by the enzyme in a given amount of time under given conditions per milligram of enzyme. It is also a measure of the purity of the enzyme. The equation used in order to calculate the specific activities is the following:

$$v = \frac{1}{t} \times ln\left(\frac{limit}{limit - \mu molPi}\right) \times limit$$

✓ *v: reaction rate*   ✓ *limit: concentration of G1P used in the assay × total*
✓ *t: reaction time*   *volume of the reaction × percentage of hydrolyzed G1P*
(78%)

The K_m and V_{max} values were calculated based on the Michaelis-Menten equation:

$$v = \frac{vmax \times [S]}{Km + [S]}$$

✓ *v: initial rate of reaction*
✓ *[S]: substrate concentration*
✓ *v_{max}: maximum rate of reaction*
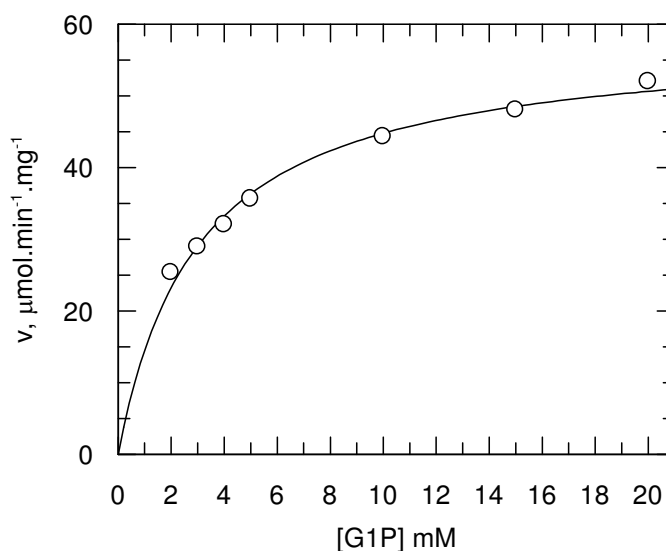
Figure 19. A curve obtained from a GPb assay: K_m: 2.0 ± 0.2 mM

& V_{max}:50.2 ± 2.8 $\mu mol.min^{-1}.mg^{-1}$

2.4 Kinetics: The IC$_{50}$ experiment

The IC$_{50}$ value is the concentration of the inhibitor which reduces the enzyme's activity by 50 %. The procedure followed during an experiment for the determination of the IC$_{50}$ is exactly the same with that used for the determination of the K$_m$, but the experiment is carried out in the presence of only one concentration of G1P (2 mM) and in the presence of an inhibitor. Inhibitors were usually dissolved in dimethyl sulfoxide (DMSO) at a final concentration of 1 % or 2 % w/v in the assay. In some cases inhibitors were fully soluble in water, if hydrophilic groups were present. As in the previous experiments for the determination of the K$_m$, substrate mixtures also contained AMP (final concentration 1 mM) which activates the reaction. Using the program Grafit, after the specific activities (s.a) were calculated, the % inhibition values were calculated for each concentration of inhibitor using the following formula:

$$\% \ inhibition = \frac{s.\,a\ control - s.\,a\ inhibitor}{s.\,a\ control} \times 100$$

The IC$_{50}$ value was derived by plotting % inhibition vs. inhibitor concentration as seen below:
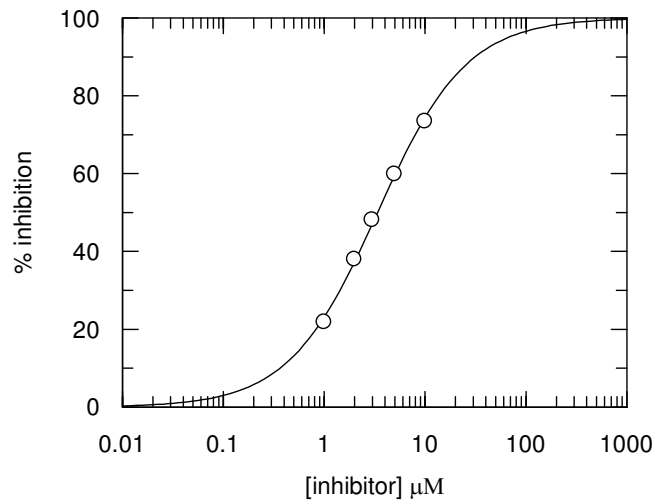
Figure 20. The IC$_{50}$ curve. IC$_{50}$ = 3.4 ± 0.1 μM

2.5 Kinetics: The K$_i$ experiment

The basic procedure to determine the K$_i$ value for an inhibitor is the same as for an IC$_{50}$ experiment, however more parameters are involved. K$_i$ is the dissociation, inhibition constant for the enzyme-inhibitor combination.
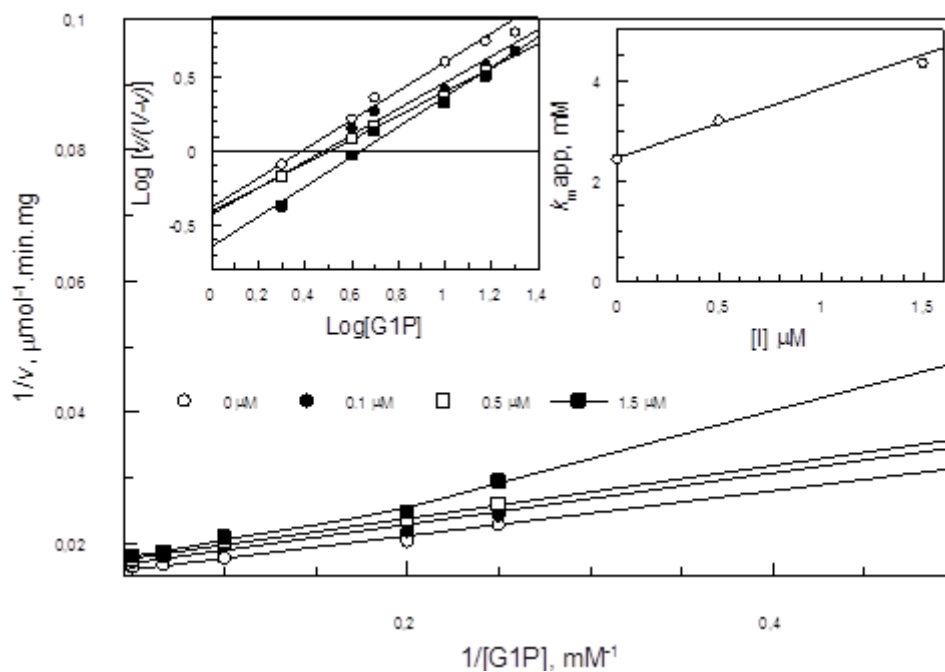
Figure 21. The K$_i$ graph (K$_i$: 1.8 ± 0.2 μM).

It is carried out with respect to either G1P or AMP (based on the location of binding) at 6 different G1P or AMP concentrations vs. 3 different inhibitor concentrations. Using the program Grafit, a Lineweaver-Burk plot of 1/v vs. 1/[G1P] is created. The Lineweaver-Burk plot is one way of visualizing the effect of inhibitors and determining the K_m constant and the V_{max} from a set of measurements of velocity at different substrate concentrations. A straight line is obtained where the slope is equal to K_m/V_{max} and the y-intercept is equal to $-1/V_{max}$. Kinetic data are then transferred into Hill plots, which yield the values for the apparent K_m values and the Hill coefficients. A Hill coefficient provides a way to quantify the binding of a ligand to a macromolecule. From the plot of the K_m apparent values vs. inhibitor concentrations the K_i value is calculated (figure 21).

The K_i can also be estimated based on the IC_{50} value using the formula: $$Ki = \frac{IC50}{1 + [S]/Km}$$

2.6 X-ray crystallography

The most common experimental means of obtaining a detailed structure of a large molecule is to interpret the diffraction of X-rays from many identical molecules in an ordered array like in a crystal. This is defined as X-ray crystallography. Currently, the Protein Data Bank, the world's largest repository of macromolecular models obtained from experimental data, contains more than 64000 structures of proteins and nucleic acids determined by X-ray crystallography.

Obtaining an image from an object

When we see an object, light rays are diffracted by the object and enter the eye through the lens, which reconstructs an image of the object and focuses it on the retina. Something analogous to this happens in X-ray crystallography. X-rays diffracted from the object are received and measured by a detector. The measurements are fed to a computer, which simulates the action of a lens to produce a graphics image of the object.
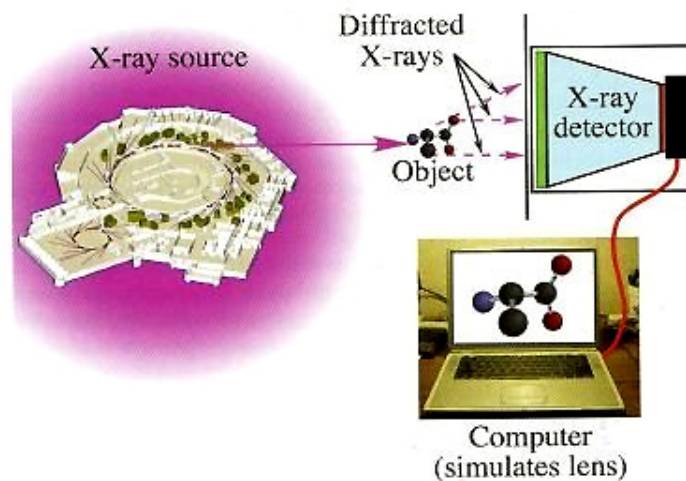
Figure 22. Crystallographic analogy of lens action [87].

Properties of protein crystals

Under certain circumstances proteins solidify to form crystals. In entering the crystalline state from solution, individual molecules of the protein adopt a specific orientation. The resulting crystal is an orderly three dimensional array of molecules. Protein crystals are held together by primarily hydrogen bonds between hydrated protein surfaces. They are extremely fragile and therefore growing, handling and mounting for analysis require very gentle techniques.

Early protein crystallographers examined dry protein crystals and obtained no diffraction pattern. However, in 1934 John Desmond Bernal and Dorothy Crowfoot Hodgkin measured diffraction from pepsin crystals still in their mother liquor. To their surprise they recorded sharp diffraction patterns, with reflections that corresponded in real space to the distances between atoms. The announcement of their success was the birth of protein crystallography. Careful analysis of electron density maps usually reveals many ordered water molecules on the surface of crystalline proteins. Additional disordered water molecules are presumed to occupy regions of low density between ordered particles. The quantity of water varies among proteins and even among different crystal forms of the same protein.

Figure 23. Crystals are not perfectly ordered. They consist of many small arrays in rough alignment with each other [87].

Unit cells and lattices

The image of a crystal is that of a perfect array of unit cells stretching throughout. A crystal is divided into identical unit cells. The dimensions of a unit cell are designated by six numbers: the lengths of three unique edges *a*, *b* and *c*; and three unique angles α, β and γ. If $a=b \neq c$, and $\alpha=\beta=\gamma=90°$ the cell is tetragonal as in the case of glycogen phosphorylase crystals.
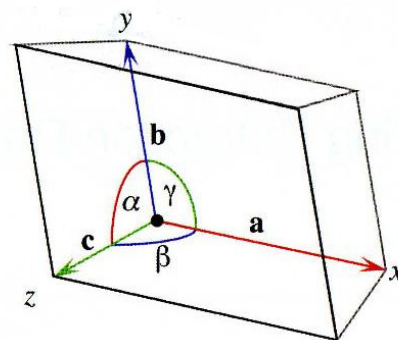
Figure 24. A unit cell with edges a, b, c and angles α, β and γ [87].
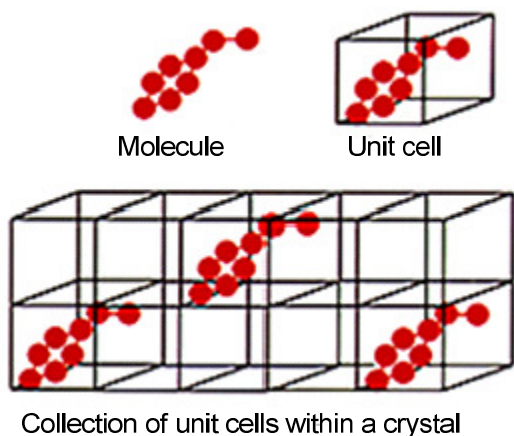
Figure 25. A unit cell for a molecule [128].

The unit cell is the smallest and simplest volume element that is completely representative of the whole crystal. The unit cells make up the lattice of the crystal. The most readily apparent sets of planes in a crystalline lattice are those determined by the faces of the unit cells.

These can be thought of as sources of diffraction and can be designated by a set of three numbers called lattice indices or Miller indices. Three indices *hkl* identify a particular set of equivalent, parallel planes. When it comes to data collection the internal symmetry of the unit cell is fundamental. The symmetry of a unit cell and its contents is described by its space group, which describes the cell's internal symmetry elements. The space group of glycogen phosphorylase is *P4$_3$2$_1$2*. The capital letter indicates the lattice type and the numbers represent the symmetry operators that can be carried out on the unit cell without changing its appearance. Mathematicians in the late 1800s showed that there are exactly 230 possible space groups and 13 allowable lattices, known as the *Bravais lattices*.

X-ray sources

X-rays are electromagnetic radiation of wavelengths 0.1-100 Å. X-rays can be produced by bombarding a metal target (most commonly copper, molybdenum or chromium) with electrons produced by a heated filament and accelerated by an electric field.
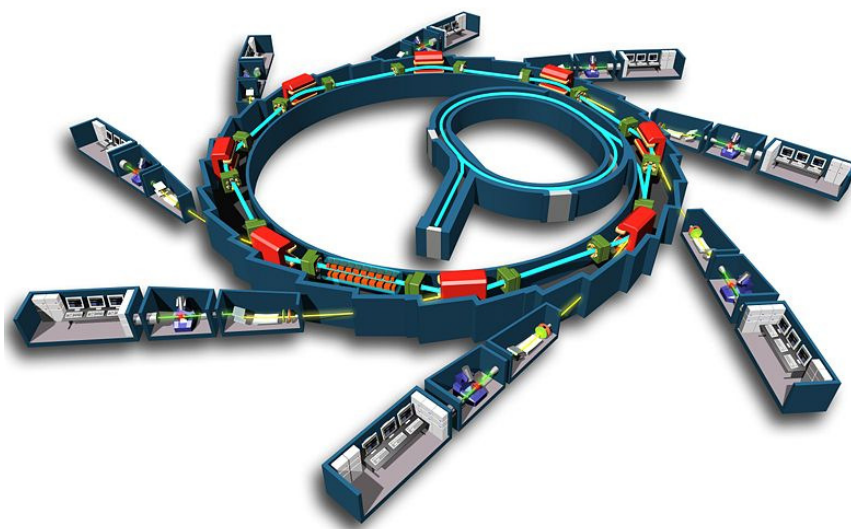
Figure 26. The circular ring is the synchrotron, i.e. a particle accelerator that brings electrons to very high speeds. The synchrotron emits radiation (X-rays) which is sent into the various beamlines.

A high energy electron collides with and displaces an electron from a low-lying orbital in a target metal atom. Then an electron from a higher orbital drops into the resulting vacancy, emitting its excess energy as an X-ray photon. The electrons circulate at velocities near the speed of light, driven by energy from radio frequency transmitters and are maintained in

circular motion by powerful magnets. Accessory devices called *wigglers* cause additional bending of the beam, thus increasing the intensity of radiation. The beam is directed through a *collimator*, a narrow metal tube that selects and reflects the X-rays into parallel paths, producing a narrow beam. During data collection, the direct beam is blocked just after the crystal by a piece of lead called the *beam stop*, which is used to prevent excessive radiation from reaching the detector (almost 95 % of the incident beam passes through the crystal and only 5 % is diffracted), thus obscuring low-angle reflections [87].

X-ray data collection, processing and model building

A crystal is mounted on a *goniometer head*, a device that allows the crystal orientation to be set and rotated precisely. The goniometer head with the crystal are mounted onto a system of movable circles called a *goniostat*, which allows automated, highly precise movements of the crystal into almost any orientation with respect to the X-ray beam. The crystal is mounted between an X-ray source and an X-ray detector.

Figure 27. X-ray instrumentation used at the EMBL Synchrotron Outstation in Hamburg, Germany

The crystal lies in the path of a narrow beam of X-rays coming from the source. The simplest source is an X-ray tube, and the simplest detector is an X-ray film, which when developed exhibits dark spots where X-ray beams have impinged. These spots are called *reflections* because they emerge from the crystal as if reflected from planes of atoms.
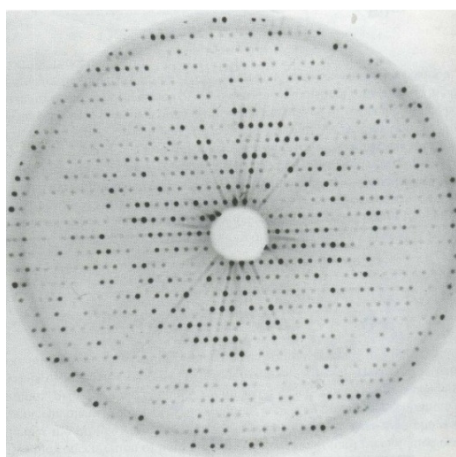
Figure 28. Diffraction pattern from a protein crystal [87].

However, simple detectors have now been replaced with image plates and charge-coupled devices (CCD). The latter are photon counters, solid state devices that accumulate charge (electrons) in direct proportion to the amount of light that strikes them. An optical scanner precisely measures the position and the intensity of each reflection and transmits the information in digital form to a computer for analysis. The crystal diffracts the source beam into many discrete beams, each of which produces a distinct reflection on the film. When an X-ray beam is directed toward a crystal, the actual diffractors of the X-rays are the clouds of electrons in the molecules of the crystal. The greater the intensity of the X-ray beam that reaches a particular position, the darker the reflection. Area detectors collect many reflections at once.
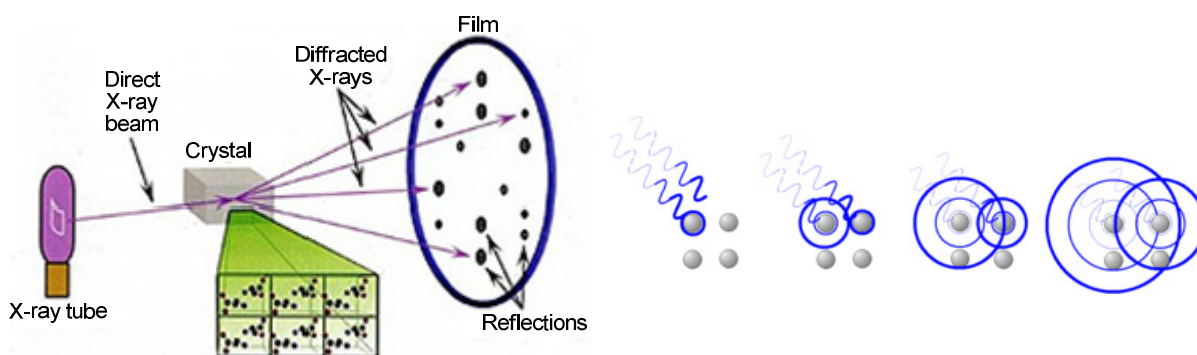
Figure 29. Crystallographic data collection. The positions and intensities of these reflections contain the information needed to determine molecular structures (left) and the way X-rays interact with atoms in a crystal (right) [87].

The position of a reflection can be used to obtain the direction in which that particular beam was diffracted by the crystal. The intensity of a reflection is obtained by measuring the optical absorbance of the spot on the film, giving a measure of the strength of the diffracted beam that produced the spot. The computer program that reconstructs an image of the molecules in the unit cell requires these two parameters: a) the position *hkl* for each diffracted beam that produces a reflection at the detector and b) the intensity I_{hkl}. The *intensity* is a number that indicates how dark the reflection is in comparison to others. The beam direction is specified by the Miller indices, a set of three-dimensional coordinates, *h*, *k* and *l* for each reflection. The result of X-ray data collection is a list of intensities, each assigned an index *hkl* corresponding to its position in the reciprocal lattice. The intensity

assigned to reflection *hkl* is a measure of the relative strength of the reflection from the set of lattice planes having indices *hkl*. The frames collected are then merged into one data set by multiplying all intensities in each frame by a *scale factor*. A *merging R factor* gives the level of agreement among the different frames of data after scaling. In the last stages of structure determination, cycles of map calculation and model building, which are forms of real-space refinement of the model, are interspersed with computerized attempts to improve agreement of the model with the original intensity data. Early in refinement the whole model is held rigid to refine its position in the unit cell. Then, blocks of the model are held rigid while their positions refine with respect to each other. In the end individual atoms are freed to refine with only stereochemical restraints. The *temperature factor B*, is a measure of how much an atom oscillates around its position, while *occupancy* is a measure of the fraction of molecules that an atom actually occupies in a given position. The *R factor* is a measure of the agreement between the calculated and the observed data. Finally, the demanding and revealing criterion of model quality is the *free R factor*. This is a small set of randomly chosen intensities, the "test set", which are set aside from the beginning and are not used during refinement. They are only used in cross validation, a quality control that entails assessing the agreement between calculated and observed data.

Bragg's law

In 1912 William Lawrence Bragg, working with his father Sir William Henry Bragg, realized that focusing effects arise if X-rays are reflected by series of atomic planes. He formulated a direct relationship between the crystal structure and its diffraction pattern with the following equation:

$$n\lambda = 2d\ sin\vartheta$$

This formula shows that a set of parallel planes with index *hkl* and interplanar spacing d_{hkl} produces a diffracted beam when X-rays of wavelength λ impinge upon the planes, at an angel θ and are reflected at the same angle, where *n* is an integer. Bragg's law confirmed the existence of real particles at the atomic scale, as well as providing a powerful new tool for studying crystals in the form of X-ray and neutron diffraction. Father and son were awarded the Nobel Prize in Physics in 1915 for their work in determining crystal structures beginning with NaCl, ZnS and diamond.

The Fourier transform and structure factors

The French mathematician Jean Baptiste Joseph Fourier (1768-1830) showed that even the most intricate periodic functions can be described as the sum of simple sine and cosine functions, whose wavelengths are integral fractions of the wavelength of the complicated function. Such a sum is called a *Fourier series*. Following data collection, computers are used to produce images of molecules in the crystals using the Fourier transform. This lens-simulating operation describes precisely the mathematical relationship between an object and its diffraction pattern. The transform allows us to convert a Fourier sum description of the reflections to a Fourier sum description of the electron density. Each diffracted X-ray that arrives at the film to produce a recorded reflection can also be described as the sum of the contributions of all scatterers in the unit cell. The sum that describes a diffracted ray is called a *structure factor equation*. The computed sum of the reflection *hkl* is called a *structure factor F_{hkl}*. A reflection can therefore be described by the structure-factor equation, containing one term for each atom or for each volume element in the unit cell. Every atom in the unit cell contributes to every reflection in the diffraction pattern. F_{hkl} is therefore a wave created by the superposition of many individual waves F_j, each resulting from diffraction by an individual atom. In other words, the electron density is described by a Fourier sum in which each term is a structure factor. The Fourier series is used to convert the structure factors *hkl* of the two dimensional diffraction pattern to *ρ(x, y, z)*, the desired electron density within the crystal [87].

The phase problem

The phase problem is the most demanding element that crystallographers face and involves the determination of the phase angle α_{hkl} for each reflection. There are three common methods for overcoming this obstacle. These include *isomorphous replacement*, *anomalous scattering* and *molecular replacement*. Each of these techniques yields only estimates of phases, which must be improved before an interpretable electron density map can be obtained.

Isomorphous replacement

Each atom in the unit cell contributes to every refection in the diffraction pattern. A specific atom contributes to some reflections strongly, to some weakly or not at all.

Therefore the principle of isomorphous replacement is to add one or a very small number of atoms to identical sites in all unit cells of the crystal, in order to track down changes in the diffraction pattern, as the result of the additional contributions of the added atoms. The slight perturbation in the diffraction pattern caused by the added atom(s) can be used to obtain initial estimates of phases. In order for these perturbations to be large enough to measure, the added atom must be a strong diffractor and therefore it should have a much larger atomic number than those usually present in a protein (C, N, O, H, S, P). Such atoms are called "heavy atoms" such as mercury, lead, platinum, gold, osmium, xenon, holmium, etc. [96].

Anomalous scattering

A second means of obtaining phases from heavy atom derivatives takes advantage of the heavy atom's capacity to absorb X-rays of specified wavelength. As a result of this absorption, the reflections *hkl* are not equal in intensity. This inequality of symmetry related reflections is called anomalous scattering or anomalous dispersion. Elements absorb X-rays and emit them, and this absorption drops sharply at wavelengths just below their characteristic emission wavelength. This sudden change in absorption is called *absorption edge*. An element exhibits anomalous scattering when the X-ray wavelength is near the element's absorption edge. Absorption edges of light atoms in the unit cell are not near the wavelength of X-rays used in crystallography, so carbon, nitrogen and oxygen do not contribute to anomalous scattering. However, absorption edges of heavy atoms are in this range [96].

Molecular replacement

This is the technique where phases from structure factors of a known protein are used as initial estimates of phases for a new protein. This gives the crystallographer the opportunity to determine the structure of a new protein from a single native data set. The known protein is superimposed onto the new protein in order to create the best phasing model and the new unit cell dimensions and symmetry can be calculated. Measured amplitudes $|F_{calc}|$ obtained from diffraction intensities of the new protein are compared to the structure factor $|F_{obs}|$ of the model, in order to calculate the *R factor*, which indicates the agreement between calculated and observed data and helps find the best location of the model protein.

$$R\ factor = \frac{\sum||Fobs| - |Fcal||}{\sum|Fobs|}$$

Difference *Patterson maps* are created in order to find the best orientation of the model protein. If the observed and calculated intensities agree with each other the *R factor* is small. For perfect agreement, all the differences equal zero and the *R factor* equals zero.

Experimental procedure

Diffraction data were collected from single crystals at the EMBL-Hamburg outstation and the Daresbury Radiation Source-UK. Data reduction and integration followed by scalling and merging of the intensities obtained was performed with Denzo and Scalepack respectively as implemented in the HKL suite [87]. Crystallographic refinement of the complexes was performed by maximum-likelihood methods using REFMAC [88]. The starting model employed for the refinement of the complexes was the 100 K structure of the native T state GPb determined at 2.0 Å [89]. 2Fo-Fc and Fo-Fc electron density maps calculated were visualized using the program for molecular graphics "O" [90]. Ligand models of the compounds were fitted to the electron density maps after adjustment of their torsion angles. Alternate cycles of manual rebuilding with COOT [91] and refinement with REFMAC improved the quality of the models. The stereochemistry of the protein residues was validated by PROCHECK [92, 93]. Hydrogen bonds and van der Waals interactions were calculated with the program CONTACT as implemented in CCP4 [93] applying a distance cut off of 3.3 Å and 4.0 Å, respectively. Protein structures were superimposed using LSQKAB as implemented in CCP4 [93]. The majority of figures were prepared with the program MolScript and rendered with Raster3D [95] while some were prepared with the program PyMol [94, 130].

2.7 Growing protein crystals with various methods

Growing protein crystals requires very gentle techniques. A protein is usually grown by slow, controlled precipitation from an aqueous solution under conditions that do not denature the protein. In most common methods of growing protein crystals, purified protein is dissolved in an aqueous buffer containing a precipitant, such as ammonium

sulphate or polyethylene glycol, at a concentration just below that necessary to precipitate the protein. Then water is removed by controlled evaporation to raise both protein and precipitant concentrations resulting in precipitation. Crystallographic structure determination begins with the growth of a suitable crystal. Crystal formation occurs in two stages: *nucleation* and *growth*. Nucleation, the initial formation of molecular clusters from which crystals grow, requires protein and/or precipitant concentrations higher than those optimal for slow precipitation.
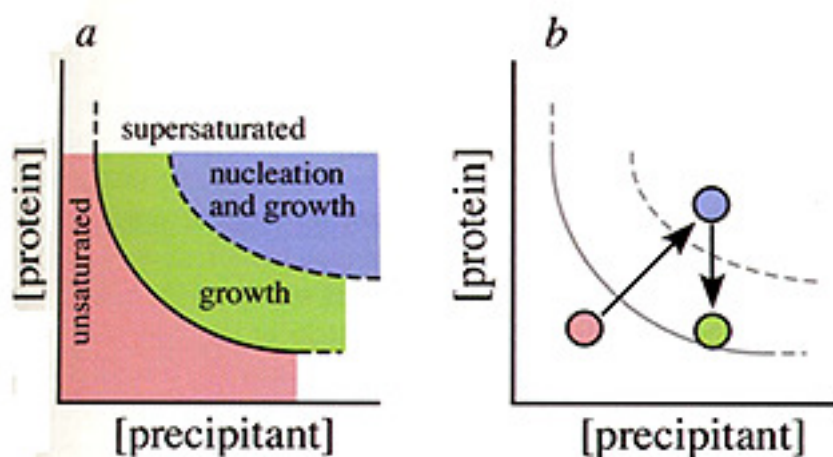
Figure 30. Phase diagram for crystallization mediated by a precipitant. The pink region represents concentrations of protein and precipitant at which the solution is not saturated with protein, so neither nucleation nor growth occurs. The green and blue regions represent unstable solutions that are supersaturated with protein. Conditions in the blue region support both nucleation and growth, while conditions in the green support growth only [96].

The batch method

In batch crystallization methods all components are combined into a single solution, which is then left undisturbed. Given the static nature of the batch crystallization experiment, success requires that super-saturation levels sufficient for nucleation be achieved on mixing. Optimization then involves altering experimental conditions to control the number of crystals and the time required for crystals to reach the desired size. Crystal number reflects nucleation rate which in general is strongly dependent on super-saturation [134].

The vapour diffusion method

Vapour diffusion is the standard method used for protein crystallization. Conditions within a protein-containing solution are manipulated remotely by diffusion through air. It is suitable for use with small volumes, easy to set-up and to monitor reaction progress. A common format involves the "hanging drops" containing protein solution and precipitant at a concentration insufficient to precipitate the protein.
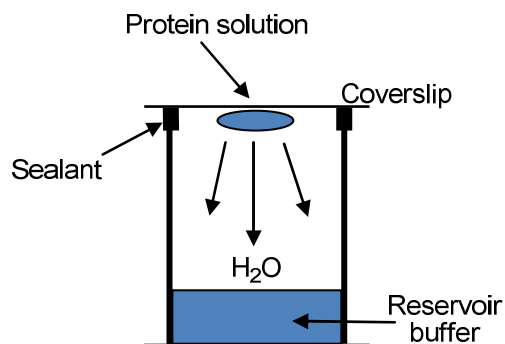
Figure 31. The "hanging drop" method of protein crystallization [128].

The drop is equilibrated against a larger reservoir of solution containing precipitant and after sealing the chamber equilibration leads to super-saturating concentrations that induce protein crystallization in the drop [128].

The dialysis method

Like batch methods, in the dialysis method the macromolecular concentration remains constant during crystallization by dialysis. However, in this method solution composition is altered by diffusion of low molecular weight components through a semi-permeable membrane. The ability to change the protein solution composition accurately any number of times and with small incremental changes, makes this one of the most versatile crystallization methods. It is also a convenient method for crystallization in the presence of volatile reagents such as alcohols [141].

The seeding method

Given that ideal conditions for nucleation and growth differ, a logical crystallization strategy involves the separate optimization of these processes. This can be accomplished by seeding, a technique where crystals are transferred from nucleation conditions to those that will support only growth.

There are two basic seeding methods. In macroscopic seeding, one crystal is transferred from the mother liquor where nucleation and initial growth occur to a less supersaturated solution for continued growth. On the other hand, microscopic seeding involves transferring nuclei to the growth medium.

Figure 32. Glycogen phosphorylase native crystals.

Although success in both seeding methods involves finding optimal growth conditions, crystal growth by microseeding can also involve preparing stock seed solutions, which when added to the growth solution will produce only a few large crystals. Seed solutions can be prepared by crushing crystals, then testing a set of serially diluted solutions to see which gives the desired number of crystals [141]. This was the method used for growing glycogen phosphorylase crystals.

Materials

- Dialysis tubing cellulose: SIGMA, 25x16 mm
- Spermine-tetrahydrochloride: SIGMA, MW 348.19 g/mol
- Inosine monophosphate (IMP): SIGMA, MW 348.21 g/mol
- Active charcoal: SIGMA
- Buffer solution BES (10 mM), EDTA (0.1 mM), DTT (0.5 mM), NaN$_3$ (0.01 %)
    - ✓ *(N,N-bis[2-Hydroxymethyl]-2-aminoethanesulfonic acid) (BES): SIGMA, MW 213.20 g/mol*
    - ✓ *EDTA: SERVA, MW 372.30 g/mol*
    - ✓ *DL-Dithiothreitol (DTT): SIGMA, MW 154.25 g/mol*
    - ✓ *Sodium azide (NaN$_3$): GPR, MW 65.01 g/mol*

- Millipore Millex-GV syringe driven filter unit (0.22 µM)
- Small centrifugation tubes
- Centrifuge: Sorvall Instruments, RC5C
- UV-Visible Spectrophotometer: CARY 100 Conc

Dialysis of the enzyme for AMP/glycerol removal

The enzyme is dialyzed in 500 ml of buffer solution (10 mM BES, 0.1 mM EDTA, 0.5 mM DTT, 0.01% NaN_3 pH 6.7). The solution is placed at 4°C for at least 2 hours. The buffer solution is then replaced with 500 ml of fresh buffer solution, and left at 4°C overnight. After dialysis, the ratio A_{260}/A_{280} is calculated by measuring the enzyme absorbance at 260 and 280 nm, after diluting 20 μl of enzyme in 980 μl of buffer. The ratio at this time should be ~ 0.62-0.64, which means that nucleotides (AMP) are present. Active charcoal is added to the enzyme at a 2:1 w/w ratio and stirred gently and continuously for 40 minutes using a glass rod. This is done so that the charcoal can absorb the AMP in the enzyme. Removal of active charcoal is achieved by centrifugation at 17500 rpm (37000 g) for 10 minutes, at 25-30°C. The supernatant is collected and filtered, using a syringe so as to remove any traces of active charcoal. Since AMP removal is crucial for crystal formation, the ratio A_{260}/A_{280} nm is measured again, where 260 nm is the wavelength at which nucleotides (AMP) absorb. The ratio must be ~ 0.53-0.54 so crystal formation can occur. If this is not so, the above procedure must be repeated, active charcoal must be added to the enzyme for another 40 minutes to achieve nucleotide removal.

Glycogen phosphorylase crystal growth

In this seeding method, fractures of crystals were used as seeds to grow large crystals. An enzyme solution was prepared, and then GPb seeds were added to this solution. The solution was then allowed to rest for several days at 14°C. The solution required for GPb crystal formation contains 3 mM DTT, 1 mM spermine and 1 mM IMP. Once the mother liquor was prepared, it was separated into 500 μl aliquots. Crushed crystals were then added to the first aliquot with a cut pipette tip, and then serially diluted. The diluted seed solutions were then transferred to glass capillaries using a syringe, closed with parafilm and placed at 14 °C so the crystals could grow.

Soaking of GPb native crystals with inhibitors

During this method a native GPb crystal is placed into a capillary tube containing approximately 300-500 µM of an inhibitor. This is left to "soak" for several hours depending on the concentration of the inhibitor solution and the binding strength predicted by kinetic experiments. During this time, the inhibitor solution is given the chance to bind to the enzyme. Soaking is performed at room temperature. Following the soaking time, the inhibitor solution is removed and the crystal is mounted for X-ray diffraction data collection.

GPb-inhibitor co-crystallization

Another technique used is that of growing GPb crystals in the presence of an inhibitor. The technique used is that of growing native GPb crystals but with the addition of the inhibitor solution in the reagents. This technique is good for inhibitors with high affinity for the enzyme, i.e. low K_i, as low concentrations of the inhibitor are used. More time is given to the inhibitor to bind and most importantly no crystal packing disorder is observed as in the case of soaking, where the inhibitor must penetrate the crystal canals in order to bind to the enzyme.

Cryocrystallography

For many years crystallographers have been aware of the advantages of collecting X-ray data at very low temperatures. In theory, lowering the temperature should increase molecular order in the crystal and improve diffraction. In practice however, early attempts to freeze crystals resulted in damage due to the formation of ice rings, as protein crystals contain internal water. In addition to better diffraction, other advantages of cryocrystallography include reduction of radiation damage to the crystal and hence the possibility of collecting more data from a single crystal; reduction of X-ray scattering from water, resulting in cleaner backgrounds in diffraction patterns; and the possibility of safe storage, transport and re-use of crystals. However, in the case of glycogen phosphorylase, X-ray experiments were conducted at room temperature. The reason for this is that the cryoprotectants such as glycerol bind to different sites of the enzyme [133].

3.0 Results & Discussion

3.1 Crystallographic and computational studies on 4-phenyl-*N*-[β-D-glucopyranosyl]-1*H*-1,2,3-triazole-1-acetamide, an inhibitor of glycogen phosphorylase: Comparison with α-D-glucose, *N*-acetyl-β-D-glucopyranosylamine and *N*-benzoyl-*N*´-β-D-glucopyranosyl urea binding

Organic synthesis *by Professor Duraikkannu Loganathan, Department of Chemistry, Indian Institute of Technology Madras, Chennai, India*

Kinetic studies of 4-phenyl-*N*-[β-D-glucopyranosyl]-1*H*-1,2,3-triazole-1-acetamide (glucosyltriazolylacetamide)

The inhibitory efficiency of glucosyltriazolylacetamide was tested with kinetic experiments on GPb [135]. The design of glucosyltriazolylacetamide (**1**) was based on the replacement of the -Cl group of the chloroacetamido analogue (**2**) (K_i: 45.0 µM) by a substituted triazole. The latter group is regarded as an isosteric replacement for the benzamide moiety of *N*-benzoyl-*N*´-β-D-glucopyranosyl urea (**3**), which is one of the most potent inhibitors developed to date [97]. This replacement resulted in a decrease of the inhibitory effect on GPb (K_i: 179.0 µM).
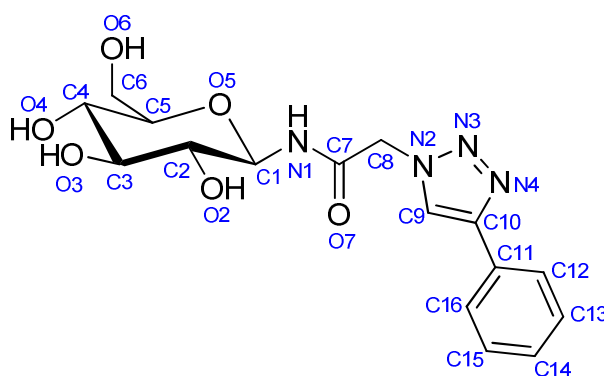
(1) N-(4-phenyl-1,2,3-triazoleacetyl)-β-D-glucopyranosylamine (glucosyltriazolylacetamide)

(K_i: 179.0 µM)
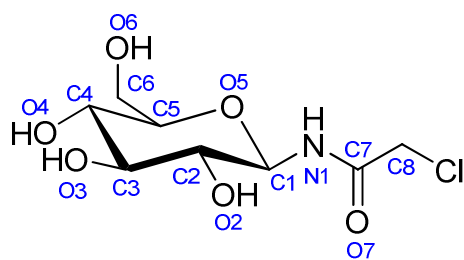
(2) N-chloroacetyl-β-D-glucopyranosylamine (K$_i$: 45.0 μM)
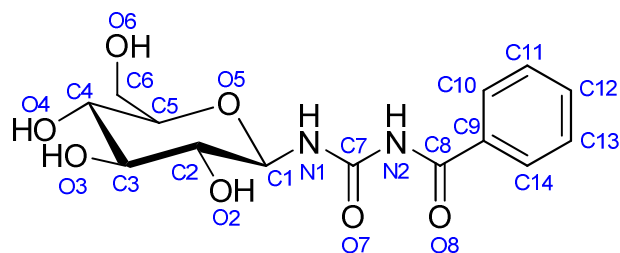
(3) N-benzoyl-N´-β-D-glucopyranosyl urea (K$_i$: 4.6 μM)
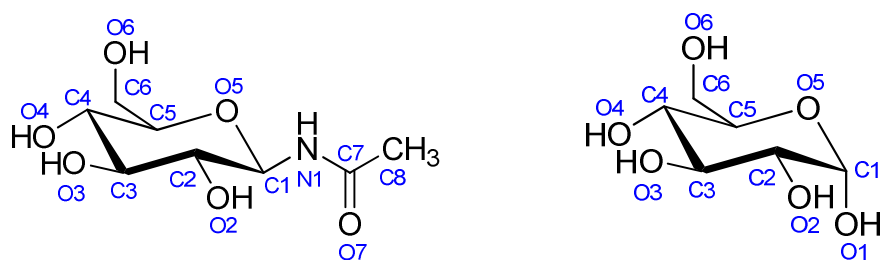
(4) N-acetyl-β-D-glucopyranosylamine (NAG) (K$_i$: 32.0 μM) and (5) α-D-glucose (K$_i$: 1.7 mM)

Figure 33. The chemical structures of glucosyltriazolylacetamide, N-chloroacetyl-β-D-glucopyranosylamine, N-benzoyl-N´-β-D-glucopyranosyl urea, N-acetyl-β-D-glucopyranosylamine (NAG) and α-D-glucose with atom numbering used.

The compound displayed competitive inhibition with respect to the substrate G1P, at constant concentrations of glycogen (0.2% w/v) and AMP (1 mM). The inhibition constant of glucosyltriazolylacetamide for rabbit muscle GPb was found to be K_i: 179.0 ± 11.0 μM, ~ 10 or ~ 41 times decreased than the parent compounds α-D-glucose (K_i: 1.7 mM) or β-D-glucose (K_i: 7.4 mM) respectively, but ~ 6 times increased than the lead compound NAG (K_i: 32.0 μM), indicating a difference in the binding free energy between glucosyltriazolylacetamide and NAG of about 1.0 kcal/mol.
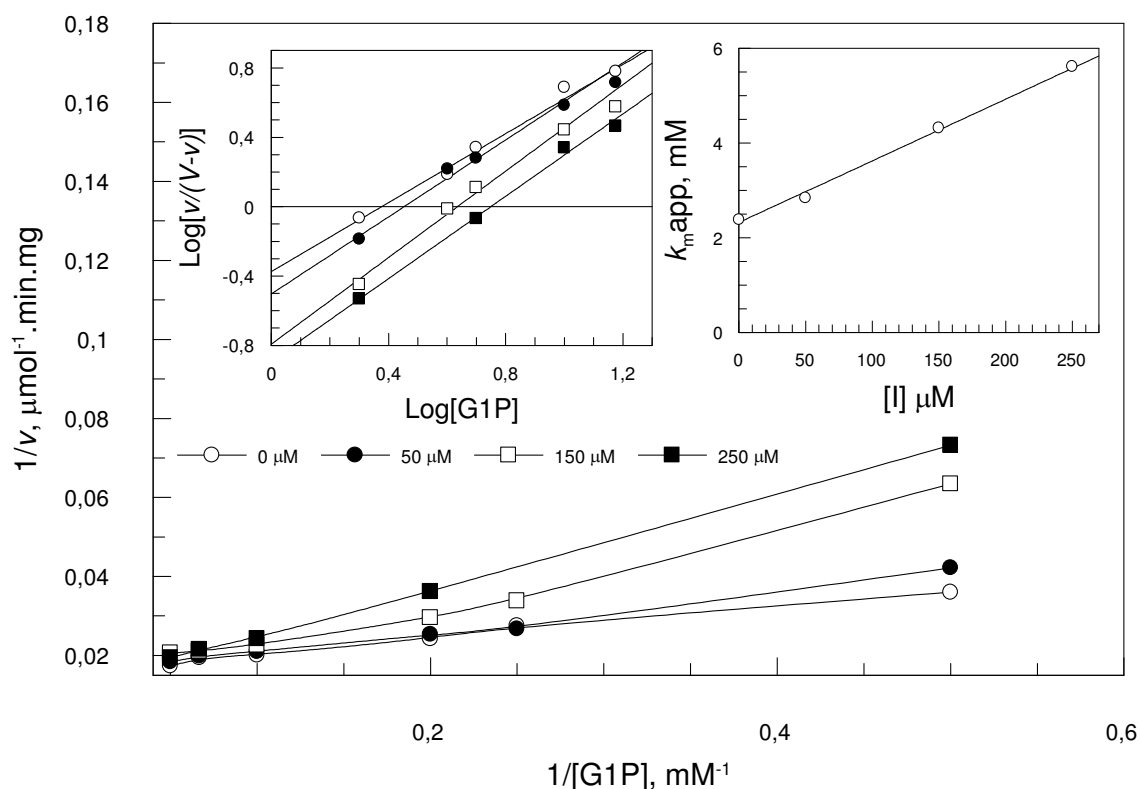
Figure 34. Kinetics of glucosyltriazolylacetamide inhibition of GPb with respect to G1P (2, 4, 5, 10, 15 and 20 mM) in the direction of the glycogen synthesis (30° C, pH 6.8). Double reciprocal plots of initial reaction velocity versus [G1P] at constant concentrations of AMP (1 mM) and glycogen (0.2% w/v) and various concentrations of glucosyltriazolylacetamide. Inhibitor concentrations (μM) were as follows: 0 (○), 50 (●), 150 (□) and 250 (■). Inset: Hill plots for G1P, which yielded the apparent K_m values for G1P and the Hill coefficient. The apparent K_m values and the Hill coefficients (top left) were 2.4 ± 0.1 mM (n=1.0), 2.8 ± 0.14 mM (n=1.1), 4.3 ± 0.3 mM (n=1.2) and 5.6 ± 0.2 mM (n=1.2). From the secondary plot (top right) of the apparent K_m values versus inhibitor concentration, a K_i value of 179.0 ± 11.0 μM was calculated.

ORTEP depiction with atom numbering is shown in figure 35 below.
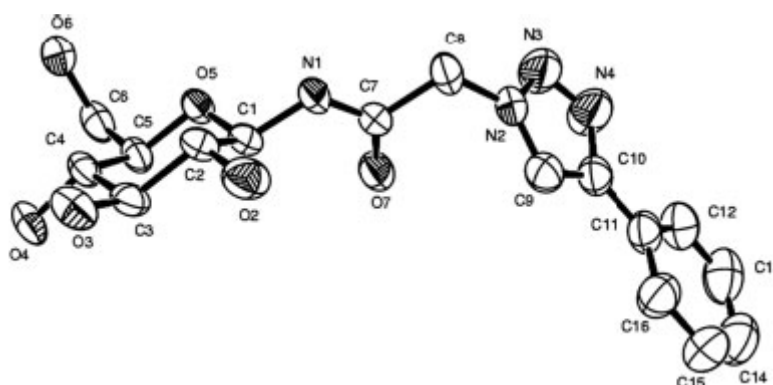
Figure 35. ORTEP (50% probability level) with atom numbering of glucosyltriazolylacetamide.

Selected geometrical parameters are listed in figure 36. The dimensions of the N-glycosidic bond, namely, C1-N1 bond length and angles, O5-C1-N1, C2-C1-N1 and C1-N1-C7, are comparable with the values of 1.431 Å, 108.08°, 111.48° and 122.68°, respectively reported for NAG [98].

Bond length				Torsion angle	
				Free form of 5	GPb-5 complex
C1—N1	1.435 (4)	O5—C5—C6—O6		−67.8 (3)	−62.3
C8—N2	1.467 (5)	C4—C5—C6—O6		54.0 (3)	57.1
C1—O5	1.435 (4)	O5—C1—N1—C7		−99.2 (3)	−102.7
C5—O5	1.441 (4)	C1—N1—C7—C8		−171.2 (3)	178.7
N2—N3	1.330 (5)	N1—C7—C8—N2		175.1 (3)	174.5
N3—N4	1.297 (5)	C7—C8—N2—N3		110.2 (4)	47.4
C10—N4	1.363 (5)	N4—C10—C11—C12		−9.9 (6)	7.8
Bond angle					
N2—N3—N4	107.9 (3)				
N4—C10—C11	121.0 (4)				
O5—C1—N1	109.3 (3)				

Figure 36. Selected geometrical parameters for glucosyltriazolylacetamide.

The lesser extent of delocalization of the lone pair of electrons of N2 relative to that of N1 is evident from the values, 1.467 Å and 1.435 Å of C8-N2 and bond C1-N1 bond lengths respectively, the former being longer than the latter. The length of the N3-N4 bond of the triazole moiety is found to be shorter than that of N2-N3, indicating the greater double character of the former. The torsion angles, O5-**C5-C6**-O6 and C4-**C5-C6**-O6, are close to 260° and 60° respectively, indicating that the primary hydroxyl group adopts a *gg* conformation. The primary hydroxyl group of NAG has also been reported to take up the same conformation [99]. Similarly, as observed earlier for NAG, the acetamido moiety of

the glucosyltriazolylacetamide exists in the *Z-anti* conformation as revealed by the values, -99.2° and -171.2° for torsion angles O5-**C1-N1**-C7 and C1-**N1-C7**-C8 respectively, which compare well with the values of -93.8° and -179.2° noted earlier for NAG. The conformation about the C7-C8 bond turns out to be *anti* as shown by the value 175.1° of the torsion angle, N1-**C7-C8**-N2. The value of this torsion angle differs considerably from those (115° and 131° respectively) of the corresponding torsion angle reported for the two known GPb inhibitors, namely, GlcbNHCOCH$_2$CH$_3$ (K$_i$: 39.0 μM) and GlcbNHCOCH$_2$Cl (K$_i$: 45 μM) [100]. The other two torsion angles, C7-C8-N2-N3 and N4-C10 -C11-C12, which are also critical for defining the aglycon conformation, were found to be 110.2° and 29.9° respectively. The latter value makes it clear that the triazole ring and the phenyl ring are not coplanar and that the phenyl ring is slightly twisted. Presumably, this twisting arises from steric interactions between the five-membered ring and the six-membered ring, analogous to the more severe twist (~ 30°–40°) observed in biphenyl derivatives arising from interactions between the two 6-membered rings [101]. Meticulous analysis of the crystal packing of the glucosyltriazolylacetamide was performed to understand the key features governing its molecular assembly and also to understand their effect on the molecular conformation. Parameters of both the regular hydrogen bonds and the weaker C-H⋯X (O/N) interactions are listed in figure 37 below.

Hydrogen bonds	d (D-H)	d (H-A)	d (D-A)	<DHA	Symmetry code
O3—OH3⋯N3	0.82	2.1	2.797 (5)	143.4	−1 + x, 1 + y, z
O3—OH3⋯N4	0.82	2.68	3.369 (4)	142.4	−1 + x, 1 + y, z
N1—NH1⋯O6	0.88 (7)	2.11 (7)	2.940 (4)	156 (6)	−1 − x, −1/2 + y, 2 − z
O6—OH6⋯N1	0.82	2.21	2.940 (4)	148.2	−x − 1, y + 1/2, 2 − z
O4—OH4⋯O6	0.82	2.54	3.097 (3)	126.5	−x − 1, y + 1/2, 2 − z
C14—H14⋯O2	0.93	2.5	3.417 (6)	168.0	−x, y − 1/2, −z + 1
C5—H5⋯O3	0.98	2.37	3.270 (4)	152.0	x + 1, y, z
C6—H6A⋯O4	0.97	2.47	3.436 (4)	176.0	−x, y − 1/2, − z

Figure 37. The molecular packing of glucosyltriazolylacetamide.

The molecular packing of glucosyltriazolylacetamide displaying regular hydrogen bonds and C-H⋯O interactions is shown in figure 38 below. Among the three infinite networks of hydrogen bonds observed, the first one involves O3 as a bifurcated donor to the relatively electron-rich N3 and N4 atoms of the triazole ring and also an acceptor to the H5 of the sugar ring. The second one is built up through the C14-H14⋯O2 interaction between the aromatic phenyl ring and the sugar oxygen atom. In the third network, O4 is seen to interact as an acceptor for C6-H6 under fairly ideal conditions, particularly in terms of bond angle, while acting as a donor to O6 at the same time.
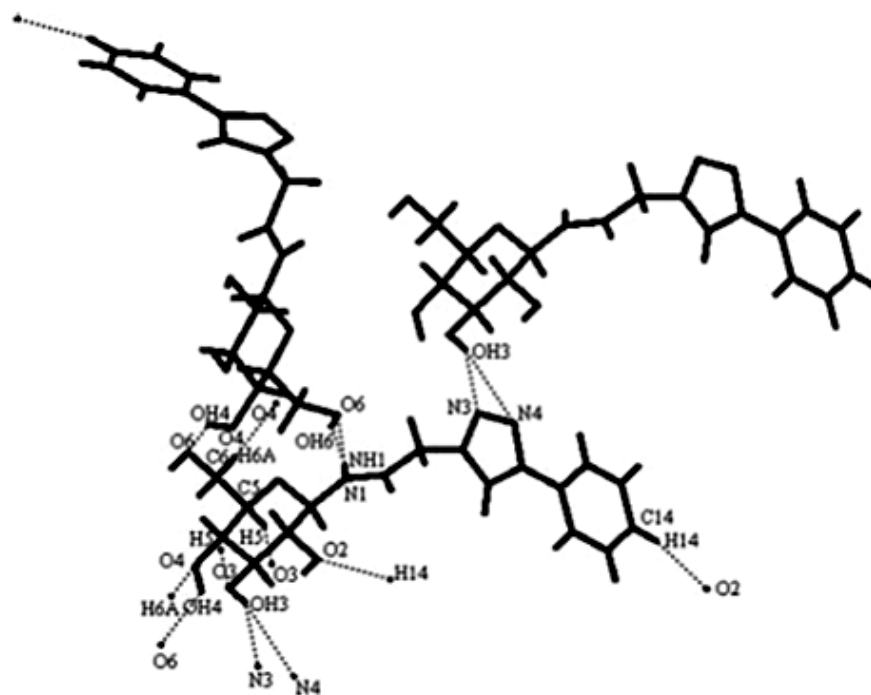
Figure 38. The molecular packing of glucosyltriazolylacetamide displaying regular hydrogen bonds and C-H⋯O interactions.

X-ray crystallographic studies of glucosyltriazolylacetamide

To elucidate the structural basis of the mechanism of inhibition, the crystal structure of glucosyltriazolylacetamide in complex with GPb was determined at 100 K to 2.03 Å resolution, as well as in the free form using X-ray crystallography. Also for comparison, the structure of the GPb in complex with glucose was determined to 1.93 Å resolution at 100 K.

Binding of α-D-glucose at the catalytic site

On binding to the catalytic site, α-D-glucose promotes the less active T state through stabilization of the closed position of the 280s loop (residues 282–287) which blocks access for the substrate (glycogen) to the catalytic site. The binding of glucose to the catalytic site is dominated by multiple neutral hydrogen bonds from each of the peripheral hydroxyl groups to protein atoms. The inhibition constant of α-D-glucose for GPb is only 1.7 mM, despite its extensive hydrogen bonding interactions with the protein [102]. This could be explained by the fact that the mean normal blood glucose level in humans is 5 mM. It should be noted that α-D-glucose is very unstable and it converts to β-D-glucose very quickly. Therefore during the X-ray experiment, the native GPb crystal was soaked

with α-D-glucose for 30-60 seconds only, and it was targeted with X-rays immediately before it had a chance to convert to β-D-glucose.
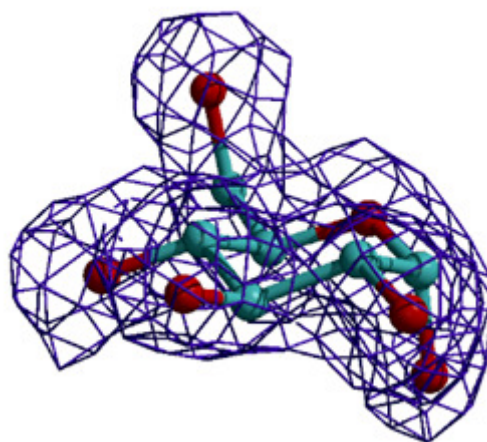
Figure 39. 2Fo-Fc electron density map of α-D-glucose bound at the catalytic site of GPb. The map is contoured at l.0 σ level and the refined model of α-D-glucose is displayed.

Two pockets have been identified in the vicinity of the catalytic site: a small water-filled side pocket, accessible to α-C1 substituents, and a large channel adjacent to the 280s loop, accessible to β-C1 substituents, the so called β-pocket. The β-pocket is lined by both polar and non-polar groups, directed towards residue His341, but with no access to the bulk solvent. At the catalytic site water molecules either participate in the binding of the glucopyranose ring by direct or water mediated interactions or fill the two channels in contact with protein residues or other water molecules [102, 103]. The mode of binding and the interactions that α-D-glucose makes with residues of the catalytic site in the 100 K GPb-α-D-glucose complex structure are almost identical with those previously described at room temperature from a 2.3 Å resolution crystallographic experiment [102]. There are 12 water molecules, namely Wat257, Wat346, Wat604, Wat631, Wat726, Wat748, Wat752, Wat777, Wat803, Wat805, Wat808 and Wat812, that are unique in the 100 K GPb-α-D-glucose complex structure, while 7 water molecules, Wat43, Wat217, Wat744, Wat747, Wat754, Wat796 and Wat798 (Wat421, Wat279, Wat453, Wat422, Wat25, Wat458 and Wat473 respectively in the room temperature complex structure) are shifted by 0.4–0.9 Å. There are in total 16 hydrogen bonds and 56 van der Waals interactions (4 non-polar-non-polar, 11 polar-polar, and 41 non-polar/polar).
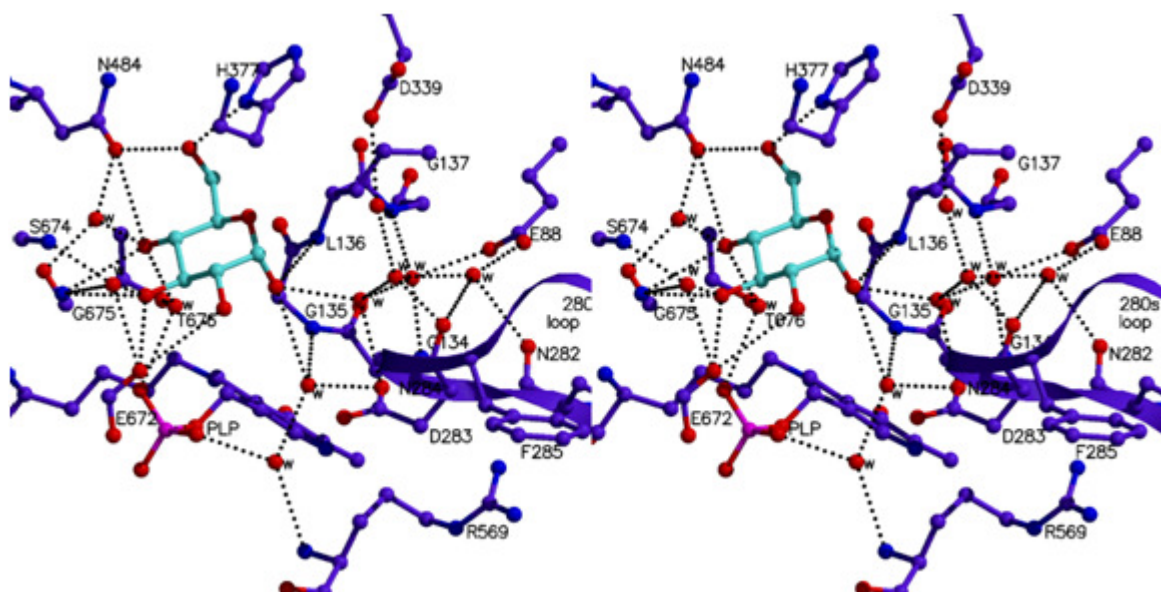
Figure 40. Stereo diagram showing interactions between α-D-glucose and protein in the vicinity of the catalytic site.

Binding of glucosyltriazolylacetamide

The mode of binding and the interactions that glucosyltriazolylacetamide makes with GPb, are similar to those described previously for the structure of the GPb-NAG complex [99]. The hydrogen bond of the amide nitrogen (N1) with His377 O is retained, an interaction that is conserved in all β-D-glucopyranosylamine analogues [100,104-107], spiro-hydantoin analogues, and spiro-diketopiperazine of β-D-glucopyranose [89, 103, 107-112], and also the compound 2-(β-D-glucopyranosyl)-benzimidazole [113]. O7 is hydrogen bonded to Glu88 OE2 and residues of the glycine helix (residues 134–150), Gly134 N, and Gly137 through four water molecules (Wat268, Wat43, Wat415, Wat670). The 1,2,3-triazole moiety is located between the side-chains of Leu136, Asp339, His341, and Ala383. There are two additional hydrogen bonds in comparison to the GPb-NAG complex; N3 and N4 atoms of the 1,2,3-triazole group make water-mediated interactions that involve residues Glu88 and Asn133.
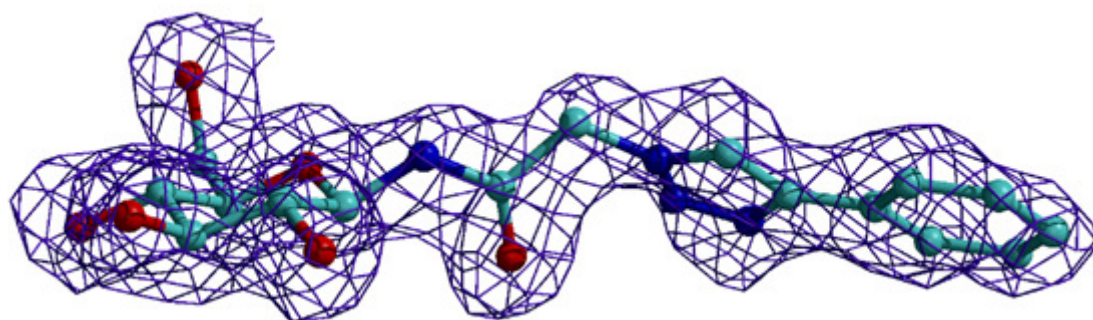
Figure 41. 2Fo-Fc electron density map of glucosyltriazolylacetamide bound at the catalytic site of GPb. The map is contoured at l.0 σ level and the refined model of the inhibitor is displayed.

The importance of this stabilization motif, involving N3 and N4 atoms of the 1,2,3-triazole group for binding, could be discerned from the change in the conformation about the C8-N2 bond as shown by the difference in the values of the torsion angle, C7-C8-N2-N3, observed for the complex of glucosyltriazolylacetamide with GPb and its free form (47.4° and 110.2° respectively). The triazole ring has turned more than 62° to facilitate the formation of the two additional hydrogen bonds. This result is consistent with the acceptor capability of N3 and N4 seen in the free form of glucosyltriazolylacetamide. But for the change in the conformation about the C8-N2 bond, negligible differences are seen in the molecular conformation, as defined by the torsion angle about C5-C6, C1-N1, N1-C7, C7-C8, and C10-C11 bonds, between the free form of glucosyltriazolylacetamide and its complex with GPb. The phenyl group of glucosyltriazolylacetamide occupies a pocket lined by residues of the 280s loop, which undergoes conformational changes, Ala383 of the 380s loop (residues 377–384), and several water molecules. In the GPb-glucosyltriazolylacetamide complex, the aromatic ring of Phe285 is inclined by ~ 85° toward Phe286, so that Phe285 CE1 is ~ 3.8 and 4.0 Å from CE1 and CE2 of Phe286, respectively resulting in the closure of the active site. Similar but not identical shifts of the 280s loop were observed previously on binding of *N*-benzoyl-*N´*-b-D-glucopyranosyl urea to GPb [97]. There are in total 17 hydrogen bonds and 115 van der Waals interactions (11 non-polar–non-polar, 14 polar–polar, and 90 non-polar/polar) in the GPb-glucosyltriazolylacetamide complex.
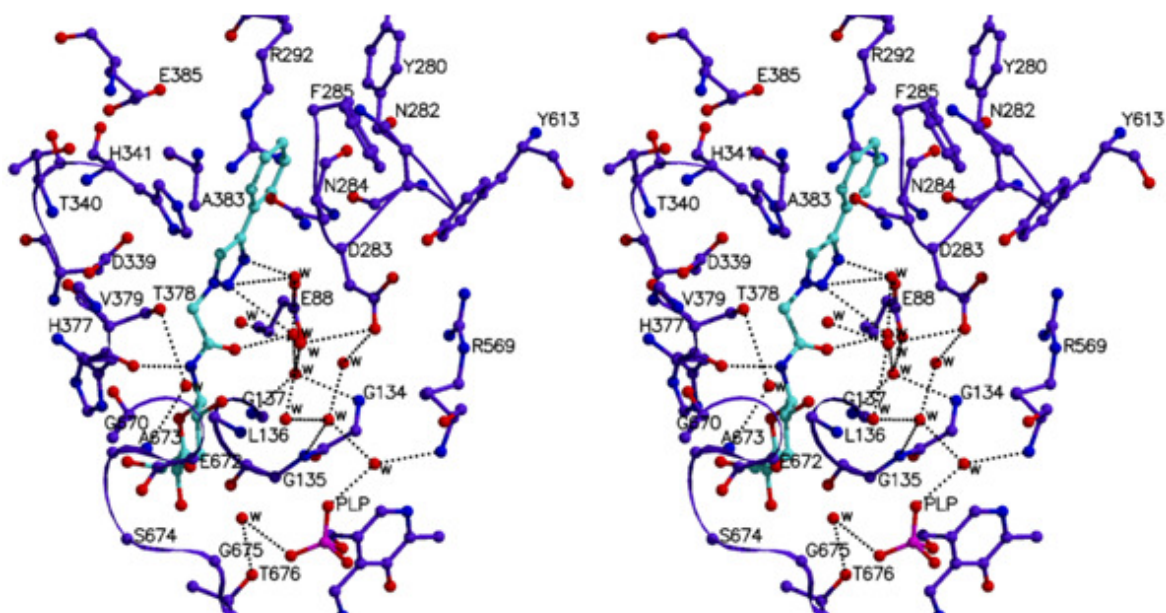
Figure 42. Stereo diagrams showing interactions between glucosyltriazolylacetamide and the protein in the vicinity of the catalytic site.

On glucosyltriazolylacetamide binding to GPb, 5 water molecules (Wat744, Wat752, Wat754, Wat803, and Wat808 in the GPb-α-D-glucose complex structure) were displaced, while waters Wat631, Wat677, and Wat726 were shifted by 1.2–1.7 Å, in addition to those displaced by the glucopyranose. Furthermore, three new water molecules, Wat653, Wat670, and Wat720, not detected in the GPb-α-D-glucose complex structure, are recruited into the GPb-glucosyltriazolylacetamide complex structure. Wat653 is hydrogen-bonded to Asp283 OD2 through Wat720, and Wat670 makes a direct hydrogen bond to Asp283 OD2. These waters occupy the position previously occupied by Asp283 OD1 (Wat670) or are positioned close to the positions of OD1 and CG atoms of Asp284 (Wat653 and Wat720) in the GPb-α-D-glucose complex structure and appear to stabilize the new position of Asp283.

Structural comparisons

Structural comparisons between GPb-glucosyltriazolylacetamide complex structure and (a) GPb-α-D-glucose, (b) GPb-*N*-acetyl-β-D-glucopyranosylamine (NAG) and (c) GPb-*N*-benzoyl-*N´*-β-D-glucopyranosyl urea complex structures in the vicinity of the catalytic site are shown in figures 43-45.
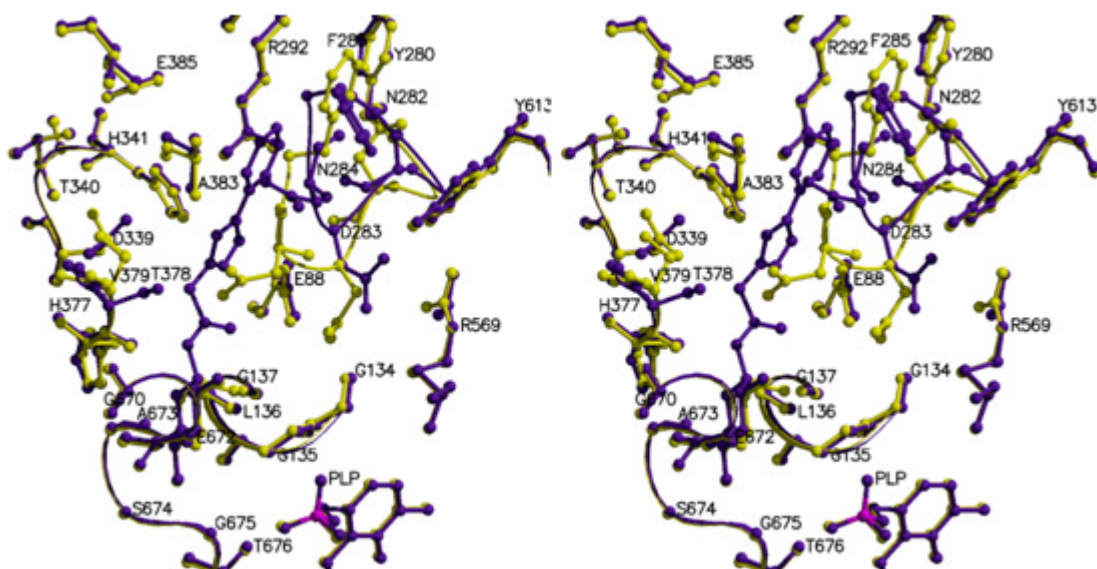
Figure 43. Comparison between GPb-glucosyltriazolylacetamide complex (purple) and T state GPb-α-D-glucose (yellow).
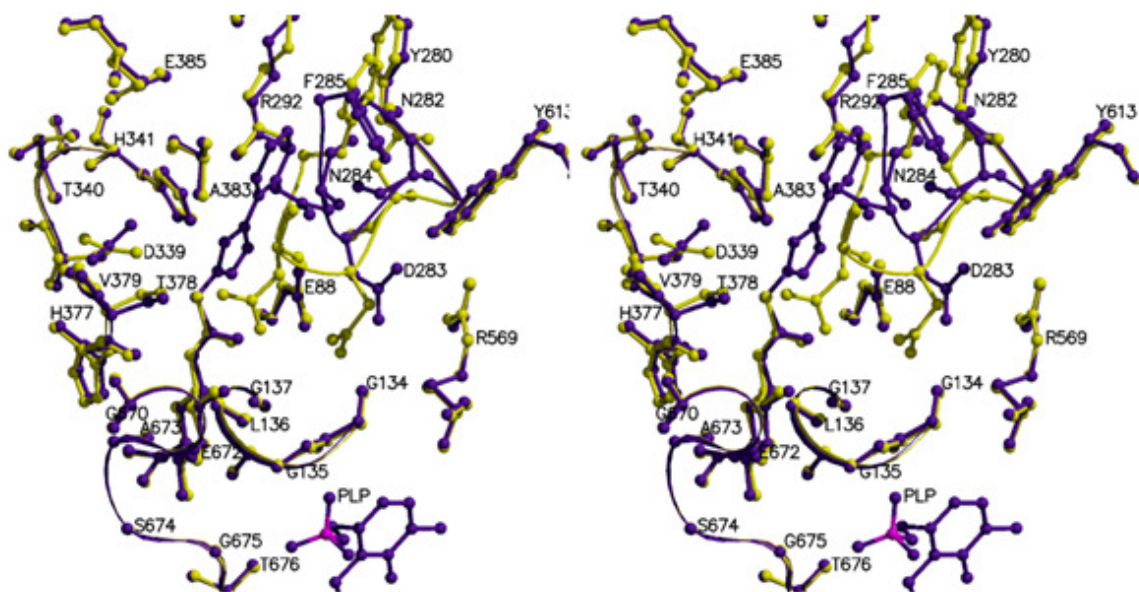
Figure 44. Comparison between GPb-glucosyltriazolylacetamide complex (purple) and T state GPb-N-acetyl-β-D-glucopyranosylamine NAG (yellow).
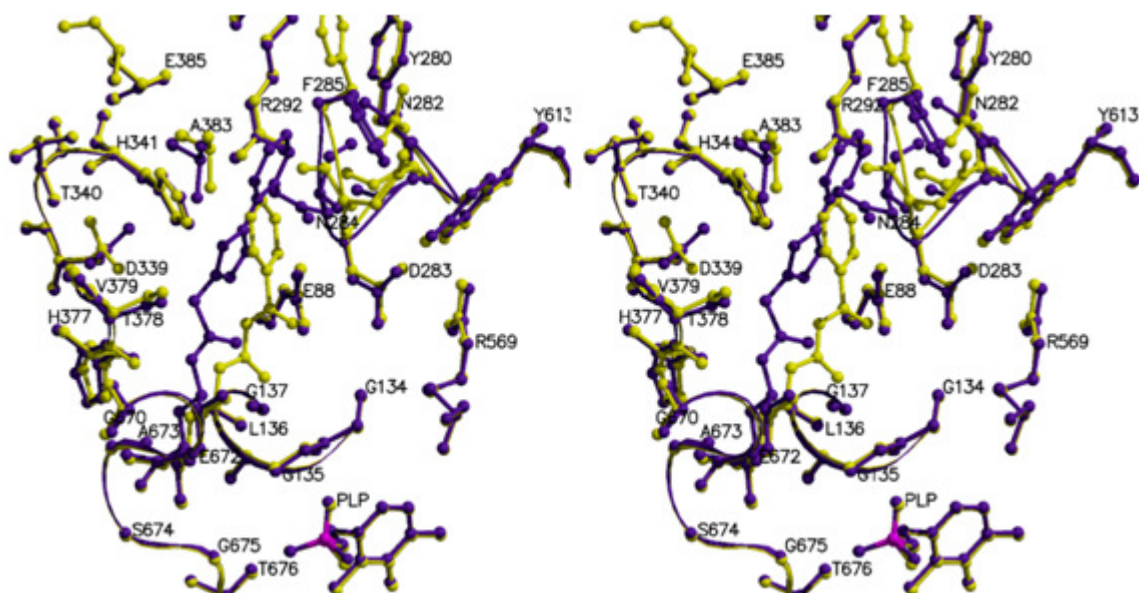
Figure 45. Comparison between GPb-glucosyltriazolylacetamide complex (purple) and T state GPb-GPb-N-benzoyl-N´-β-D-glucopyranosyl urea (yellow).

In the GPb-glucosyltriazolylacetamide structure, the atomic positions of C1, C2 and O5 of D-glucopyranose moiety are shifted ~ 0.3–0.5 Å compared to that of GPb-α-D-glucose and ~ 0.5–0.8 Å compared to the GPb-*N*-benzoyl-*N´*-β-D-glucopyranosyl urea complex. The largest shifts between the positions of glucosyltriazolylacetamide, NAG, and *N*-benzoyl-*N´*-β-D-glucopyranosyl urea are in the atomic positions of the amide group (~ 1.3–1.9 Å), and reflect the presence (glucosyltriazolylacetamide and NAG) or absence (*N*-benzoyl-*N´*-β-D-glucopyranosyl urea) of a hydrogen bond between N1 and main chain O of His377 in their complexes with the protein.

Inhibitor atom	GPb/α-D-glucose		GPb-glucosyltriazolylacetamide	
	Protein atom	Distance (Å)	Protein atom	Distance (Å)
N1	-	-	His377 O	2.8
N3	-	-	Wat268	3.3
	-	-	Wat415	3.3
N4	-	-	Wat415	2.7
O1	Leu136 N	3.3	-	-
	Wat726	2.8	-	-
	Wat812	3.2	-	-
O2	Asp284 OD1	3.0	Tyr573 OH	3.1
	Tyr573 OH	3.1	Glu672 OE1	3.2
	Glu672 OE1	3.2	Wat168	3.0
	Wat796	2.8	Wat653	3.3
	Wat812	2.9	Wat687	2.7
O3	Glu672 OE1	2.7	Glu672 OE1	2.7
	Ser674 N	3.1	Ser674 N	3.0
	Gly675 N	3.1	Gly675 N	3.1
O4	Asn284 OD1	2.8	Gly675 N	2.8
	Gly675 N	2.9	Wat44	2.7
	Wat44	2.7	-	-
O6	His377 ND1	2.7	His377 ND1	2.6
	Asn284 OD1	2.8	Asn284 OD1	2.9
O7	-	-	Wat268	2.9

Figure 46. Hydrogen bond interactions between α-D-glucose (left) and glucosyltriazolylacetamide (right) with residues of the catalytic site of GPb.

N3	...Wat268	...Wat43	...Glu88 OE2		
			...Gly134 N		
			...Gly137 N		
		...Wat415	...Glu88 OE2		
			...Asn133 N		
		...Wat670	...Asp283 OD2		
			...Wat233	...Gly135 N	
				...Wat29	...Arg569 N
					...PLP O2P
N4	...Wat415				
O2	...Wat168	...Thr378 OG1			
		...Thr671 O			
		...Ala673 N			
	...Wat653	...Wat720	...Asp283 OD2		
			...Wat687		
	...Wat687	...Tyr573 OH			
		...Lys574 NZ			
		...Wat233			
O4	...Wat44	...Thr676 OG1			
		...PLP O3P			
O7	...Wat268				

Figure 47. Water hydrogen bonding network of glucosyltriazolylacetamide at the catalytic site of GPb.

O1	**...Wat726**	...Asp283 OD2						
	...Wat43	...Glu88 OE2						
		...Gly134 N						
		...Gly137 N						
	...Wat217	...Gly135 N						
		...Asp283 OD1						
		...Wat29	...Arg569 N					
			...PLP O2P					
		...Wat812						
	...Wat752	...Asn284 N						
		...Wat748	...Glu88 OE1					
			...Asn282 O					
		...Wat754	...Asp339 OD1					
			...Wat803	...Ala383 O				
				...Wat777	...Asp339 OD2			
					...His342 NE2			
					...Ala383 O			
					...Wat631	**...Wat744**		
						...Wat798	...Glu385 OE2	
				...Wat744	...Phe285 O			
					...Wat747	...Asn282 O		
						...Wat257	...Glu88 OE1	
							...Arg292 NH1	
							...Arg292 NH2	
						...Wat805	...Asn282 ND2	
							...Wat346	...Glu287 O
								...Glu287 N
								...Wat798
			...Wat808	...His377 O				
	...Wat812	...PLP O2P						
		...Tyr573 OH						
		...Lys574 NZ						
		...Glu672 OE1						
O2	**...Wat796**	...His377 O						
		...Ala673 N						
		...Wat604	...Thr378 OG1					
			...Thr671 O					
	...Wat812							
O4	**...Wat44**	...Thr676 OG1						
		...Thr676 N						
		...PLP O3P						

Figure 48. Water hydrogen bonding network of α-D-glucose binding at the catalytic site of GPb.

68

	GPb/α-D-glucose		GPb-glucosyltriazolylacetamide	
Inhibitor atom	**Protein atom**	**No. of contacts**	**Protein atom**	**No. of contacts**
N1	-	-	His377 C, CB; Wat653	3
N2	-	-	Asp339 OD1; Wat613, Wat653	3
N3	-	-	Leu136 CD1; His341 CE1	2
N4	-	-	His341 CE1, NE1; Wat268	3
C1	Leu136 N; Wat726, Wat808	3	His377 O; Wat687	2
O1	Gly135 C, N, CA	3	-	-
C2	His377 O; Glu672 OE1; Wat796, Wat808, Wat812	5	His377; Glu672 OE1; Wat168, Wat687	4
O2	Asn284 ND2, CG; His377 O; Wat808	4	His377 O; Wat720	2
C3	Glu672 OE1; Gly675 N; Wat44, Wat796, Wat812	5	Glu672 OE1; Gly675 N; Wat44, Wat687	4
O3	Glu672 CG, CD; Ala673 C, N, CA, CB; Ser674 C, CA; Gly675 CA; Wat796	10	Glu672 C, CG, CD; Ala673 C, CA, CB, N; Ser674 CA, C; Gly675 CA; Wat168	11
C4	Asn484 OD1; Gly675 N; Wat44	3	Gly675 N; Wat44	2
O4	Ser674 CB, C; Gly675 C, O, CA	5	Asn484 OD1; Ser674 C, CB; Gly675 C, CA, O	6
C5	Gly135 O, CA, C; Leu136 N; Wat44	5	Gly135 C; Leu136 N; Wat44	3
O5	Leu135 C; Leu136 N, CA, CB; His377 CB, CG, ND1	7	Leu136 N; His377 O, CB, CG, ND1	5
C6	Gly135 O, C; Leu136 N; Leu139 CD2; His377 ND1; Asn484 OD1	6	Gly135 O, C; Leu136 N, CA; His377 ND1; Asn484 OD1	6
O6	Leu139 CD2; His377 CG, CE1; Val455 CB, CG2, CG1; Asn484 CG, ND2	8	Leu139 CD2; His377 CE1, CG; Asn484 CG; Val455 CB, CG1, CG2	7
C7	-	-	Leu136 CD1; His377 CB, O; Wat653	4
C8	-	-	Leu136 CD1; Asp339 OD1; His377 CB, O; Thr378 CG2; Wat613; Wat653	7
C9	-	-	Asp283 O; Wat613	2
C10	-	-	Asp283 C, O; Wat415; Wat423	4
C11	-	-	Asp283 C, CA, O; Wat423	4
C12	-	-	Asn282 O; Asp283 CA; Wat415, Wat420, Wat423	5
C13	-	-	Asn282 O, ND2, Wat336, Wat420	4
C14	-	-	Asn282 O, ND2; Asn284 O; Phe286 CA, N	5
C15	-	-	Asn284 N, C, CA, O; Phe285 N, C; Phe286 CA, N; Ala383 O	9
C16	-	-	Asp283 C, O; Asn284 N, CA; Ala383 O, CA, CB; Wat423	18

Figure 49. Van der Waals interactions between α-D-glucose or glucosyltriazolylacetamide and residues of the catalytic site of GPb.

	GPb-α-D-glucose	GPb-glucosyltriazolylacetamide
Experiment	50 mM α-D-glucose in 10 mM BES, pH 6.7, 25% DMSO, 30-60seconds	9 mM inhibitor in 10 mM BES, pH 6.7, 30% DMSO, 2,5 hrs
Oscillation range (°)[a]	0.8	0.8
No. of images (°)	74	100
Space Group	$P4_32_12$	$P4_32_12$
Unit cell dimensions	$a=b=125.7$ Å, $c=114.9$ Å, $\alpha=\beta=\gamma=90°$	$a=b=125.9$ Å, $c=115.3$ Å, $\alpha=\beta=\gamma=90°$
Resolution (Å)	30.0–1.93	30.0-1.88
No. of observations	982397	1099089
No. of unique reflections (outermost)	69442	75693
R_{symm} (outermost shell) [b]	0.051 (0.432)	0.051 (0.338)
Completeness (outermostshell) (%)	99.6 (100.0)	99.9 (100.0)
Outermost shell (Å)	1.96-1.93	1.91-1.88
$< I /\sigma (I) >$ (outermost shell) [c]	18.2 (4.2)	24.5 (6.1)
Redundancy (outermost shell)	4.9 (4.9)	6.6 (6.7)
Refinement resolution range (Å)	88.7-1.93	89.1-1.88
No of reflections used (free)	65895 (3511)	71717 (3802)
Residues included	(10-251) (261–315) (325–835)	(10-251) (261–315) (325–835)
No. of protein atoms	6594	6583
No. of water molecules	960	878
No. of heteroatoms	12 (Glc), 15 (PLP), 72 (DMSO)	26 (inhibitor), 15 (PLP), 40 (DMSO)
Final R (R_{free}) (%)[d]	19.0 (23.5)	20.0 (23.8)
R (R_{free}) (outermost shell)	24.9 (28.3)	23.7 (28.2)
r.m.s.d. in bond lengths (Å)	0.007	0.007
r.m.s.d. in bond angles (°)	1.104	0.995
Average B ($Å^2$) for residues	(10-251) (261–315) (325–835)	(10-251) (261–315) (325–835)
Overall	18.5	21.1
CA, C, N, O	17.9	20.5
Side chain	18.9	21.7
Average B ($Å^2$) for heteroatoms	13.3 (GLC), 13.1 (PLP), 43.9 (DMSO)	23.2 (inhibitor), 15.3 (PLP), 38.8 (DMSO)
Average B ($Å^2$) for water molecules	30.8	33.6

a Native T state RMGPb crystals, grown in the tetragonal lattice, space group $P4_32_12$ were soaked with various concentrations of inhibitors in buffered solutions at pH 6.7 in the presence of DMSO. X-ray diffraction data were collected using synchrotron radiation source at Daresbury Laboratory, UK and EMBL Hamburg outstation at DESY, Germany, and processed with the HKL package. Complex structure determination and analysis were performed according to standard protocols as implemented in the CCP4 package.

b $R_{symm} = \Sigma_h\Sigma_i|I(h) – I_i(h)/\Sigma_h\Sigma_iI_i(h)$ where $I_i(h)$ and $I(h)$ are the ith and the mean measurements of the intensity of reflection h.

c $\sigma(I)$ is the standard deviation of I.

d $R_{cryst} = \Sigma_h|F_o – F_c|/\Sigma_hF_o$, where F_o and F_c are the observed and calculated structure factors amplitudes of reflection h, respectively. R_{free} is equal to R_{cryst} for a randomly selected 5% subset of reflections not used in the refinement. Values in parentheses are for the outermost shell.

Figure 50. Diffraction data and refinement statistics for the GPb complexes at 100 K.

In Figure 51 below, the positions of glucosyltriazolylacetamide, α-D-glucose, NAG, and *N*-benzoyl-*N´*-β-D-glucopyranosyl urea within the catalytic site of GPb are compared.
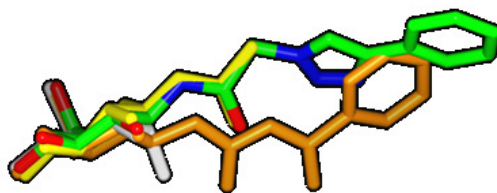
Figure 51. Comparison of the positions of glucosyltriazolylacetamide (green), NAG (yellow), N-benzoyl-N´-b-D-glucopyranosyl urea (orange) and α-D-glucose (white) at the catalytic site of GPb.

In the GPb-glucosyltriazolylacetamide structure, the atomic positions of C1, C2 and O5 of the D-glucopyranose moiety are shifted by ~ 0.3–0.5 Å compared to that of GPb-α-D-glucose and by ~ 0.5–0.8 Å compared to GPb-*N*-benzoyl-*N´*-β-D-glucopyranosyl urea complex. The largest shifts between the positions of glucosyltriazolylacetamide, NAG and *N*-benzoyl- *N´*-β-D-glucopyranosyl urea are in the atomic positions of the amide group (~ 1.3–1.9 Å), and that reflects the presence (glucosyltriazolylacetamide and NAG) or absence (*N*-benzoyl-*N´*-β-D-glucopyranosyl urea) of a hydrogen bond between N1 and main chain O of His377 in their complexes with protein. In Figure 52 below, a structural comparison of glucosyltriazolylacetamide, as defined by small molecule X-ray crystallography with glucosyltriazolylacetamide when bound to the catalytic site of GPb, is shown.
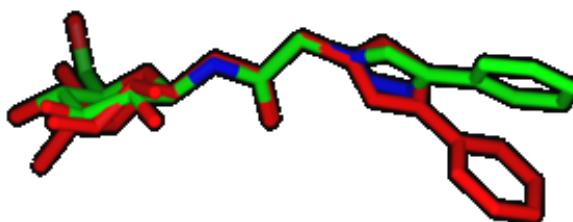
Figure 52. Single crystal glucosyltriazolylacetamide structure (red) superimposed on glucosyltriazolylacetamide structure from the GPb-glucosyltriazolylacetamide complex (green).

Conclusions

Replacement of the acetamido group of NAG (K_i: 32.0 μM) by 4-phenyl-1,2,3-triazoleacetamido group in glucosyltriazolylacetamide resulted in a less potent competitive inhibitor (K_i: 179.0 μM) of the enzyme. The glucosyltriazolylacetamide analogue binds with an approximately six-fold decreased affinity relative to the lead compound NAG. A possible explanation for the difference in K_i may lie in the rearrangement of the 280s loop within the catalytic site on binding of glucosyltriazolylacetamide. The new position of the 280s loop creates more space for the ligand to be accommodated at the catalytic site, causing displacement of five water molecules and the shift of two water molecules. In addition, three new water molecules are recruited, to contribute to the stabilization of the new position of the 280s loop. The hydrogen bonding interactions of the 1,2,3-triazole group with existing water molecules, as well as recruitment of new water molecules that become involved in hydrogen bonding networks may provide additional stabilization. On the contrary, examination of the van der Waals contacts of the phenyl moiety shows this group to be largely in an unfavourable polar environment. Despite the entropy gain due to the net displacement of two water molecules in the glucosyltriazolylacetamide complex, the induced structural perturbation (restructuring of the 280s loop and shift of existing water molecules) would presumably have an energetic cost, perhaps explaining the moderate affinity of glucosyltriazolylacetamide for the enzyme. In general, the rearrangement of the 280s loop within the catalytic site on binding to glucosyltriazolylacetamide does not lead to increased contacts between the inhibitor and the protein as in the case of the *N*-benzoyl-*N´*-β-D-glucopyranosyl urea binding. Indeed, the low μM affinity (K_i: 4.6 μM) of the latter compound for GPb could be interpreted in terms of its increased interactions with the protein [99]. Fewer such interactions observed in the GPb-glucosyltriazolylacetamide complex, and the steric bulk of the 4-phenyl-1,2,3-triazoleacetamido group inducing unfavourable conformational changes in the 280s loop, appear to have led to decreased affinity.

3.2 Naturally occurring pentacyclic triterpenes as inhibitors of glycogen phosphorylase: Structure-activity relationships, kinetic and X-ray crystallographic studies

Organic synthesis *by Professor Hongbin Sun and colleagues at the China Pharmaceutical University, Nanjing, China*

Pentacyclic triterpenes

Pentacyclic triterpenes are widely distributed throughout the plant kingdom and a variety of biological properties have been ascribed to this class of compounds [114]. Pentacyclic triterpenes can be classified into three major types based on their structural skeleton (figure 53): (a) oleanane type of triterpenes (e.g. **1**-**9**, **18**), (b) ursane type of triterpenes (e.g. **10**-**17**, **19**-**22**) and (c) lupane type of triterpenes (e.g. **23**-**25**).
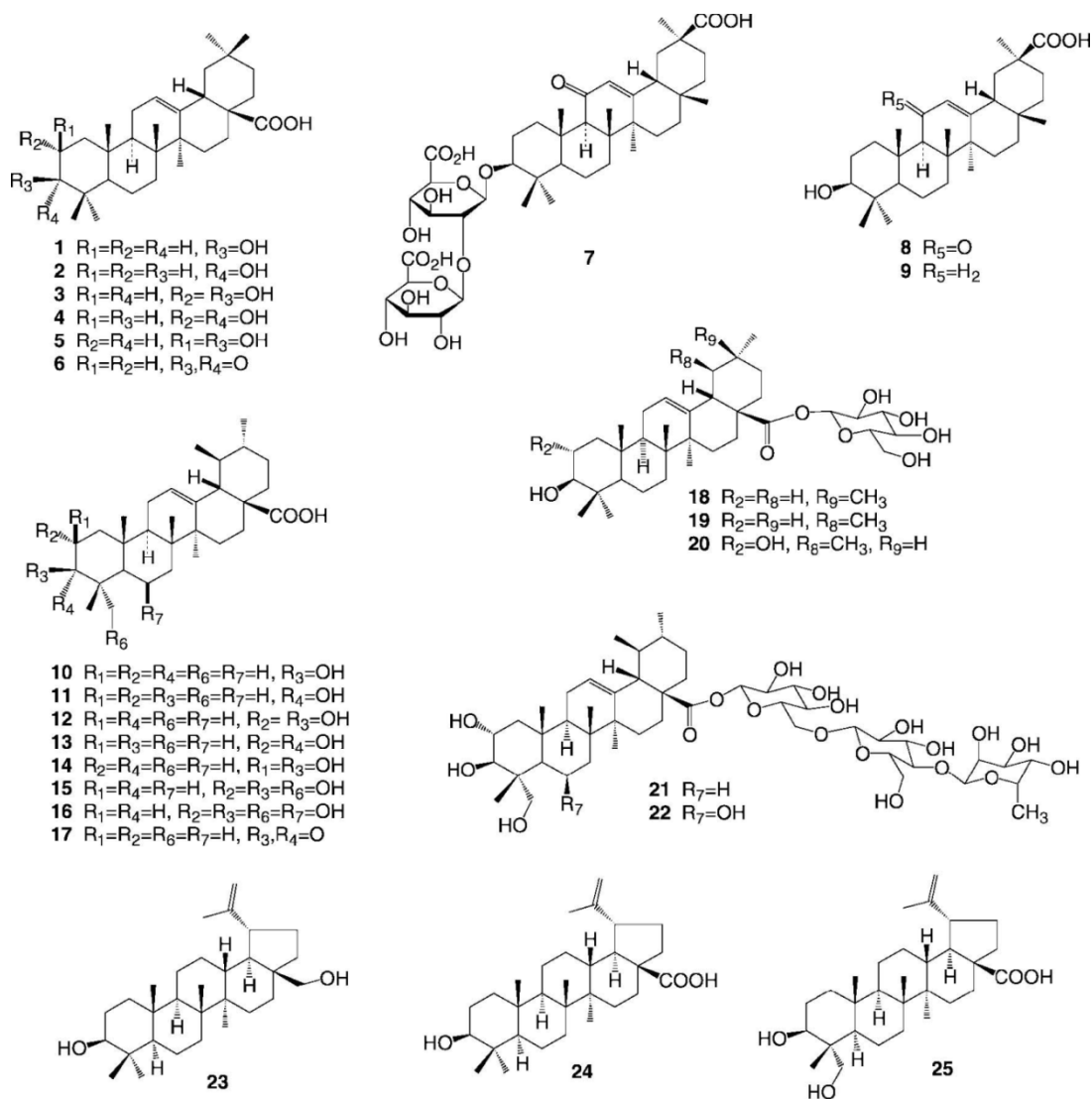
Figure 53. The chemical structures of some naturally occurring pentacyclic triterpenes [136].

Terpenes are produced primarily by a wide variety of plants particularly conifers. They are the major component of resin. In addition to their roles as end-products in many organisms, terpenes are major biosynthetic building blocks within nearly every living creature. They are derived biosynthetically from units of isoprene (C_5H_8). The most well-known member of pentacyclic triterpenes is probably oleanolic acid (**1**) [115] which has been clinically used as a hepatoprotective/antihepatitis drug in China for more than 20 years. Glycyrrhizic acid (**7**) has also been marketed as an antihepatitis drug in China and Japan. Moreover, several other pentacyclic triterpenes have entered clinical trials as anti-HIV or antitumor agents [116-118]. In a recent human test, Japanese researchers proved for the first time that corosolic acid (**12**) exhibited a glucose-lowering effect on post challenge plasma glucose levels in humans [119].

Enzyme assay with GPa and SAR analysis *(by Professor Hongbin Sun and colleagues at the China Pharmaceutical University, Nanjing, China)*

Twenty-five naturally occurring pentacyclic triterpenes were biologically evaluated for their inhibitory activity against rabbit muscle GPa (RMGPa). The activity of RMGPa was measured through detection of the release of phosphate from G1P in the direction of glycogen synthesis.

Compound	GPa IC$_{50}$[a]	Compound	GPa IC$_{50}$[b]
1	14	**14**	116
2	21	**15**	17
3	28	**16**	na[b]
4	144	**17**	57
5	34	**18**	293
6	18	**19**	97
7	822	**20**	106
8	66	**21**	na[b]
9	82	**22**	na[b]
10	9	**23**	17
11	19	**24**	43
12	20	**25**	16
13	213	**caffeine**	114

[a] values are the mean of three experiments, [b] na=no activity

Figure 54. IC$_{50}$ values (µM) for RMGPa.

Most of the tested triterpenes exhibited moderate inhibitory activity against GPa. It seems that the diversity of their structural skeleton of pentacyclic triterpenes does not have a significant impact on GP inhibition, since all the three types of tested triterpenes, including oleanane triterpenes (e.g., **1-9**, **18**), ursane triterpenes (e.g., **10-15**, **17**, **19**, **20**) and lupine triterpenes (e.g., **23-25**), exhibited inhibitory activity against GPa. The amount and positioning of hydroxyl groups of triterpenes seemed to have some impact on potency. Both 2α-hydroxyoleanolic acid (**3**) (IC$_{50}$: 28.0 µM) and 2β-hydroxyoleanolic acid (**5**) (IC$_{50}$: 34.0 µM) were less active than the parent compound (**1**) (IC$_{50}$: 14.0 µM), suggesting that the introduction of hydroxyl group at C2 resulted in a loss of potency. The same tendency was also observed with ursolic acid (**10**) (IC$_{50}$: 9.0 µM), since both 2α-hydroxyursolic acid

(**12**) (IC$_{50}$: 20.0 μM) and 2β-hydroxyursolic acid (**14**) (IC$_{50}$: 116.0 μM) were less potent than (**10**). On the other hand, in two cases examined (**12** vs. **15**; **24** vs. **25**), incorporation of a hydroxyl group at C23 resulted in slight increases in potency. Surprisingly, as in the case of madecassic acid (**16**), incorporation of a hydroxyl group at C6 resulted in a complete loss of potency.

The effects of configuration of hydroxyl groups on GP inhibition were further examined. Conversion of 3β-hydroxyl group of oleanolic acid (**1**) or ursolic acid (**10**) to 3α-hydroxyl group resulted in a slight loss of potency (**1** vs. **2**; **10** vs. **11**). Conversion of 3β-hydroxyl group of (**1**) or (**10**) to 3-carbonyl group did not result in a significant loss of potency (**1** vs. **6**; **10** vs. **17**).

The presence of a sugar moiety in triterpene saponins resulted in a markedly decreased activity (**7**, **18**-**20**) or no activity (**21**, **22**). Glycyrrhizic acid (**7**) (IC$_{50}$: 822.0 μM) was 12-fold less potent than its aglycone (**8**) (IC$_{50}$: 66.0 μM). 3β-hydroxyolean-12-en-28-oic acid β-D-glucopyranosyl ester (**18**) (IC$_{50}$: 293.0 μM) was 20-fold less potent than its aglycone (**1**) (IC$_{50}$: 14.0 μM). The potency difference between (**15**) (IC$_{50}$: 17.0 μM) and (**21**), (a saponin derived from (**15**), was quite intriguing because of the fact that while (**15**) was relatively quite active, (**21**) was inactive at 2 mM. Despite of the low potency or no activity of the triterpene saponins, these saponins might find their value as potential natural prodrugs which are much more water-soluble than the corresponding aglycones. For example, asiaticoside (**21**) was reported to undergo degradation in human bodies to release the biologically active asiatic acid (**15**) [120].

X-ray crystallographic studies of asiatic (15) and maslinic acid (3)

In order to elucidate the structural basis of GP inhibition by pentacyclic triterpenes, the crystal structures of GPb in complex with asiatic acid (**15**) and maslinic acid (**3**) were determined.
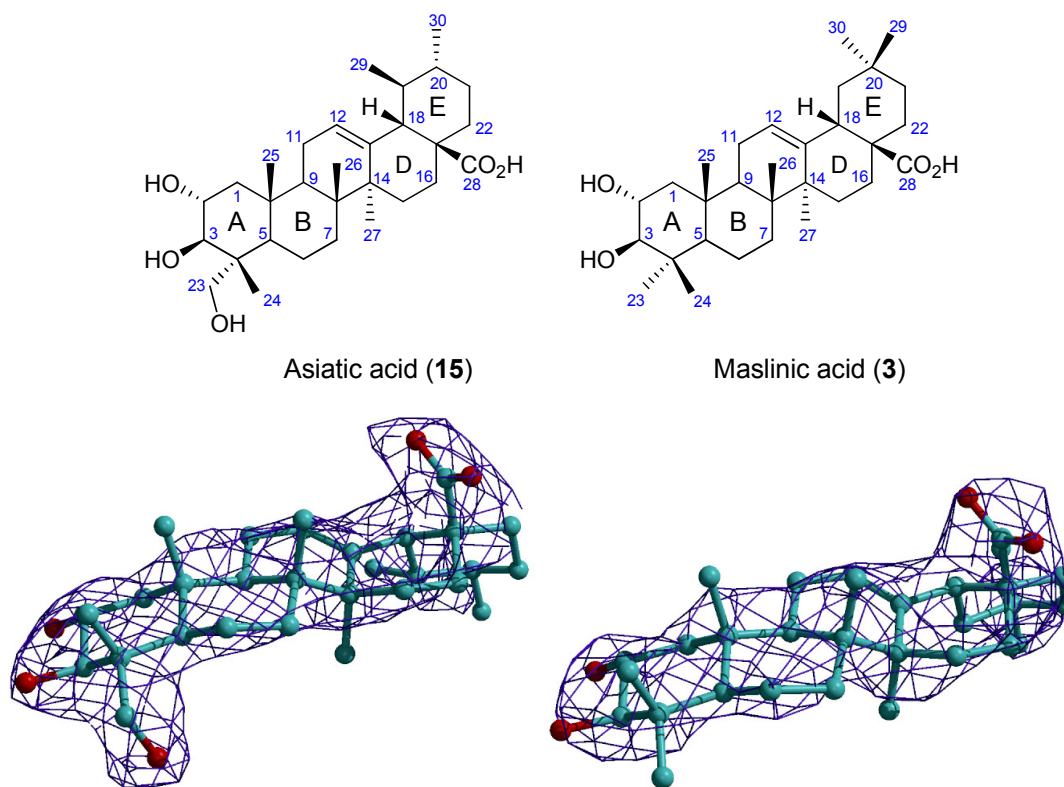
*Figure 55. Chemical structures showing the numbering system used and 2Fo-Fc electron density maps of asiatic acid (**15**) and maslinic acid (**3**). The maps are contoured at 1σ level. The refined models are displayed.*

Binding of asiatic acid (15)

Asiatic acid was found to bind at the interface of the dimer forming the allosteric (AMP) site some 30 Å from the catalytic site (IC_{50}: 141.6 ± 13.0 µM). On binding at the allosteric site, asiatic acid makes a total of 6 hydrogen bonds with the protein, involving all potential hydrogen bonding groups except the hydroxyl group O2, and 48 van der Waals interactions (8 polar/polar, 26 polar/ non-polar, and 14 non-polar/non-polar interactions). There are 13 contacts with residues Asp42′, Asn44′ and Val45′ from the symmetry related subunit. Specifically, hydroxyl O3 and hydroxyl O23 make hydrogen bonding interactions with Gln72 NE2, Asp42′ OD1 and Asp42′ OD2. Carboxylate oxygens O28 and O29 exploit the allosteric effector phosphate-recognition subsite by forming hydrogen bonding interactions with Arg310 NE and NH1.
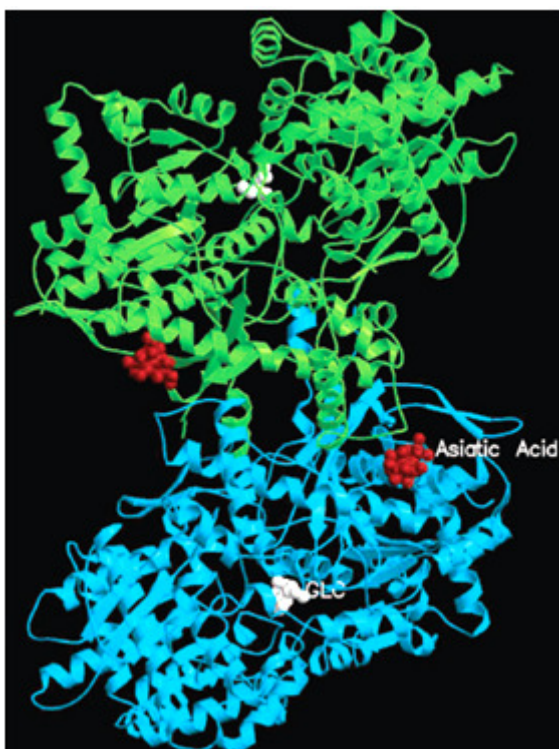
The phosphate-recognition subsite recognizes the phosphate of a variety of phosphorylated compounds, such as AMP, ATP, glucose-6-P_i and the carboxylate of the non-physiological inhibitors W1807 and FR258900 [121-123]. The inhibitor becomes buried on forming the complex with GPb. On the protein surface, a total of 367 Å^2 (309 Å^2 in one subunit and 58 Å^2 in the symmetry related subunit) solvent accessible surface area becomes inaccessible on binding to the ligand. The total buried surface area (protein plus ligand) for the GPb-ligand complex is 854 Å^2.

*Figure 56. Schematic diagram of the T state GPb dimeric molecule, showing the bound asiatic acid (**15**) at the allosteric site (red), and glucose at the catalytic site (white).*
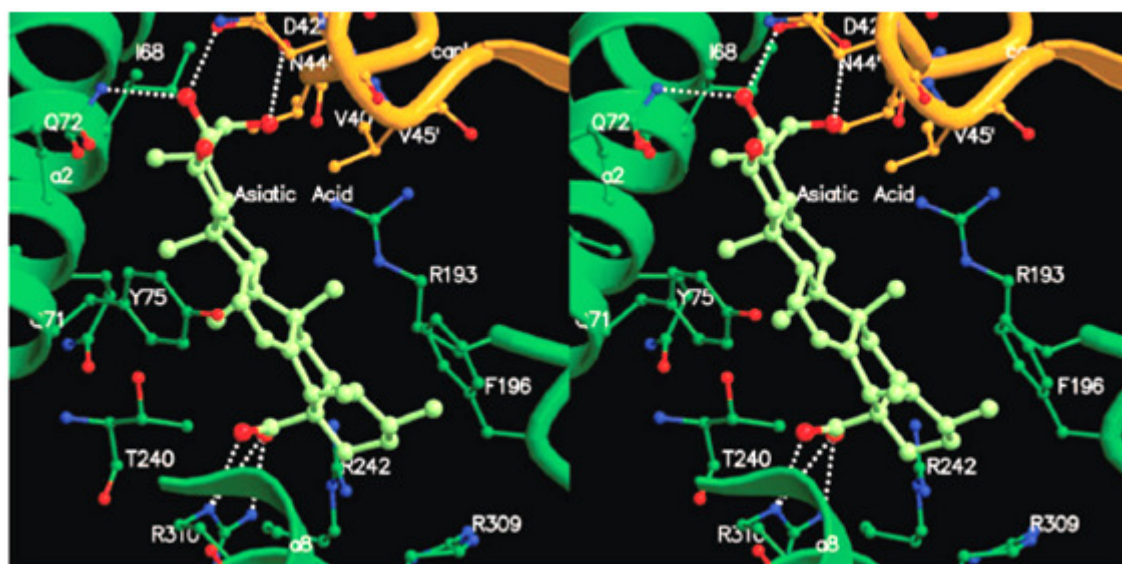
*Figure 57. Stereo diagram showing interactions between asiatic acid (**15**) and GPb in the vicinity of the allosteric site.*

Structural comparison with native T state GPb

Superposition of the activation locus, residues 24-78, 94-111 and 118-125 from both subunits of the structure of the native T state GPb with the activation locus of structure of the GPb-asiatic acid complex gave a root mean square deviation of 0.34 Å for CA atoms, indicating that the two structures have very similar overall conformations within the limits of the 2.4 Å resolution data.
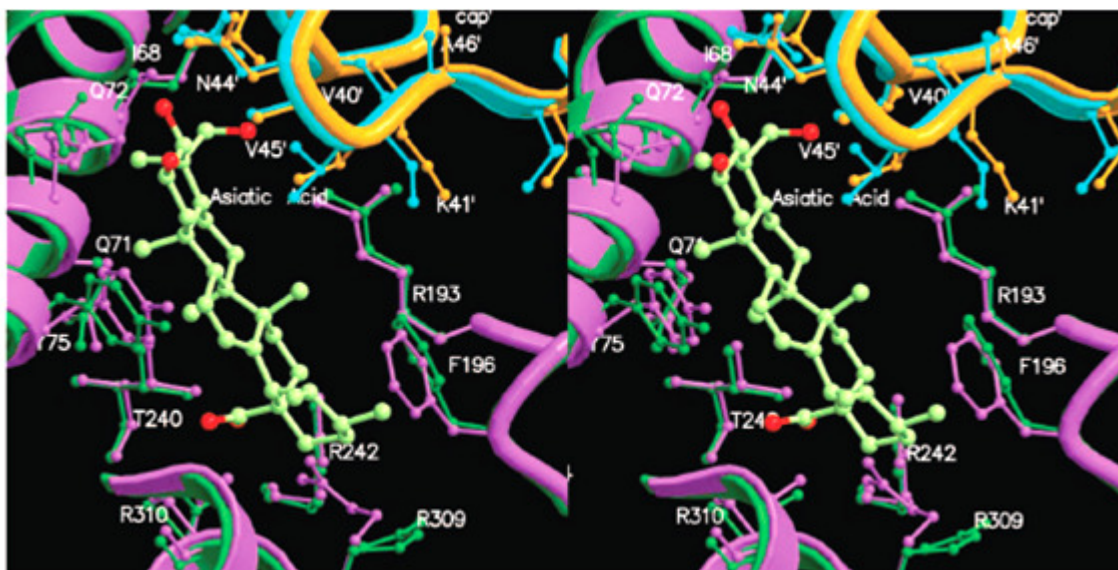
*Figure 58. Stereo diagram showing a comparison between GPb-asiatic acid (**15**) complex (subunit A: green; subunit B: orange) and T state GPb (subunit A: purple; subunit B: cyan).*

The major conformational changes on binding of asiatic acid to rabbit muscle GPb occur in the vicinity of the allosteric site. Shifts for CA atoms are observed for residues 41′-48′ (between 0.4 and 0.7 Å) and residues 71-78 (between 0.4 and 0.7 Å) that affect the subunit-subunit interface in the region between the *cap′* and the *α2* helix. The major shifts for the side chain atoms are observed for residue 72 by about 0.9-1.9 Å and for residue 196 by about 0.6-1.7 Å to optimize their hydrogen bonding and van der Waals interactions with the ligand.

Structural comparison with R state GPa

Comparison of the GPb-asiatic complex with the R state GPa suggests that the inhibitor is likely to have lower affinity for the R state conformation. Superposition of the activation loci of the structure of the R state GP (subunit A) with the activation locus of the structure

of the GPb-asiatic acid complex gave a root mean square deviation of 1.18 Å for CA atoms. If asiatic acid were to be superimposed into the R state GPa, that would result in clashes with Asp42′ atoms OD1, OD2, CG, and CB, Asn44′ atom CG, and Asn72 atoms CA, CB, and NE2. Hence, it would be anticipated that the affinity of asiatic acid for the R state would be less than that of the T state, but there is no direct experimental evidence.
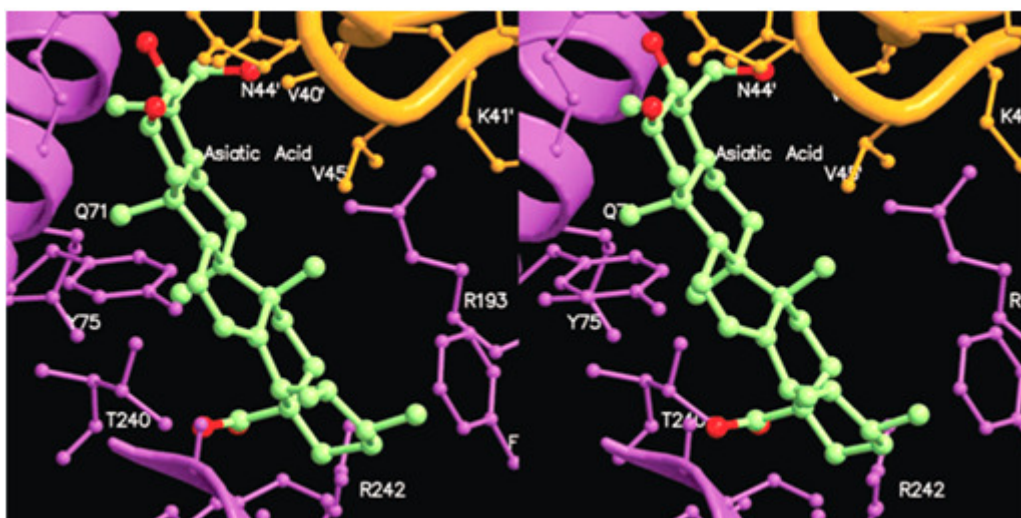
Figure 59. Stereo diagram showing the GPa complex in the R state (subunit A: purple; subunit B: orange). The position of asiatic acid (15) (green) is superimposed.

Structural comparison with AMP
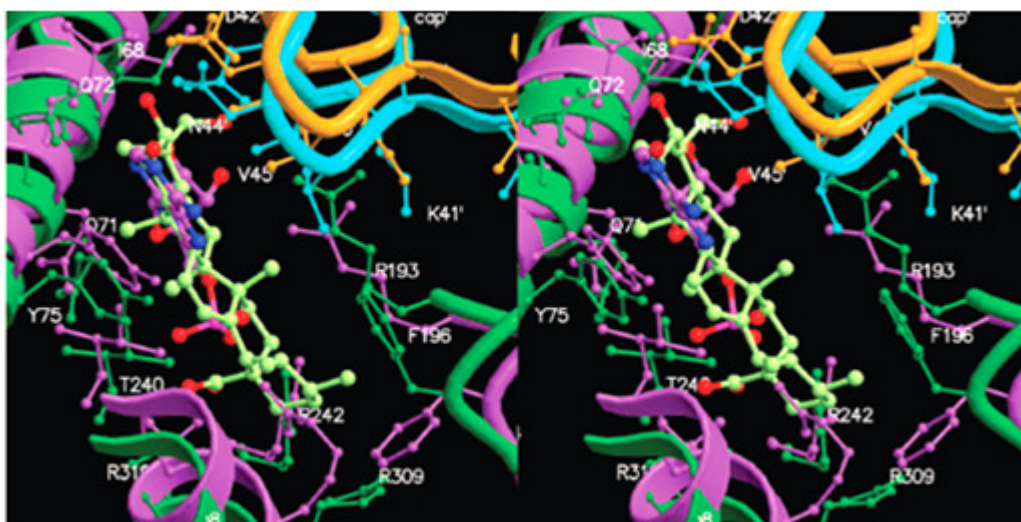
Figure 60. Stereo diagram showing a comparison between GPb-asiatic acid (15) complex (subunit A: green; subunit B: orange) and R state human liver GPa-AMP complex (subunit A: purple; subunit B: cyan).

The adenine and ribose partially overlap with A and B rings of the steroid-like structure, and the phosphate group partially overlaps with the D ring of the cis-fused decalin moiety, while the carboxylate and the phosphate groups are positioned very close to each other in the phosphate-recognition subsite (P/C28 and O1P/O29 separations are respectively 2.2 and 1.8 Å).

Binding of maslinic acid (3)

The position and conformation of maslinic acid, bound at the allosteric site, are also similar to those observed for asiatic acid. The electron density observed for maslinic acid exhibits many common features with the corresponding density of asiatic acid. Interestingly, a similar lack of density for C21, C22, and the methyl C24 is also observed. The main difference between the two structures is the lack of density for O23 that is absent in maslinic acid, although no density is observed for the existing C23 either. The pattern of polar and non-polar interactions between the inhibitor and the enzyme is maintained when comparing the complex structures of asiatic and maslinic acids except that there is no a hydrogen bonding interaction between O23 and Asp42′ OD1 in the maslinic acid complex.
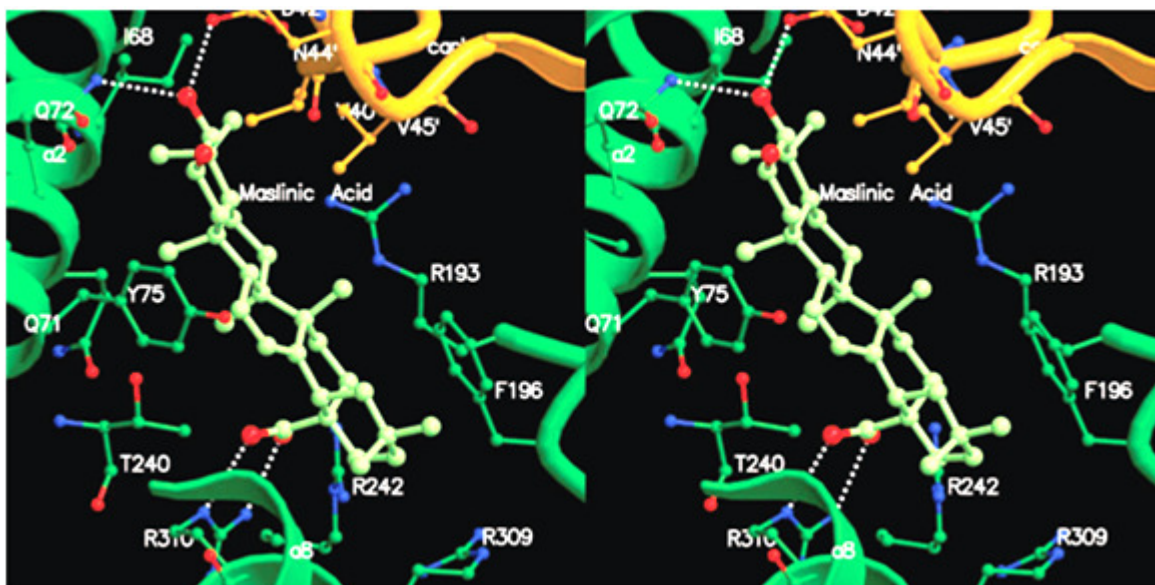
Figure 61. Stereo diagrams showing interactions between maslinic acid (3) and GPb in the vicinity of the allosteric site.

Conclusions

Further studies are needed to address the detailed molecular mechanisms and to biologically evaluate natural and synthetic pentacyclic triterpenes as promising antidiabetic agents with preventive effects against diabetic complications such as ischemic heart and brain diseases. The network of interactions appears important in stabilizing the inactive T state of the enzyme and might explain why asiatic and maslinic acids are micromolar inhibitors.
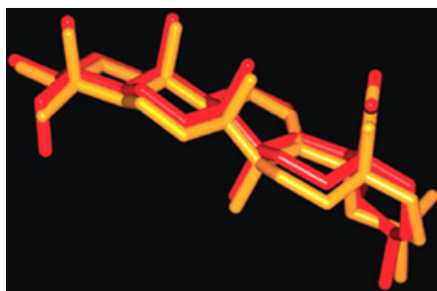
Figure 62. Comparison of the position of asiatic acid (15) (red) to that of maslinic acid (3) (orange) at the allosteric site after superimposing the GPb-maslinic acid (3) complex structure onto the GPb-asiatic acid (15) complex structure.

3.3 Organic synthesis, followed by kinetic and X-ray crystallographic studies of 1-(β-D-glucopyranosyl)-4-hydroxymethyl-1,2,3-triazole. A potential drug target for diabetes type 2 therapeutics

Organic synthesis (*carried out at the Department of Organic Chemistry, University of Debrecen, Hungary, under the supervision of Professor Somsák László, in March 2007*)

Penta-*O*-acetyl-β-D-glucopyranose (**1**) was dissolved in absolute CH_2Cl_2 and Me_3SiN_3 and $SnCl_4$ were added to the solution. The reaction mixture was stirred at room temperature for 3 hours. It was then diluted with water. The organic phase was decanted and extracted with ice water (3 times), then with cold saturated $NaHCO_3$ (twice) and finally with water. The organic phase was dried over $MgSO_4$. The solvent was removed under vacuum and the product [2,3,4,6-tetra-*O*-acetyl-β-D-glucopyranosyl-azide] (**2**) was re-crystallized from ethanol as a white solid. The purity was checked with thin layer chromatography. The melting point of the azide was found to be 127°C and the reaction yield was 65%.

(1)   **(2)**
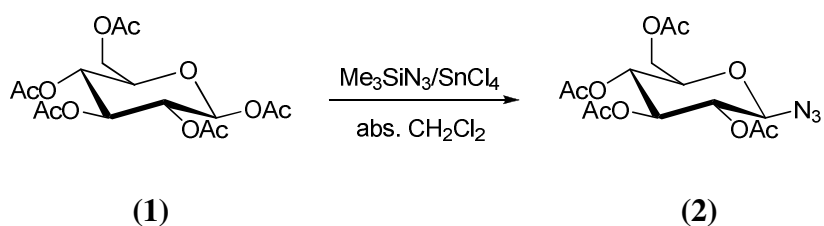
The second step of the synthesis, involved the conversion of the azide (**2**) into 1-(2,3,4,6-tetra-*O*-acetyl-β-D-glucopyranosyl)-4-hydroxymethyl-1,2,3-triazole (**3**). The azide, $CuSO_4$, ascorbic acid and 2-propyn-1-ol were heated together in water at 70°C for 8 hours. The reaction mixture was then cooled down to room temperature in an ice bath. The solid product was filtered and washed with water and methanol. The melting point of the triazole was found to be 150°C and the reaction yield was 55%.

(2)   **(3)**
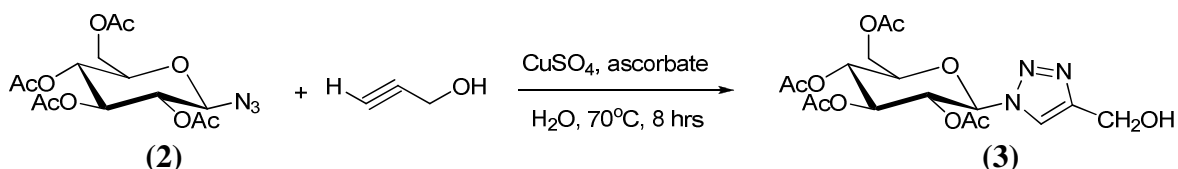
In the last step of the synthesis, the triazole (**3**) was dissolved in absolute methanol and methanolic sodium methoxide solution was added (pH 8-9). The reaction mixture was kept at room temperature. It was then neutralized with a cation exchange resin, Amberlyst 15. Filtration and removal of the solvent resulted in the deacylated triazole product, 1-(β-D-

glucopyranosyl)-4-hydroxymethyl-1,2,3-triazole (**4**). The final product was purified with a silica chromatography column. The reaction yield was 67%.

(3)   **(4)**
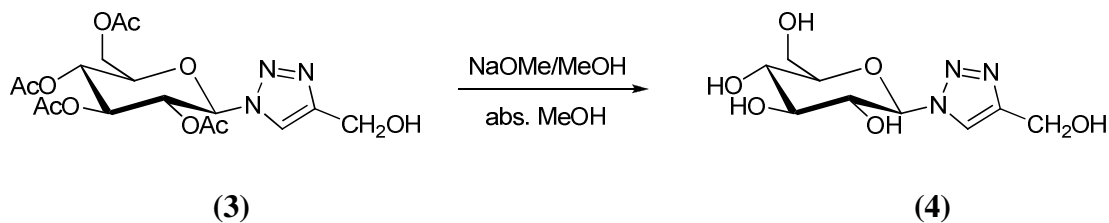
Nuclear Magnetic Resonance Spectroscopy (NMR)

The purity of (**4**) was checked with ^{1}H and ^{13}C NMR.

^{1}H NMR (300 MHz, CD$_3$OD)

δ (ppm): 8.11 (s, 1H), 5.60 (d, J=9.0 Hz, 1H), 4.70 (s, 2H), 3.88 (d, J=11.0 Hz, 2H), 3.79-3.40 (m, 3H).

^{13}C NMR (75 MHz, CD$_3$OD)

δ (ppm): 55.03, 60.98, 69.47, 72.60, 77.08, 79.70, 88.15, 121.90, 147.60.

Kinetic studies of 1-(β-D-glucopyranosyl)-4-hydroxymethyl-1,2,3-triazole (4)

In order to check the affinity of (**4**) for GPb, an IC_{50} experiment was carried out in the direction of glycogen synthesis, at 30°C and pH 6.8 as previously described. The IC_{50} was found to be 23.9 ± 1.9 µM.
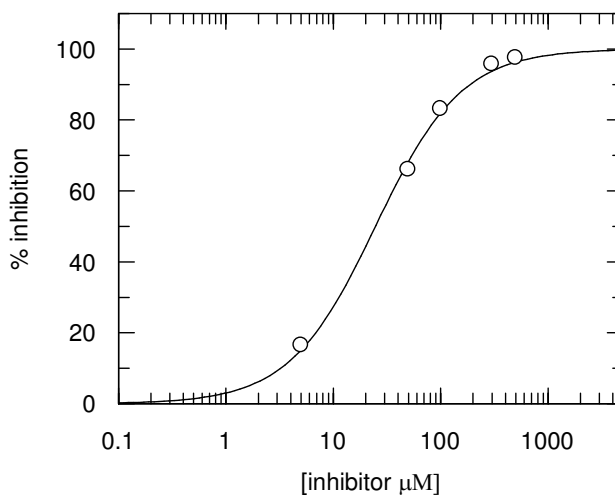
*Figure 63. The IC_{50} inhibition curve for (**4**). The IC_{50} was calculated by plotting % inhibition vs. [inhibitor].*

X-ray crystallographic studies of 1-(β-D-glucopyranosyl)-4-hydroxymethyl-1,2,3-triazole (4)

The inhibitor showed a high affinity for GPb and X-ray crystallographic studies were carried out, in order to elaborate the binding of this inhibitor to the enzyme. The compound was found to be bind specifically at the catalytic site of GPb.
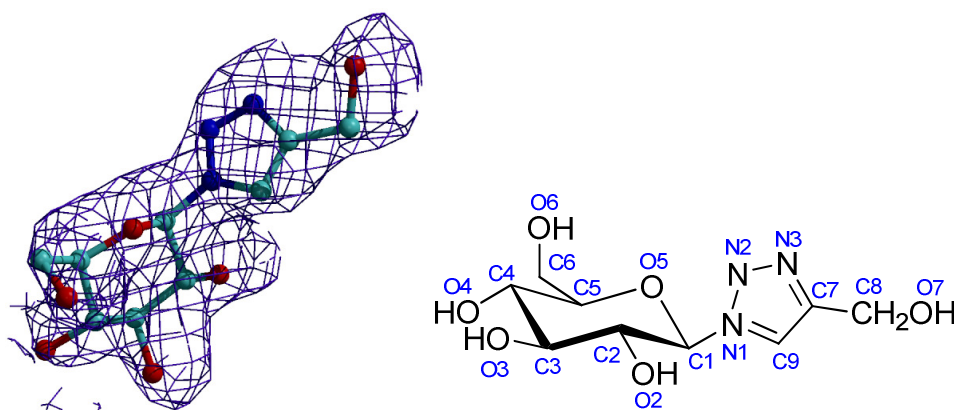
*Figure 64. 2Fo-Fc electron density map of (**4**) bound at the catalytic site of GPb and the numbering used.*
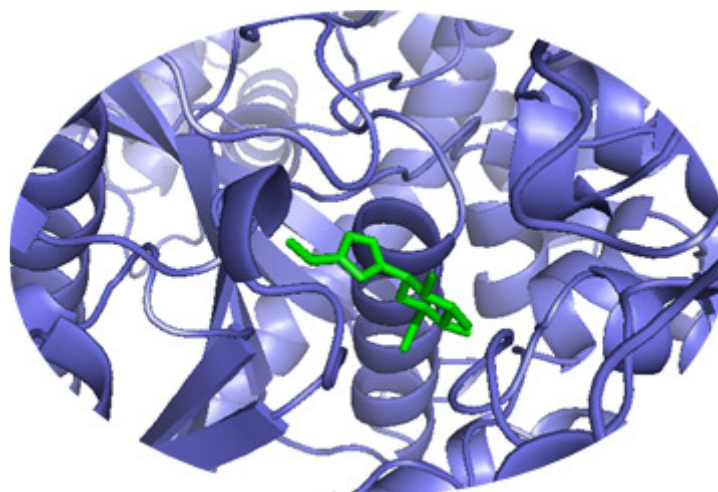
*Figure 65. (**4**) (green) bound at the catalytic site of GPb.*

The inhibitor occupies the so called β-pocket, a subsite of the catalytic site. There are in total 16 hydrogen bonds and 74 van der Waals interactions in the GPb-(**4**) complex.
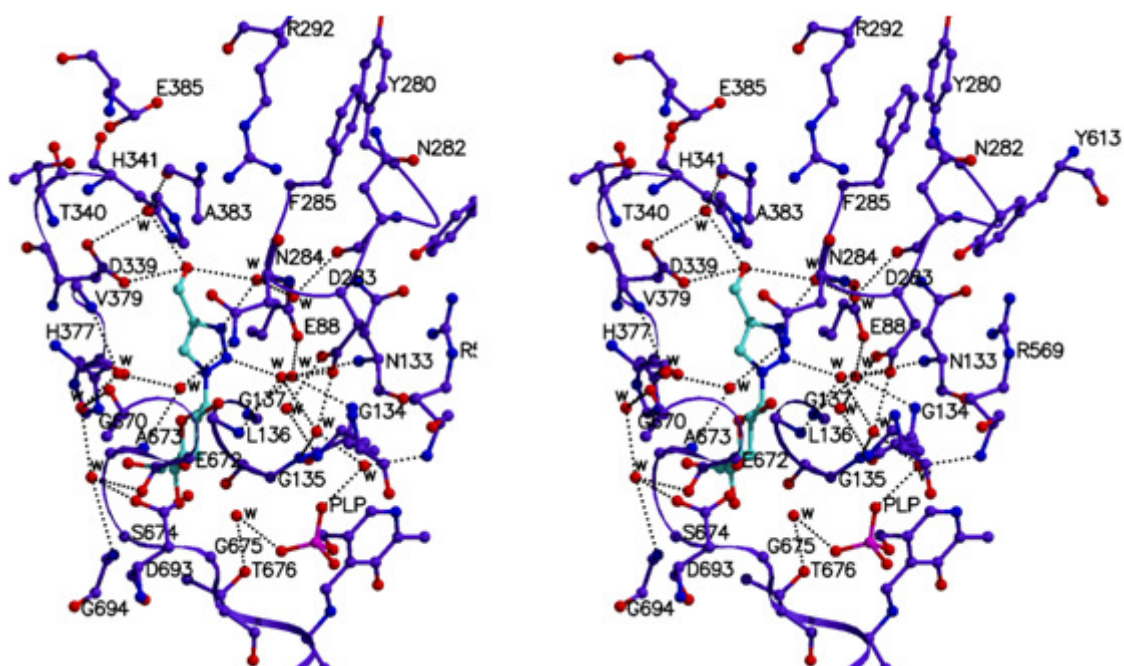
*Figure 66. Stereo diagram showing interactions between (**4**) and GPb in the vicinity of the catalytic site.*

N2 is hydrogen bonded to Glu88 OE2 and residues of the glycine helix (residues 134-150), Asn133 N, Gly134 N and Gly137 N, through three water molecules (Wat245, Wat54, Wat76). O7 is hydrogen bonded to Glu88 OE1 and Asn282 O through two water molecules (Wat258, Wat273).

Structural comparison with *N*-acetyl-β-D-glucopyranosylamine

Since the X-ray crystallographic studies showed that (**4**) is well defined at the catalytic site of the enzyme in accordance with results obtained from the kinetic experiments, a structural comparison between GPb-(**4**) complex and GPb-*N*-acetyl-β-D-glucopyranosylamine complex was carried out.
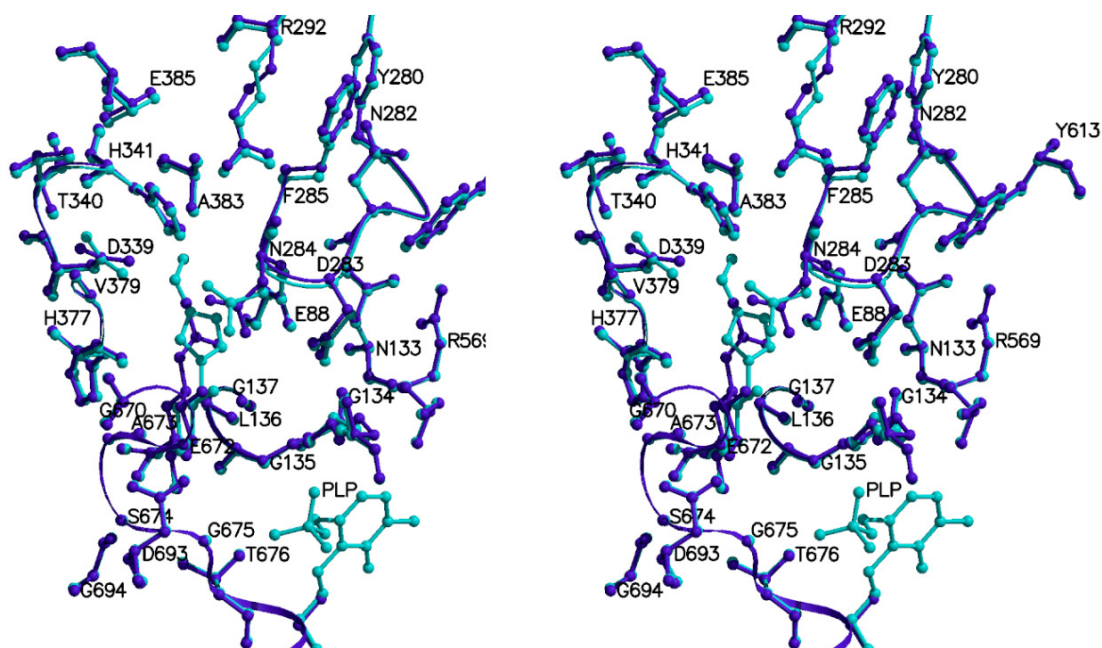
*Figure 67. Stereo diagram showing a comparison between the GPb-(**4**) complex (cyan) and the GPb-N-acetyl-β-D-glucopyranosylamine complex (purple).*

Wat109 is displaced from the *N*-acetyl-β-D-glucopyranosylamine-GPb complex. Wat110 is shifted by 1.21 Å and Wat355 is shifted by 0.58 Å. No new water molecules are recruited into the *N*-acetyl-β-D-glucopyranosylamine-GPb complex. The side chain of Asn284 is shifted by 136.32°. The phenyl ring of the side chain of Phe285 is shifted by 65.48°, while the phenyl ring of the side chain of Phe286 is shifted by 105.17°. There is a negligible shift of Glu287. The side chain of Arg138 of the glycine helix is shifted by 153.89°. The side chain of Leu144 changes orientation and is shifted by 69.66°. The rest of the residues of the glycine helix undergo negligible changes. There is negligible conformational change for the amino acids of the 280s loop. Both *N*-acetyl-β-D-glucopyranosylamine and (**4**) bind similarly to rabbit muscle GPb.

Inhibitor atom	Protein atom	Distance (Å)	Angle (°)
N2	Wat245	2.8	-
N3	Wat258	2.7	-
O2	Tyr573 OH	2.9	146.1
	Glu672 OE1	3.1	176.6
	Wat247	2.8	-
	Wat252	2.9	-
O3	Glu672 OE1	2.7	122.8
	Ser674 N	3.0	176.5
	Gly675 N	3.1	147.0
O4	Gly675 N	2.8	126.5
	Wat118	2.7	-
O6	His377 ND1	2.7	156.7
	Asn484 OD1	2.8	137.0
O7	Asp339 OD2	2.9	136.4
	Wat258	3.1	-
	Wat260	2.9	-

*Figure 68. Hydrogen bond interactions between (**4**) and residues of the catalytic site of GPb.*

N2	**...Wat245**	**...Wat54**	...Gly135 N		
			...Asp283 OD1		
			...Wat57	...Arg569 N	
				...PLP O2P	
		...Wat76	...Glu88 OE2		
			...Asn133 N		
			...Gly134 N		
			...Gly137 N		
N3	**...Wat258**	...Asn284 N			
		...Wat273	...Glu88 OE1		
			...Asn282 O		
O2	**...Wat247**	...Asn284 ND2			
		...Thr671 O			
		...Ala673 N			
		...Wat93	...Val379 N		
			...Thr671 O		
			...Wat250	...Gly670 O	
				...Wat97	...Glu672 O
					...Asp693 OD2
					...Gly694 N
	...Wat252	...Asp283 OD2			
		...Tyr573 OH			
		...Lys574 NZ			
		...Wat54			
O4	**...Wat118**	...Thr676 OG1			
		...PLP O3P			
O7	**...Wat258**				
	...Wat260	...Asp339 OD1			
		...Ala383 O			

*Figure 69. Water hydrogen bonding network of (**4**) at the catalytic site of GPb.*

Inhibitor atom	Protein atom	No. of contacts
N1	Wat245	1
N2	Leu136 CB; Wat258	2
N3	Asn284 CA, N; Wat245	3
C1	Wat252	1
C2	His377 O; Glu672 OE1; Wat247, Wat252	4
O2	Asn284 CG	1
C3	Glu672 OE1; Gly675 N; Wat118	3
O3	Glu672 C, CD, CG; Ala673 C, CA, CB; Ser674 C, CA; Gly675 CA; Wat247	10
C4	Gly675 N; Wat118	2
O4	Asn484 OD1; Ser674 C, CB; Gly675 C, O, CA; Thr676 CG2	7
C5	Gly135 C; Leu136 N; Wat118	3
O5	Leu136 CA, CB, N; His377 CB, ND1	5
C6	Gly135 O, C; Leu136 CA, N; Leu139 CD2; His377 ND1; Asn484 OD1; Wat118	8
O6	Leu139 CD2; His377 CG, CE1; Val455 CG2, CG1; Asn484 CG	6
C7	Asn284 CG, OD1; His377 C, CB, O	5
C8	Asn284 CG, OD1; Asp339 OD2; Wat258	4
C9	Asn284 OD1; Asp339 OD2; Thr378 CB, CG2; Wat258, Wat260	6
O7	Asp339 CG; His341 CE1, NE1	3

*Figure 70. Network of van der Waals interactions between (**4**) and residues of the catalytic site of GPb.*

Experiment	T state GPb crystals soaked with 100 mM inhibitor in 10mM BES for 3 hrs
Wavelength (Å)	1.11665
Oscillation range (°)[a]	0.8
No. of images (°)	80
Space Group	$P4_32_12$
Unit cell dimensions	$a=b$=128.629 Å, c=116.498 Å, $\alpha=\beta=\gamma$=90°
Resolution (Å)	30.0 -2.03
No. of observations	1100864
No. of unique reflections (outermost)	62261 (3036)
R_m (outermost shell) [b]	0.059 (0.428)
Completeness (outermost shell) (%)	98.0 (97.0)
Outermost shell (Å)	2.06–2.03
$< I /\sigma (I) >$ (outermost shell) [c]	24.25 (4.32)
Redundancy (outermost shell)	5.2 (5.1)
B-values (Å^2) (Wilson plot)	32.0
Resolution range (Å)	90.91–2.03
No. of reflections used (free)	59055 (3156)
Residues included	(12-254) (261–314) (324–836)
No. of protein atoms	6597
No. of water molecules	282
No. of heteroatoms	18 (inhibitor), 15 (PLP)
Final R (R_{free}) (%)[d]	0.193 (0.215)
R (R_{free}) (outermost shell)	0.237 (0.276)
r.m.s.d. in bond lengths (Å)	0.007
r.m.s.d. in bond angles (°)	1.008
Average B (Å^2) for residues	(12-254) (261–314) (324–836)
Overall	31.1
CA, C, N, O	30.3
Side chain	31.9
Average B (Å^2) for heteroatoms	21.9 (inhibitor) 20.4 (PLP)
Average B (Å^2) for water molecules	36.2

a Native T state RMGPb crystals, grown in the tetragonal lattice, space group $P4_32_12$ were soaked with various concentrations of inhibitors in buffered solutions at pH 6.7 in the presence of DMSO. X-ray diffraction data were collected using synchrotron radiation sources at Daresbury Laboratory, UK and EMBL-Hamburg outstation at DESY, Germany and processed with the HKL package. Complex structure determination and analysis were performed according to standard protocols as implemented in the CCP4 package. **b** $R_{symm} = \Sigma_h\Sigma_i|I(h) - I_i(h)|/\Sigma_h\Sigma_i I_i(h)$ where $I_i(h)$ and $I(h)$ are the ith and the mean measurements of the intensity of reflection h. **c** $\sigma(I)$ is the standard deviation of I.

d $R_{cryst} = \Sigma_h|F_o - F_c|/\Sigma_h F_o$, where F_o and F_c are the observed and calculated structure factors amplitudes of reflection h, respectively. R_{free} is equal to R_{cryst} for a randomly selected 5% subset of reflections not used in the refinement. Values in parentheses are for the outermost shell.

Figure 71. Diffraction data and refinement statistics for (4).

Conclusions

(**4**) was synthesized in a three step reaction. It showed moderate inhibition against GPb. The structure was well defined at the catalytic site of the enzyme by the electron density map. Structural comparisons with *N*-acetyl-β-D-glucopyranosylamine showed no considerable conformational changes. Further studies could give more insight on the mechanism of action of this inhibitor of glycogen phosphorylase.

3.4 Amide 1,2,3-triazole comparison of glycogen phosphorylase inhibitors: a bioisosterism case

Bioisosterism

Bioisosterism is a strategy used in medicinal chemistry for the rational design of new drugs, applied with a lead compound, as a special process of molecular modification. The lead compound should be of a completely well known chemical structure and possess an equally well known mechanism of action, if possible at the level of interaction with the receptor, including knowledge of its pharmacophoric group [124].

During the past years, the similarities between the amide moiety (**A**) and the 1,2,3-triazole ring (**B**) have gathered a lot of interest [125-127].
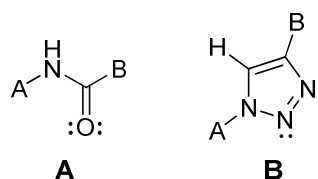
The similarities of the two moieties can be seen in size (distance between substituents 3.8–3.9 Å in amides and 5.0–5.1 Å in triazoles), the dipolar character (amide ~ 4 Debye and triazole ~ 5 Debye) and the H-bond acceptor capacity (lone pairs of the amide oxygen as well as of the triazole nitrogens).

Organic synthesis (*by Professor Somsák László, Department of Organic Chemistry, University of Debrecen, Hungary*)
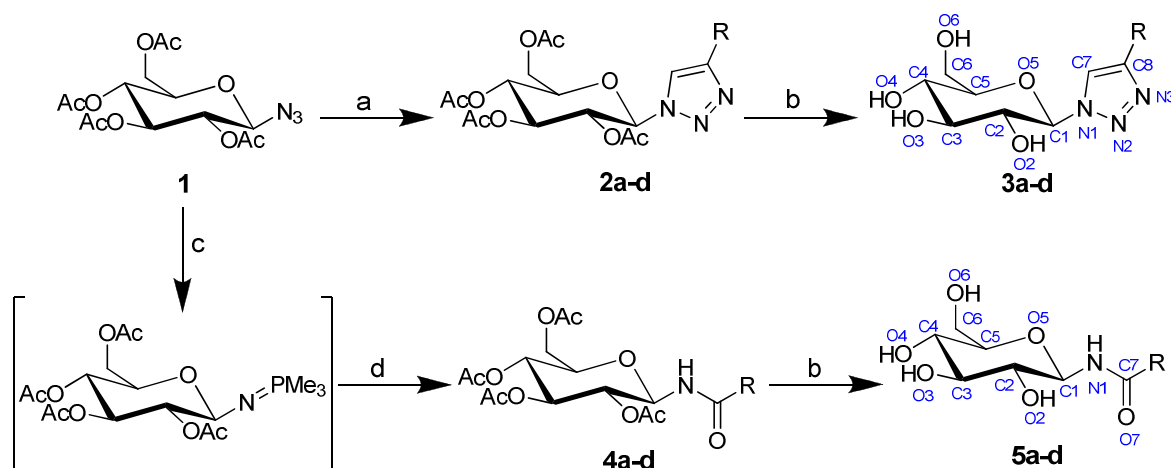
a) R-C≡CH, CuSO$_4$, ascorbic acid, water, 70°C, 8hrs; b) NaOMe (cat.), MeOH, rt.; c) PMe$_3$,
b) dry CH$_2$Cl$_2$, rt.; ~10 minutes, followed by d) RCOOH in CH$_2$Cl$_2$, rt.

*Figure 72. Synthesis and crystallographic numbering of 1-(β-D-glucopyranosyl)-4-substituted-1,2,3-triazoles (**3**) and N-acyl-β-D-glucopyranosylamines (**5**) [137].*

Kinetics studies

Compounds (**3a–d**) and (**5a–d**) were assayed in the direction of glycogen synthesis for their inhibitory effect on rabbit muscle GPb. Each compound exhibited competitive inhibition with respect to the substrate G1P, at constant concentrations of glycogen (0.2% w/v) and AMP (1 mM). Comparison of the inhibition constants (K_i) measured for triazoles and amides having the same R groups showed reasonable agreement for the two series, as shown in figure 73.
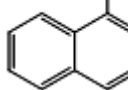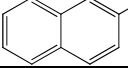
	R group	Amide (5) K_i (µM)	Triazole (3) K_i (µM)
a		81	151.3 ± 2.3
b		190.7 ± 23.7	135.9 ± 9.5
c		12.8 ± 1.6	16.1 ± 1.3
d	CH_2OH	17.9 ± 0.4	13.7 ± 1.0

Figure 73. Inhibitory effect (K_i) against rabbit muscle GPb.

X-ray crystallographic studies of triazole (3a) vs. amide (5a)
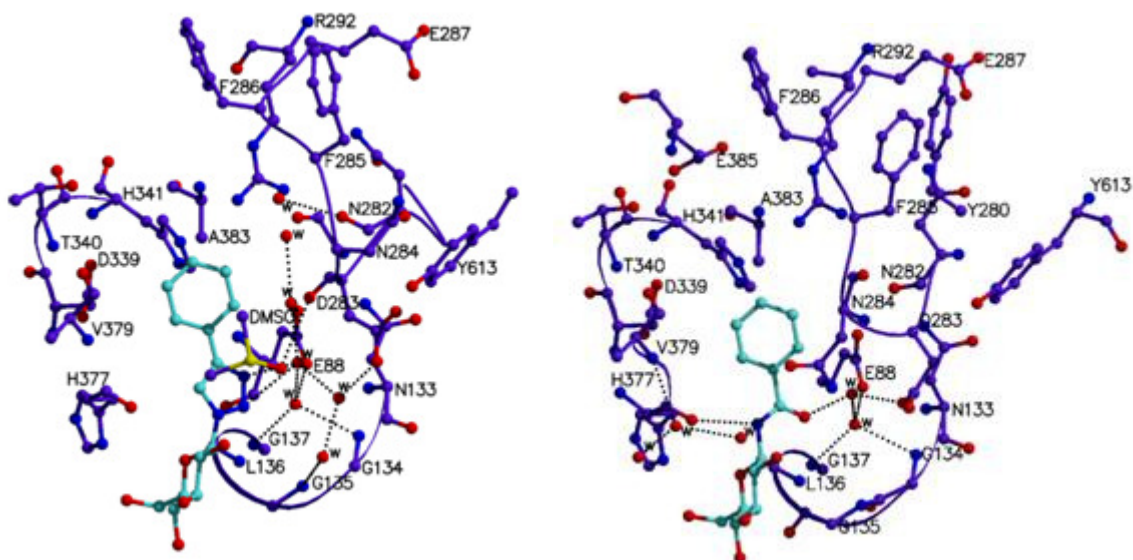
*Figure 74. Comparing the network of interactions between (**3a**) (left) and (**5a**) (right) with residues of the catalytic site of GPb.*

Triazole (**3a**) binds at the catalytic site of the enzyme forming 13 hydrogen bonds and 83 van der Waals interactions, with a DMSO molecule also bound at the same site. The latter is mainly involved in van der Waals interactions with O2 of the glucopyranose ring and the three nitrogens of the triazole moiety. A number of changes are induced upon binding of (**3a**) to the catalytic site, especially in residues coming from the 280s loop, compared to the corresponding amide analogue.

*Figure 75. Stereo diagram showing a comparison between the GPb-(**3a**) complex (purple) and the GPb-(**5a**) complex (yellow).*

Comparing (**3a**) and (**5a**) in more detail the following could be observed: all glucopyranose atoms lie almost at identical positions at the catalytic site of the enzyme except C1 that shifts by ~ 0.6 Å to best accommodate the triazole ring and maintains the orientation of the rest of the ligand atoms along the catalytic channel. The nitrogen atoms N2 and N3 of (**3a**) form water-meditated interactions with residues from the glycine-rich helix (residues 130–137) Gly134 N and Gly137 N and Glu88 OE2 (through waters Wat204 and Wat87). Focusing on (**3a**) phenyl group, it is subjected to a rotation of ~ 25° and the corresponding atom shifts vary from ~ 0.7 to ~ 1.0 Å, resulting in the displacement of a water molecule (Wat200) of (**5a**). This adjustment of the aromatic ring is due to both the binding of a DMSO molecule and modifications observed in the residues of the 280s loop. The DMSO molecule is located in the position previously occupied by the Asn284 side chain in the (**5a**) complex structure. The new orientation adopted by the Asn284 side chain is mainly responsible for the rearrangement of the rest of the 280s loop residues to comply with

stereochemical conditions. Even if the structural results show that the differences outlined above are significant this is not reflected in the potency of (**3a**) and (**5a**) as inhibitors of GPb, indicating that the arrangement of the catalytic site components is almost equally favourable in both complex structures.

X-ray crystallographic studies of triazole (3b) vs. amide (5b)

Comparison of triazole (**3b**) and amide (**5b**) complex structures shows that both compounds are well defined at the catalytic site of the enzyme in accordance with the results obtained from the kinetic studies. In particular, (**3b**) forms a total of 14 hydrogen bonds and 88 van der Waals interactions, while (**5b**) is involved in 13 hydrogen bonds and 99 van der Waals interactions. The position of the glucopyranose moiety is specific and a shift of the C1 atom by ~ 0.6 Å compared to the reference structure (**5b**) is observed. This shift is similar to the one detected in (**3a**) due to the introduction of the triazole moiety. The nitrogen atoms of (**3b**), N2 and N3, interact with a direct hydrogen bond with Leu136 N and water-mediated hydrogen bonds with Asp283 OD1 (through Wat64), with the glycine-rich helix N atoms of residues Gly134 and Gly137 as well as OE1 and OE2 atoms of Glu88 (through waters Wat63, Wat64 and Wat65). The naphthyl group adopts a different orientation (rotation by ~ 160°) with regard to the (**5b**) complex. The position of the second phenyl group is now occupied by Wat63 implicated in a network of water-mediated contacts with the triazole nitrogens, optimizing the ligand interactions on binding.

*Figure 76. Comparing the network of interactions between (**3b**) (left) and (**5b**) (right) with residues of the catalytic site of GPb.*

The differences observed in the naphthyl group atoms are interrelated with the changes in the 280s loop residues. These involve changes in Asn284 that now points to the inhibitor site between Phe285 and Tyr613 aromatic rings, to avoid clashes with the naphthyl group at its new position. As a result the rest of the residues lining the loop are also subjected to changes in their conformation to satisfy stereochemical conditions imposed by Asn284. These are summarized as follows: Asn282 (CA atom shifts by ~ 0.5 Å), Asp283 (CA moves by ~ 0.7 Å), Phe285 (CA shifts by ~ 2.4 Å), and Phe286 (CA shifts by ~ 0.9 Å). Minor shifts in the range of ~ 0.4 Å are also observed for all atoms of His377. Further adjustments in the water structure in the vicinity of the catalytic site are also observed due to the reorganization of the 280s loop residues to improve the overall network of interactions formed on binding of (**3b**): Wat280 located at the inhibitor site in (**5b**) complex is now displaced due to stereochemical clashes with the Asn284 side chain atoms and a new water (Wat86) is recruited to optimize Asn284 interactions at the inhibitor site. Despite the differences mapped upon binding of (**3b**) to the catalytic site of GPb compared to those of (**5b**), the number of hydrogen bond and van der Waals interactions formed between the two inhibitors is equivalent. This finding suggests that the similar inhibition potency exhibited by both compounds might reveal that an energetically favourable conformation is adopted both for the 280s loop residues and the ligands in the GPb-(**3b**) and GPb-(**5b**) complex structures.
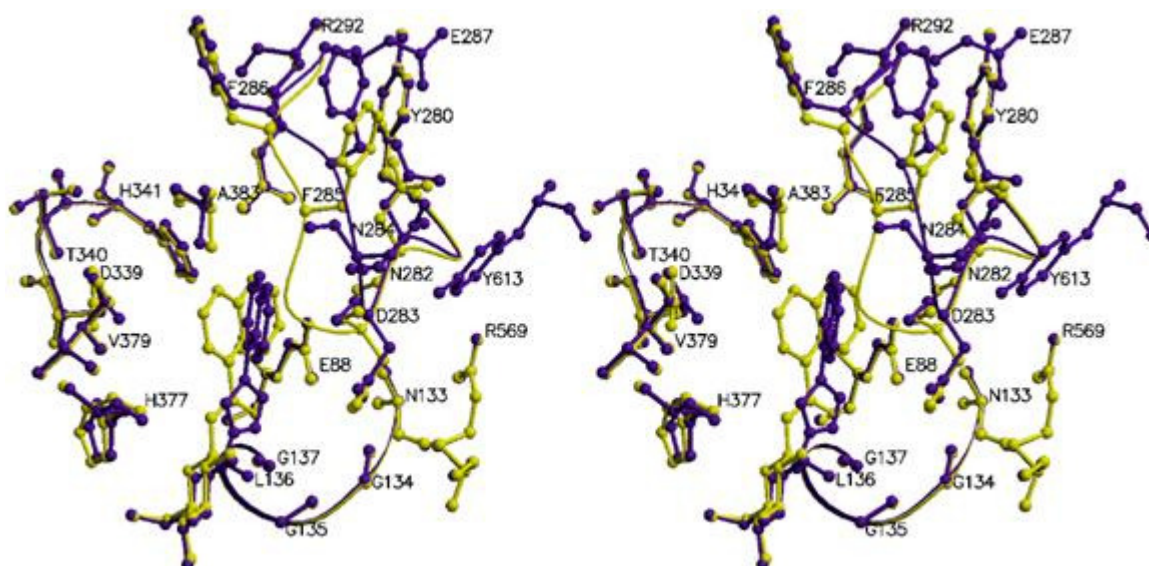
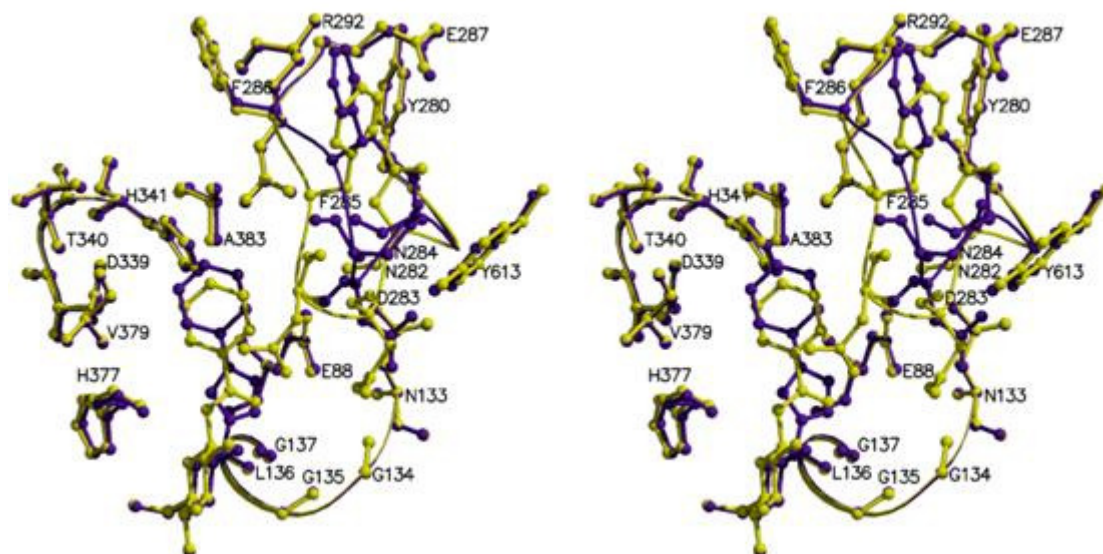*Figure 77. Stereo diagram showing a comparison between the GPb-(**3b**) complex (purple) and the GPb-(**5b**) complex (yellow).*

X-ray crystallographic studies of triazole (3c) vs. amide (5c)

It was found that (**3c**) binds along the catalytic channel of GPb forming in total 14 hydrogen bonds and 109 van der Waals interactions. The naphthyl group occupies the so-called β-pocket, a subsite of the catalytic site, similar to the benzoyl moiety in the GPb–*N*-benzoyl-*N´*-β-D-glucopyranosylurea complex [97].
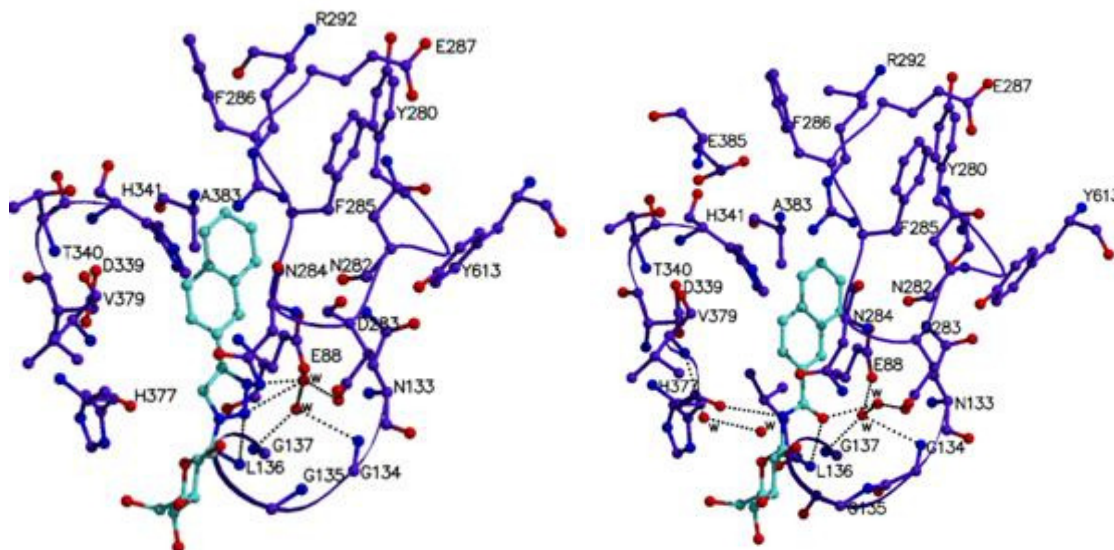
Figure 78. Comparing the network of interactions between (3c) (left) and (5c) (right) with residues of the catalytic site of GPb.

In detail, the phenyl group of *N*-benzoyl-*N´*-β-D-glucopyranosylurea lies next to the 280s catalytic loop, as dictated by the orientation of the urea moiety, inducing a dramatic shift of the residues lining the loop. This shift is not observed upon binding of (**3c**) since the atoms forming the urea are now replaced by the triazole and the naphthyl ring is accommodated in the β-pocket with no perturbation of the neighbouring residues. The same applies for (**5c**) in which the urea part is also absent and replaced by the amide group. Comparison of (**3c**) with (**5c**) binding mode shows no notable changes at the catalytic site of GPb except small changes in the conformation of the Asn284 side chain e.g. Wat43 (Wat109 in (**5c**) complex) moves by ~ 0.8 Å to improve its hydrogen bonding interaction with N3. Overall both (**3c**) and (**5c**) bind at GPb similarly. Although the amide nitrogen N1 of (**5c**) is hydrogen bonded to His377 O forming a favourable interaction characteristic for most glucose analogues [89, 108] with an amide group at C1 position of the pyranose ring, it does not exhibit improved affinity for the enzyme compared to (**3c**). The absence of this interaction in the (**3c**) could be counterbalanced by the direct hydrogen bond interaction between N2-Leu136 N and N3-Asp283 OD1 (through Wat43).
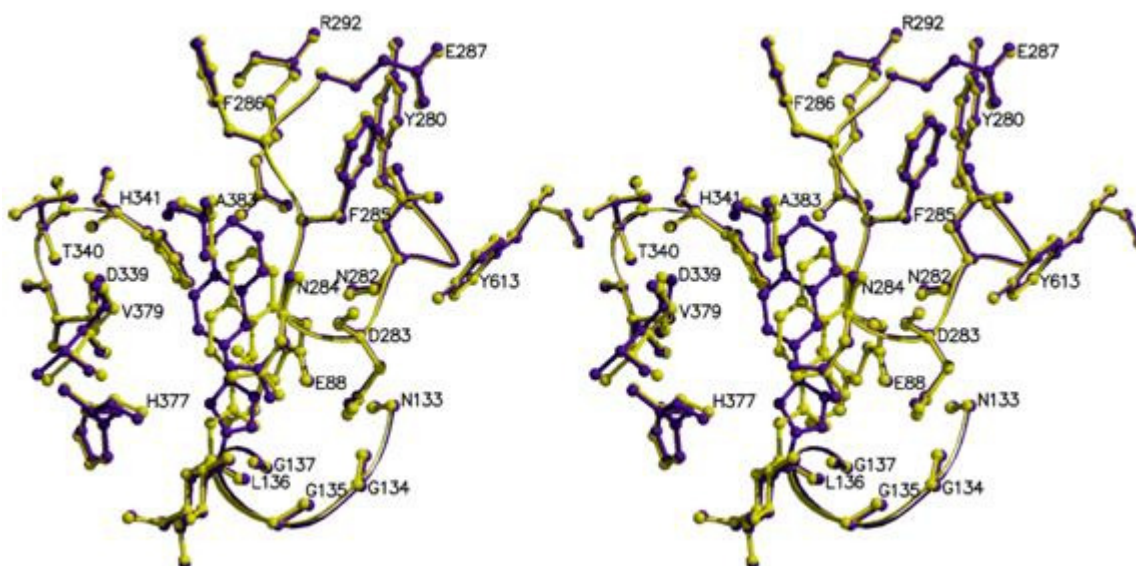
*Figure 79. Stereo diagram showing a comparison between the GPb-(**3c**) complex (purple) and the GPb-(**5c**) complex (yellow).*

X-ray crystallographic studies of triazole (3d) vs. amide (5d)

It was shown that (**3d**) binds at the catalytic site of GPb forming a total of 16 hydrogen bonds and 91 van der Waals interactions, in a similar fashion to its amide analogue (**5d**) (14 hydrogen bonds, 89 van der Waals interactions).
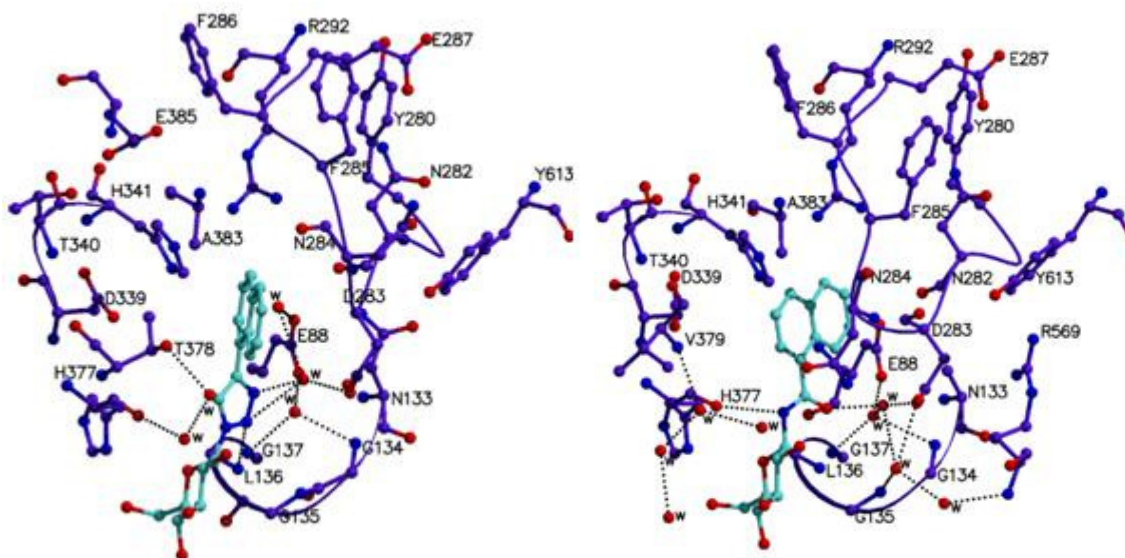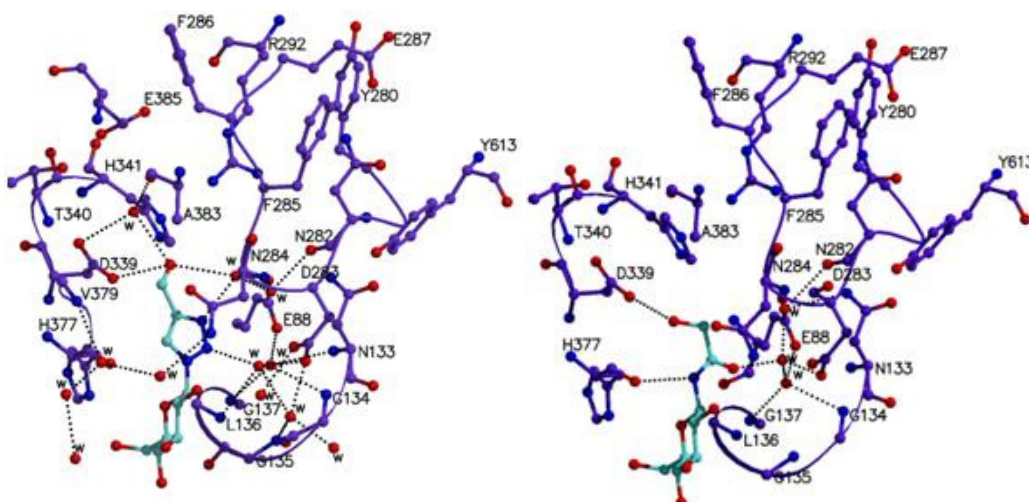

*Figure 80. Comparing the network of interactions between (**3d**) (left) and (**5d**) (right) with residues of the catalytic site of GPb*

.

Although the characteristic hydrogen bond interaction formed between the amide nitrogen of (**5d**) and the backbone oxygen atom of His377 is not present in the GPb-(**3d**) complex structure, it seems that the additional water-mediated interactions formed between N2 and N3 of the ligand with Asp283 OD1, Leu136 N (through Wat245) and Asn284 N (through Wat258), respectively compensate for this loss resulting in similar affinities. Minor changes are also observed in the catalytic residues Asn284 and Phe285 to optimize the network of interactions upon the binding of (**3d**). These changes induce shifts in Phe285 atoms by ~ 0.5 Å. In general, the crystal structures of both (**3d**) and (**5d**) do not exhibit overall changes but only localized, favourable though as reflected in their inhibitory effect, alterations in the 280s loop.
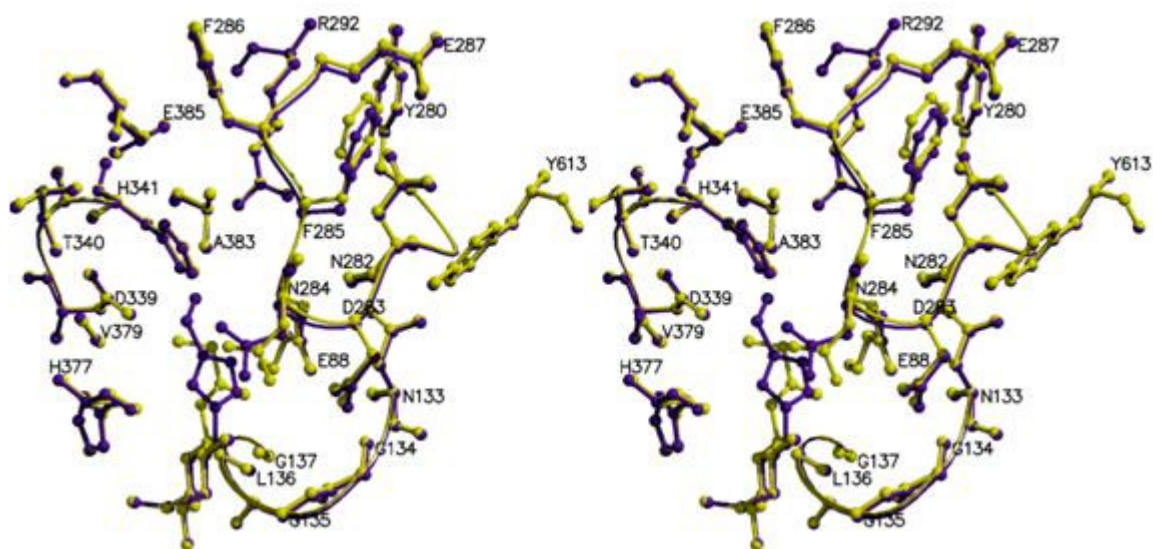
*Figure 81. Stereo diagram showing a comparison between the GPb-(**3d**) complex (purple) and the GPb-(**5d**) complex (yellow).*

Reactivity of the naphthyl group

Between the four pairs of compounds studied, the most potent inhibitor was (**5c**) with a K_i: 12.8 ± 1.6 μM. The change of the naphthyl group from the alpha position to the beta position, between (**3b-5b**) and (**3c-5c**) resulted in an almost 9 fold drop of the K_i value. This can be explained by the fact that the naphthyl group can undergo electrophilic aromatic substitution reactions. Usually electrophiles attack the alpha position.

Alpha position   **Beta position**
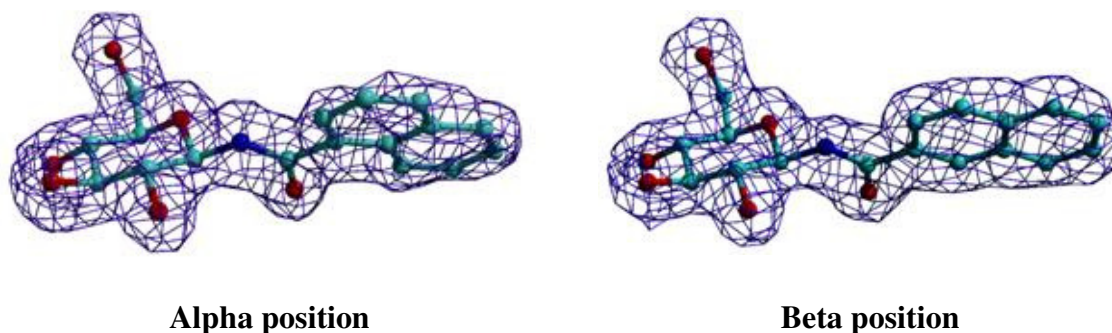
Figure 82.2Fo-Fc electron density map of α-N-naphthoyl-β-D-glucopyranosyl urea (left) and β-N-naphthoyl-β-D-glucopyranosyl urea (right) bound at the catalytic site of GPb. The map is contoured at 1σ level. The refines models are displaced.

This selectivity for alpha over beta substitution can be explained in terms of the resonance structure of the intermediates: for the alpha substitution intermediate, seven resonance structures can be drawn, of which four preserve an aromatic ring. For beta substitution, the intermediate has only six resonance structures, and only two of these are aromatic. Therefore in the case of (**3c**) and (**5c**), the alpha position is free to react, and the K_i is lowered, making these compounds more potent inhibitors than the corresponding (**3b**) and (**5b**) pair.

Conclusions

All ligands bound at the catalytic site of the enzyme at well-defined positions as clearly indicated by the structural data (2.0–2.3 Å resolution for all complexes). In the case of the α-naphthyl derivatives, the triazole compound induced significant conformational changes to the architecture of the 280s loop at the catalytic site, mainly caused by flipping of Asn284 side chain that was intercalated between Phe285 and Tyr613 side chains forming the inhibitor site of the enzyme. However, these changes were not observed in the corresponding amide compound and the flexibility of the 280s loop residues might explain this difference. In contrast, for the β-naphthyl and hydroxymethyl derivatives the binding mode of both triazole and amide compounds proved to be very similar. This study provides a new example of the amide-1,2,3-triazole bioisosterism and supports the use of this. Comparing the amide derivatives (**5b**) and (**5c**), as well as the triazole derivatives (**3b**) and (**3c**), a significant decrease of the K_i values is observed. As already mentioned above, this can be attributed to the reactivity of the α-naphthyl functional groups. The architecture of the binding site of interest of the molecular target under investigation should also be taken into consideration in the design of potential bioisosteres.

3.5 A new class of *C*-glucosyl derivatives of hydroquinone and the discovery of a new binding site of glycogen phosphorylase

Organic synthesis *by Professor Jean-Pierre Praly and colleagues, Laboratoire de Chimie Organique, Université Claude Bernard, Villeurbanne, France*

Kinetic studies

2,5-dihydroxy-3-(β-D-glucopyranosyl)-chlorobenzene/ 2,5-dihydroxy-4-(β-D-glucopyranosyl)-chlorobenzene

IC$_{50}$: 140.0 ± 10.0 μM

(**1a,b**)

3-(β-D-glucopyranosyl)-2-hydroxy-5-methoxy-chlorobenzene

IC$_{50}$: 39.8 ± 0.3 μM

(**2**)

2,5-dihydroxy-4-(β-D-glucopyranosyl)-bromobenzene

IC$_{50}$: 136.4 ± 4.9 μM

(**3**)

2,5-dihydroxy-4-(β-D-glucopyranosyl)-chlorobenzene

IC$_{50}$: 169.9 ± 10.0 μM

(**4**)
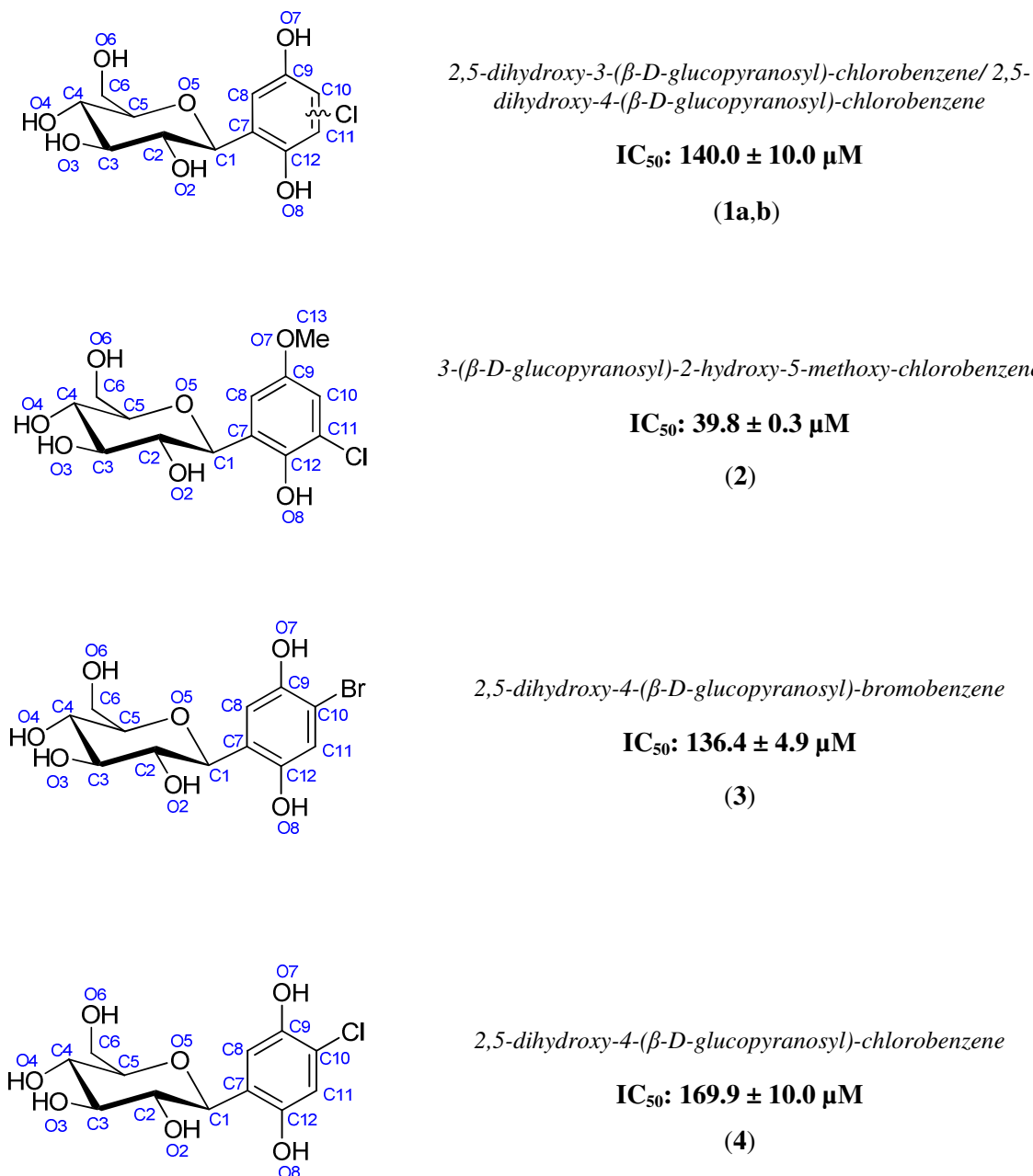
Figure 83. The chemical structures, the numbering used and the kinetic results of the C-glucosyl derivatives of hydroquinone studied.

Four derivatives of hydroquinone were studied and the *in vitro* kinetic studies revealed IC_{50} values ranging from 38.9 µM to 169.9 µM, reflecting the effect of the various substituents on inhibition.

X-ray crystallographic studies of isomers 2,5-dihydroxy-3-(β-D-glucopyranosyl)-chlorobenzene (1a) and 2,5-dihydroxy-4-(β-D-glucopyranosyl)-chlorobenzene (1b)

The two structural isomers (**1a**) and (**1b**) were found to bind at the catalytic site of GPb. These compounds were synthesized as a mixture.
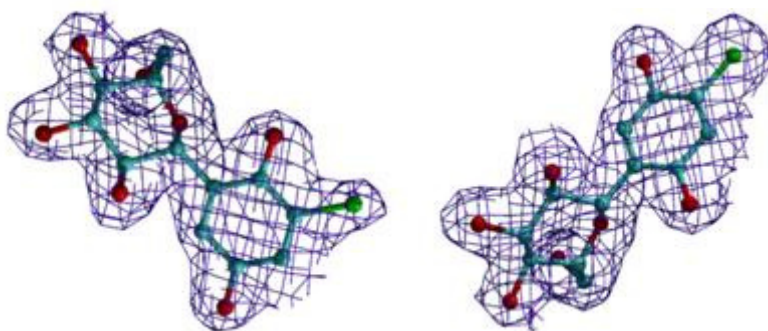
*Figure 84. 2Fo-Fc electron density maps of (**1a**) (left) and (**1b**) (right) bound at the catalytic site of GPb. The map is contoured at 1 σ level and the refined models of the inhibitors are displayed.*
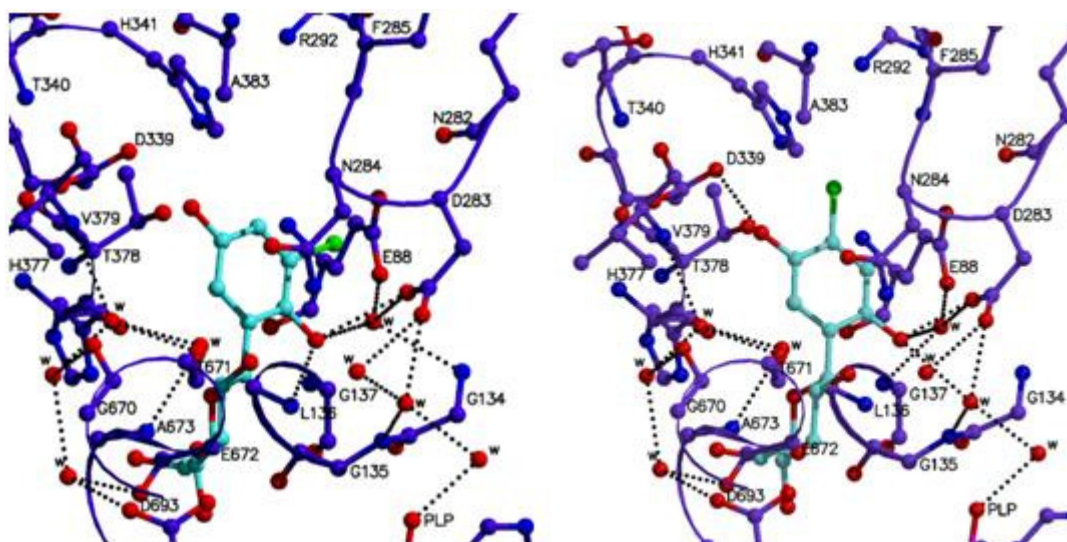
*Figure 85. The network of hydrogen bond interactions of (**1a**) (left) and (**1b**) (right) with residues of the catalytic site of GPb.*

Upon binding, (**1a**) forms a total of 13 hydrogen bonds and 89 van der Waals interactions, stabilizing the T state of the enzyme. In comparison, (**1b**) forms an extensive number of 17 hydrogen bonds and 96 van der Waals interactions.

Structural comparison with *N*-acetyl-β-D-glucopyranosylamine

As expected the mode of binding between the two isomers is almost identical. A structural comparison with *N*-acetyl-β-D-glucopyranosylamine revealed that upon binding the C1 atom of (**1a**) is shifted by 0.66 Å. In order for the inhibitor to fit into the binding site, it is observed that a number of water molecules are displaced (Wat335, Wat106, Wat105, Wat110, Wat341 and Wat109). Negligible changes were observed in the 280s loop. As expected, a similar binding mode was observed in the case of (**1b**). The inhibitor shifted by 110.43°, while water molecules Wat105, Wat106, Wat109, Wat110 and Wat355 were displaced. Conformational changes in the 280s loop were also negligible.

*Figure 86. A structural comparison between (**1a**) (purple) and N-acetyl-β-D-glucopyranosylamine (yellow) at the catalytic site of GPb (left) and (**1b**) (purple) and N-acetyl-β-D-glucopyranosylamine (yellow) at the catalytic site of GPb (right).*

Binding of 2,5-dihydroxy-4-(β-D-glucopyranosyl)-chlorobenzene (1b) to a novel binding site of GPb

The X-ray crystallographic studies of the above mixture of structural isomers revealed, that apart from binding to the catalytic site of GPb, (**1b**) binds to another novel binding site on the enzyme.

*Figure 87. 2Fo-Fc electron density map of (**1b**) bound at a novel site on GPb. The map is contoured at 1σ level and the refined model is displayed.*

An interesting process of visualizing this new binding site begun. It was found that upon binding the inhibitor forms 6 hydrogen bonds and only one water-mediated interaction, as well as 61 van der Waals interactions.
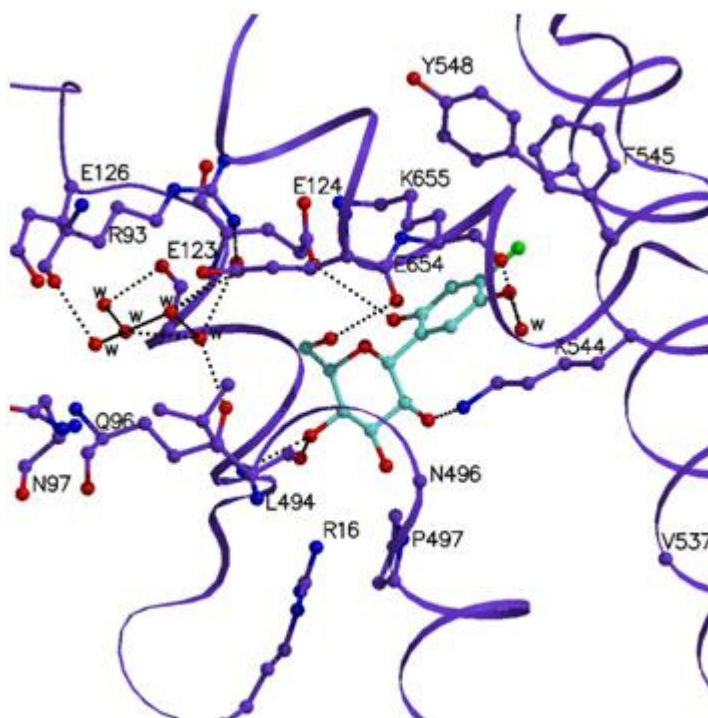
*Figure 88. The network of hydrogen bond interactions between (**1b**) and residues of the novel binding site of GPb.*

This novel binding site was found to be located ~ 26.9 Å from the catalytic site, ~ 28.1 Å from the new allosteric site, ~ 38.4 Å from the allosteric site and ~ 44.9 Å from the new benzimidazole site. The binding pocket is formed by residues 122-124 (of the *α5*-helix residues 118-124), residues 124-129 (of the *β3* strand-residues 129-131), residues 494-508 (of the *α16* helix-residues 496-508), residues 527-553 (of the *α17* helix-residues 527-553) and residues 649-657 (of the *α20* helix-residues 649-657). The inhibitor is surrounded by a hydrophobic pocket formed by the aromatic hydrophobic amino acids Tyr548 and Phe545. It is also surrounded by Lys545 and Lys544. Lysine contains four methylene groups capped by an ammonium ion at neutral pH. Although sometimes lysine is considered as a hydrophobic amino acid, the apolar methylene groups of the residue often participate in favourable hydrophobic interactions within folded peptides and proteins. In addition, when found in a hydrophobic environment, lysine stabilizes this environment by forming salt bridges [128]. Therefore, it is likely to assume that these two lysines surrounding the binding pocket possibly play a role in stabilizing the hydrophobic environment surrounding the inhibitor. It is noteworthy that O2, O3 and O4 of glucose are exposed to the solvent. O2 forms a hydrogen bond with Lys544, while O4 forms a hydrogen bond with Leu494 and Gln96. O7 forms a hydrogen bond with Lys655 via Wat229.
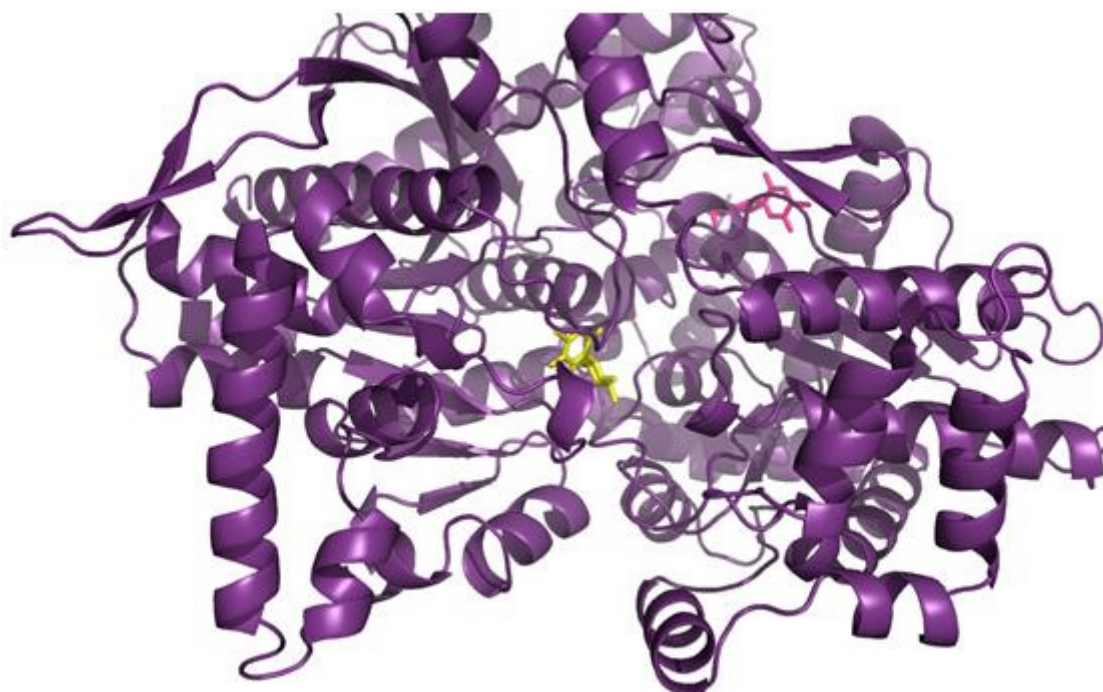
Figure 89. The monomer of GPb and the location of the catalytic site (yellow) and the novel site (pink).

X-ray crystallographic studies of 3-(β-D-glucopyranosyl)-2-hydroxy-5-methoxy-chlorobenzene (2)

(**2**) was found to bind at the catalytic site of GPb. Among this group of compounds studied, this inhibitor displayed the best inhibitory effect on GPb.
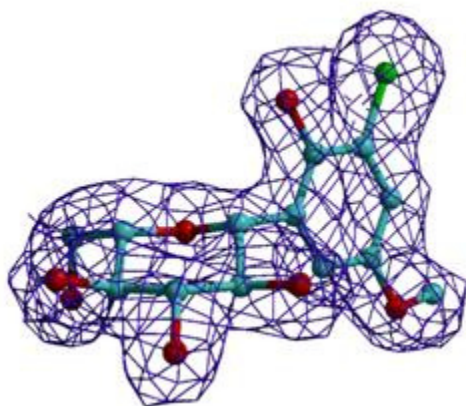
*Figure 90. 2Fo-Fc electron density map of (**2**) bound at the catalytic site of GPb. The map is contoured at 1σ level and the refined model is displayed.*

Upon binding, the inhibitor forms 14 hydrogen bonds and 95 van der Waals interactions, as well as an extensive network of water-mediated interactions, stabilizing the T state of the enzyme.
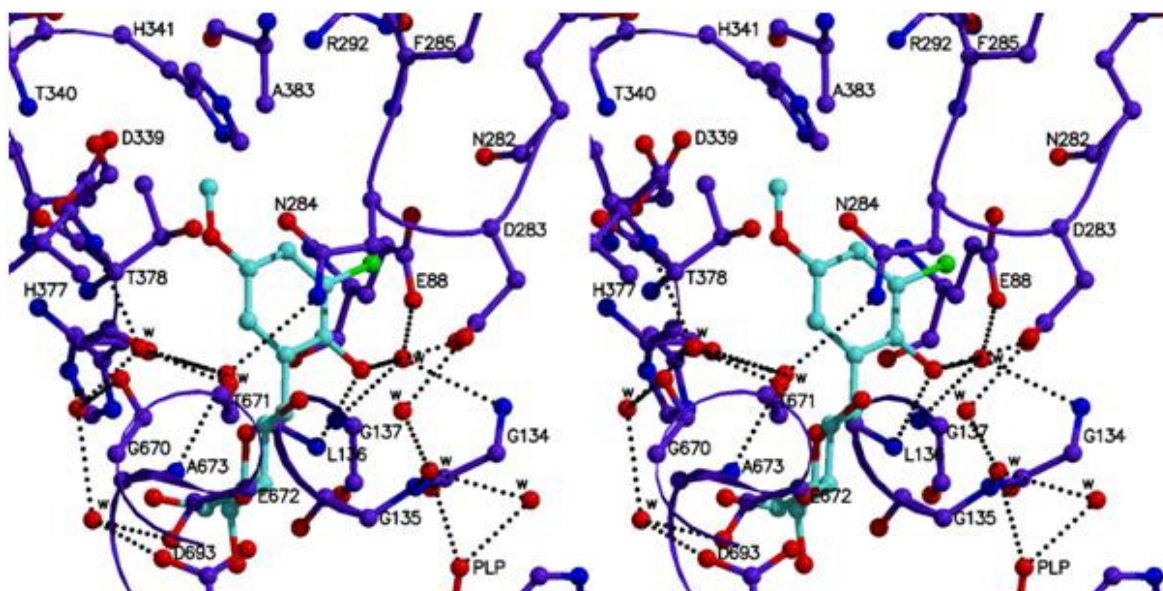
*Figure 91. Stereo diagram showing the network of interactions formed between (**2**) and residues of the catalytic site of GPb.*

Structural comparison with *N*-acetyl-β-D-glucopyranosylamine

A structural comparison with *N*-acetyl-β-D-glucopyranosylamine revealed conformational changes upon binding of (**2**). In more detail, the C1 atom is shifted by 0.98 Å. Wat105, Wat109 and are displaced upon binding. Wat110 is shifted by 1.81 Å, Wat355 is shifted by 2.27 Å, Wat106 is shifted by 2.42 Å and Wat258 is shifted by 0.63 Å. O6 makes a characteristic hydrogen bond with a nitrogen atom of His377.
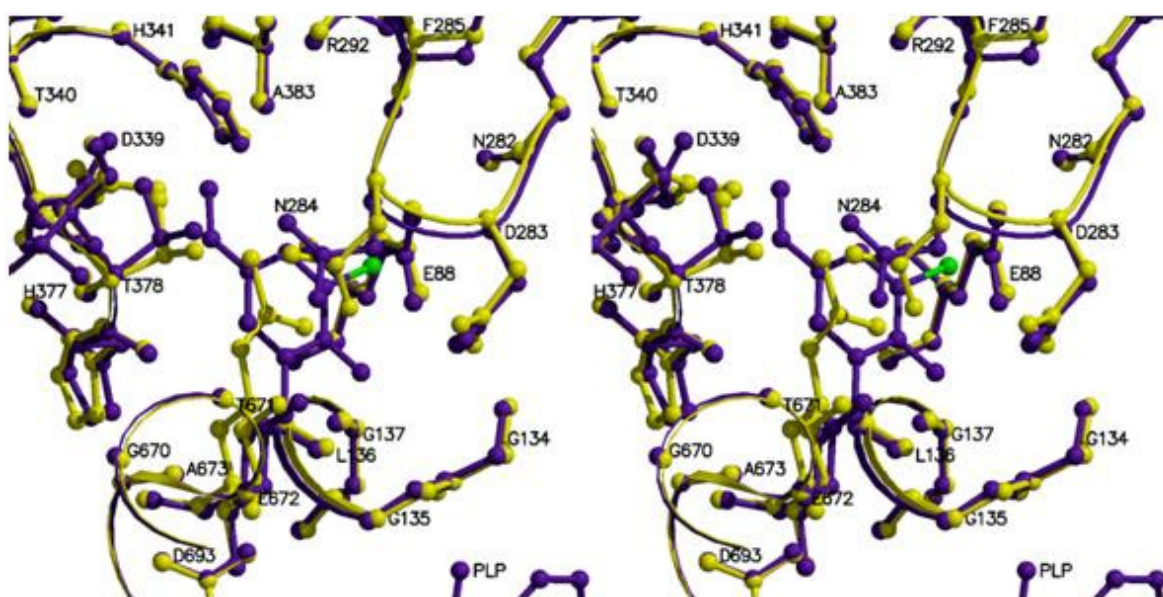
*Figure 92. A stereo diagram showing a structural comparison between (**2**) (purple) and N-acetyl-β-D-glucopyranosylamine (yellow) at the catalytic site of GPb.*

The side chain of Asn284 is shifted by 85.16°; Asn284 is shifted by a torsion angle of 72.03° [ND2-**CG-CB**-CA]; the phenyl ring of Phe285 is shifted by a torsion angle of 8.42° [CA-**CB-CG**-CD2]; Phe286 is shifted by a torsion angle of 5.02° [CA-**CB-CG**-CD1]. O8 of the inhibitor is hydrogen bonded to Glu88 OE2 and residues of the glycine helix (134-150) Gly136 N and Gly134 N, and Gly137 N via Wat76. O2 is hydrogen bonded to residues of the 280s loop (282-287) via Wat93 and Wat297.

X-ray crystallographic studies of 2,5-dihydroxy-4-(β-D-glucopyranosyl)-bromo-benzene (3)

(**3**) was found to bind at the catalytic site of GPb.
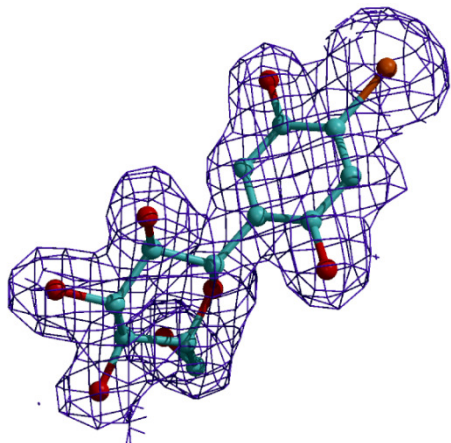
*Figure 93. 2Fo-Fc electron density map of (**3**) at the catalytic site of GPb. The map is contoured at 1σ level and the refined model is displayed.*

Upon binding it forms an extensive network of 16 hydrogen bonds and 88 van der Waals interactions.
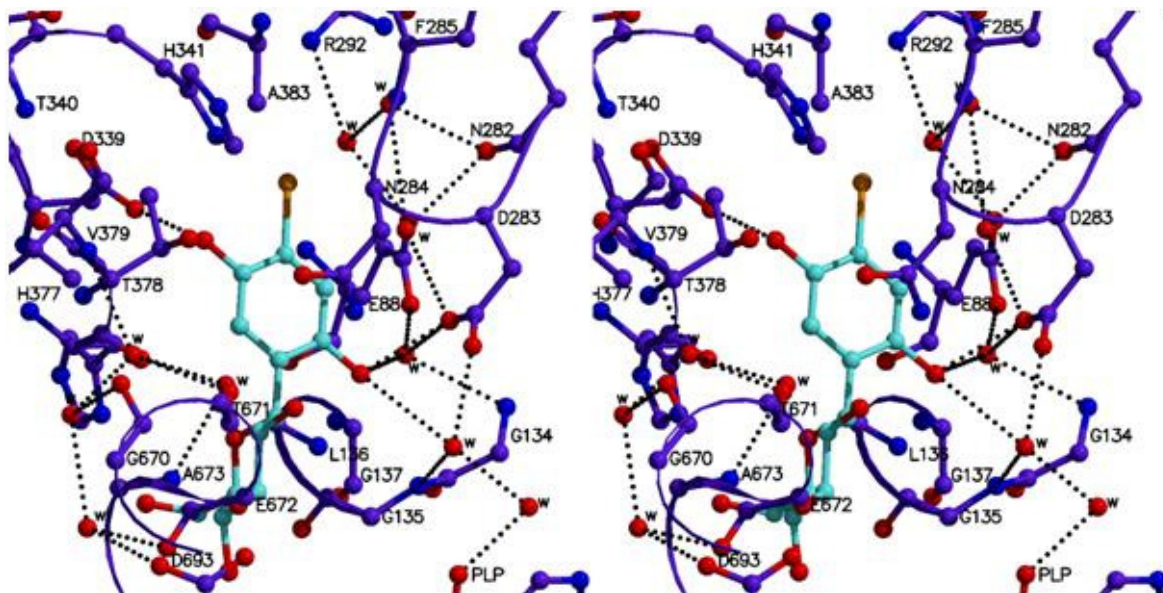
*Figure 94. Stereo diagram showing the network of interactions formed between (**3**) and residues of the catalytic site of GPb.*

O8 of the inhibitor is hydrogen bonded to residues of the glycine helix (134-150) Leu136 N and Gly135 N, Gly134 N and Gly137 N via Wat55 and Wat75. It is also hydrogen

bonded to residues of the 280s loop via Wat55, Wat75, Wat244 and Wat290. O6 is hydrogen bonded to a nitrogen atom of His377, a reoccurring bond at the catalytic site.

Structural comparison with *N*-acetyl-β-D-glucopyranosylamine

A structural comparison with *N*-acetyl-β-D-glucopyranosylamine revealed minor conformational changes upon binding of the inhibitor.
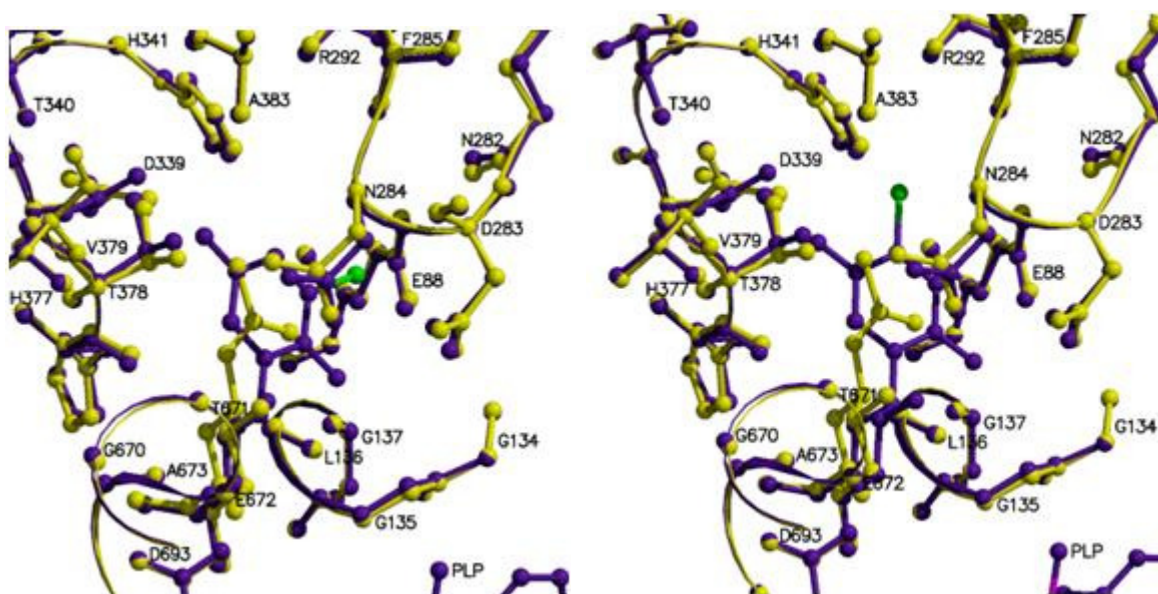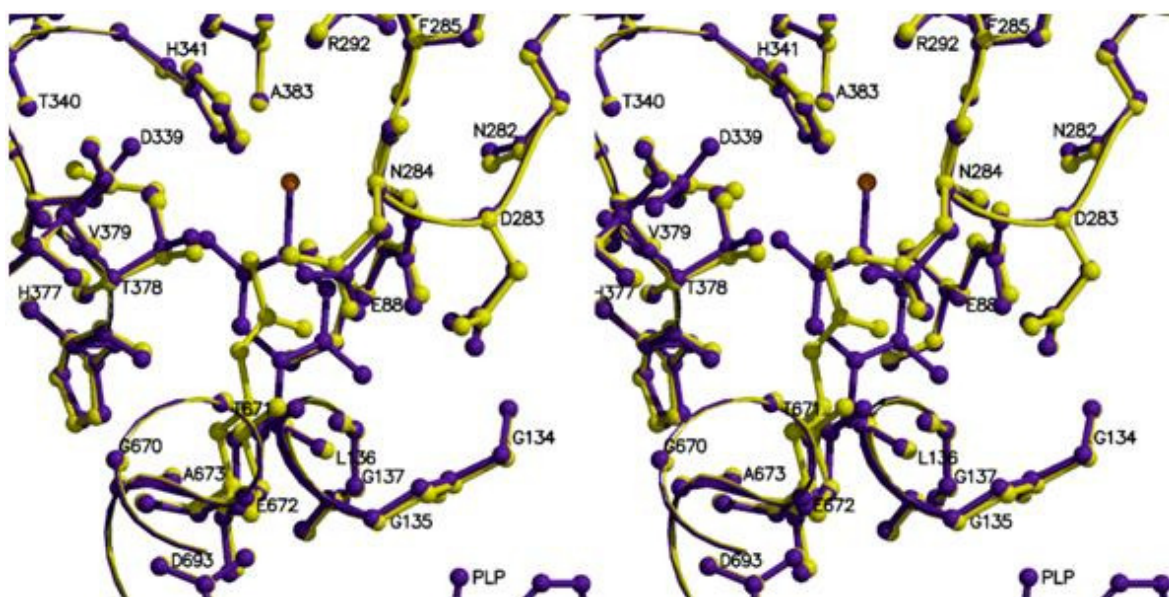

Figure 95. A stereo diagram showing a structural comparison between (3) (purple) and N-acetyl-β-D-glucopyranosylamine (yellow) at the catalytic site of GPb.

Upon binding to the enzyme the C1 atom of the inhibitor is shifted by 0.8 Å. Wat105, Wat110 and Wat314 are displaced from the site in order for the inhibitor to fit, while Wat244 is recruited into the structure. Wat355 is shifted by 1.86 Å. Apart from the side chain of Asp283 which is shifted by 154.35°, the amino acids of the 280s loop undergo negligible conformational changes.

X-ray crystallographic studies of 2,5-dihydroxy-4-(β-D-glucopyranosyl)-chlorobenzene (4)

(**4**) is the pure product of the previously mentioned mixture of structural isomers. It binds at the catalytic site of GPb. As expected the interactions made are almost identical to the ones made by the equivalent isomer of the mixture.
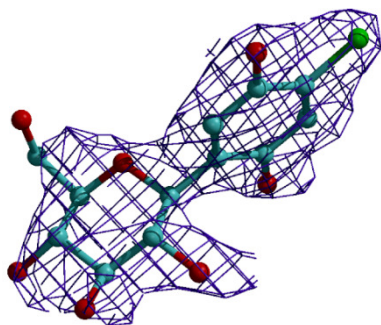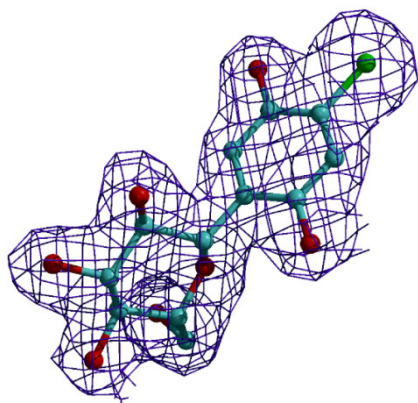

*Figure 96. 2Fo-Fc electron density map of (**4**) at the catalytic site of GPb. The map is contoured at 1σ level and the refined model is displayed.*

Upon binding the inhibitor forms 18 hydrogen bonds and 93 van der Waals interactions.
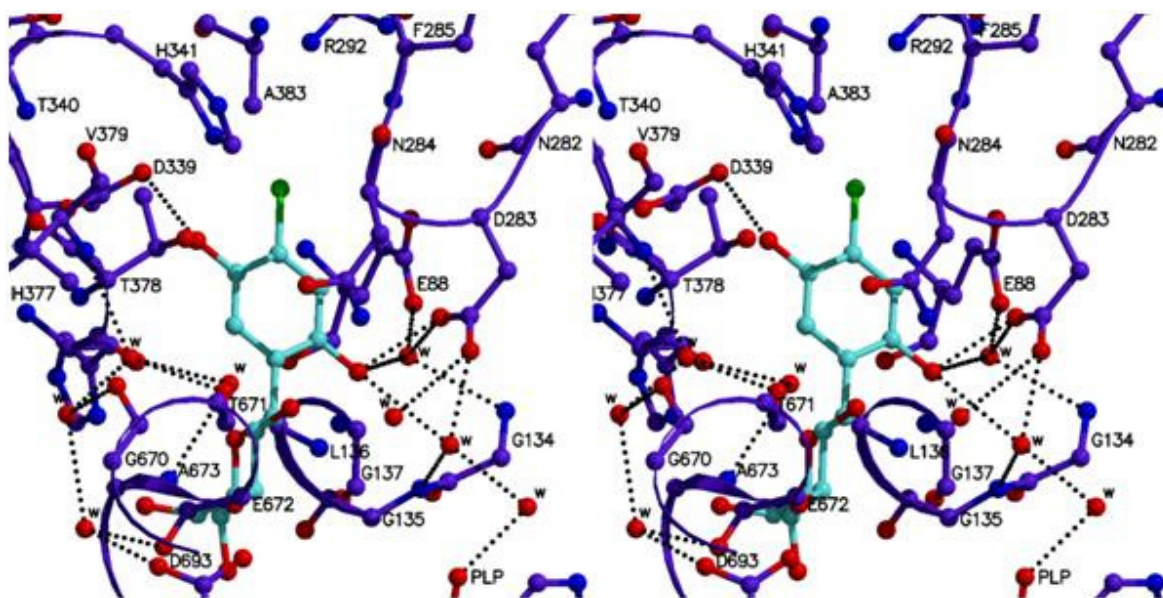
*Figure 97. Stereo diagram showing the network of interactions formed between (**4**) and residues of the catalytic site of GPb.*

O8 atom of the inhibitor is hydrogen bonded to Glu88 OE2 and residues of the glycine helix (134-150) Leu136 N, Gly134 N, Gly135 N and Gly137 N via Wat54 and Wat73. It is also hydrogen bonded to residues of the 280s loop (282-287) directly and via Wat54, Wat73 and Wat259. O2 atom also makes direct hydrogen bonds with Asn284 of the loop. The nitrogen atom of His377 is hydrogen bonded to O6 atom of the inhibitor.

Structural comparison with *N*-acetyl-β-D-glucopyranosylamine

Structural comparisons with *N*-acetyl-β-D-glucopyranosylamine revealed that the C1 atom of the inhibitor is shifted by 0.81Å. Wat105, Wat106, Wat355, Wat109 and Wat110 are displaced from the GPb-(**4**) complex, while Wat222 and Wat260 are recruited into the GPb-(**4**) complex. A closer look at the amino acids of the 280s loop revealed that the side chain of Asp283 is shifted by 143.14°, the side chain of Asn284 is shifted by 148.59°, while the phenyl ring of Phe285 undergoes a minor shift of 67.83°. In general no profound conformational changes are noted.
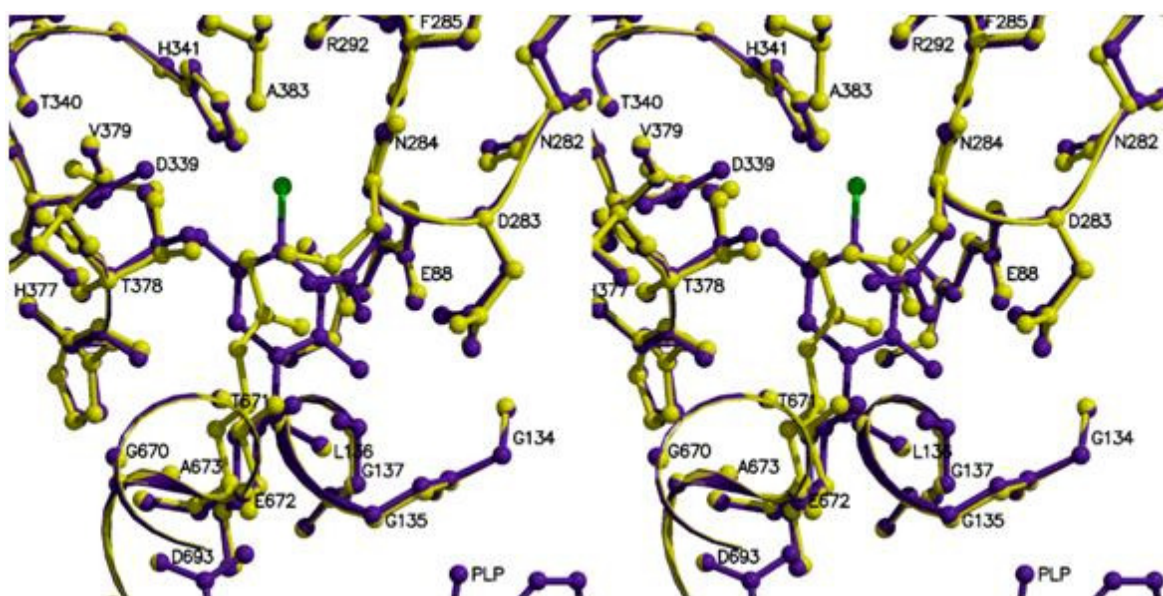
*Figure 98. A stereo diagram showing a structural comparison between (**4**) (purple) and N-acetyl-β-D-glucopyranosylamine (yellow) at the catalytic site of GPb.*

Inhibitor atom	Protein atom	Distance (Å)	Angle (°)	Inhibitor atom	Protein atom	Distance (Å)	Angle (°)
O2	Lys544 NZ	2.1	-	O8	Leu136 N	3.0	163.7
O4	Gln96 NE2	2.6	151.2		Asp283 OD1	2.6	132.2
	Leu494 O	2.3	152.4		Wat76	3.1	-
O6	Glu654 O	3.2	97.9	O2	Tyr573 OH	3.0	149.0
O7	Wat229	2.6	-		Glu672 OE1	3.1	172.2
O8	Glu124 OE1	3.3	124.3		Wat93	2.8	-
				O3	Glu672 OE1	2.8	119.1
					Ser674 N	3.1	175.0
					Gly675 N	3.2	147.4
				O4	Gly675 N	2.8	126.5
					Wat121	2.6	-
				O6	His377 ND1	2.7	158.2
					Asn484 OD1	2.8	140.5

*Figure 99. The network of hydrogen bond interactions of (**1b**) at the novel binding site (left) and of (**2**) at the catalytic site of GPb (right).*

O2	...Wat93	...Asn284 ND2			
		...His377 O			
		...Thr671 O			
		...Ala673 N			
		...Wat98	...Val379 N		
			...Thr671 O		
			...Wat95	...Gly670 O	
				...Wat102	...Glu672 O
					...Asp693 OD2
					...Gly694 N
	...Wat297	...Asp283 OD2			
		...Tyr573 OH			
		...Lys574 NZ			
		...Wat56	...Gly135 N		
			...PLP O2P		
			...Wat58	...Arg569 N	
				...PLP O2P	
O4	**...Wat121**	...Thr676 OG1			
		...PLP O3P			
O8	**...Wat76**	...Glu88 OE2			
		...Gly134 N			
		...Gly137 N			

*Figure 100. The water hydrogen bonding network of (**2**) at the catalytic site of GPb.*

Inhibitor atom	Protein atom	No. of contacts	Inhibitor atom	Protein atom	No. of contacts
CL	Lys544 C, O; Phe545 N, CA; Tyr548 CB, CG, CD2	7	**CL**	Glu88 OE1; Asp283 CA, OD1; Asn284 N; Wat76 O; Wat243; Wat302	7
C12	Lys544 CE, NZ	2	**C12**	Leu136 N, CB; Asp283 OD1; Wat76	4
C1	Lys544 NZ	1	**C1**	Leu136 N; Wat297	2
O8	Glu120 OE1; Glu124 OE1; Lys544 NZ	3	**O8**	Gly135 N, CA, C; Leu136 CA, CB; Asp283 CG, OD2; Wat56; Wat297	9
C7	Lys544 CE, NZ	2	**C7**	Leu136 CB	1
C2	Lys544 NZ	1	**C2**	His377 O; Glu672 OE1; Wat93; Wat297	4
O2	Glu120 CD, OE1, OE2; Lys544 CD, CE	5	**O2**	Asn284 CG	1
C8	Lys544 CD; Lys655 CG; Wat229	3	**C8**	His377 CB, C, O	3
O3	Arg16 NH2; Pro497 CG, CD	3	**C3**	Glu672 OE1; Gly675 N; Wat121	3
C9	Lys544 CD; Lys655 CG, CB; Wat229	4	**O3**	Glu672 CG, CD, C; Ala673 CB, CA, C; Wat93	7
C4	Gln96 NE2; Leu494 O; Cys495 O, CA	4	**C9**	Asn284 OD1; His377 CB	2
O7	Phe545 CB, CD1; Lys655 CA, CB, O	5	**C4**	Gly675 N; Wat121	2
O4	Gln96 CD; Leu494 C	2	**O7**	Asn284 OD1; Asp339 OD1; His377 O, C, CB; Thr378 CG2, CB	7
C10	Lys544 CD, CE; Lys655 CG, CD	4	**O4**	Asn484 OD1; Ser674 CB, C; Gly675 C, O, CA; Thr676 N, CG2	8
C5	Gln96 OE1	1	**C10**	Leu136 CD1; Asn284 N, CA; Wat302	4
C11	Lys544 CE; Lys655 CE	2	**C5**	Gly135 CA, C, O; Leu136 N; Wat121	5
C6	Gln96 OE1; Leu494 CD2; Glu654 CB, OE2; Wat244	5	**O5**	Leu135 C; Leu136 CB, N, CA; His377 ND1	5
O6	Leu494 CD2; Cys495 CA, CB; Glu654 CB, OE2, CA, C	7	**C11**	Leu136 CB; Asp283 OD1; Asn284 N; Wat302	4
			C6	Gly135 C, O; Leu136 CA, N; His377 ND1; Asn484 OD1	6
			O6	Leu139 CD2; His377 CE1, CG; Val455 CG2, CG1; Asn484 CG	8
			C13	Asp339 OD1, CG, OD2; Thr378 CG2; Wat302, Wat303	6

*Figure 101. The van der Waals network of interactions of (**1b**) at the novel binding site (left) and of (**2**) at the catalytic site of GPb (right).*

111

Inhibitor atom	Protein atom	Distance (Å)	Angle (°)	Inhibitor atom	Protein atom	Distance (Å)	Angle (°)
O8	Leu136 N	3.1	156.8	O8	Leu136 N	3.1	159.9
	Asp283 OD1	2.7	116.1		Asp283 OD1	2.6	111.2
	Wat55	3.2	-		Wat54	3.2	-
	Wat75	3.3	-		Wat73	3.3	-
O2	Asn284 ND2	3.0	155.0	O2	Asn284 OD1	3.3	91.6
	Tyr573 OH	3.0	149.6		Asn284 ND2	3.0	154.6
	Glu672 OE1	3.2	175.2		Tyr573 OH	3.1	149.1
	Wat92	2.9	-		Glu672 OE1	3.1	177.6
O3	Glu672 OE1	2.8	121.9		Wat89	2.8	-
	Ser674 N	3.1	176.6		Wat259	2.7	-
	Gly675 N	3.2	143.3	O3	Glu672 OE1	2.8	120.0
O4	Gly675 N	2.8	128.1		Ser674 N	3.0	178.5
	Wat119	2.6	-		Gly675 N	3.2	145.5
O7	Asp339 OD1	2.8	160.7	O4	Gly675 N	2.8	129.1
O6	His377 ND1	2.7	159.0		Wat116	2.7	-
	Asn484 OD1	2.8	138.1	O7	Asp339 OD1	2.6	165.6
					Asp339 OD2	3.0	109.2
				O6	His377 ND1	2.8	160.0
					Asn484 OD1	2.8	140.1

*Figure 102. The hydrogen bonding network of (**3**) (left) and of (**4**) (right) at the catalytic site of GPb.*

O2	**...Wat92**	...Thr671 O			
		...Ala673 N			
		...Wat96	...Val379 N		
			...Thr671 O		
			...Wat94	...Glu670 O	
				...Wat100	...Glu672 O
					...Asp693 OD2
					...Gly694 N
O4	**...Wat119**	...Thr676 OG1			
		...PLP O3P			
O8	**...Wat55**	...Gly135 N			
		...Asp283 OD2			
		...Wat57	...Arg569 N		
			...PLP O2P		
	...Wat75	...Glu88 OE2			
		...Gly134 N			
		...Gly137 N			
		...Wat290	...Glu88 OE1		
			...Asn282 O		
			...Asp283 OD1		
			...Wat244	...Asn282 O	
				...Wat195	...Glu88 OE1
					...Arg292 NH2

*Figure 103. The water hydrogen bonding network of (**3**) at the catalytic site of GPb.*

Inhibitor atom	Protein atom	No. of contacts	Inhibitor atom	Protein atom	No. of contacts
BR	His341 CE1, NE2; Asn284 N	3	**CL**	Asn284 N; Asp339 OD1, OD2; His341 CE1, NE2; Wat222	6
C12	Leu136 CB, N; Asp283 OD1; Asn284 ND2	4	**C12**	Leu136 CB, N; Asp283 CG, OD1; Asn284 ND2	5
C1	Leu136 N; Asn284 ND2	2	**C1**	Leu136 N; Asn284 ND2, Wat259	3
O8	Gly135 N, CA, C; Leu136 CA, CB; Asp283 CG, OD2; Asn284 ND2	8	**O8**	Leu135 N, CA; Leu136 CA, CB; Asp283 CG; Asn284 ND2; Wat259	7
C7	Leu136 CB; Asn284 ND2	2	**C7**	Leu136 CB; Asn284 ND2	2
C2	Asn284 ND2; His377 O; Glu672 OE1; Wat92	4	**C2**	Asn284 ND2; His377 O; Glu672 OE1; Wat89, Wat259	5
O2	Asn284 CG, OD1	2	**O2**	Asn284 CG	1
C8	Asn284 ND2; His377 CB, C, O	4	**C8**	Asn284 ND2; His377 CB, C, O	4
C3	Glu672 OE1; Gly675 N; Wat119	3	**C3**	Glu672 OE1; Gly675 N; Wat116	3
O3	Glu672 C, CD, CG; Ala673 CA, CB, N, C; Ser674 CA, C; Wat92	10	**O3**	Glu672 CG, CD; Ala673 C, CA, CB; Ser674 CA, C; Wat89	8
C9	Asn284 ND2; Asp339 OD1; His377 CB	3	**C9**	Asp339 OD1, OD2; His377 CB	3
C4	Gly675 N; Wat119	2	**C4**	Gly675 N; Wat116	2
O7	Asp339 OD1, OD2; His377 CB, C; Thr378 CB, CG2	6	**O7**	Asp339 CG, OD1; His377 CB, C; Thr378 CB, CG2	6
O4	Asn484 OD1; Ser674 CB, C; Gly675 C, O, CA; Thr676 N, CG2	8	**O4**	Asn484 OD1; Ser674 CB, C; Gly675 C, O, CA; Thr676 N	7
C10	Leu136 CD1; Asn284 ND2, N	3	**C10**	Leu136 CD1; Asn284 ND2, N	3
C5	Gly135 C, O; Leu136 N; Wat119	4	**C5**	Leu135 CA, C; Leu136 N; Wat116	4
O5	Leu136 N, CA, CB; His377 CB, ND1	5	**O5**	Gly135 C; Leu136 CA, CB, N; His377 ND1	5
C11	Leu136 CB; Asp283 OD1; Asn284 ND2, N; Wat290	5	**C11**	Leu136 CB; Asp283 CG, OD1; Asn284 ND2, N	5
C6	Gly135 C, O; Leu136 N, CA; His377 ND1; Asn484 OD1	6	**C6**	Gly135 C, O; Leu136 CA, N; Leu139 CD2; His377 ND1; Asn484 OD1	7
O6	Leu139 CD2; His377 CG, CE1; Val455 CG1, CG2; Asn484 CG	6	**O6**	Leu139 CD2; His377 CE1, CG; Val455 CG2, CG1; Asn484 CG	6

*Figure 104. The van der Waals network of interactions of (**3**) (left) and (**4**) (right) at the catalytic site of GPb.*

O2	**...Wat89**	..Thr671 O			
		...Ala673 N			
		...Wat93	...Val379 N		
			...Thr671 O		
			...Wat91	...Gly670 O	
				...Wat97	...Glu672 O
					...Asp693 OD2
					...Gly694 N
	...Wat259	...Asp283 OD2			
		...Tyr573 OH			
		...Lys574 NZ			
		...Wat54	...Gly135 N		
			...Asp283 OD2		
			...Wat56	...Arg569 N	
				...PLP O2P	
				...Wat54	
O4	**...Wat116**	...Thr676 OG1			
		...PLP O3P			
O8	**...Wat54**				
	...Wat73	...Glu88 OE2			
		...Gly134 N			
		...Gly137 N			
		...Asp283 OD1			

*Figure 105. The water hydrogen bonding network of (**4**) at the catalytic site of GPb.*

X-ray crystallographic analysis

	(1a,b)	**(2)**	**(3)**	**(4)**
Experiment	T state GPb crystals soaked with 100 mM (**1a,b**) in 10mM BES for 21 hours	T state GPb soaked with 10 mM (**2**) in 10mM BES for 2.5 hours	T state GPb crystals soaked with 20 mM (**3**) in 10mM BES for 6 hrs	T state GPb crystals soaked with 70.1 mM (**4**) in 10 mM BES for 7 hrs
Wavelength (Å)	1.0	0.8638	1.488	0.8156
Oscillation range (°) a	0.8	0.8	0.8	0.8
No. of images (°)	71	70	60	80
Space Group	P4₃2₁2	P4₃2₁2	P4₃2₁2	P4₃2₁2
Unit cell dimensions	$a=b$=128.7 Å c=116.2 Å $\alpha=\beta=\gamma$=90°	$a=b$=127.9 Å c=115.6 Å, $\alpha=\beta=\gamma$=90°	$a=b$=128.7 Å c=116.4 Å $\alpha=\beta=\gamma$=90°	$a=b$=128.4 Å c=116.4 Å $\alpha=\beta=\gamma$=90°
Resolution (Å)	30.0–2.05	30.0–2.00	30.0–1.97	30.0–2.00
No. of observations	380693	460082	368477	634277
No. of unique reflections (outermost)	2641 (60600)	63987 (3140)	64845 (3109)	65452 (3213)
R_m **(outermost shell) b**	0.339 (0.061)	0.050 (0.295)	0.065 (0.298)	0.040 (0.398)
Completeness (%) (outermost shell)	86.8 (97.8)	98.0 (97.3)	93.9 (90.9)	98.7 (99.0)
Outermost shell (Å)	2.09-2.05	2.03–2.00	2.00–1.97	2.03–2.00

$< I / \sigma\,(I) >$ (outermost shell)[c]	3.9 (14.8)	16.1 (4.65)	11.3 (4.2)	21.2 (5.2)
Redundancy (outermost shell)	3.9 (3.1)	4.0 (3.7)	3.7 (3.8)	5.4 (5.4)
B-values (Å^2) (Wilson plot)	29.8	22.3	26.5	31.1
Resolution range (Å)	90.91–2.05	90.54–2.00	90.9–1.97	90.9–2.00
No. of reflections used (free)	57482 (3070)	60665 (3238)	61530 (3267)	62101 (3308)
Residues included	(12-254) (258-314) (324-836)	(12-254) (261-314) (324-836)	(12–254) (261–314) (324–836)	(12-254) (261-314) (324–836)
No. of protein atoms	6619	6594	6600	6600
No. of water molecules	250	326	335	265
No. of heteroatoms	20 (**1a,b**) 15 (PLP)	21 (**2**) 15 (PLP)	20 (**3**) 15 (PLP)	20 (**4**) 15 (PLP)
Final R (R_{free}) (%)[d]	0.19 (0.22)	0.19 (0.21)	0.19 (0.21)	0.19 (0.21)
R (R_{free}) (outermost shell)	0.25 (0.29)	0.22 (0.249)	0.23 (0.26)	0.24 (0.27)
r.m.s.d. in bond lengths (Å)	0.007	0.007	0.007	0.007
r.m.s.d. in bond angles (°)	1.039	0.014	1.022	1.028
Average B (Å^2) for residues	(12- 254) (258-314) (324-836)	(12-254) (261-314) (324-836)	(12–254) (261–314) (324–836)	(12-254) (261-314) (324–836)
Overall	32.3	24.9	27.5	35.0
CA, C, N, O	31.5	24.1	26.7	34.2
Side chain	33.1	25.8	28.3	35.8
Average B (Å^2) for heteroatoms	19.7 (**1a**,catalytic) 20.3 (**1b**, catalytic) 51.7 (**novel site**) 22.2 (PLP)	14.3 (**2**) 14.8 (PLP)	20.1 (**3**) 17.5 (PLP)	25.0 (**4**) 23.9 (PLP)
Average B (Å^2) for water molecules	35.8	31.9	35.2	39.8

a Native T state RMGPb crystals, grown in the tetragonal lattice, space group $P4_32_12$ were soaked with various concentrations of inhibitors in buffered solutions at pH 6.7 in the presence of DMSO. X-ray diffraction data were collected using synchrotron radiation sources at Daresbury Laboratory, UK and EMBL-Hamburg outstation at DESY, Germany and processed with the HKL package. Complex structure determination and analysis were performed according to standard protocols as implemented in the CCP4 package.

b $R_{symm} = \Sigma_h\Sigma_i|I(h) - I_i(h)/\Sigma_h\Sigma_iI_i(h)$ where $I_i(h)$ and $I(h)$ are the ith and the mean measurements of the intensity of reflection h.

c $\sigma(I)$ is the standard deviation of I.

d $R_{cryst} = \Sigma_h|F_o - F_c|/\Sigma_hF_o$, where F_o and F_c are the observed and calculated structure factors amplitudes of reflection h, respectively. R_{free} is equal to R_{cryst} for a randomly selected 5% subset of reflections not used in the refinement. Values in parentheses are for the outermost shell.

Figure 106. Diffraction data and refinement statistics.

3.6 A new group of glucopyranosylidene-spiro-iminothiazolone compounds as inhibitors of glycogen phosphorylase

Organic synthesis *by Professor Somsák László, Department of Organic Chemistry, University of Debrecen, Hungary*

Kinetic studies

Four glucopyranosylidene-spiro-iminothiazolone derivatives were studied kinetically and revealed high binding affinities for GPb.

Glucopyranosylidene-spiro-iminothiazolone

K_i: 14.1 ± 0.8 μM

(1)

Glucopyranosylidene-spiro-benzoyliminothiazolone

K_i: 8.9 ± 0.2 μM

(2)

Glucopyranosylidene-spiro-2-naphthoyliminothiazolone

K_i: 3.7 ± 0.4 μM

(3)

Glucopyranosylidene-spiro-1-naphthoyliminothiazolone

K_i: 7.7 ± 0.3 μM

(4)
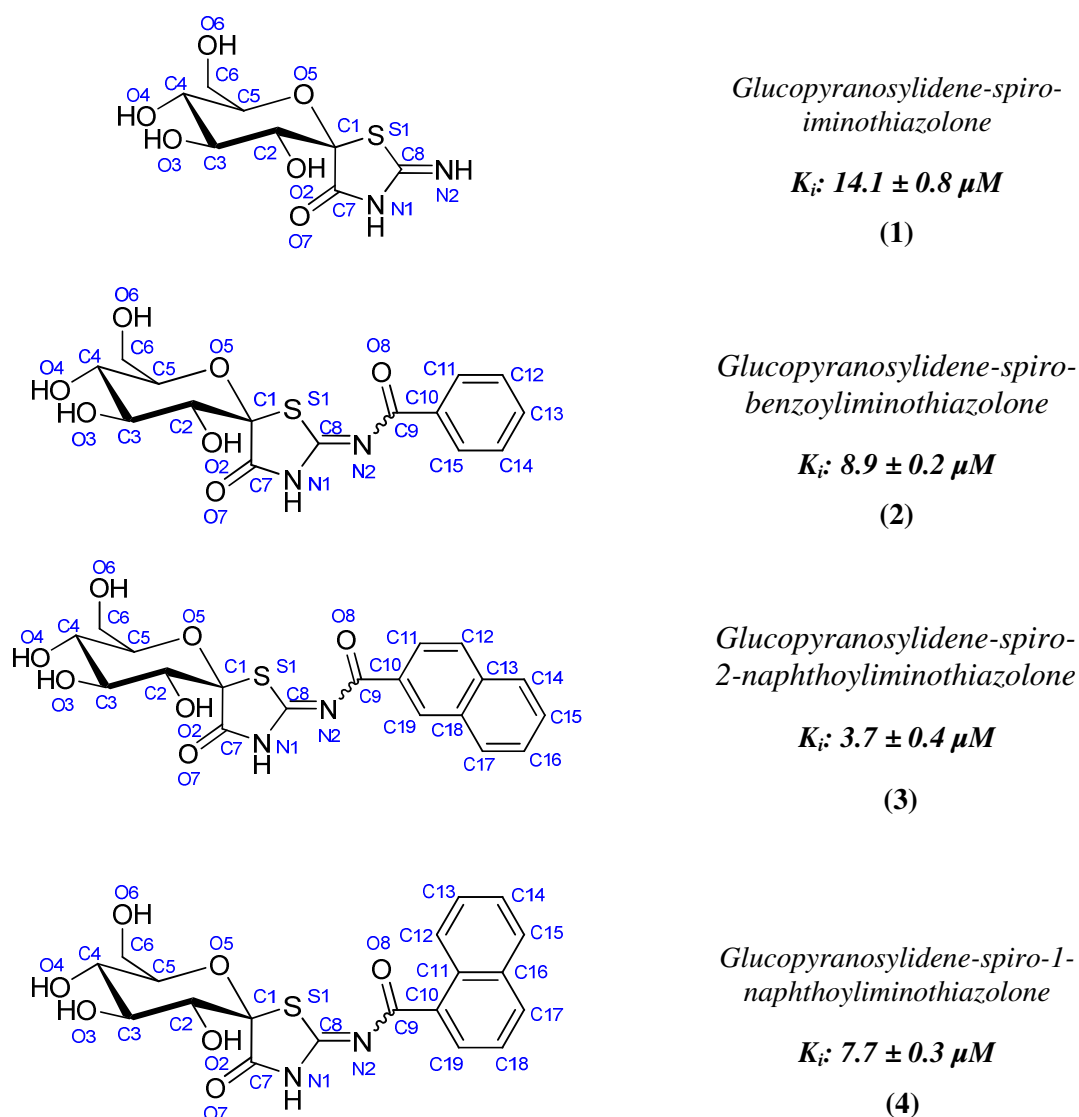
Figure 107. The chemical structures, numbering used and kinetic results of the compounds studied.
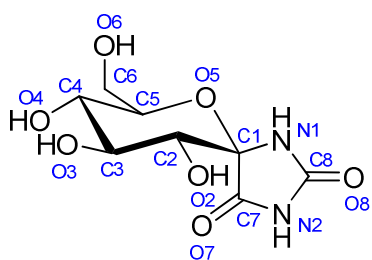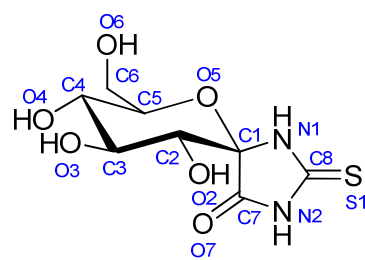
Hydantoin K_i: 3.1 μM   **Thiohydantoin K_i: 5.1 μM**

Figure 108. The chemical structures, numbering system and inhibitory effects of hydantoin (left)
and thiohydantoin (right).

X-ray crystallographic studies of glucopyranosylidene-spiro-iminothiazolone (1)

(**1**) was found to bind at the catalytic site of GPb.
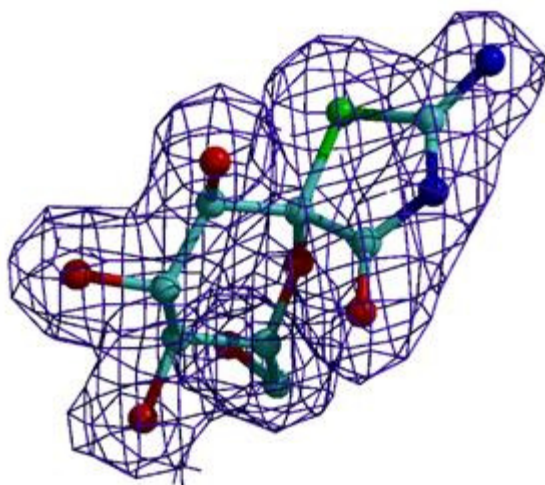
Figure 109. 2Fo-Fc electron density map of
*(**1**) bound at the catalytic site of GPb. The*
map is contoured at 1σ level and the refined
model of the inhibitor is displayed.

Upon binding (**1**) forms 17 hydrogen bonds and 75 van der Waals interactions as well as an extensive network of water mediated interactions, stabilizing the inhibitor in the binding site and the T state of the enzyme. The N1 atom of the inhibitor forms a hydrogen bond with Glu88 OE2 and residues of the glycine helix (134-150) Gly134 N and Gly137 N and residues of the 280s loop (282-287) Asp283 OD1 via Wat50, Wat53 and Wat54. O6 atom of the inhibitor forms the characteristic bond with a nitrogen atom of His377 of the surrounding protein environment.
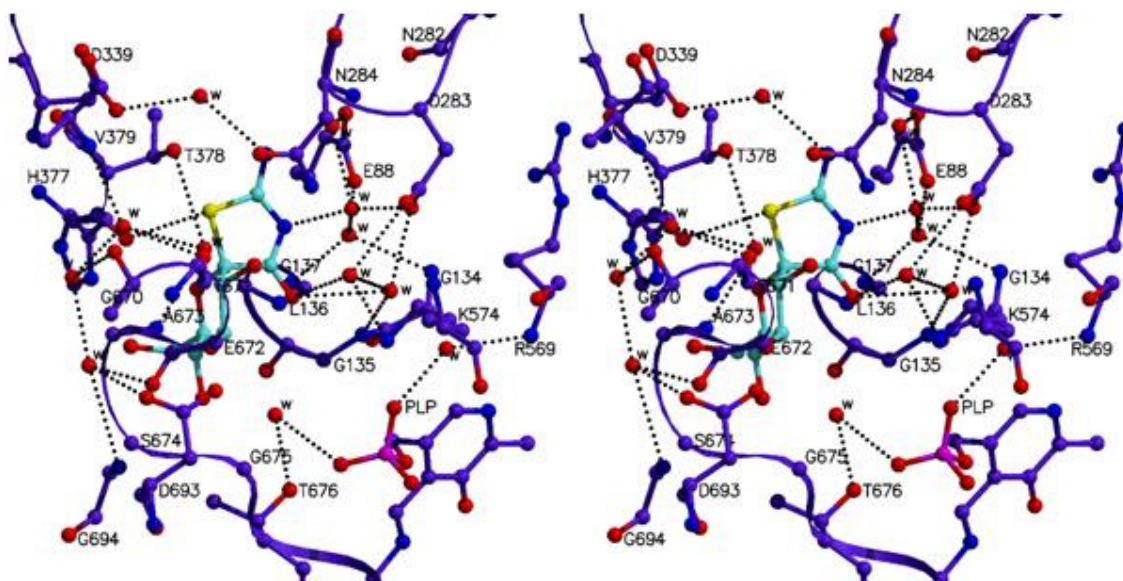
*Figure 110. Stereo diagram showing the network of interactions formed between (**1**) and residues of the catalytic site of GPb.*

Structural comparison with α-D-glucose
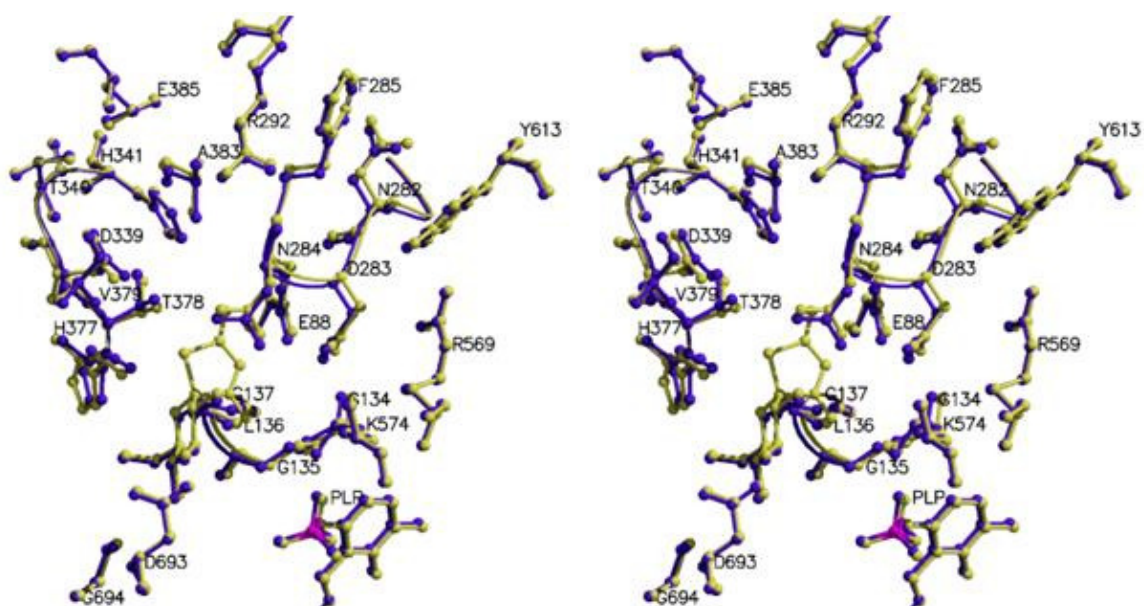
*Figure 111. A stereo diagram showing a structural comparison between (**1**) (yellow) and α-D-glucose (purple) at the catalytic site of GPb.*

In order to get a better insight on the conformational changes that occur upon binding of the inhibitor at the catalytic site, a structural comparison was made with α-D-glucose. The glucopyranose moiety is shifted by 103.76° and rotated by a torsion angle of 6.84° [C3-**C2-C1**-O5]. A number of water molecules are displaced upon binding, in order to accommodate the bulkier inhibitor into the binding site, notably Wat752, Wat808, Wat604, Wat803, Wat777, Wat747, Wat744, Wat631 and Wat800. Water molecules Wat56, Wat188 and Wat119 are recruited into the new structure. Many water molecules are also shifted, notably Wat812 by 1.52Å. A minor shift was observed at the amino acids of the 280s loop (282-287).

Structural comparison with hydantoin

*Figure 112. A stereo diagram showing a structural comparison between (**1**) (yellow) and hydantoin (purple) at the catalytic site of GPb.*

A structural comparison with hydantoin revealed no considerable conformational changes. Wat176 is shifted by 0.92 Å, while Wat52 and Wat54 are recruited into the GPb-(**1**) structure. No conformational change is observed for the glucopyranose moiety and there is a negligible shift of the amino acids of the 280s loop (282-287).

Structural comparison with thiohydantoin

Almost identical changes were observed as in the case of hydantoin. Wat165 was shifted by 1.06 Å, and Wat10 was shifted by 1.01 Å. Wat214 is displaced, while Wat52, Wat56 Wat57 and Wat214 are displaced from the thiohydantoin-(**1**) structure. No conformational change is observed for the glucopyranose moiety and a negligible shift is observed at the amino acids of the 280s loop.
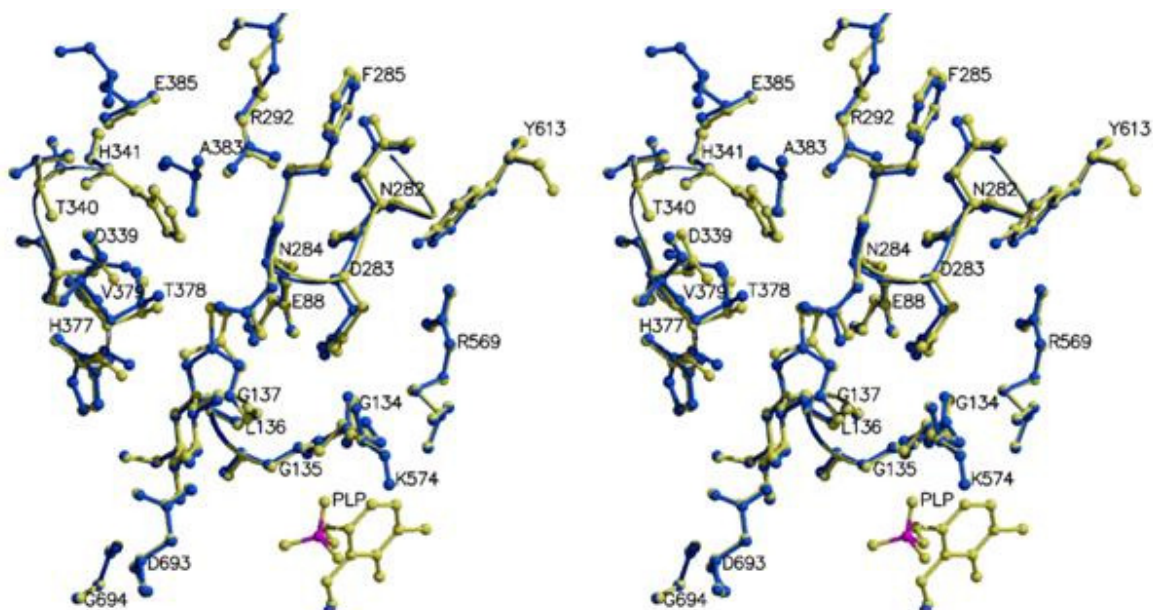
*Figure 113. A stereo diagram showing a structural comparison between (**1**) (yellow) and hydantoin (blue) at the catalytic site of GPb.*

X-ray crystallographic studies of glucopyranosylidene-spiro-benzoyliminothiazolone (**2**)
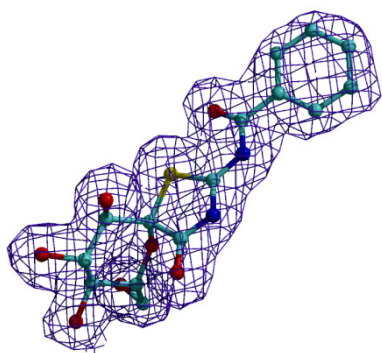
*Figure 114. 2Fo-Fc electron density map of (**2**) bound at the catalytic site of GPb. The map is contoured at 1σ level and the refined model is displayed.*

(**2**) was found to bind at the catalytic site of GPb. Upon binding to the enzyme, (**2**) forms 17 hydrogen bonds and 114 van der Waals interactions and a very extensive network of water-mediated interactions.
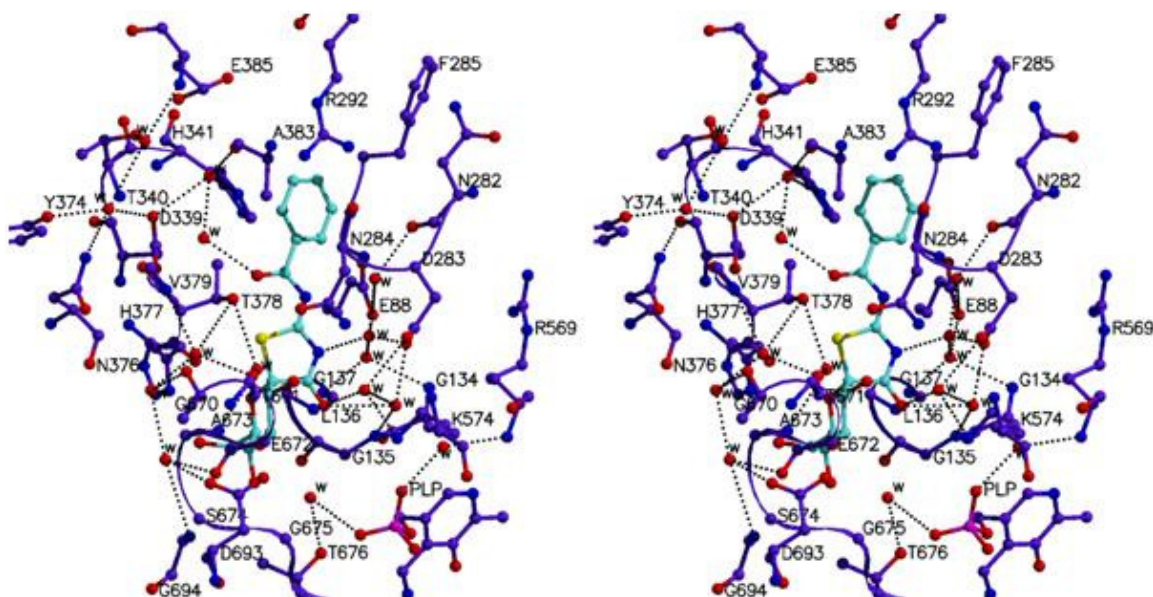

*Figure 115. Stereo diagram showing the network of interactions formed between (**2**) and residues of the catalytic site of GPb.*

N1 of the inhibitor is hydrogen bonded to residues of the glycine helix (134-150) via Wat143, Wat157 and Wat158. O2 atom of the inhibitor is hydrogen bonded directly to residues of the 280s loop (282-287), and indirectly via Wat158, Wat142, Wat143, Wat159 and Wat158. O6 atom is hydrogen bonded to a nitrogen atom of His377 of the surrounding protein environment.

Structural comparison with α-D-glucose

Due to the bigger size of (**2**), compared to that of α-D-glucose, upon binding many water molecules are displaced, notably Wat752, Wat744, Wat631, Wat803, Wat754, Wat808 and Wat604. In addition, water molecules are also shifted notably Wat726 by 1.39 Å, Wat747 by 1.51 Å, Wat748 by 0.88 Å, Wat805 by 0.90 Å, Wat812 by 1.45 Å, Wat800 by 2.17 Å and Wat777 by 0.66 Å. There are negligible conformational changes at the amino acids of the 280s loop (282-287) and residues of the glycine helix (134-150).

Figure 116. A stereo diagram showing a structural comparison between (2) (yellow) and α-D-glucose (purple) at the catalytic site of GPb.

Structural comparison with hydantoin

Figure 117. A stereo diagram showing a structural comparison between (2) (yellow) and hydantoin (purple) at the catalytic site of GPb.

Wat200 is shifted by 1.06 Å and Wat176 by 1.04 Å. Wat10 is displaced in order for the bulkier inhibitor to fit, while Wat142, Wat157, Wat160, Wat161, Wat164, Wat165 and Wat172 are recruited into the GPb-(2) structure. The side chain of Asn284 is rotated by a

torsion angle of 20.36° [ND2-**CG-CB**-CA]. The phenyl ring of Phe285 is rotated by a torsion angle of 5.35° [CA-**CB-CG**-CD2]. The side chain of Glu287 undergoes a major shift and is rotated by a torsion angle of 109.32° [OE1-**CD-CG**-CB]. The NH1 atom of Arg138 of the glycine helix is shifted by 2.26 Å, while the NE atom by 0.96 Å and the CD atom by 0.89 Å.

Structural comparison with thiohydantoin

There is a negligible shift of the glucopyranose ring and many water molecules shifted, notably Wat165 by 1.17 Å, Wat10 by 2.46 Å and Wat214 by 3.21 Å. Wat157, Wat172, Wat160, Wat161 and Wat142 were recruited into the GPb-(**2**) structure. The side chain of Asn284 is shifted by 148.66°, while the side chain of Glu287 is shifted by 118.71°. The NE atom of Arg138 of the glycine helix is shifted by 1.03 Å and the CD atom by 0.88 Å. The side chain of Leu144 changes orientation and is rotated by a torsion angle of 102.21° [CD2-**CG-CB**-CA].
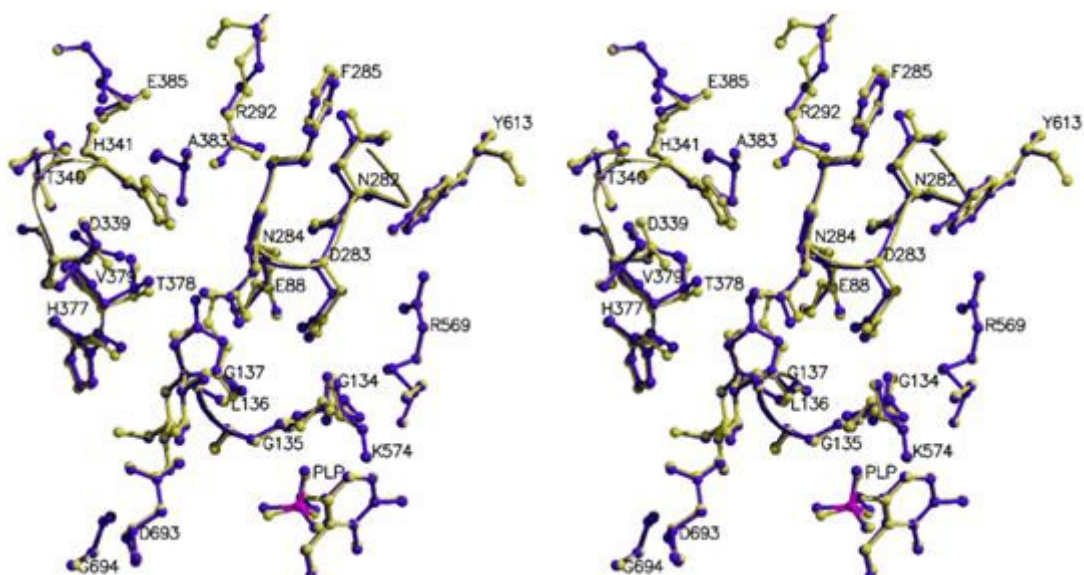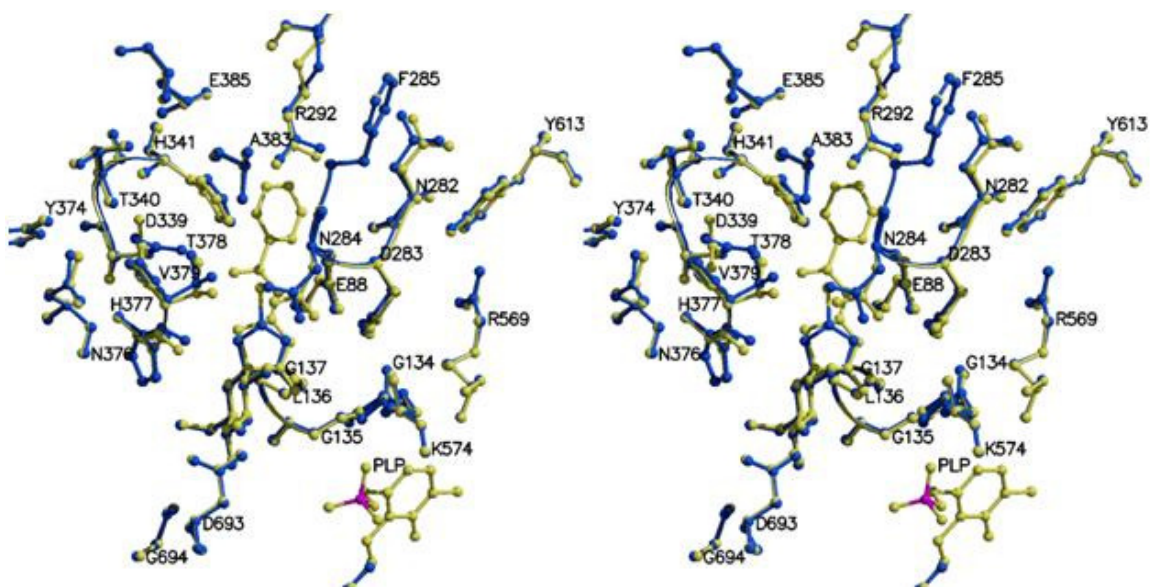

Figure 118. A stereo diagram showing a structural comparison between (2) (yellow) and thiohydantoin (blue) at the catalytic site of GPb.

X-ray crystallographic studies of glucopyranosylidene-spiro-2-naphthoyl-iminothiazolone (3)

(**3**) was found to bind at the catalytic site of GPb.
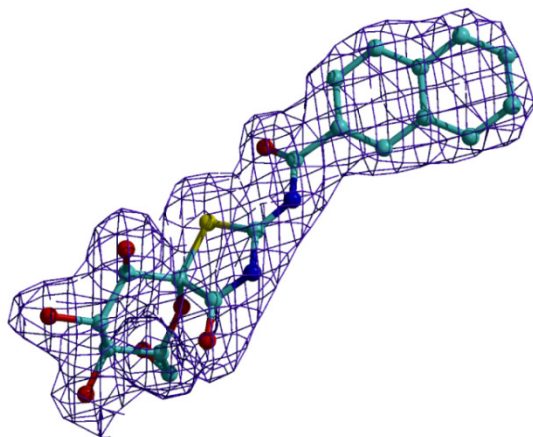
*Figure 119. 2Fo-Fc electron density map of (**3**) at the catalytic site of GPb. The map is contoured at 1σ level and the refined model is displayed.*

Upon binding (**3**) forms 15 hydrogen bonds and 126 van der Waals interactions.
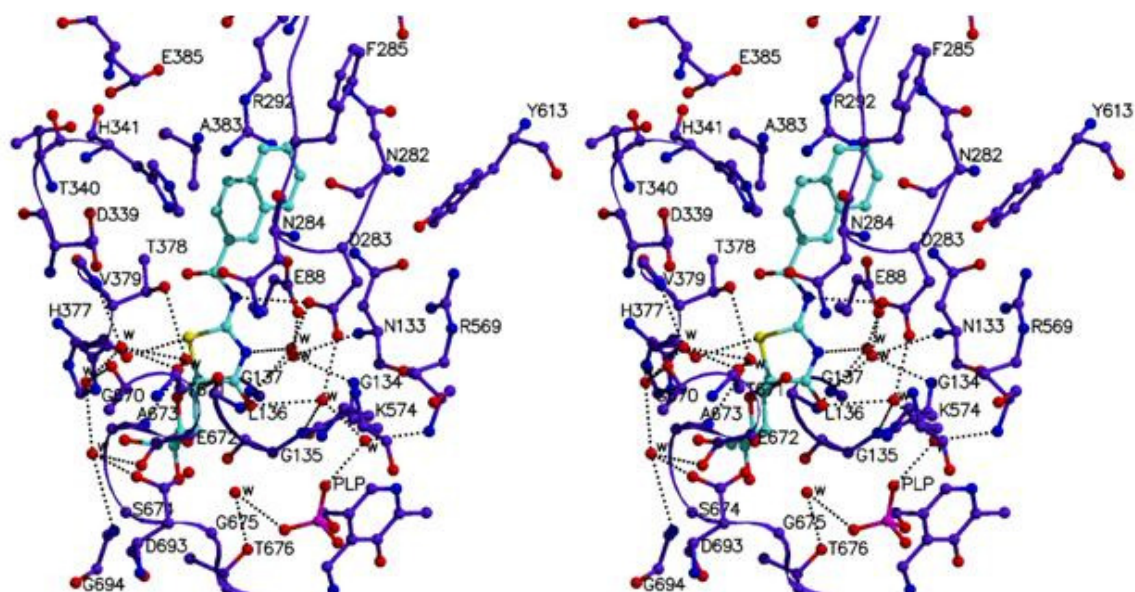
*Figure 120. Stereo diagram showing the network of interactions formed between (**3**) and residues of the catalytic site of GPb.*

N1 and O7 atoms of the inhibitor are hydrogen bonded to residues of the glycine helix (134-150) Gly134 N, Leu135 N, Gly135 N and Gly137 N, via Wat27, Wat197 and Wat198. N2 atom of the inhibitor is directly hydrogen bonded to Asp283 OD1 of the 280s loop (282-287) and O2 atom of the inhibitor is hydrogen bonded to Asn284 ND2. The

inhibitor also makes indirect hydrogen bonds with residues of the 280s loop via Wat27 and Wat197. O6 atom of the inhibitor forms the characteristic bond with a nitrogen atom of His377.

Structural comparison with α-D-glucose

A structural comparison between (**3**) and α-D-glucose revealed a number of significant changes. The glucopyranose moiety is shifted by 101.94°. In order for the bulkier inhibitor to fit, many water molecules are displaced, notably Wat812, Wat726, Wat753, Wat748, Wat747, Wat805, Wat744, Wat631, Wat803, Wat800 and Wat808. In addition, Wat726 is shifted by 1.27 Å, Wat43 by 0.94 Å, Wat257 by 0.93 Å, and Wat346 by 1.10 Å.
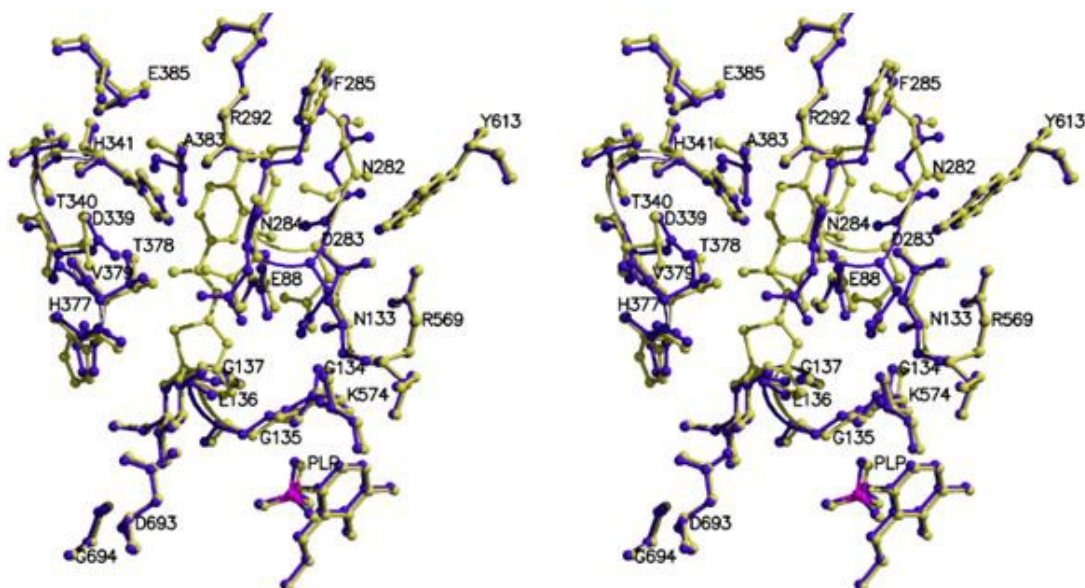
*Figure 121. A stereo diagram showing a structural comparison between (**3**) (yellow) and α-D-glucose (purple) at the catalytic site of GPb.*

Profound conformational changes occur in the amino acids of the 280s loop. In more detail, the CA atom of Asn282 is shifted by 1.06 Å, the CB atom by 1.33 Å, the C atom by 1.22 Å and the main chain oxygen is shifted by 2.14 Å. The side chain is rotated by 130.21°. The CA and CB atoms of Asp283 are shifted by 0.91 Å, the C atom is shifted by 0.84 Å and the O atom by 0.68 Å. The side chain is rotated by 133.43°. The CA atom of Asn284 is shifted by 0.85 Å, the CA atom by 0.90 Å, the C atom by 0.74 Å and the O by

0.69 Å. The side chain is rotated by 80.43°. The CA atom of Phe285 is shifted by 0.71 Å, the N atom by 0.80 Å, the C atom by 0.79 Å and the O atom by 1.02 Å. The side chain is rotated by 139.95°. The changes in Phe286 are less profound and the phenyl ring of the side chain is rotated by 75.21°. Finally, the side chain of Glu287 is rotated by a torsion angle of 22.85° [OE2-**CD-CG**-CB].

Structural comparison with hydantoin

It can be noted that Wat10 and Wat200 are displaced from the GPb-(**3**) complex, while Wat155 and Wat157 are recruited into the structure. The CA atom of Asn282 is shifted by 0.97 Å and the side chain is shifted by 122.64°. The side chain of Asp283 is shifted by 150.04° and that of Asn284 is shifted by 113.56°. The phenyl ring of Phe285 is shifted by 176.74° and that of Phe286 by 136.73°. The side chain of Glu287 undergoes a profound rotation by 40.17°.
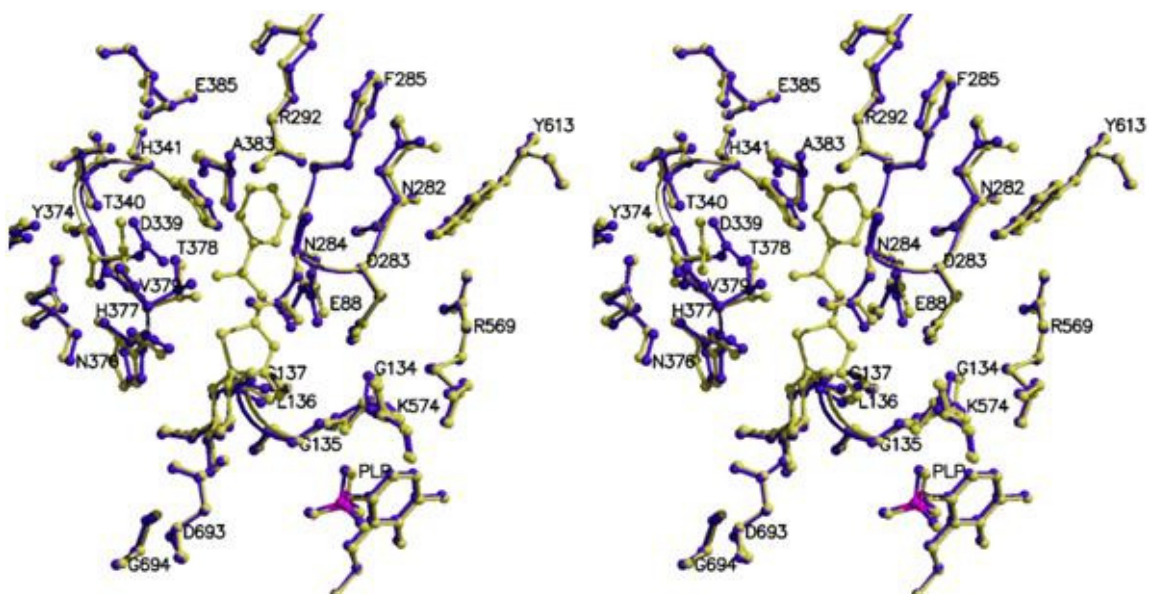

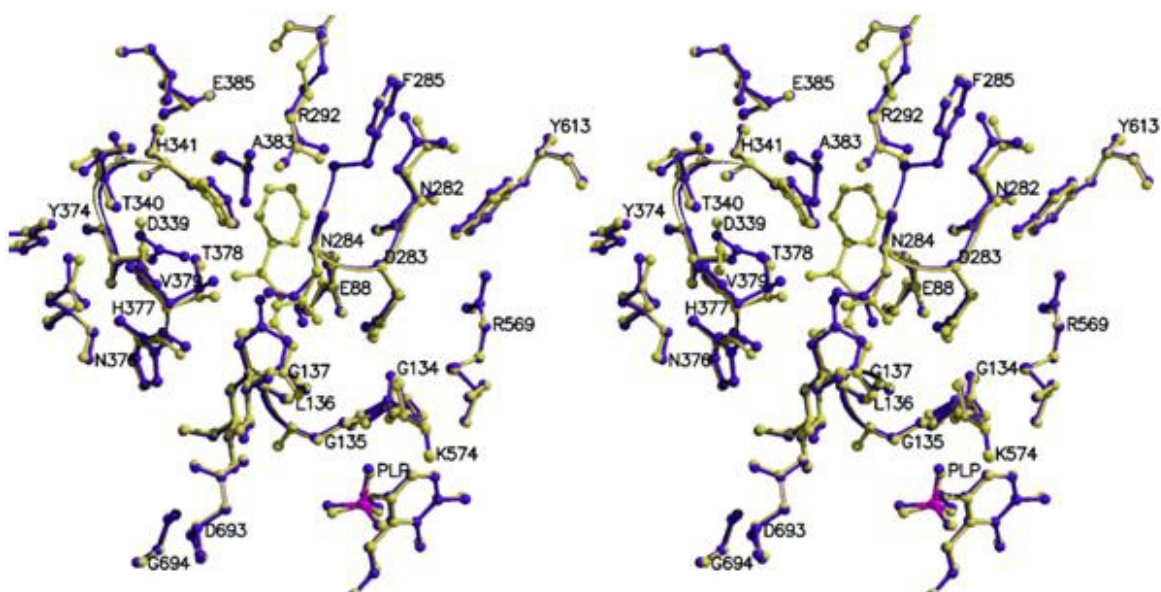*Figure 122. A stereo diagram showing a structural comparison between (3) (yellow) and hydantoin (purple) at the catalytic site of GPb.*

Structural comparison with thiohydantoin
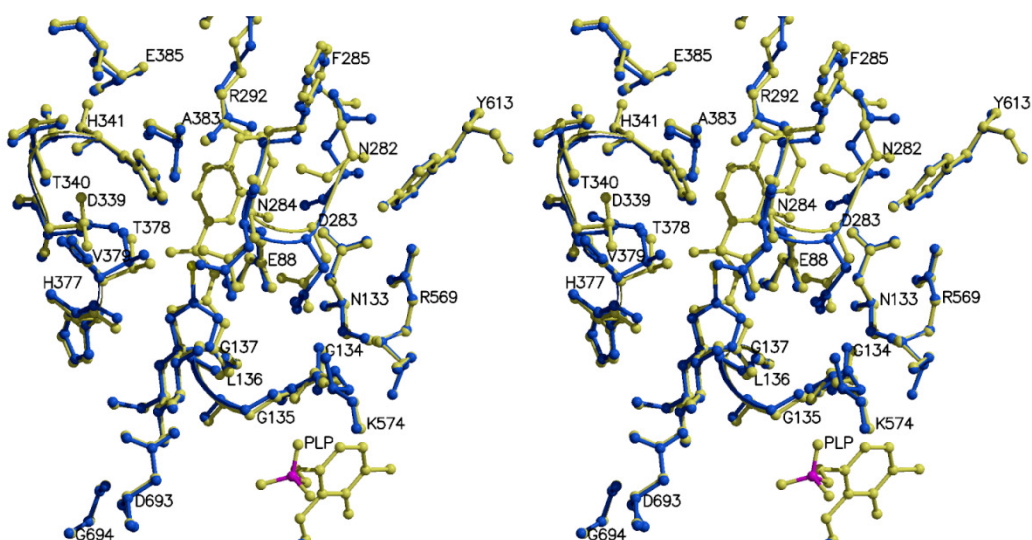
Figure 123. A stereo diagram showing a structural comparison between (3) (yellow) and thiohydantoin (blue) at the catalytic site of GPb.

A comparison with the thiohydantoin-GPb structure revealed that in order for the bulkier inhibitor to fit into the catalytic site, Wat10, Wat214 and Wat183 are displaced; Wat155 and Wat198 are recruited into the new structure, while Wat175 is shifted by 0.86 Å. Regarding the residues of the 280s loop (282-287), the side chain of Asn282 is shifted by 123.70°, the side chain of Asp283 is shifted by 61.67° and that of Asn284 104.12°. The phenyl ring of Phe285 is shifted by 179.04° and that of Phe286 by 125.98°. Finally, the side chain of Glu287 is rotated by a torsion angle of 24.82° [OE2-**CD-CG**-CB]. The side chain of Arg138 of the glycine helix is rotated by a torsion angle of 179.38° [NH1-**CZ-NE**-CD].

X-ray crystallographic studies of glucopyranosylidene-spiro-1-naphthoyliminothiazolone (4)

(**4**) was found to bind at the catalytic site of GPb. Upon binding to the enzyme, (**4**) forms 13 hydrogen bonds and 116 van der Waals interactions with water molecules and the surrounding protein environment. The N1 and O2 atoms of the inhibitor are directly hydrogen bonded to residues of the 280s loop (282-287), Asn284 ND2 and Asp283 OD1 respectively. O6 atom is hydrogen bonded to ND1 atom of His377, a reoccurring bond at the catalytic site.
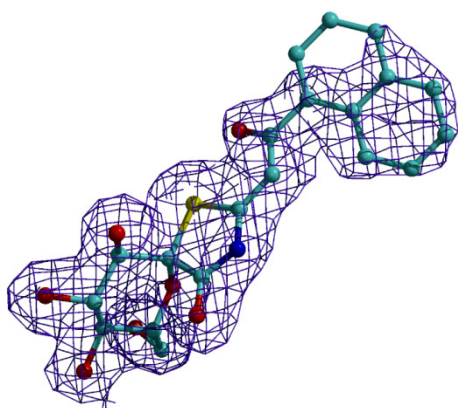
Figure 124. 2Fo-Fc electron density map of (4) bound at the catalytic site of GPb. The map is contoured at 1σ level and the refined model is displayed.
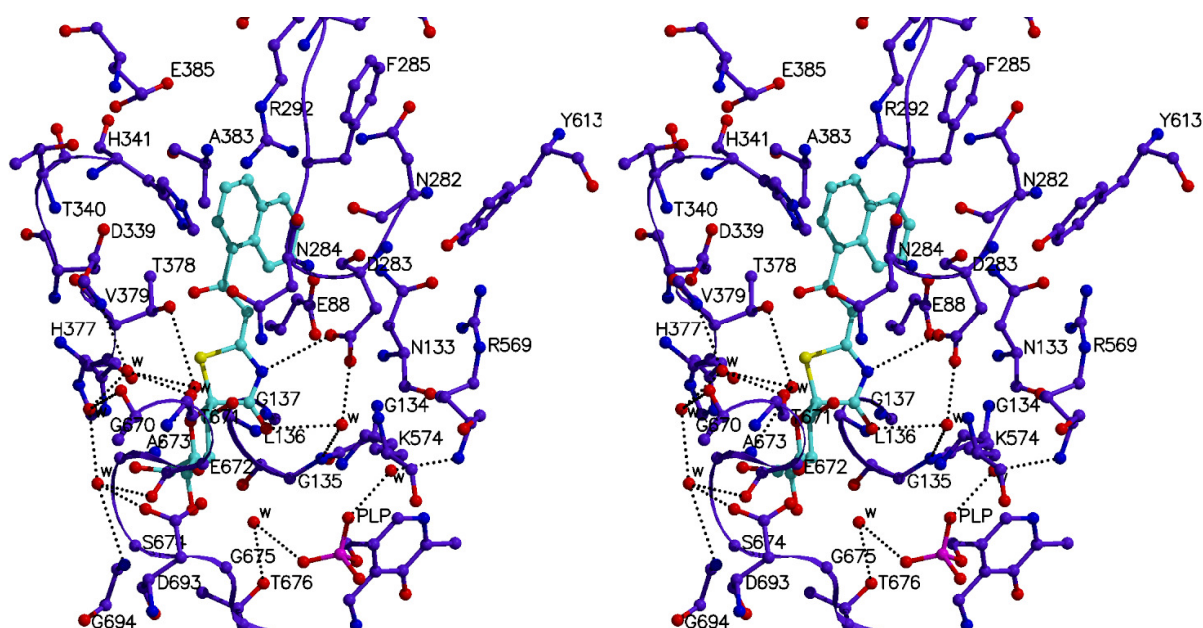
Figure 125. Stereo diagram showing the network of interactions formed between (4) and residues of the catalytic site of GPb.

Structural comparison with α-D-glucose

(**4**) is a much bulkier ligand than glucose and displaced a number of water molecules upon binding (Wat726, Wat748, Wat752, Wat257, Wat747, Wat744, Wat631, Wat777, Wat803, Wat754, Wat808, Wat805 and Wat812). The glucopyranose moiety is shifted by 113.11°. Wat43 is shifted by 0.53 Å, and Wat796 is shifted by 0.68 Å. The side chain of Asn282 is shifted by 31.28°. The side chain of Asp283 is shifted by 59.63°. The side chain of Asn284 is shifted by 169.36°. The phenyl ring of Phe285 undergoes a slight shift of 110.24°, and

that of Phe286 is shifted by 76.34°. The side chain of Glu287 undergoes a major rotation of 36.67° [OE1-**CD-CG**-CB].
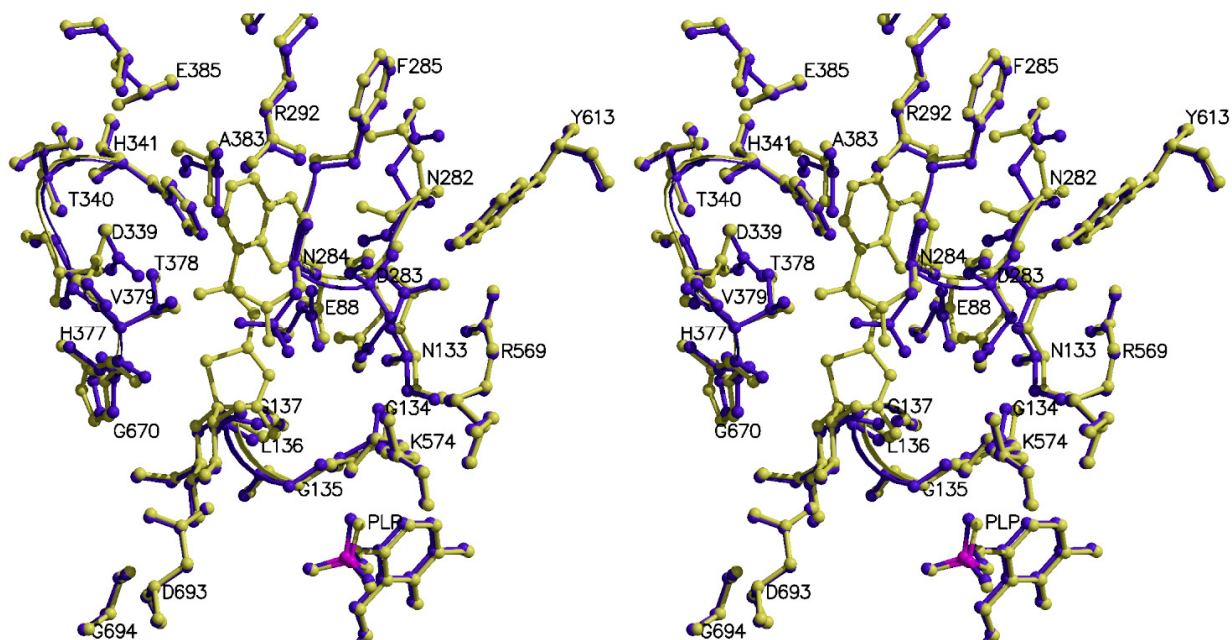
*Figure 126. A stereo diagram showing a structural comparison between (**4**) (yellow) and α-D-glucose (purple) at the catalytic site of GPb.*

Structural comparison with hydantoin

Wat10 and Wat200 are displaced from the GPb-(**4**) complex, and Wat176 is shifted by 1.35 Å. The side chain of Asn282 is shifted by 93.39°. The side chain of Asp283 is shifted by 155.47°. The side chain of Asn284 is shifted by 174.80°. The phenyl ring of the Phe285 side chain is shifted by 42.25°, the phenyl ring of Phe286 is shifted by 57.85°, while the side chain of Glu287 is rotated by 55.65° [OE1-**CD-CG**-CB].
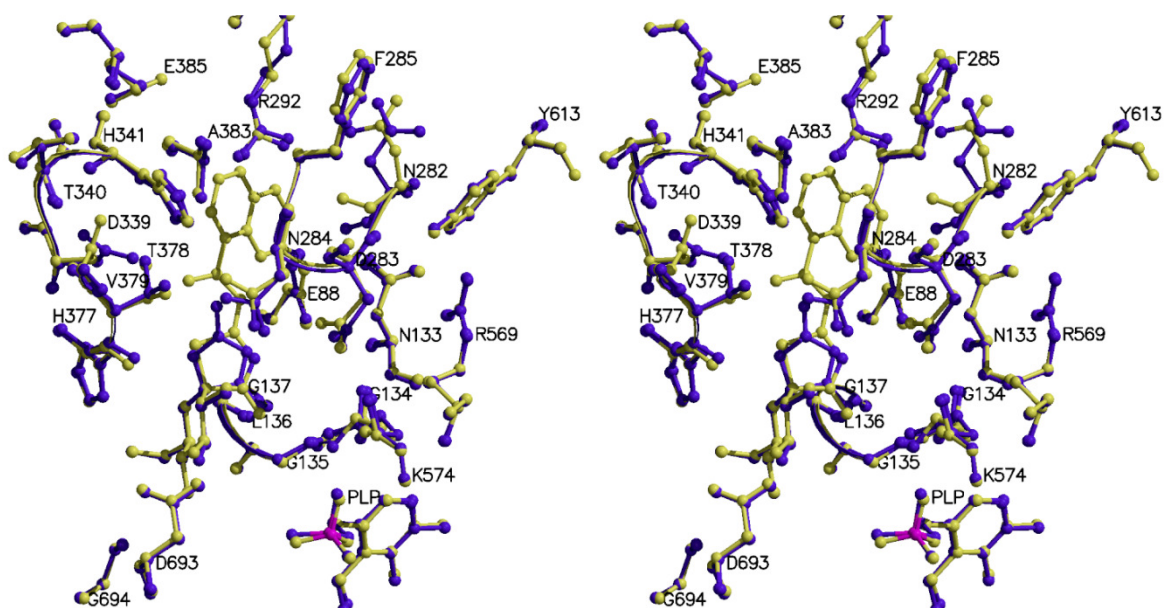
*Figure 127. A stereo diagram showing a structural comparison between (**4**) (yellow) and hydantoin (purple) at the catalytic site of GPb.*

Structural comparison with thiohydantoin

Wat10, Wat183 and Wat214 are displaced from the GPb-(**4**) complex while Wat165 is shifted by 1.22 Å. There is almost no shift of the glucopyranose moiety.
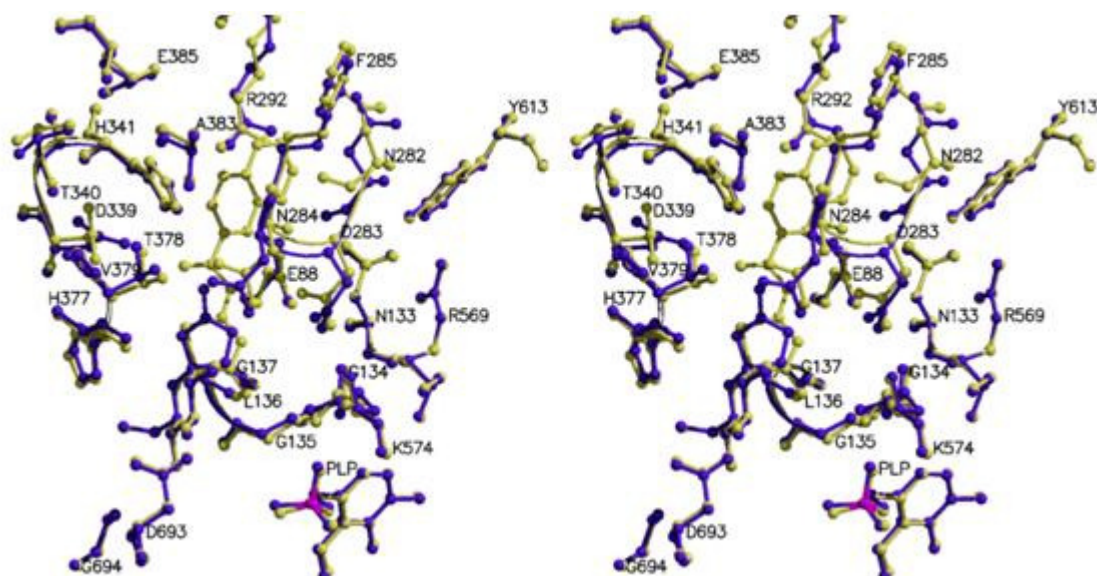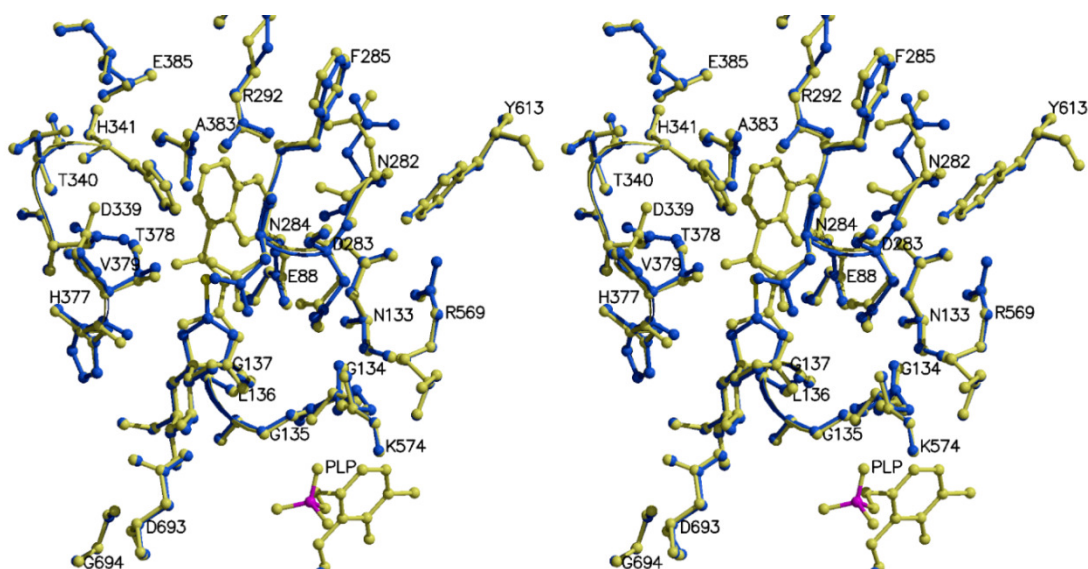

*Figure 128. A stereo diagram showing a structural comparison between (**4**) (yellow) and thiohydantoin (blue) at the catalytic site of GPb.*

The side chain of Asn282 is shifted by 82.05°. The side chain of Asp283 is shifted by 81.43°. The side chain of Asn284 is shifted by 74.42°. The phenyl rings of the side chains Phe285 and Phe286 are shifted by 115.34° and 69.81° respectively. The side chain of Glu287 is rotated by 11.09° [OE1-**CD-CG**-CB].

Inhibitor atom	Target atoms	Distance (Å)	Angle (°)	Inhibitor atoms	Target atoms	Distance (Å)	Angle (°)
O2	Asn284 ND2	3.1	157.1	**O2**	Asn284 ND2	3.2	143.4
	Tyr573 OH	3.1	145.8		Asn284 OD1	3.1	100.9
	Glu672 OE1	3.3	176.7		Tyr573 OH	3.0	143.1
	Wat52	3.0	-		Glu672 OE1	3.3	177.7
	Wat189	3.0	-		Wat141	3.0	-
O3	Glu672 OE1	2.7	121.2		Wat142	3.0	-
	Ser674 N	3.1	177.3	**O3**	Glu672 OE1	2.7	123.3
	Gly675 N	3.1	143.3		Ser674 N	3.1	177.4
O4	Gly675 N	2.9	128.9		Gly675 N	3.2	140.4
	Wat49	2.5	-	**O4**	Gly675 N	2.8	132.5
O6	His377 ND1	2.7	162.8		Wat154	2.6	-
	Asn484 OD1	2.8	137.5	**O6**	His377 ND1	2.7	168.2
O7	Wat50	3.1	-		Asn484 OD1	2.8	138.2
	Wat52	3.2	-	**O7**	Wat142	3.0	-
N1	Wat53	2.8	-		Wat143	3.0	-
N2	Wat60	2.8	-	**O8**	Wat165	2.7	-
S1	His377 O	3.3	105.8	**N1**	Wat158	2.8	-

*Figure 129. The network of hydrogen bond interactions of (**1**) (left) and (**2**) (right) at the catalytic site of GPb.*

O2	**…Wat52**	…Asp283 OD2			
		…Tyr573 OH			
		…Lys574 NZ			
	…Wat189	...Thr378 OG1			
		…Thr671 O			
		…Ala673 N			
		…Wat188	…Val379 N		
			…Thr671 O		
			…Wat187	…Gly670 O	
				…Wat186	…Glu672 O
					…Asp693 OD2
					…Gly694 N
O4	**…Wat49**	…Thr676 OG1			
		…PLP O3P			
O7	**…Wat50**	…Gly135 N			
		..Asp283 OD1			
		…Wat51	…Arg569 N		
			…PLP O2P		
	…Wat52	…Asp283 OD2			
		…Tyr573 OH			

		…Lys574 NZ		
N1	**…Wat53**	…Asp283 OD1		
		…Wat54	…Glu88 OE2	
			…Gly134 N	
			…Gly137 N	
		…Wat55	…Glu88 OE1	
N2	**…Wat60**	…Asp339 OD1		

*Figure 130. The water hydrogen bonding network of (**1**) at the catalytic site of GPb.*

O2	**…Wat141**	…Thr378 OG1		
		…Thr671 O		
		…Ala673 N		
		…Wat140	…Thr378 OG1	
			…Val379 N	
			…Thr671 O	
			…Wat138	…Gly670 O
				…Wat139
				…Asp693 OD2
				…Gly694 N
	…Wat142	...Gly135 N		
		…Asp283 OD1		
		…Wat144	…Arg569 N	
			…PLP O2P	
O4	**…Wat154**	…Thr676 OG1		
		…PLP O3P		
O7	**...Wat142**			
	…Wat143	…Gly135 N		
		…Asp283 OD1		
		…Wat144		
O8	**…Wat165**	**…Wat164**	…Asp339 OD2	
			…His341 NE2	
			…Ala383 O	
			…Wat167	…Thr340 OG1
				…Glu385 N
			…Wat166	…Asp339
				…Tyr374 OH
				…Asn376 ND2
N1	**…Wat158**	…Asp283 OD1		
		…Wat157	…Glu88 OE2	
			…Gly134 N	
			…Gly137 N	

*Figure 131. Water hydrogen bonding network of (**2**) at the catalytic site of GPb.*

Inhibitor atom	Protein atom	No. of contacts	Inhibitor atom	Protein atom	No. of contacts
C1	His377 O	1	C1	His377 O	1
C2	His377 O; Glu672 OE1; Wat189	3	C2	His377 O; Glu672 OE1; Wat141; Wat142	4
C3	Glu672 OE1; Gly675 N; Wat49	3	C3	Glu672 OE1; Gly675 N; Wat154	3
C4	Gly675 N; Wat49	2	C4	Gly675 N; Wat154	2
C5	Gly135 C; Leu136 N; Wat49	3	C5	Gly135 C; Leu136 N; Wat154	3
C6	Gly135 O; Leu139 CD2; His377 ND1; Asn484 OD1	4	C6	Gly135 C, O; Leu139 CD2; His377 ND1; Asn484 OD1	5
C7	Leu136 N; Asn284 ND2; Wat50, Wat52, Wat53	5	C7	Leu136 N; Asn284 ND2; Wat142; Wat143; Wat158	5
C8	Leu136 CB; Asn284 ND2, CG; Wat53, Wat60	5	C8	Leu136 CB; Asn284 ND2, CG, OD1; Wat158	5
O2	Asn284 CG, OD1	2	C9	Leu136 CD1; Asn284 CA, N; Wat165	4
O3	Glu672 CG, CD, C; Ala673 CA, N, C, CB; Ser674 CA, C; Gly675 CA;Wat189	11	C10	Asn284 CA, N; His341 CE1; Wat165	4
O4	Asn 484 OD1; Ser674 CB, C; Gly675 CA, C, O	6	C11	Phe285 N; His341 CE1, NE2; Ala383 O; Wat164; Wat165	6
O5	Gly136 CB, N; His377 CB, ND1, O	5	C12	Phe285 C, N, O; His341 CE1, NE2; Ala383 O; Wat164	7
O6	Leu139 CD2; His377 CG, CE1; Val455 CG1, CG2; Asn484 CG	6	C13	Phe285 C, O; His341 CE1, NEl Wat161; Wat163	6
O7	Gly135 N, CA, C; Wat49	4	C14	Asn282 O; His341 CE1; Wat159; Wat160	4
N1	Leu136 CB, N; Asn284 ND2; Wat50, Wat52	5	C15	Asn282 O; Asn284 N; His341 CE1; Wat159	4
N2	Asn284 ND2, CG, N; Wat53,Wat55	5	O2	Asn284 CG	1
S1	Asn284 ND2; His377 CB, C, O; Wat60	5	O3	Glu672 CG,CD, C; Ala673 CA,C,CB; Ser674 CA,C; Wat141	9
			O4	Asn 484 OD1; Ser674 CB,C; Gly675 CA,C,O	6
			O5	Gly136 N; His377 CB,ND1,O	4
			O6	Leu139 CD2; His377 CG, CE1; Val455 CB, CG1, CG2; Asn484 CG	7
			O7	Gly135 N, CA, C; Leu136 N; Wat154, Wat158	6
			O8	Leu136 CD1; Thr378 CG2	2
			N1	Leu136 CB, N; Asp283 OD1; Wat142; Wat143	5
			N2	Leu136 CD1; Asn284 ND2, CG, N, CA; Wat158	6
			S1	Asn284 OD1,ND2; His377 CB, C,O	5

Figure 132. The network of van der Waals interactions of (1) (left) and (2) (right) at the catalytic site of GPb.

Inhibitor atoms	Target atoms	Distance (Å)	Angle (°)	Inhibitor atoms	Target atoms	Distance (Å)	Angle (°)
O2	Asn284 ND2	3.2	156.2	O2	Asn284 ND2	2.8	126.3
	Tyr573 OH	3.2	145.4		Tyr573 OH	3.1	145.6
	Glu672 OE1	3.3	175.0		Glu672 OE1	3.2	179.4
	Wat72	2.8	-		Wat74	2.9	-
O3	Glu672 OE1	2.7	123.1	O3	Glu672 OE1	2.8	121.3
	Ser674 N	3.1	176.2		Ser674 N	3.1	175.6
	Gly675 N	3.1	144.6		Gly675 N	3.1	141.4
O4	Gly675 N	2.8	128.5	O4	Gly675 N	2.9	131.9
	Wat28	2.6	-		Wat87	2.6	-
O6	His377 ND1	2.7	173.3	O6	His377 ND1	2.8	163.9
	Asn484 OD1	2.8	138.4		Asn484 OD1	2.8	138.9
O7	Wat27	3.0	-	O7	Wat37	3.0	-
N1	Wat197	3.0	-	N1	Asp283 OD1	3.3	-
N2	Asp283 OD1	3.1	132.6				
S1	His377 O	3.2	110.5				

Figure 133. The network of hydrogen bond interactions of (3) (left) and (4) (right) at the catalytic site of GPb.

O2	…Wat72	…Thr378 OG1		
		…Thr671 O		
		…Ala673 N		
		…Wat71	…Val379 N	
			…Thr671 O	
			…Wat70	…Gly670 O
				…Wat69
				…Asp693 OD2
				…Gly694 N
O4	…Wat28	…Thr676 OG1		
		…PLP O3P		
O7	…Wat27	…Gly135 N		
		…Asp283 OD2		
		…Wat26	…Arg569 N	
			…PLP O2P	
N1	…Wat197	…Leu136		
		…Asp283 OD1		
		…Wat198	…Glu88 OE2	
			...Asn133 N	
			…Gly134 N	
			…Gly137 N	

Note: In the row with "…Wat69", adjacent column shows "…Glu672 O".

Figure 134. The water hydrogen bonding network of (3) at the catalytic site of GPb.

Inhibitor atom	Protein atom	No. of contacts	Inhibitor atom	Protein atom	No. of contacts
C1	His377 O	1	C1	His377 O	1
C2	His377 O; Glu672 OE1; Wat72	3	C2	Asn284 ND2; His377 O; Glu672 OE1; Wat74	4
C3	Glu672 OE1; Gly675 N; Wat28	3	C3	Glu672 OE1; Gly675 N; Wat87	3
C4	Gly675 N; Wat28	2	C4	Gly675 N; Wat87	2
C5	Gly135 C; Leu136 N; Wat28	3	C5	Gly135 C; Leu136 N; Wat87	3
C6	Gly135 O; Leu139 CD2; His377 ND1; Asn484 OD1	4	C6	Gly135 O; Leu139 CD2; His377 ND1; Asn484 OD1	4
C7	Leu136 N, CB; Wat27; Wat197	4	C7	Leu136 N; Wat37	2
C8	Leu136 CB; Asn283 OD1; Asn284 ND2; Wat197	4	C8	Leu136 CB; Asn283 OD1; Asn284 ND2	3
C9	Leu136 CD1; Asn284 N, OD1	3	C9	Asp283 OD1; Asn284 CG, ND2, N, CA	5
C10	Asn284 CA, N; His341 CE1	3	C10	Asn284 CA, N	2
C11	Asp283 OD1; Asn284 N; His341 CE1	3	C11	Asn284 CA, N	2
C12	Asn282 O; Asn284 N; His341 CE1; Wat155	4	C12	Asn284 N; His341 CE1, NE2	3
C13	Glu88 OE1; Asn133 ND2; Asn282 O; Wat155	4	C13	Asp283 OD1; Asn284 N; His341 CE1	3
C14	Tyr280 O; Asn282 C, O; Arg292 CZ, NH1, NH2; Wat155	7	C14	Glu88 CD, OE1; Asn133 ND2; Asn282 O; Asp283 OD1	5
C15	Asn282 O, ND2; Arg292 CZ, NH2; Wat194	5	C15	Glu88 OE1; Asn133 ND2; Asn282 O; Arg292 NH2	4
C16	Asn282 O; Phe285 O; Arg292 NH2; Wat194	4	C16	Asn282 O, ND2; Arg292 NH2	3
C17	Asn341 NE2; Asn282 O	2	C17	Asn341 CE1, NE2; Asn282 O; Phe285 O	4
C18	Phe285 N; His341 NE2; Wat157	3	C18	Phe285 N, C, O; His341 NE2; Wat44	5
C19	Asn284 CA, N; His341 CE1, NE2; Wat157	5	C19	Phe285 N, C, O; His341 NE2; Ala383 CB, C, O	7
O2	His377 O; Glu672 OE1	2	C20	Asn284 CA; Phe285 N; Ala383 CB, O	4
O3	Glu672 CG, CD, C; Ala673 CA, C, CB, N; Ser674 CA, C; Gly675 CA; Wat72	11	O3	Glu672 CG, CD, C; Ala673 CA, C, CB, N; Ser674 CA, C; Gly675 CA; Wat74	11
O4	Ser674 CA, CB, C, OG, N; Gly675 C,O	7	O4	Asn484 OD1; Ser674 CB, C; Gly675 C, O, CA	6
O5	Gly136 CA, CB, N; His377 CB,ND1,O	6	O5	Gly136 CB, N; His377 CB,ND1,O	5
O6	Leu139 CD2; His377 CG, CE1, CB; Val455 CB, CG1, CG2; Asn484 CG	8	O6	Leu139 CD2; His377 CG, CE1, CB; Val455 CB, CG1, CG2; Asn484 CG	7
O7	Gly135 N, CA, C; Leu136 N; Wat28, Wat197	6	O7	Gly135 N, CA, C; Leu136 N; Wat87;	5
O8	Leu136 CD1; Asn284 OD1; Asp339 OD1; Thr378 CB, CG2	5	O8	Asn284 OD1; Thr378 CG2	2
N1	Leu136 CB, N; Asp283 OD1, OD2; Asn284 ND2; Wat27	6	N1	Leu136 CB, N; Asp283 CG, OD1, OD2; Asn284 ND2; Wat37	7
N2	Asn284 ND2, CG, N; Wat197	4	S1	Asn284 ND2; His377 CB, C, O	4
S1	His377 CB, C, O; Thr378 CB	4			

Figure 135. The network of van der Waals interactions of (3) (left) and (4) (right) at the catalytic site of GPb.

135

O2	…Wat74	…Thr378 OG1			
		…Thr671 O			
		…Ala673 N			
		…Wat73	…Val379 N		
			…Thr671 O		
			…Wat72	…Gly670 O	
				…Wat75	…Glu672 O
					…Asp693 OD2
					…Gly694 N
O4	…Wat87	…Thr676 OG1			
		…PLP O3P			
O7	…Wat37	…Gly135 N			
		…Asp283 OD2			
		…Wat36	…Arg569 N		
			…PLP O2P		

*Figure 136. The water hydrogen bonding network of (**4**) at the catalytic site of GPb.*

	(**1**)	(**2**)	(**3**)	(**4**)
Experiment	T state GPb crystals soaked with 10 mM (**1**) in 10% DMSO for 4.5 hrs	T state GPb crystals soaked with 10 mM (**2**) in 10% DMSO for 4.5 hrs	T state GPb crystals soaked with 10 mM (**3**) in 10% DMSO for 4.5 hrs	T state GPb crystals soaked with 10 mM (**4**) in 10% DMSO for 4.5 hrs
Wavelength (Å)	0.97976	0.97976	0.97976	0.97976
Oscillation range (°) [1]	0.8	0.8	0.8	0.8
No. of images (°)	80	80	80	80
Space Group	$P4_32_12$	$P4_32_12$	$P4_32_12$	$P4_32_12$
Unit cell dimensions	$a=b=128.2$ Å, $c=115.9$ Å, $\alpha=\beta=\gamma=90°$	$a=b=128.0$ Å, $c=115.8$ Å, $\alpha=\beta=\gamma=90°$	$a=b=127.8$ Å, $c=116.0$ Å, $\alpha=\beta=\gamma=90°$	$a=b=128.7$ Å, $c=116.5$ Å, $\alpha=\beta=\gamma=90°$
Resolution (Å)	35.7-1.95	35.7–1.90	35.6–2.10	30.0–1.94
No of observations	619937	672299	660330	840625
No. of unique reflections (outermost)	69137 (9822)	74351 (10763)	55833 (8085)	71490 (3474)
R_m (outermost shell) [2]	0.061 (0.376)	0.073 (0.412)	0.086 (0.428)	0.054 (0.465)
Completeness (outermost shell) (%)	98.0 (96.8)	98.2 (98.5)	99.2 (99.7)	98.2 (97.1)
Outermost shell (Å)	2.06–1.95	2.00–1.90	2.21–2.10	1.97–1.94
$< I / \sigma (I) >$ (outermost shell) [3]	20.4 (5.1)	16.6 (3.2)	15.9 (4.6)	26.3 (4.6)
Redundancy (outermost shell)	5.3 (5.2)	5.1 (4.8)	5.0 (4.9)	5.3 (5.0)
B-values (Å^2) (Wilson plot)	25.4	25.9	32.8	31.1
Resolution range (Å)	90.54–1.95	90.54–1.90	90.17–2.10	90.91–1.94
No of reflections used (free)	65604 (3502)	70557 (3734)	52967 (2836)	67835 (3616)
Residues included	(12-254) (261–314) (324–836)	(12-254) (261–314) (324–836)	(12-254) (261–314) (324-836)	(12-254) (261–314) (324–836)
No. of protein atoms	6589	6589	6589	6595
No. of water molecules	301	301	203	225

No. of heteroatoms	17 (**1**), 15 (PLP)	25 (**2**), 15 (PLP)	29 (**3**) 15 (PLP)	29 (**4**), 15 (PLP)
Final R (R_{free}) (%) [4]	0.19 (0.21)	0.19 (0.22)	0.20 (0.24)	0.19 (0.22)
R (R_{free}) (outermost shell)	0.23 (0.25)	0.25 (0.22)	0.24 (0.28)	0.25 (0.28)
r.m.s.d. in bond lengths (Å)	0.006	0.006	0.007	0.007
r.m.s.d. in bond angles (°)	1.008	0.999	1.058	1.030
Average B (Å²) for residues	(12-254) (261–314) (324–836)	(12-254) (261–314) (324–836)	(12-254) (261–314) (324–836)	(12-254) (261–314) (324–836)
Overall	28.6	30.7	38.1	35.9
CA, C, N, O	27.8	29.9	37.3	35.1
Side chain	29.4	31.5	38.8	36.9
Average B (Å²) for heteroatoms	19.3 (**1**), 18.2 (PLP)	20.9 (**2**), 20.6 (PLP)	28.1 (**3**), 28.6 (PLP)	29.9 (**4**), 25.2 (PLP)
Average B (Å²) for water molecules	35.8	37.5	38.1	39.8

a Native T state RMGPb crystals, grown in the tetragonal lattice, space group P4$_3$2$_1$2 were soaked with various concentrations of inhibitors in buffered solutions at pH 6.7 in the presence of DMSO. X-ray diffraction data were collected using synchrotron radiation sources at Daresbury Laboratory, UK and EMBL-Hamburg outstation at DESY, Germany and processed with the HKL package. Complex structure determination and analysis were performed according to standard protocols as implemented in the CCP4 package.

b $R_{symm} = \Sigma_h\Sigma_i|I(h) - I_i(h)/\Sigma_h\Sigma_iI_i(h)$ where $I_i(h)$ and $I(h)$ are the ith and the mean measurements of the intensity of reflection h.

c σ(I) is the standard deviation of I.

d $R_{cryst} = \Sigma_h|F_o - F_c|/\Sigma_hF_o$, where F_o and F_c are the observed and calculated structure factors amplitudes of reflection h, respectively. R_{free} is equal to R_{cryst} for a randomly selected 5% subset of reflections not used in the refinement. Values in parentheses are for the outermost shell.

Figure 137. Diffraction data and refinement statistics.

Conclusions

Comparing the inhibitory effects of the four compounds studied and of hydantoin and thiohydantoin, it is clear that hydantoin is the best inhibitor of GPb (K_i: 3.1 µM). This can be explained by the presence of the two nitrogen and the two oxygen atoms in the cyclopentane ring, which have hydrogen bonding capacity. Replacing one of the nitrogens with sulphur as in the case of thiohydantoin increases the K_i to 5.1 µM. As already mentioned in section 3.4, the reactivity of the naphthyl group depends on the alpha or the beta position. Comparing the inhibitory effect of (**3**) and (**4**), (**3**) has a lower K_i (K_i: 3.7 µM). This can be explained by the fact that in the case of (**3**), the alpha position (more reactive than the beta position) of the naphthyl group is free to react and undergo electrophilic aromatic substitution.

3.7 Virtual screening followed by kinetic and X-ray crystallographic studies of a new class of glycogen phosphorylase inhibitors

Virtual screening *(by Professor Alex MacKerell and colleagues at the School of Pharmacy, Computer-Aided Design Centre, University of Maryland, USA)*

Virtual screening is a powerful tool in structure based drug design. It involves rapid *in silico* assessments of large libraries of chemical structures, in order to identify those structures most likely to bind to a drug target. An *in silico* virtual screening was performed on a database of one million compounds, targeting the inhibitor site of glycogen phosphorylase. This process resulted in 175 hits, based on binding affinities (Gibb's free energy ΔG).

Kinetic studies

Out of the 175 selected compounds derived from the virtual screening process, 12 compounds were further selected for *in vitro* kinetic studies, based on their partition coefficient *log P* value. This is the ratio of the concentration of a particular compound in the two phases of a mixture of two immiscible liquids, usually water and octanol. It is a measure of the hydrophilicity/hydrophobicity for a compound. Kinetic studies were performed in the direction of glycogen synthesis at pH 6.8 and 30°C. The chemical structures of the compounds as well as the kinetic results are presented in figure 138 below.
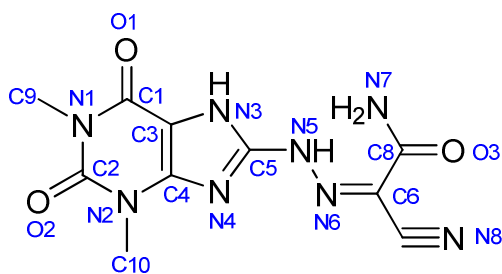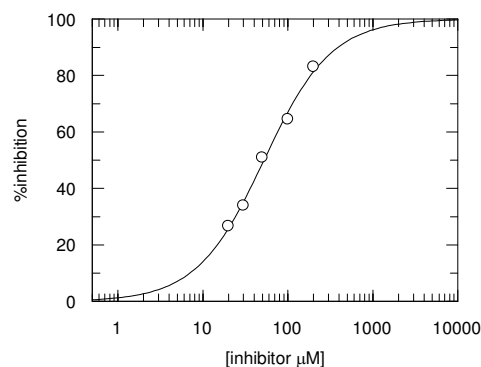
Chembridge 084363/5786622 (**1**) IC_{50}: 52.2 ± 2.4 μM
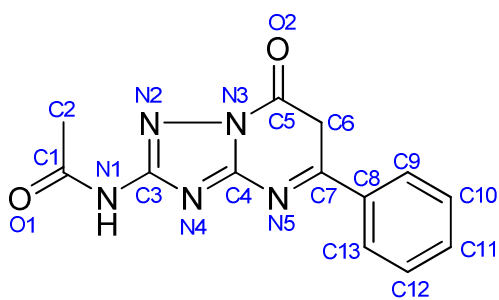
Chembridge 0146922/5846914 (**2**)
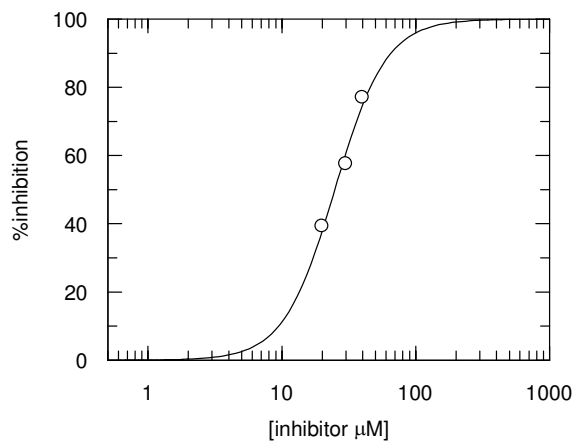
IC$_{50}$: 24.8 ± 1.2 µM
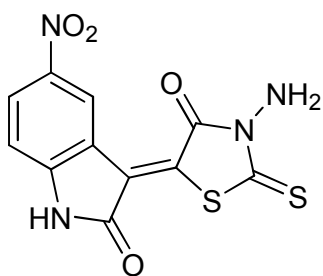
Chembridge *0223534/6635806* (**3**)
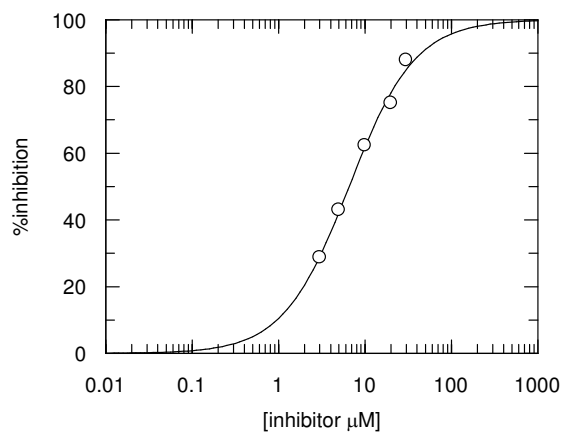
IC$_{50}$: 6.5 ± 0.3 µM
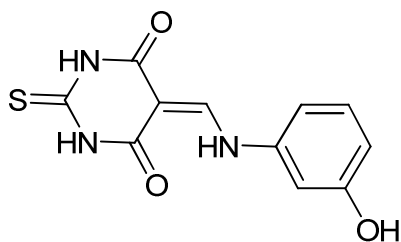
Chemdivision 8003/4196 (**4**)
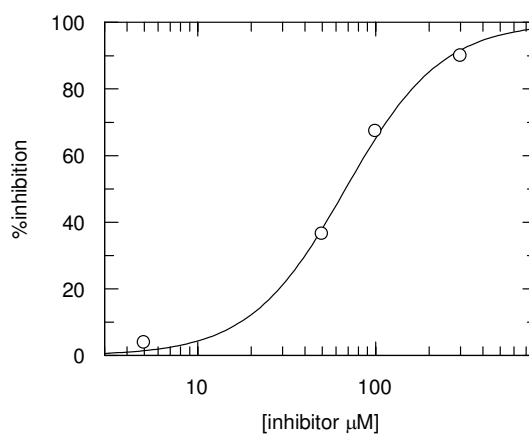
IC$_{50}$: 67.7 ± 4.9 µM
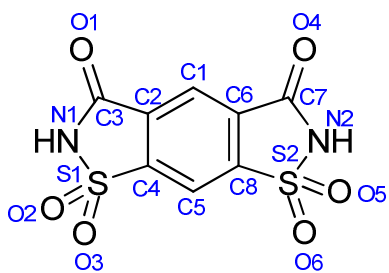
Chemdivision 0262/0300 **(5)**
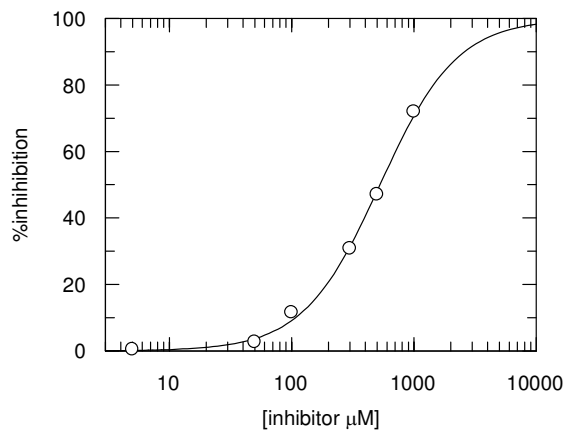
IC$_{50}$: 527.3 ± 15.3 μM
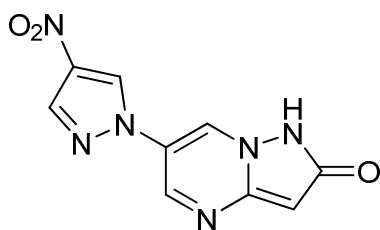
Tim Tec ST002304 **(6)**
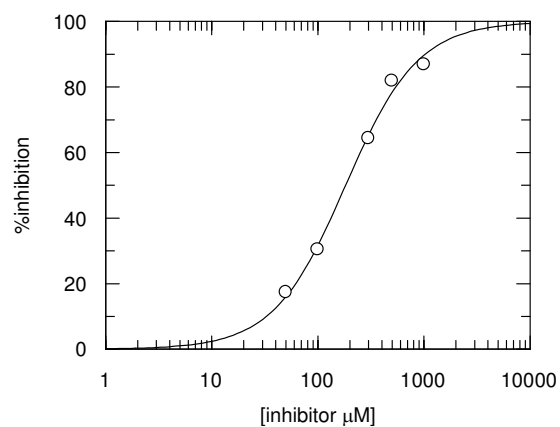
IC$_{50}$: 182.6 ± 11 μM
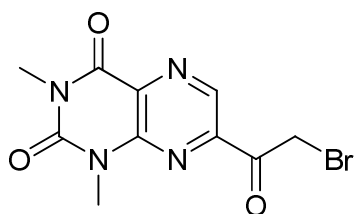
Specs AB-323/2504846 **(7)**

IC$_{50}$: 567.9 ± 26.1 μM

140
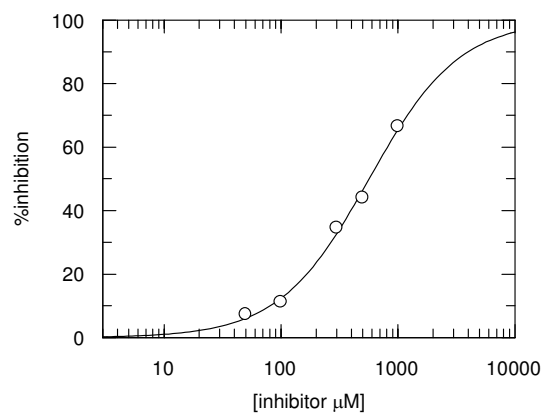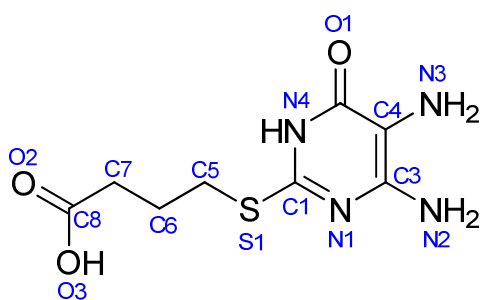
Specs AB-323/25048429 (8)
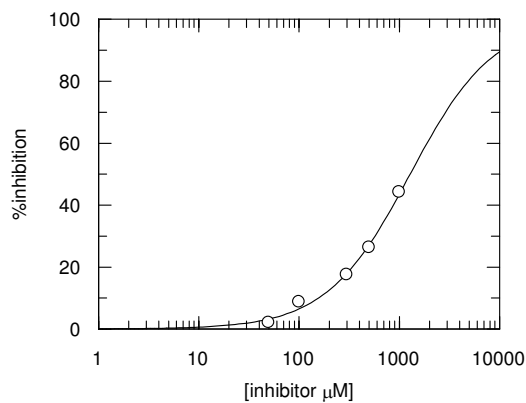
IC$_{50}$: 1.3 ± 0.1 mM
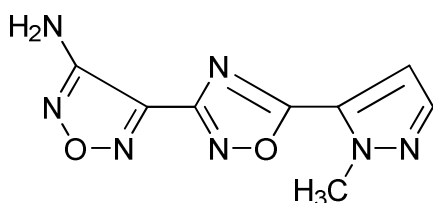
Chemdivision 8011/9762 (9)

IC$_{50}$: No inhibition up to 1 mM
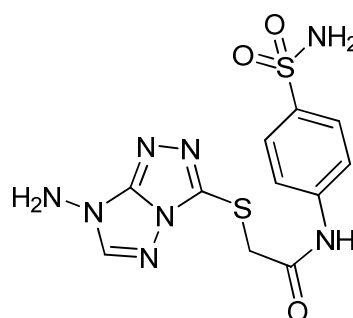
Chemdivision 8008/0569 (10)

IC$_{50}$: No inhibition at 1 mM
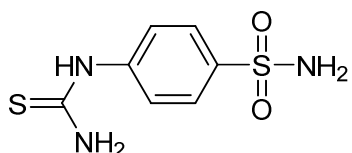
World Molecules APX000007764 (11)

IC$_{50}$: 26% inhibition up to 1 mM
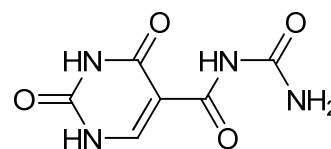
Specs AJ-030/25007249 (12)

IC$_{50}$: 21% inhibition up to 1 mM

Figure 138. The chemical structures and kinetic results from the in vitro studies of the 12 selected compounds and the numbering system used on the compounds further studied.

Out of the 12 compounds studied, 8 exhibited inhibition towards GPb. The most potent inhibitor was (**3**) with an IC$_{50}$ of 6.5 ± 0.3 µM. (**10**) and (**9**) showed no inhibition towards GPb, while (**11**) and (**12**) showed partial inhibition up to 1mM of inhibitor concentration.

X-ray crystallographic studies

To interpret the results obtained from the kinetic experiments and provide rationalizations for the binding affinities observed, X-ray studies were performed on these compounds. Out of the 12 compounds only 4 showed binding to GPb.

(2)

(N-(7-oxo-5-phenyl-6,7-dihydro[1,2,4]triazolo[1,5-a]pyrimidin-2-yl)acetamide)

(1)

((2E)-2-cyano-2-[(1,3-dimethyl-2,6-dioxo-2,3,6,9-tetrahydro-1H-purin-8-yl)hydrazono]acetamide)

(8)

(4-[(4,5-diamino-6-oxo-1,6-dihydropyrimidin-2-yl)thio]butanoic acid)

(5)

(di-4,6-disulfoisophthalsaeure-diimid or m-bisaccharin)
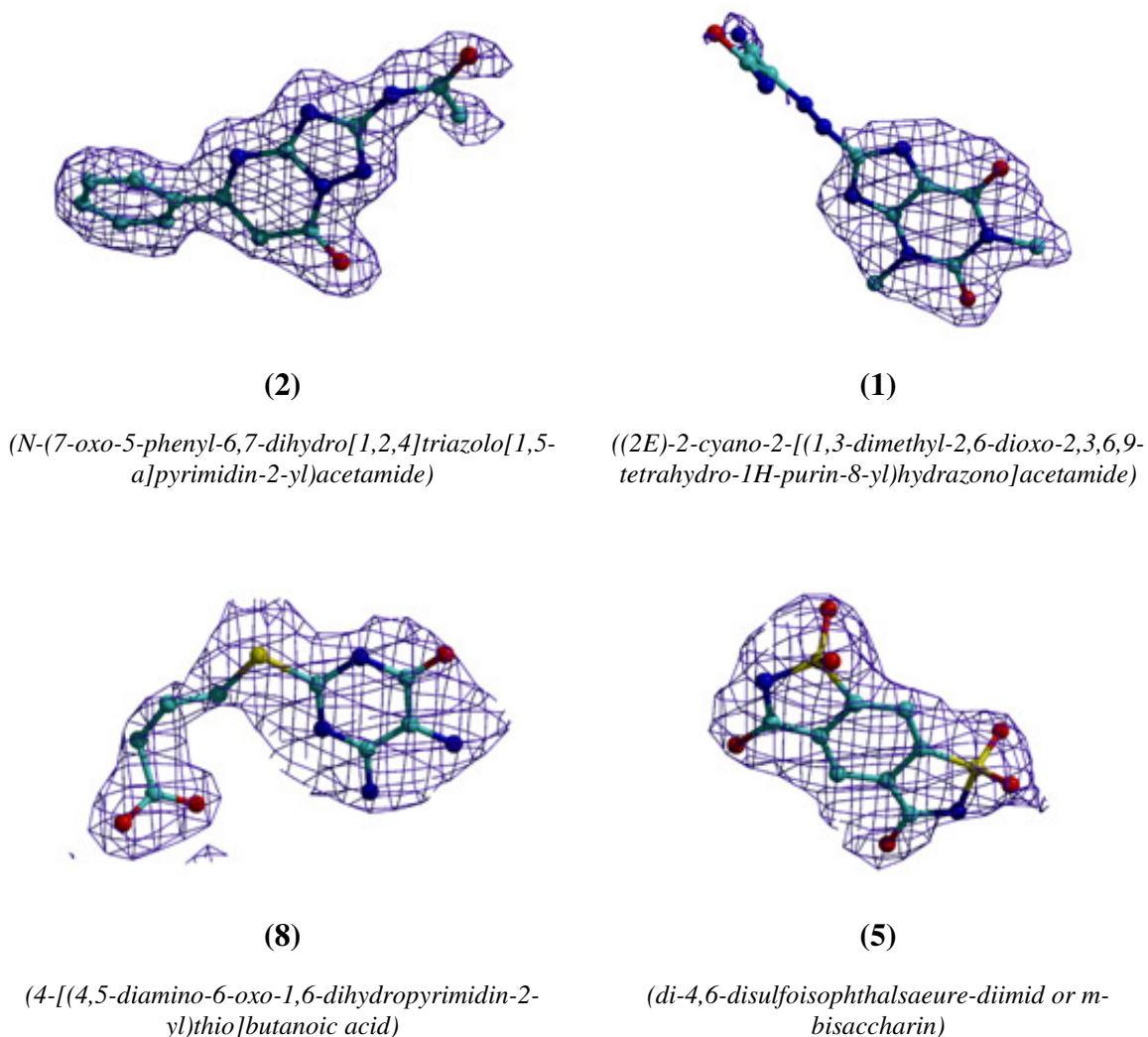
Figure 139. 2FoFc electron density maps of the four compounds bound at the inhibitor site of GPb. The maps are contoured at 1σ level and the refined models of the inhibitors are displayed.

	(2)	**(1)**	**(8)**	**(5)**
Experiment	T state GPb crystals soaked with 1 mM (**2**) in 10% DMSO for 7.5 hrs	T state GPb crystals soaked with 2 mM (**1**) in 20% DMSO for 7.5 hrs	T state GPb crystals soaked with 17.7 mM (**8**) in 30% DMSO for 5 hrs	T state GPb crystals soaked with 2 mM (**5**) in 20% DMSO for 7.5 hrs
Wavelength (Å)	0.8081	0.8081	0.8088	0.8081
Oscillation range (°) [a]	0.8	0.8	0.8	0.8
No. of images (°)	80	81	80	80
Space Group	$P4_32_12$	$P4_32_12$	$P4_32_12$	$P4_32_12$
Unit cell dimensions	$a=b=128.2$ Å $c=116.0$ Å $\alpha=\beta=\gamma=90°$	$a=b=128.9$ Å $c=116.8$ Å $\alpha=\beta=\gamma=90°$	$a=b=128.3$ Å $c=116.5$ Å $\alpha=\beta=\gamma=90°$	$a=b=128.6$ Å $c=116.5$ Å $\alpha=\beta=\gamma=90°$
Resolution (Å)	99.0-1.87	30.0–1.98	30.0–2.16	30.0–2.15
No. of observations	606139	553524	686822	583949
No. of unique reflections (outermost)	85708 (2236)	66893 (3280)	52393 (2567)	52074 (2626)
R_m (outermost shell) [b]	0.041 (0.405)	0.050 (0.444)	0.060 (0.479)	0.068 (0.486)
Completeness (outermost shell) (%)	96.1 (51.1)	98.7 (98.2)	99.3 (99.0)	99.2 (96.9)
Outermost shell (Å)	1.83–1.80	2.01–1.98	2.20–2.16	2.19–2.15
$< I /\sigma (I) >$ (outermost shell) [c]	37.0 (3.1)	29.05 (3.8)	25.96 (3.7)	22.60 (3.6)
Redundancy (outermost shell)	5.3 (2.8)	5.4 (5.4)	5.3 (5.4)	5.4 (5.5)
B-values (Å^2) (Wilson plot)	25.3	25.9	32.2	31.1
Resolution range (Å)	90.54–1.81	90.54–1.98	90.91–2.16	90.91–2.15
No. of reflections used (free)	81363 (4298)	63486 (3383)	49690 (2672)	49385 (2652)
Residues included	(12-254) (261–314) (324–836)	(12-254) (261–314) (324–836)	(12-254) (261–314) (324-836)	(12-254) (261–314) (324–836)
No of protein atoms	6621	6594	6610	6594
No of water molecules	354	305	233	259
No. of heteroatoms	20 (**2**), 15 (PLP)	21 (**1**), 15 (PLP)	16 (**8**), 15 (PLP)	18 (**5**), 15 (PLP)
Final R (R_{free}) (%) [d]	0.19 (0.22)	0.19 (0.21)	0.19 (0.23)	0.18 (0.22)
R (R_{free}) (outermost shell)	0.27 (0.27)	0.24 (0.27)	0.23 (0.23)	0.22 (0.26)
r.m.s.d. in bond lengths (Å)	0.006	0.007	0.008	0.007
r.m.s.d. in bond angles (°)	1.001	1.020	1.056	1.073
Average B (Å^2) for residues	(12-254) (261–314) (324–836)	(12-254) (261–314) (324–836)	(12-254) (261–314) (324–836)	(12-254) (261–314) (324–836)
Overall	28.0	27.8	35.2	33.5
CA, C, N, O	27.2	26.9	34.4	32.7
Side chain	28.8	28.6	35.9	34.3
Average B (Å^2) for heteroatoms	28.2 (**2**), 217.1 (PLP)	55.7 (**1**), 16.4 (PLP)	54.6 (**8**), 23.9 (PLP)	57.9 (**5**), 23.3 (PLP)
Average B (Å^2) for water molecules	37.1	34.5	37.5	37.3

a Native T state RMGPb crystals, grown in the tetragonal lattice, space group $P4_32_12$ were soaked with various concentrations of inhibitors in buffered solutions at pH 6.7 in the presence of DMSO. X-ray diffraction data were collected using synchrotron radiation sources at Daresbury Laboratory, UK and EMBL-Hamburg outstation at DESY, Germany and processed with the HKL package. Complex structure determination and analysis were performed according to standard protocols as implemented in the CCP4 package. **b** $R_{symm} = \Sigma_h\Sigma_i|I(h) - I_i(h)/\Sigma_h\Sigma_iI_i(h)$ where $I_i(h)$ and $I(h)$ are the ith and the mean measurements of the intensity of reflection h. **c** $\sigma(I)$ is the standard deviation of I. **d** $R_{cryst} = \Sigma_h|F_o - F_c|/\Sigma_hF_o$, where F_o and F_c are the observed and calculated structure factors amplitudes of reflection h, respectively. R_{free} is equal to R_{cryst} for a randomly selected 5% subset of reflections not used in the refinement. Values in parentheses are for the outermost shell.

Figure 140. Diffraction data and refinement statistics.

(2)   **(1)**

Inhibitor atom	Protein atom	Distance (Å)	Angle (°)	Inhibitor atom	Protein atom	Distance (Å)	Angle (°)
O1	Gly612 O	3.2	122.2	O1	-	-	-
N1	Wat234	2.8	-	N1	-	-	-
	Gly612 O	3.2	113.6		-	-	-
N2	Wat138	3.1	-	N2	-	-	-
N4	Wat234	3.0	-	N4	-	-	-
	Wat237	3.0	-		-	-	-
N5	Wat236	2.8	-	N5	-	-	-
N7	-	-	-	N7	Wat49	3.0	-
O2	Wat136	2.8	-	O2	Wat248	2.9	-
	Wat138	3.1	-		-	-	-

(8)   **(5)**

Inhibitor atom	Protein atom	Distance (Å)	Angle (°)	Inhibitor atom	Protein atom	Distance (Å)	Angle (°)
O1	-	-	-	O1	Wat203	2.7	-
O2	Tyr573 N	2.8	157.1		Gly612 N	3.1	131.4
O5	-	-	-	O5	Wat205	3.1	-
O3	His571 ND1	2.5	151.9	O3	-	-	-
N1	-	-	-	N1	Asn282 OD1	3.2	126.4
N3	Wat84	2.7	-	N2	-	-	-

Figure 141. Hydrogen bond network of interactions between the 4 bound compounds and residues of the inhibitor site of GPb.

N1	…Wat234	…Wat235	…Met615
N2	…Wat138	…Asn282 OD1	
		…Wat139	…Asn282 OD1
			…Gly612 N
N4	…Wat234		
	…Wat237	…Wat236	
N5	…Wat236		
O2	…Wat136	…Asp283 O	
		…Asp283 N	
		…Wat137	…Arg569 NH1
			…Ile570 O
			…Ala610 N
	…Wat138		

O2	…Wat248	…Asp283 O	
		…Asp283 N	
		…Wat249	…Arg569 NH1
			…Ile570 O
			…Ala610 N

*Figure 142. The water hydrogen bonding network of (**2**) (top) and (**1**) (bottom) at the inhibitor site of GPb.*

N3	…Wat84	…Asp283 N	
		…Asp283 O	
		...Wat85	…Arg569 NH1
			…Ile570 O
			…Ala610 N

O1	…Wat203	…Asp283 O	
		...Wat204	...Arg569 NH1
			...Ile570 O
			...Ala610 N

*Figure 143. The water hydrogen bonding network of (**8**) (top) and (**5**) (bottom) at the inhibitor site of GPb.*

Inhibitor atom	Protein atom	No. of contacts	Inhibitor atom	Protein atom	No. of contacts
C1	Gly612 C; Gly612 O; Wat234	3	C1	Phe285 CE1, CE2, CZ	3
C2	Phe285 CZ, CE2; Gly612 O; Wat138	4	C2	Phe285 CB, CG, CD1, CD2; Tyr613 CB, CG, CD1; Wat248	8
C3	Phe285 CZ, CE2; Gly612 O; Tyr613 CA; Wat234; Wat237	6	C3	Phe285 CD1, CE1; Tyr613 CG, CD2, CE2, CZ	6
C4	Phe285 CD1, CE1, CZ; Tyr613 CD2, CE2; Wat236; Wat237	7	C4	Phe285 CD1, CE1, CZ; Tyr613 CD2	4
C5	Phe285 CB, CG, CD1, CD2; Tyr613 CB, CD1, CE1, CG; Wat136; Wat138	10	C9	Asn282 OD1; Phe285 CD2, CE2; Ala610 CB; Gly612 C; Tyr613 CA, CB, N; Wat239	9
C6	Phe285 CB, CG, CD1, CD1, CE1; Wat136	6	C10	Phe285 CB, CG, CD1; His571 CE1, ND1; Tyr613 CD1, CE1, CZ; Wat248	9
C7	Phe285 CD1; Tyr613 CE1, CZ, OH; Wat236	5	O1	Phe285 CE2, CZ; Gly612 C,O; Tyr613 CA	5
C8	Glu382 CG; Tyr613 OH; Wat135; Wat236	4	O2	Phe285 CB, CG, CD2; Ala610 CB; Tyr613 CD1; Wat248	6
C9	Asn284 O; Glu382 CG; Wat135	3	N1	Phe285 CG, CD1, CD2, CE2,CZ; Tyr613 CA, CB, CG	8
C10	Asn284 O; Glu382 CD, CG; Wat135	4	N2	Phe285 CB, CG, CD1, CE1; Tyr613 CG, CD1, CE1, CZ	8
C11	Glu382 CD, CG, OE1; Phe 771 CZ; Wat135	5	N3	Phe285 CE1	1
C12	Glu382 CD, CG; Arg770 NH1; Phe771 CZ; Wat135	5	N4	Phe285 CD1, CE1; Tyr613 CE2, CZ; Wat47	5
C13	Tyr613 CZ, OH ; Wat135 ; Wat236	4			
O2	Phe285 CB, CG, CD2; Ala610 CB; Tyr613 CB, CG, CD1; Wat136; Wat138	9			
N1	Gly612 C, O; Wat234	3			
N2	Phe285 CD2, CE2, CZ; Tyr613 CA, CB, CG, N; Wat138	8			
N3	Phe285 CD1, CD2, CE1, CE2, CG, CZ; Tyr613 CB, CD1, CD2, CG; Wat138	11			
N4	Phe285 CE1, CZ; Wat236; Wat237	4			
N5	Phe285 CD1, CE1; Tyr613 CZ; Wat236	4			

*Figure 144. The network of van der Waals interactions of (**2**) (left) and (**1**) (right) at the inhibitor site of GPb.*

Inhibitor atom	Protein atom	No. of contacts	Inhibitor atom	Protein atom	No. of contacts
C1	Phe285 CD1, CE1; Tyr613 CG, CD2, CE2	5	C1	Phe285 CB, CG, CD1, CE1; Tyr613 CD1, CG	7
C2	Phe285 CD2, CE1, CE2, CZ; Tyr613 CB	5	C2	Phe285 CB, CG, CD2, CE2	4
C3	Phe285 CG, CD1, CD2, CE2; Tyr613 CB, CG	6	C3	Phe285 CB, CG, CD2; Ala610 CB; Wat203	5
C4	Phe285 CB, CG, CD1, CD2; Tyr613 CB, CG, CD1, CE1;	8	C4	Phe285 CD2, CE2	2
C5	Glu382 CG, OE1; Tyr613 OH	3	C5	Phe285 CD2, CZ; Gly612 C, O	4
C6	Glu382 OE1; Glu572 OE2; Tyr613 CZ, OH; Arg770 NH1	5	C6	Phe285 CG, CD1, CE1, CZ; Tyr613 CG, CD1, CD2	7
C7	Glu382 OE1; Tyr613 OH; Phe771 CE2, CZ	4	C7	Phe285 CD1, CE1; Tyr613 CG, CD1, CE1, CZ, CE2	7
C8	His571 ND1; Glu572 N; Tyr573 CD2, N; Tyr613 OH	5	C8	Phe285 CE1, CZ	2
O1	Phe285 CE2, CZ; Gly612 C, O	4	O1	Asn282 CA; Asp283N, O; Phe285 CB, CG; Ala610 CB	6
O2	His571 CA, CB, CG, ND1, C; Glu572 CA, CB, C, N; Tyr573 CA, CB, CD2, N, OH	14	O2	Ala610 CB; Gly612 CA, C; Tyr613 N	4
O3	His571 CB, CG, CE1, ND1; Tyr613 CE1, CZ, OH	7	O3	Asn282 OD1; Phe285 CE2, CD2; Glu287 CD, OE2	5
N1	Phe285 CD1, CE1, CZ; Tyr613 CD2	4	O4	Phe285 CD1; Tyr613 CD1, CE1, CZ, OH, CE2	6
N2	Asn282 OD1; Phe285 CG, CD2, CE2; Ala610 CB; Tyr613 CB	6	O5	Gly612 O; Tyr613 CA, CD2	3
N3	Phe285 CB, CG; Tyr613 CG, CD1, CE1; Wat84	6	O6	Phe285 CE1, CZ	2
N4	Phe285 CG, CD1, CE1; Tyr613 CG, CD1, CD2, CE1, CZ	8	N1	Asn282 CA; Phe285 CD2; Ala610 CB	3
S1	Tyr613 CE2	1	N2	Tyr613 CD2, CE2	2
			S1	Asn282 OD1	1

Figure 145. The network of van der Waal interactions of (8) (left) and (5) (right) at the inhibitor site of GPb.
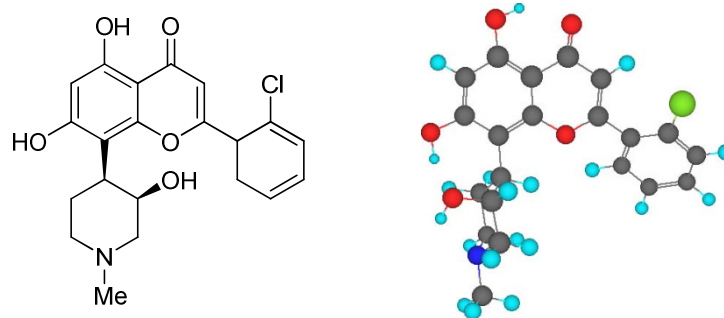
Flavopiridol

Figure 146. The structure of flavopiridol.

Flavopiridol is a very potent inhibitor of rabbit muscle GPb with an IC_{50} value in the range of 2.3 μM. It binds to the inhibitor site of GPb and is therefore used as a reference molecule in structural comparisons at the inhibitor site. It is also a cyclin dependent kinase inhibitor under clinical development for the treatment of chronic lymphocytic leukaemia. Upon binding to the inhibitor site of GPb, flavopiridol forms 2 direct hydrogen bonds and 95 van der Waals interactions. It also forms a network of 6 water mediated interactions. It interacts with Phe285 and increases the localization of the 280s loop in its inactive conformation. The key transition between the inactive T state and the active R state involves a movement of and disordering that allows Arg569 to enter the catalytic site in place of Asp283, an action which opens access of glycogen to the catalytic site [73].

Binding of Chembridge 0146922/5846914 (2) at the inhibitor site of GPb

Figure 147. 2Fo-Fc electron density map of (2) bound at the inhibitor site of GPb. The map is contoured at 1σ level and the refined model is displayed.

Inhibitor (**2**) was found to be at the inhibitor site of GPb. Upon binding, the compound forms 9 hydrogen bonds and 99 van der Waals interactions with the surrounding environment.
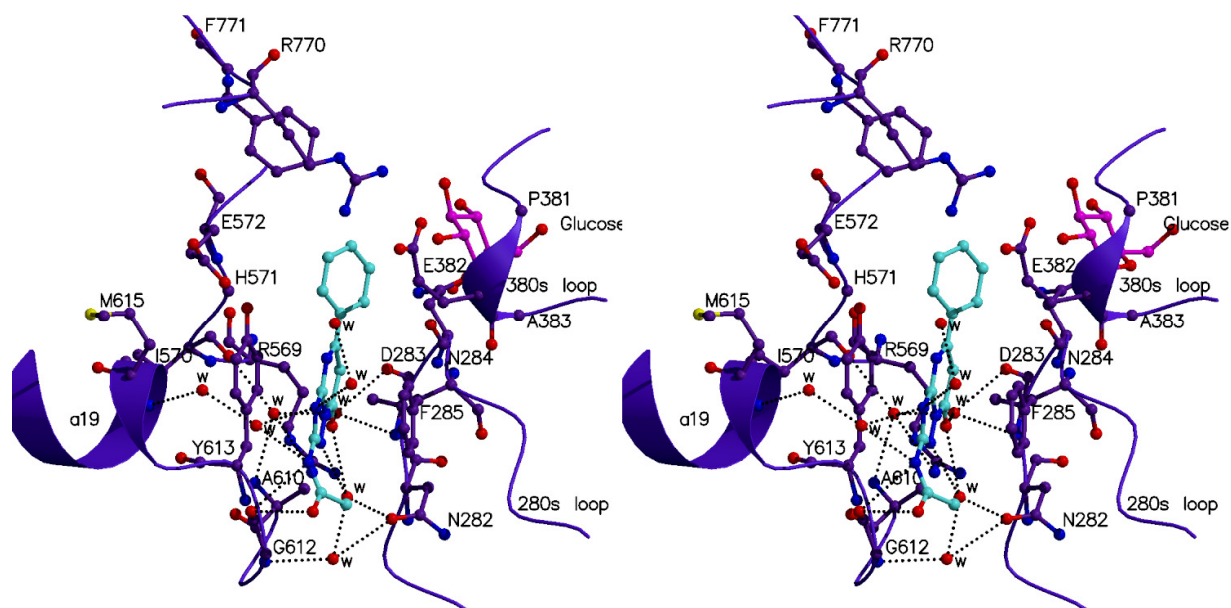
*Figure 148. Stereo diagram showing the network of interactions between (**2**) and the inhibitor site of GPb.*

Atoms O1 and N1 of the inhibitor are directly hydrogen bonded to the oxygen of Gly612 while N1 interacts with Met615 (helix *a19*) via water molecules Wat234 and Wat235. N2 forms hydrogen bonds with the nitrogen atom of Gly612 via Wat139 and with OD1 atom of Asn282 (280s loop) via Wat138 and Wat139. Binding of the inhibitor at the site is optimized further with interactions via water molecules between the O2 atom and residues of the 280s loop, Asn282 OD1 via Wat138 and Wat139 and Asp283 O and Asp283 N via Wat136. Hydrogen bonds are also formed via a broader network of water molecules by the O2 atom of the compound with residues Arg569 NH1, Ile570 O and Ala610 N via Wat136 and Wat137 as well as with Gly612 N via Wat138 and Wat139.

π-π stacking

A π-π stacking is a non-covalent interaction between organic compounds containing aromatic moieties. π-π interactions are caused by intermolecular overlapping of π-orbitals in π-conjugated systems, so they become stronger as the number of π-electrons increases [129].
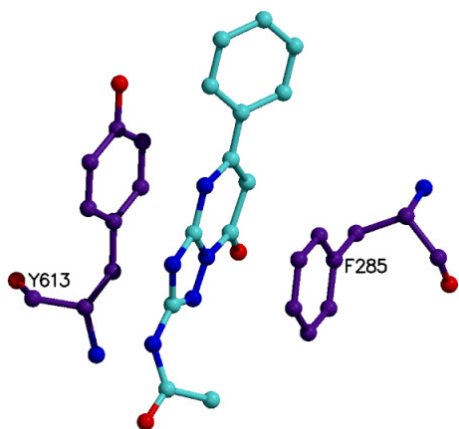
A very interesting feature of the binding of (**2**) is the fact that the inhibitor is stacked between the phenyl rings of Phe285 and Tyr613, similar to the interactions observed in previous studies [73].

Figure 149. The orientation of the inhibitor in between the aromatic rings of Phe285 and Tyr613.

These phenyl rings and the aromatic rings of the inhibitor form an extensive system of delocalised electrons, which stabilize the binding and the T state of the enzyme.

Structural comparison with flavopiridol
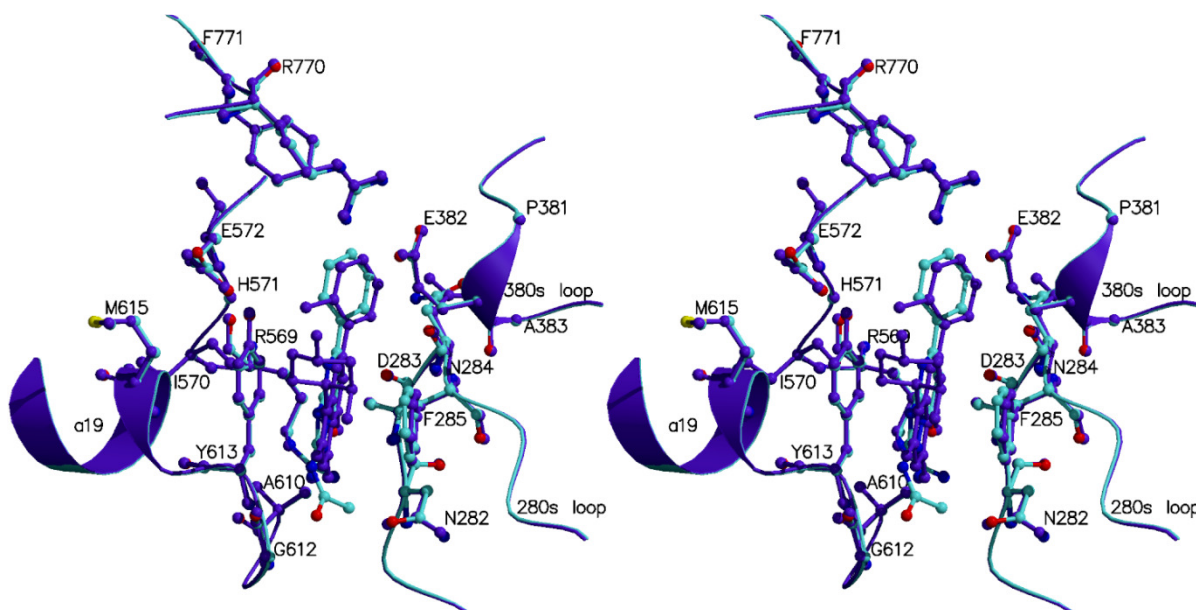
*Figure 150. A stereo diagram comparing Chembridge (**2**) binding to GPb (cyan) and flavopiridol binding to GPb (purple).*

In order to further elucidate the structural basis of inhibition, the mode of binding of (**2**) to GPb was compared to that of flavopiridol binding to GPb. The phenyl ring of the inhibitor adopts the same conformation as the chlorophenyl ring of flavopiridol in the adjacent pocket of the inhibitor site, while comparison shows only minor shifts within the range of 0.4-0.7 Å regarding the atoms of these two rings. Also, there are small shifts (0.4-0.5 Å) in

150

the side chain conformations of Phe285 and Leu380 in order to optimize the network of interactions with the phenyl ring. Wat138, Wat234, Wat236 and Wat237 are recruited into the Chembridge GPb-(**2**) complex, while Wat71 and Wat224 are displaced from this structure. Wat223 is shifted by 1.54 Å. The displacement and shifting of water molecules stabilize the binding of the inhibitor at the inhibitor site, by promoting interactions with Phe285, Tyr613, Met615 and Asn282.

Binding of Chembridge 084363/5786622 (1) at the inhibitor site of GPb

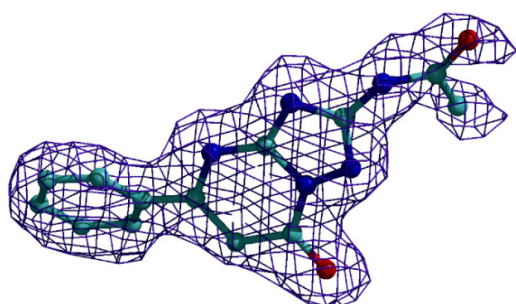(**1**) binds at the inhibitor site of GPb.
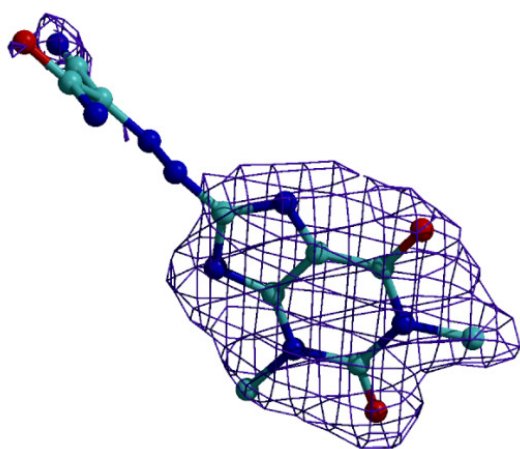
*Figure 151. 2Fo-Fc electron density map of (**1**) bound at the inhibitor site of GPb. The map is contoured at 1σ level and the refined model is displayed.*

The part of the molecule comprising the two heterocyclic rings is well defined by the electron density map but the rest of the molecule orientated towards the solvent, could not be clearly defined due to possibly multiple conformations. Upon binding the inhibitor forms 2 hydrogen bonds and 75 van der Waals interactions. As in the case of (**2**), (**1**) is also stacked between the phenyl rings of Phe285 and Tyr613. The inhibitor forms only two direct hydrogen bonds with Wat49 (via N7) and Wat248 (via O2). It is clear that the number of interactions formed at the inhibitor site of GPb, are far less than the extensive network observed at the catalytic site.
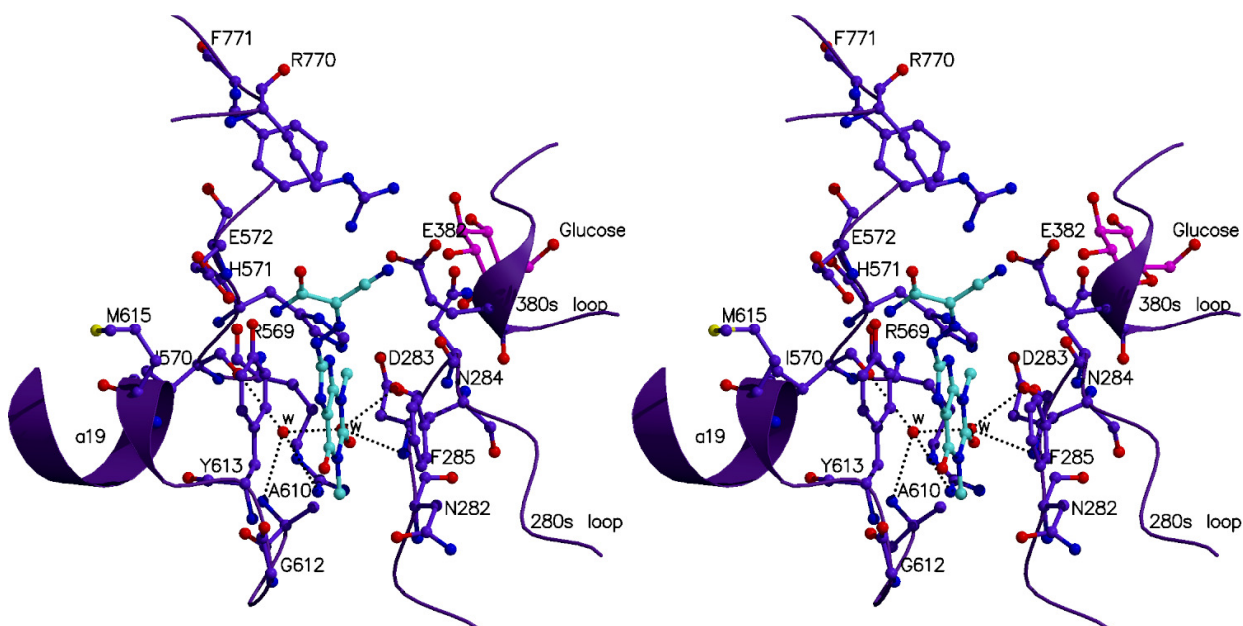
*Figure 152. Stereo diagram showing the network of interactions between (**1**) and residues of the inhibitor site of GPb.*

Structural comparison with flavopiridol

*Figure 153. Stereo diagram showing a comparison between the GPb-(**1**) complex (cyan) and the flavopiridol-GPb complex (purple).*

Compared to the much bulkier ligand, flavopiridol, upon binding (**1**) displaces Wat223 and Wat224. Wat47 and Wat49 are recruited into the GPb-(**1**) structure. In both cases the positioning of the side chain aromatic ring of Tyr613 is the same, however, in the case of

Phe285 the two phenyl rings shift by 56.82°. No conformational changes are observed in residues Asn282 and Glu612. The side chain of Arg770 is shifted by 107.16°, while the side chain of Glu382 changes orientation and shifts by 143.48°.

Binding of Specs AB-323/25048429 (8) at the inhibitor site of GPb
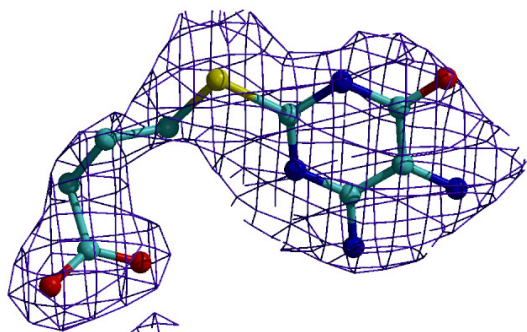
Figure 154. 2Fo-Fc electron density map of (8) bound at the inhibitor site of GPb. The map is contoured at 1σ level and the refined model is displayed.

The inhibitor is well defined at the inhibitor site by the electron density map. Upon binding it forms 3 hydrogen bonds and 87 van der Waals interactions.
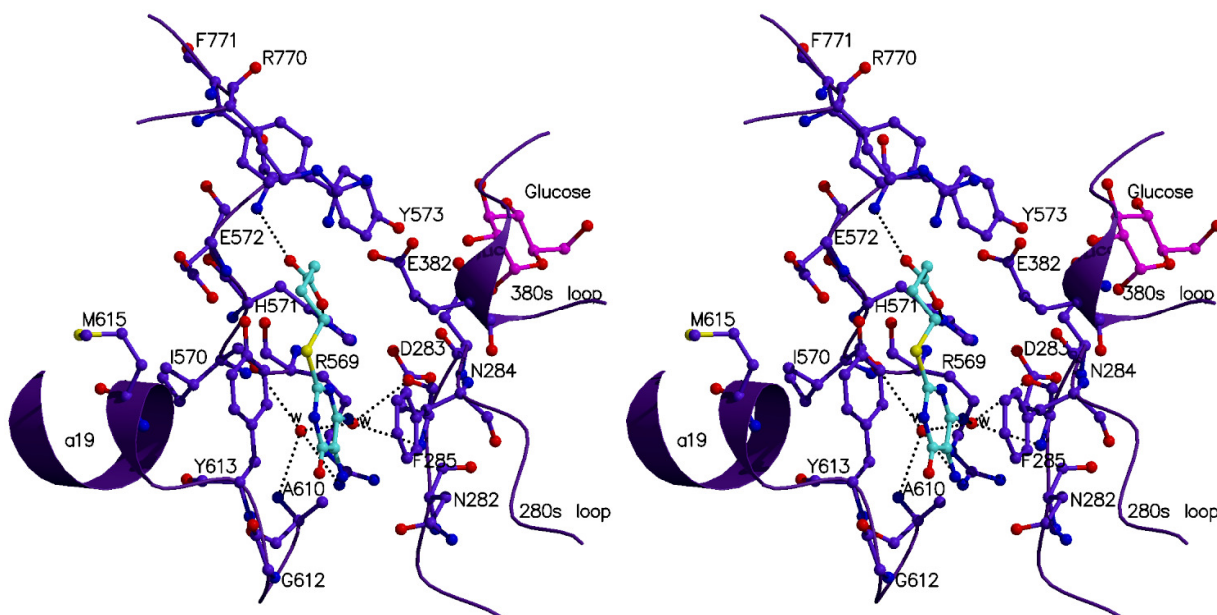
Figure 155. Stereo diagram showing the network of hydrogen bonds between (8) and residues of the inhibitor site of GPb.

Atoms O2 and O3 of the inhibitor form direct hydrogen bonds with Tyr573 N and His571 ND1 respectively. Atom N3 of the ligand interacts with Asp283 N and O of the 280s loop via Wat84. It is also hydrogen bonded with residues Arg569 NH1, Ile570 O and Ala610 N

via Wat85. The inhibitor is again stacked between the aromatic side chains of Phe285 and Tyr613.

Structural comparison with flavopiridol
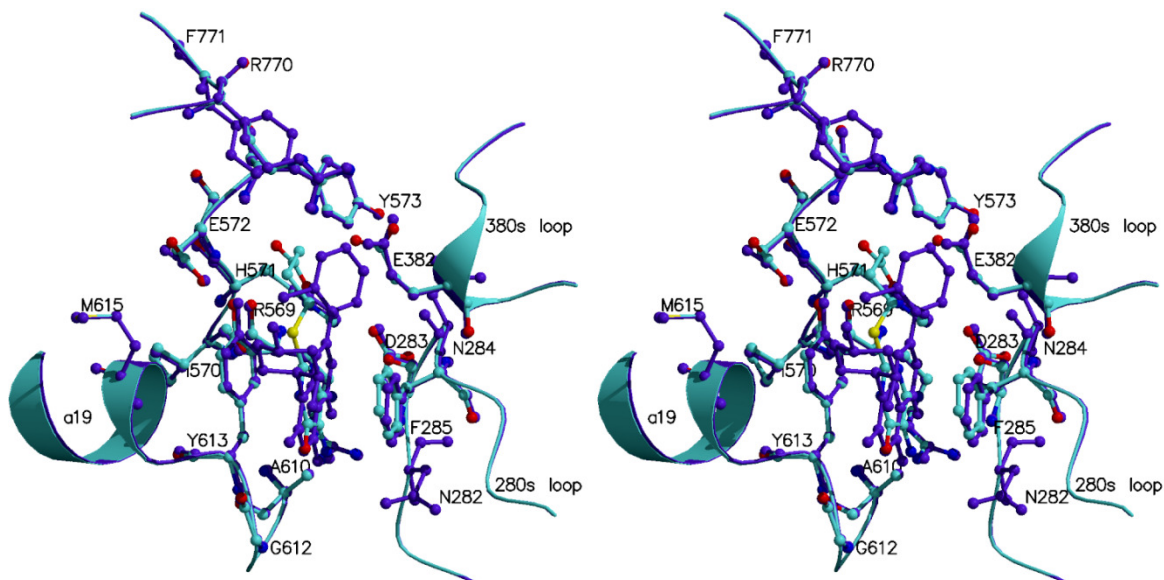
*Figure 156. A stereo diagram showing a comparison between the GPb-(**8**) complex (cyan) and the flavopiridol-GPb complex (purple).*

A comparison between the flavopiridol-GPb structure and the GPb-(**8**) structure revealed a number of conformational changes. In more detail, Wat72, Wat75 and Wat224 are displaced from the GPb-(**8**) structure. Wat198 is recruited while Wat73, Wat74, Wat220 and Wat225 undergo minor shifts in the range of 0.20-0.40 Å. The side chain of Asn284 is shifted by 101.54°. The side chain of Phe285 is shifted by 43.40°, while Tyr613 undergoes negligible changes. The side chain of Glu382 undergoes a major rotation of 83.84° [OE2-**CD-CG**-CB]. (**8**) has only one aromatic heterocyclic ring while the rest of its atoms comprise a S atom and a carboxyl group, with the latter adding more hydrophilic character to the molecule. This part of the compound occupies the neighbouring cavity formed by the more hydrophilic residues His571, Glu572 and Tyr573.

Binding of Chemdivision 0262/0300 (5) at the inhibitor site of GPb

Upon binding, (**5**) forms 3 hydrogen bonds and 71 van der Waals interactions.
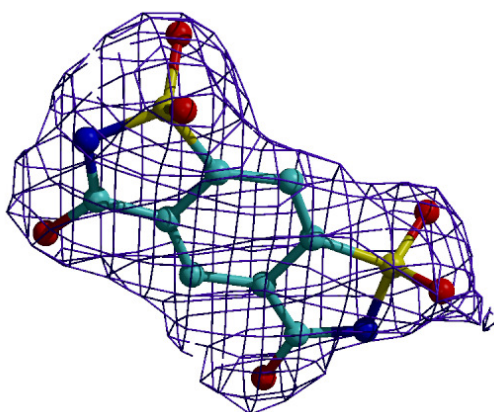
*Figure 157. 2Fo-Fc electron density map of (**5**)
bound at the inhibitor site of GPb and the
refined model is displayed.*

Atoms N1 and O2 of the inhibitor form direct hydrogen bonds with Asn282 OD1 and
Gly612 N respectively. Atom O1 is hydrogen bonded to Wat203, via which the inhibitor is
hydrogen bonded to Asp283 O of the 280s loop. Atom O1 interacts with Arg569 NH1,
Ile570 O and Ala610 N, via Wat203 and Wat204.
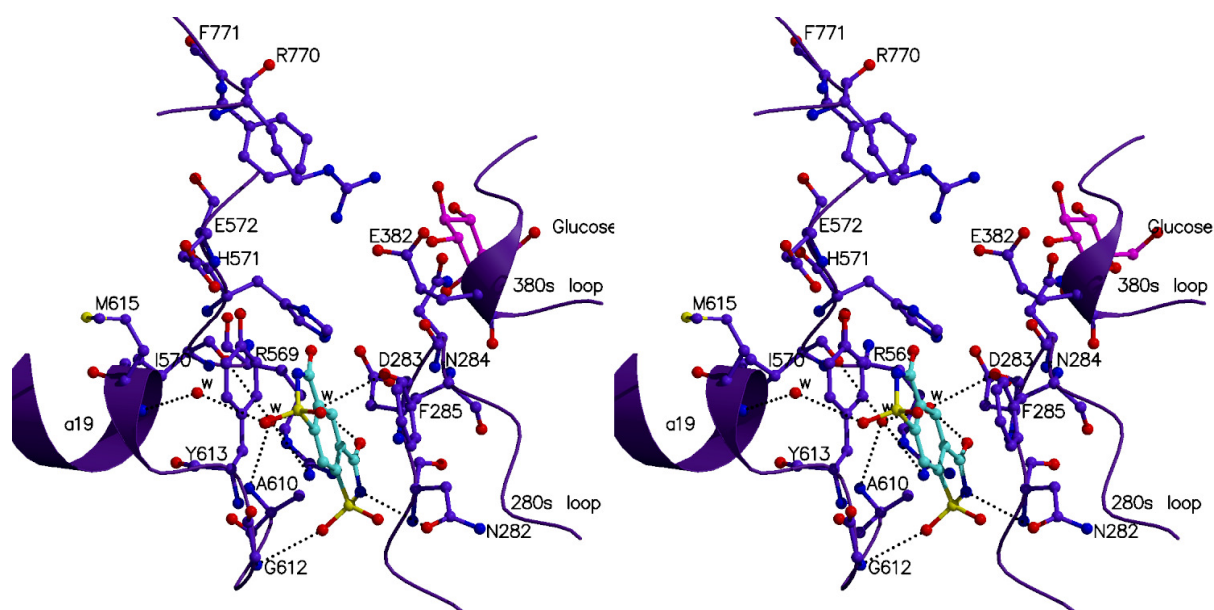
*Figure 158. Stereo diagram showing the network of hydrogen bond interactions between (**5**) and
residues of the inhibitor site of GPb.*

Structural comparison with flavopiridol

Comparing the GPb-(**5**) structure and the flavopiridol-GPb structure, profound
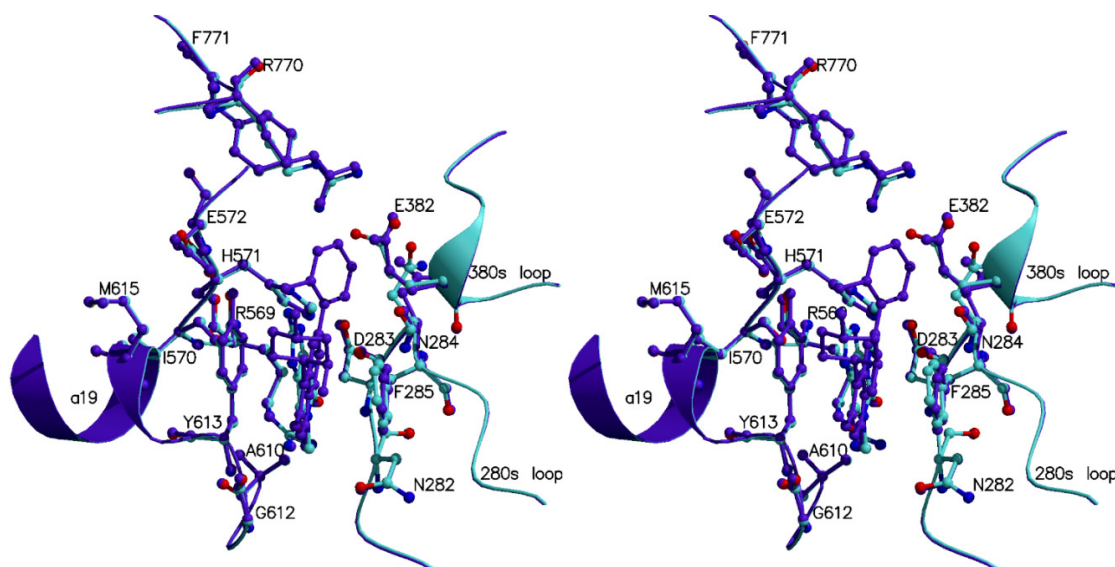conformational changes were observed.
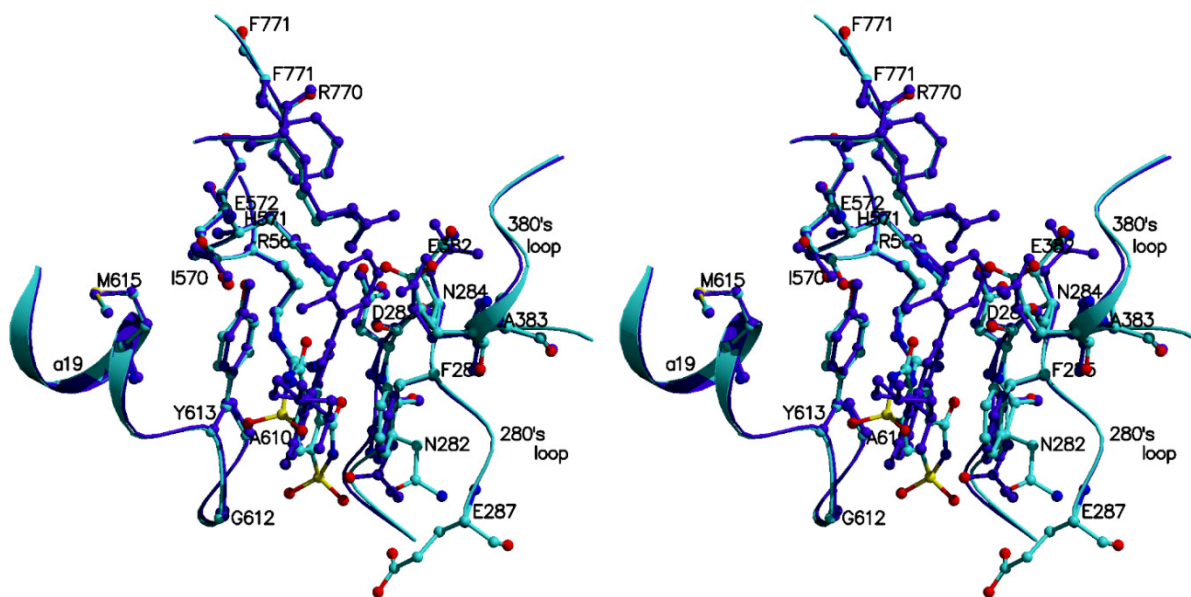
*Figure 159. Stereo diagram showing a comparison between the GPb-(**5**) complex (cyan) and the flavopiridol-GPb complex (purple).*

A different orientation of the two inhibitors at the hydrophobic area intercalating between the two aromatic rings of Phe285 and Tyr613 was observed. Upon binding of (**5**), Wat71, Wat72 and Wat224 are displaced while Wat206 is recruited into the new structure. Wat73, Wat74 and Wat225 undergo minor shifts in the range of 0.30-0.50 Å. The side chain phenyl ring of Phe285 is shifted by 125.21°, while the side chain aromatic ring of Tyr613 is shifted by 87.32°. The side chain of Asn282 is shifted by 1.61 Å. The side chain of Asn284 undergoes a major rearrangement and is rotated by 61.91° [ND2-**CG-CB**-CA]. The side chain of Glu382 also changes direction and is rotated by 73.21° [OE2-**CD-CG**-CB].

Conclusions

The detailed analysis of the four compounds that bound to GPb, as well as the structural comparison with flavopiridol, revealed interesting observations. All four compounds were comprised of aromatic rings that were stacked between the hydrophobic environment of Phe285 and Tyr613, forming π-π stacking interactions, a reoccurring feature at the inhibitor site. A prominent aspect of all these compounds was their interactions with the residues lining the 280s and 380s loops. This promoted the less active T state of the enzyme through localizing the closed position of these loops, thus blocking the access to the catalytic site and thus explaining their inhibitory effect. It is interesting to note that

none of these four inhibitors had a better inhibitory effect against GPb than flavopiridol. In addition, compounds (**3**) and (**4**) did not bind to GPb, despite their high affinity for the enzyme observed during the kinetic experiments, especially (**3**) that was the most potent inhibitor (IC$_{50}$: 6.5 ± 0.3 µM). This study demonstrated the contribution of virtual screening and docking, as an important tool in the design of lead compounds for structure based drug design. The combination of virtual screening, kinetic analysis and X-ray crystallography has proved to be an interesting and valuable pathway to the treatment of diabetes type 2.

3.8 The study of a new group of aromatic aldehyde/ketone 4-(β-D-glucopyranosyl) thiosemicarbazone compounds as inhibitors of GPb

Organic synthesis *(by Alia Cristina Tenchiu (Deleanu), Organic & Organometallic Chemistry Group, NHRF, Athens, Greece)*
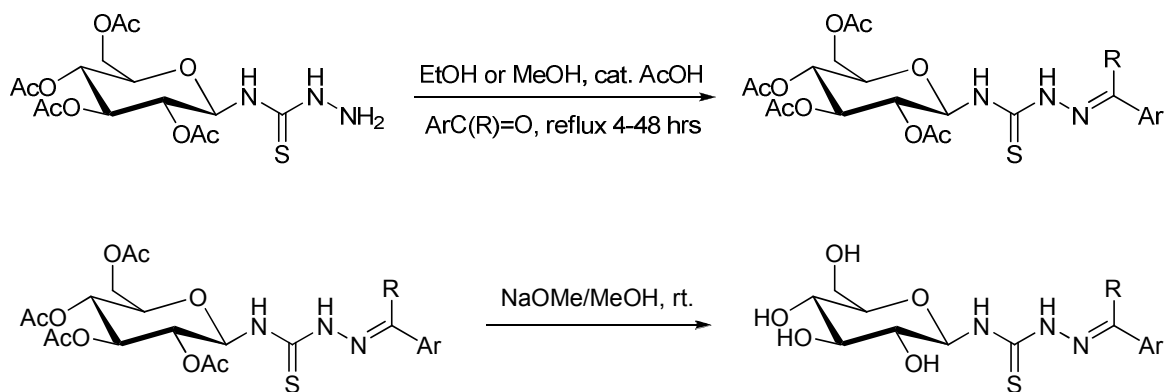
Figure 160. The organic synthesis scheme.

Originally, 26 compounds were synthesized with the various functional groups shown below.

(a)	**Ar = -C$_6$H$_4$-F-*p***	**R = H**	**(n)**	**Ar = -C$_6$H$_4$-OH-*p***	**R = H**
(b)	**Ar = -C$_6$H$_4$-Cl-*o***	**R = H**	(o)	Ar = -C$_6$H$_4$-OMe-*o*	R = H
(c)	**Ar = -C$_6$H$_4$-Cl-*m***	**R = H**	(p)	Ar = -C$_6$H$_4$-OMe-*m*	R = H
(d)	**Ar = -C$_6$H$_4$-Cl-*p***	**R = H**	**(q)**	**Ar = -C$_6$H$_4$-OMe-*p***	**R = H**
(e)	Ar = -C$_6$H$_4$-Br-*o*	R = H	**(r)**	**Ar = -C$_6$H$_4$-Me-*p***	**R = H**
(f)	**Ar = -C$_6$H$_4$-Br-*m***	**R = H**	(s)	Ar = -C$_6$H$_4$-^{t}Bu-*p*	R = H
(g)	**Ar = -C$_6$H$_4$-Br-*p***	**R = H**	(t)	Ar = 2-pyridyl	R = H
(h)	**Ar = -C$_6$H$_4$-CF$_3$-*p***	**R = H**	(u)	Ar = 3-pyridyl	R = H
(i)	**Ar = -C$_6$H$_4$-NO$_2$-*o***	**R = H**	**(v)**	**Ar = 4-pyridyl**	**R = H**
(j)	Ar = -C$_6$H$_4$-NO$_2$-*m*	R = H	(w)	Ar = ferrocenyl	R = H
(k)	**Ar = -C$_6$H$_4$-NO$_2$-*p***	**R = H**	(x)	Ar = β-naphthyl	R = H
(l)	**Ar = -C$_6$H$_4$-OH-*o***	**R = H**	(y)	Ar = -C$_6$H$_4$-OMe-*p*	R = Me
(m)	**Ar = -C$_6$H$_4$-OH-*m***	**R = H**	(z)	Ar = β-naphthyl	R = Me

However due to solubility problems, 15 out of these compounds (highlighted) were fully analyzed kinetically and X-ray crystallographically. The compounds were synthesized in a two-step reaction procedure. During the first step, the β-D-glucopyranosyl-thiosemicarbazide was dissolved in ethanol or methanol and was mixed with the corresponding aldehyde. The reaction mixture was refluxed for 4-48 hours and acetic acid was used as a catalyst. The acetyl group used for the protection of the glucopyranosyl

moiety was removed from the resulting β-D-glucopyranosyl-thiosemicarbazone during the second step, by standard methods using sodium methylate in methanol and stirred at room temperature. The yields fluctuated in the range of 30-90%, depending on the functional group of the aromatic part.

The core molecule
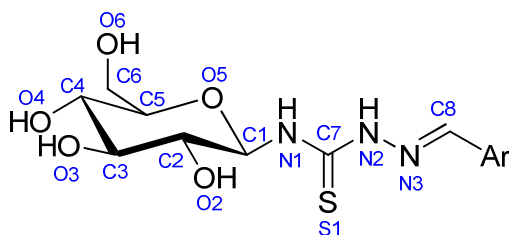
Figure 161. The chemical structure and numbering used for the core β-D-glucopyranosyl-thiosemicarbazone molecule.

All compounds were studied kinetically and crystallographically. They exhibited a variety of IC_{50} values depending on the functional groups and all compounds were found to bind at the catalytic site as well as the new allosteric site of GPb.

The bromide group
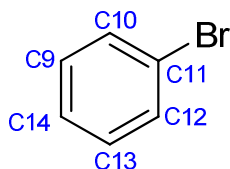
3-bromobenzaldehyde-4-(2,3,4,6-tetra-O-acetyl-β-D-glucopyranosyl) thiosemicarbazone (f)
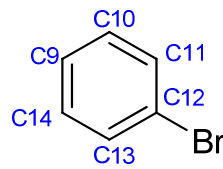
4-bromobenzaldehyde-4-(2,3,4,6-tetra-O-acetyl-β –D-glucopyranosyl) thiosemicarbazone (g)

IC_{50}: 50.4 ± 1.9 μM

IC_{50}: 93.2 ± 5.1 μM

Figure 162. The numbering and kinetic results of the bromide group at the meta and para position.

The root mean square deviation (r.m.s.d) for CA atoms of (**f**) was 0.19 Å for the catalytic site and 0.17 Å for the new allosteric site. The r.m.s.d for CA atoms of (**g**) was 0.23 Å for the catalytic site and 0.30 Å for the new allosteric site.

*Figure 163. 2Fo-Fc electron density maps of (**f**) bound at the catalytic site (left) and at the new allosteric site (right) of GPb. The maps are contoured at 1σ level and the refined models are displayed.*

*Figure 164. Representation of the molecular interactions of (**f**) when bound at the catalytic site (left) and at the new allosteric site of GPb (right).*

Kinetic studies revealed that (**f**) had the best inhibitory effect on GPb.

*Figure 165. Left: diagram showing the comparison between the GPb-(**f**) complex (cyan) and the GPb-N-acetyl-β-D-glucopyranosylamine complex (purple) in the vicinity of the catalytic site. Right: diagram showing the comparison of N´-benzoyl-β-D-glucopyranosyl urea-(**f**) complex in the vicinity of the new allosteric site. Purple: N´-benzoyl-β-D-glucopyranosyl urea-GPb complex; yellow: GPb-(**f**) complex (subunit 1); cyan: GPb-(**f**) complex (subunit 2).*

Upon binding to the catalytic site of GPb, (**f**) forms 10 hydrogen bonds and 87 van der Waals interactions. A structural comparison with *N*-acetyl-β-D-glucopyranosylamine revealed that the inhibitor shifts by ~ 60°. A number of water molecules are displaced (Wat108, Wat109, Wat110, Wat313, Wat356, Wat106, Wat355, Wat104, Wat105 and Wat314). The amino acids of the 280s loop undergo major conformational changes. The side chain of Asp283 is rotated by 79.40° [OD1-**CG-CB-**CA]. The side chain of Asn284 is rotated by 33.55° [OD1-**CG-CA-**CB]. The phenyl rings of the side chains of Phe285 and Phe286 undergo minor shifts.

Upon binding to the new allosteric site of GPb the inhibitor forms 7 hydrogen bonds and 34 van der Waals interactions. A structural comparison with *N*´-benzoyl-β-D-glucopyranosyl urea revealed minor conformational changes. The inhibitor is rotated by ~7° [O5-**C1-N1-**C7]. Water molecules are displaced (Wat239, Wat137, Wat136, Wat250 and Wat243), while Wat47 is shifted by 1.08 Å.

Inhibitor atom	Protein atom	Distance (Å)	Angle (°)	Inhibitor atom	Protein atom	Distance (Å)	Angle (°)
O2	Tyr573 OH	3.2	148.0	O2	Ala192 N	2.8	171.4
	Glu672 OE1	3.2	178.1	O3	Glu190 OE1	2.9	117.0
	Wat11	2.9	-	O4	Wat49	2.7	-
O3	Glu672 OE1	2.7	121.1	O5	Wat47	2.7	-
	Ser674 N	3.0	176.5	O6	Asn187 O	3.2	96.9
	Gly675 N	3.1	141.9		Wat48	2.7	-
O4	Gly675 N	2.7	129.2	N2	Thr38´ O	2.8	154.4
	Wat104	2.6	-				
O6	His377 ND1	2.7	152.4				
	Asn484 OD1	2.8	136.4				

*Figure 166. The network of hydrogen bond interactions between (**f**) and residues of the catalytic site of GPb (left) and residues of the new allosteric site of GPb (right).*

O2	…Wat11	…Thr671 O		O4	…Wat49	…Asn187 N
		…Ala673 N				…Glu190 OE1
		…Wat10	…Val379 N			
			…Thr671 O	O5	**…Wat47**	…Arg60 NH1
O4	**…Wat104**	…Thr676 OG1				…Arg60 NH2
		…PLP O3P				**…Wat48**

*Figure 167. The water hydrogen bond network of (**f**) at the catalytic site of GPb (left) and at the new allosteric site of GPb (right).*

Inhibitor atom	Protein atom	No. of contacts	Inhibitor atom	Protein atom	No. of contacts
C1	His377 O	1	C2	Glu190 O	1
C2	His377 O; Glu672 OE1; Wat11	3	C4	Wat49	1
C3	Glu672 OE1; Gly675 N; Wat104	3	C5	Wat47	1
C4	Asn484 OD1; Gly675 N; Wat104	3	C6	Wat47, Wat48	2
C5	Leu137 N; Gly135 C; Wat104	3	C8	Arg60 CZ, NH2; Thr38´ O	3
C6	Gly135 C, O; Leu136 N; Leu139 CD2; Asn484 OD1; His377 ND1	6	C9	Arg60 CZ, NE; Val40´ CG2	3
C7	Leu136 CB; Wat12	2	C10	Arg60 NE; Wat46; Phe37´ O; Val40´ CG2	4
C9	His341 CE1, NE2	2	C11	Val64 CG1; Wat46	2
C10	Glu88 OE1; His341 CE1, NE2; Wat52	4	C12	Wat46	1
C11	Glu88 OE1; Asn282 O; Arg292 NH2; His341 CE1, NE2; Wat52	6	C13	Wat46	1
C12	Asn282 ND2, O	2	O2	Ala192 CB	1
C13	Asn282 O	1	O3	Tyr226 CE2	1
C14	Asp283 O	1	O6	Asn187 C; Wat47	2
O2	His377 O; Wat12	2	BR1	Trp189 C, O; Glu190 N; Pro229 CD	4
O3	Glu672 C, CD, CG; Ala673 C, CA, CB; Ser674 C, CA; Gly675 CA; Wat11	10	N1	Glu190 O; Wat47	2
O4	Asn484 OD1; Ser674 C, CA, CB, N, OG; Gly675 C, CA, O; Thr676 N	10	N2	Arg60 NH2; Lys191 CD	2
O5	Leu136 CA, N; His377 CB, ND1	4	N3	Arg60 CZ, NH2; Thr38´ O	3
BR1	Asn282 ND2, O; Asn284 O; Phe285 C, O; Phe286 CA, CB, N	8			
N1	His377 CB, O; Wat12	3			
N2	Wat12	1			
N3	Wat12	1			

*Figure 168. The van der Waals network of interactions of (**f**) at the catalytic site of GPb (left) and at the new allosteric site of GPb (right).*

The chloride group

2-chlorobenzaldehyde-4-(2,3,4,6-tetra-O-acetyl-β-D-glucopyranosyl) thiosemicarbazone (*b*)	3-chlorobenzaldehyde-4-(2,3,4,6-tetra-O-acetyl-β-D-glucopyranosyl) thiosemicarbazone (*c*)	4-chlorobenzaldehyde-4-(2,3,4,6-tetra-O-acetyl-β-D-glucopyranosyl) thiosemicarbazone (*d*)
IC$_{50}$: 370 ± 9.7 μM	*IC$_{50}$: 23.2 ± 0.5 μM*	*IC$_{50}$: 28.3 ± 1.7 μM*

Figure 169. The numbering and kinetic results of the chloride group at the ortho, meta and para position.

The root mean square deviation (r.m.s.d) for CA atoms of (**b**) was 0.17 Å for the catalytic site and 0.23 Å for the new allosteric site. The r.m.s.d for CA atoms of (**c**) was 0.17 Å for the catalytic site and 0.23 Å for the new allosteric site. The r.m.s.d for CA atoms of (**d**) was 0.20 Å for the catalytic site and 0.19 Å for the new allosteric site.
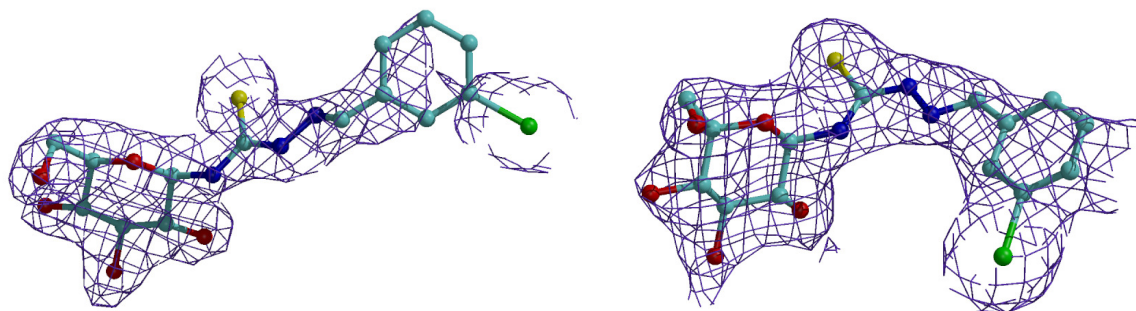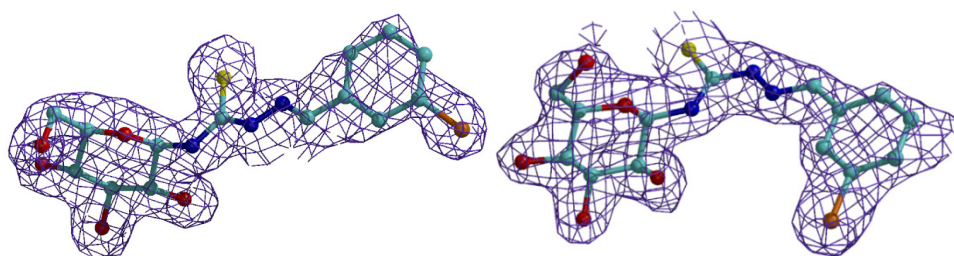

Figure 170. 2Fo-Fc electron density maps of (c) bound at the catalytic site (left) and at the new allosteric site (right) of GPb. The maps are contoured at 1σ level and the refined models are displayed.
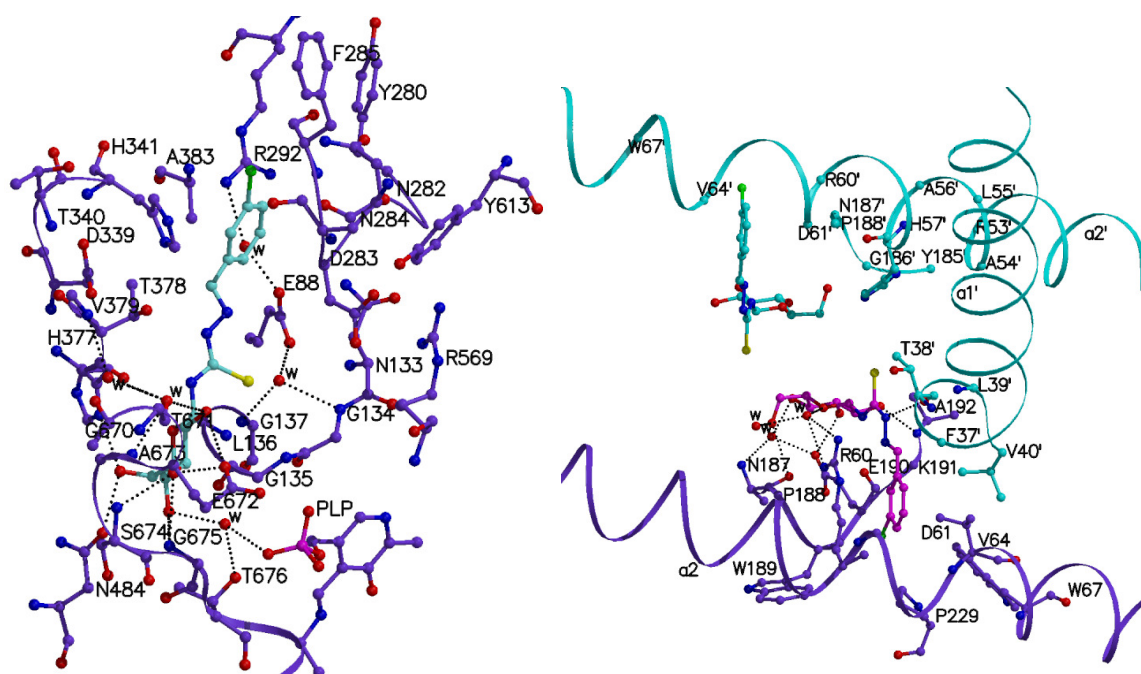
Kinetic studies revealed that (**c**) had the best inhibitory effect on GPb, although there was no significant difference with (**d**).
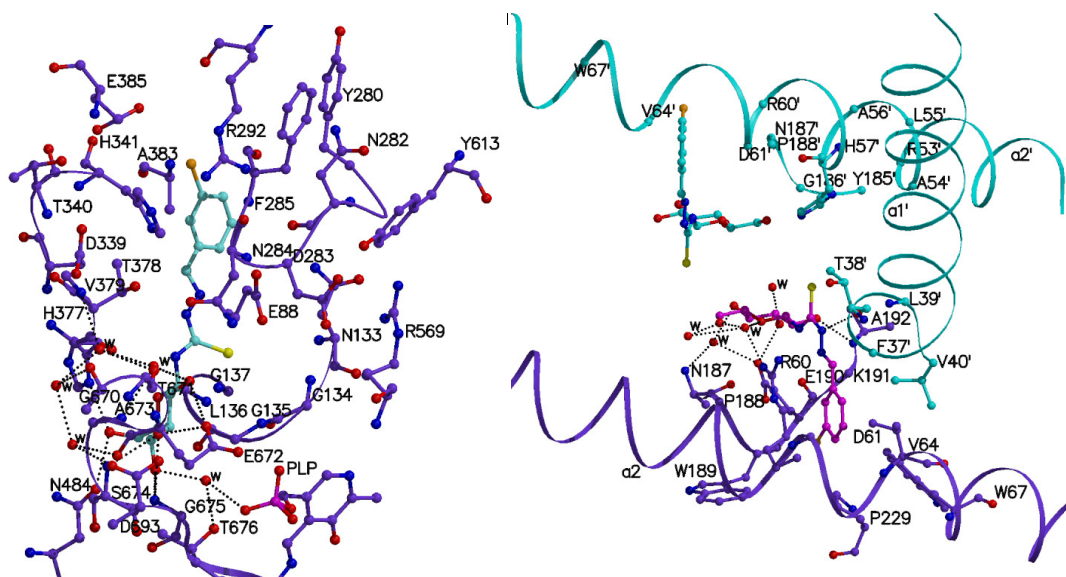
*Figure 171. Representation of the molecular interactions of (**c**) when bound at the catalytic site (left) and at the new allosteric site of GPb (right).*
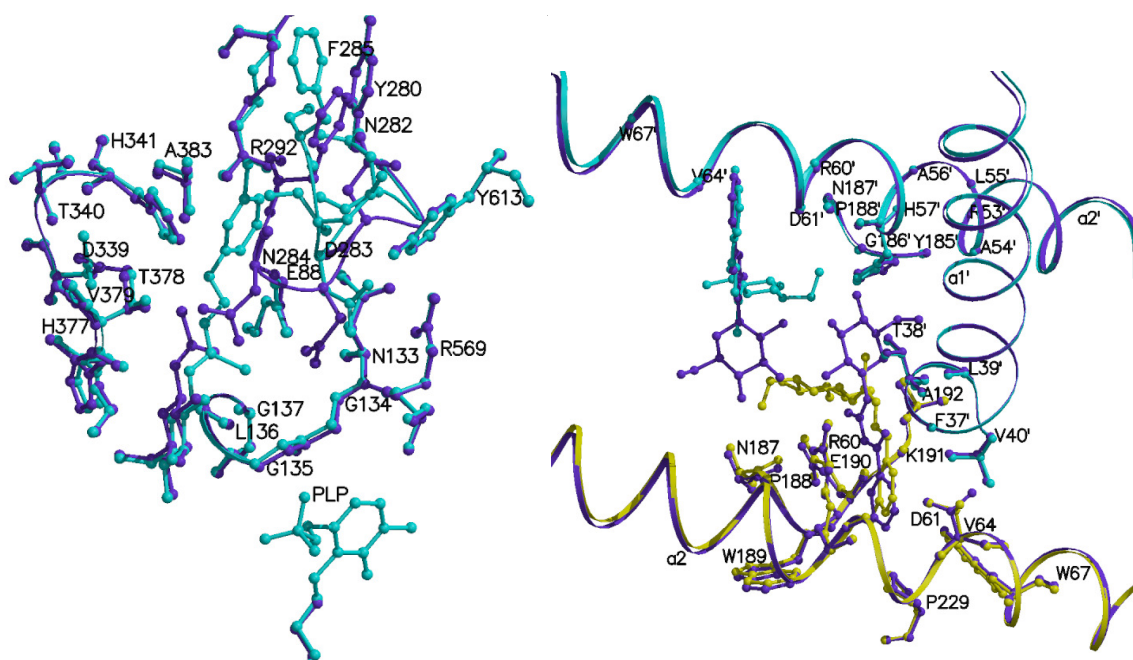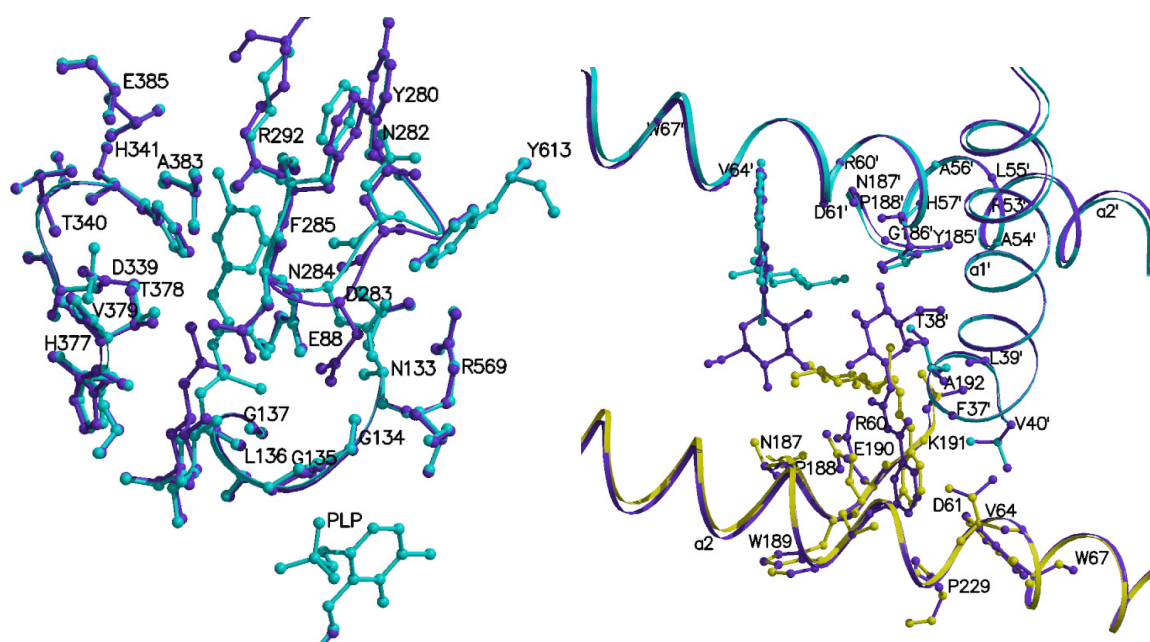

*Figure 172. Left: diagram showing the comparison between the GPb-(**c**) complex (cyan) and the GPb-N-acetyl-β-D-glucopyranosylamine complex (purple) in the vicinity of the catalytic site. Right: diagram showing the comparison of N´-benzoyl-β-D-glucopyranosyl urea-(**c**) complex in the vicinity of the new allosteric site. Purple: N´-benzoyl-β-D-glucopyranosyl urea-GPb complex; yellow: GPb-(**c**) complex (subunit 1); cyan: GPb-(**c**) (subunit 2).*

Upon binding to the catalytic site of GPb, (**c**) forms 10 hydrogen bonds and 99 van der Waals interactions with the surrounding protein environment and water molecules. A

structural comparison with *N*-acetyl-β-D-glucopyranosylamine revealed that the inhibitor shifts by ~ 54° upon binding to the enzyme. A number of water molecules are displaced (Wat355, Wat109, Wat110, Wat104 and Wat314), while Wat105 is shifted by ~ 1 Å. The main structural changes occur at the amino acids of the 280s loop. In more detail, Asn282 rotates by 9.83° [O-**C-CA-**CB], Asp283 rotates by 71.83° [OD1-**CG-CB-**CA] while Phe285 rotates by 6.64° [CG-**CB-CA-**C]. Asn284, Phe286 and His377 undergo negligible conformational changes. Upon binding to the new allosteric site, (**c**) forms 8 hydrogen bonds and 79 van der Waals interactions. A structural comparison with *N´*-benzoyl-β-D-glucopyranosyl urea revealed that the glucopyranose moiety shifts to opposite directions by ~ 93°. Water molecules were displaced (Wat136, Wat137, Wat239) while Wat328 shifted by ~ 1 Å. No other considerable conformational changes were noted.

Inhibitor atom	Protein atom	Distance (Å)	Angle (°)	Inhibitor atom	Protein atom	Distance (Å)	Angle (°)
O2	Tyr573 OH	3.1	149.6	O2	Ala192 N	2.8	177.0
	Glu672 OE1	3.1	173.6	O3	Glu190 OE1	2.8	123.2
	Wat242	3.0	-		Wat280	2.9	-
O3	Glu672 OE1	2.8	116.9	O4	Wat182	2.8	-
	Ser674 N	3.0	177.6	O5	Wat328	2.5	-
	Gly675 N	3.2	141.7	O6	Wat262	2.4	-
O4	Gly675 N	2.8	128.2		Wat328	2.0	-
	Wat114	2.6	-	N2	Thr38´ O	2.8	153.5
O6	His377 ND1	2.7	157.0				
	Asn484 OD1	2.8	136.4				

*Figure 173. The network of hydrogen bond interactions between (**c**) and residues of the catalytic site of GPb (left) and residues of the new allosteric site of GPb (right).*

Inhibitor atom	Protein atom	No. of contacts	Inhibitor atom	Protein atom	No. of contacts
C1	His377 O	1	C1	Glu190 O; Wat328	2
C2	His377 O; Glu672 OE1; Wat24	3	C2	Glu190 O; Ala192 N	2
C3	Glu672 OE1; Gly675 N; Wat114	3	C3	Glu190 OE1; Wat280	2
C4	Asn484 OD1; Gly675 N; Wat114	3	C4	Glu190 OE1; Wat182	2
C5	Gly135 C; Leu136 N; Wat114	3	C5	Wat328	1
C6	Gly135 C, O; Leu136 N; Leu139 CD2; His377 ND1; Asn484 OD1	6	C6	Wat262, Wat328	2
C7	Leu136 CB; Asn284 ND2, OD1	3	C7	Lys191 CD; Wat328; Thr38´ O	3
C8	Asn284 N	1	C8	Arg60 CZ, NH1, NH2, NE; Phe37´ O; Thr38´ O; Val40´ CG2	7
C9	Asn284 N; His341 CE1, NE2	3	C9	Arg60 CD, CZ, NH2, NE; Val40´ CG2	5
C10	Ala383 O; Asn284 N; His341 NE2	3	C10	Arg60 CZ, NE; Pro188 O; Glu190 O	4
C11	His341 NE2; Phe285 O	2	C11	Arg60 CG, NE; Trp67 CZ3	3
C12	Asn282 O; Phe285 O; His341 NE2; Wat89	4	C12	Arg60 CG; Trp67 CZ3	2
C13	Asn282 O; His341 CE1, NE2; Wat183	4	C13	Arg60 CD, CG, O; Val64 CG1; Val40´ CG2	5
C14	Asn282 O; Asp283 CA; Asn284 N; His341 CE1, NE2	5	C14	Arg60 CD, CG, NE; Val64 CG1; Wat265	5
O2	Asn284 CG, ND2, OD1; His377 O	4	O2	Glu190 O; Lys191 C, CA, CD; Ala192 CA, CB	6
O3	Glu672 C, CD, CG; Ala673 C, CA, CB; Ser674 CA, C; Wat242	9	O3	Glu190 CD, CG; Tyr226 CD2, CE2; Wat182	5
O4	Asn484 OD1; Ser674 CA, CB, C; Gly675 C, CA, O; Thr676 CG2, N	9	O4	Wat280	1
CL1	Phe285 C, O; Phe286 C, CA, CB; Ala383 O; Wat89	7	CL1	Pro188 O; Trp189 CA, C, O; Glu190 C, CA, N; Pro229 CD, CG	9
N1	Asn284 ND2, OD1; His377 CB, O	4	N1	Arg60 NH1, Glu190 O, Lys191 CD; Wat328 OH2	4
N2	Leu136 CD1; Asn284 CG, ND2	3	N2	Arg60 NH1; Lys191 CD; Thr38´ C	3
N3	Asn284 CG, ND2, OD1	3	N3	Arg60 CZ, NH1, NH2; Lys191 CD; Thr38´ O	5
S1	Gly135 N; Leu136 CB, N; Asn284 ND2; Wat72	5	S1	Thr38´ O	1

*Figure 174. The van der Waals network of interactions of (**c**) at the catalytic site of GPb (left) and at the new allosteric site of GPb (right).*
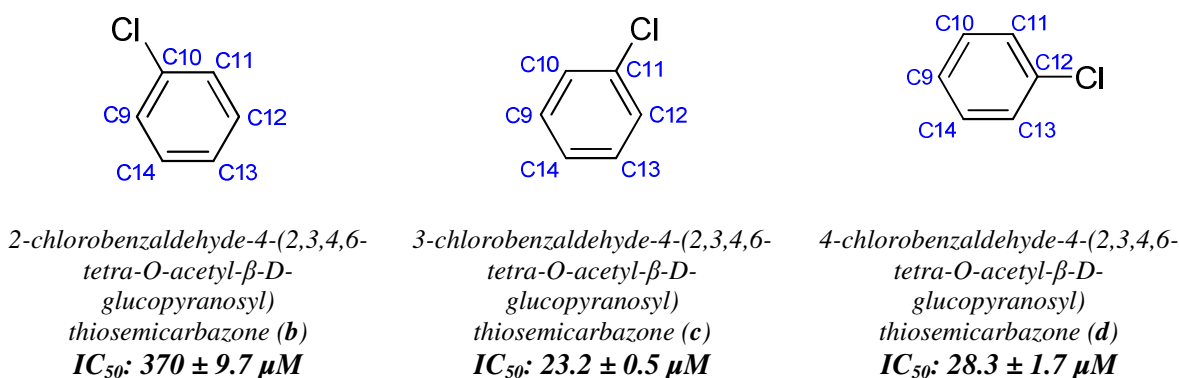
O2	…Wat242	…Thr671 O			
		…Ala673 N			
		…Wat88	…Val379 N		
			…Thr671 O		
			….Wat270	…Gly670 O	
				…Wat92	…Glu672 O
					…Asp693 OD2
O4	**…Wat114**	…Thr676 OG1			
		…PLP O3P			

O3	**…Wat280**	…Tyr226 OH
O4	**…Wat182**	…Asn187 N
		…Glu190 OE1
O5	**…Wat328**	…Arg60 NH1
		…Wat262
O6	**…Wat328**	… Arg60 NH1
		… Wat262

*Figure 175. The water hydrogen bond network of (**c**) at the catalytic site of GPb (top) and at the new allosteric site of GPb (bottom).*

The hydroxyl group
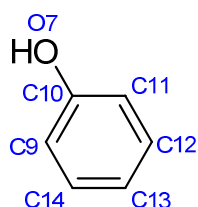
2-hydroxybenzaldehyde-4-(2,3,4,6-tetra-O-acetyl-β-D-glucopyranosyl) thiosemicarbazone (**l**)
IC$_{50}$: 26.6 ± 3.3 μM
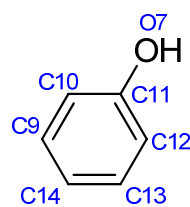
3-hydroxybenzaldehyde-4-(2,3,4,6-tetra-O-acetyl-β-D-glucopyranosyl) thiosemicarbazone (**m**)
IC$_{50}$: 180.0 ± 7.8 μM
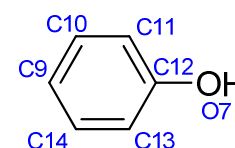
4-hydroxybenzaldehyde-4-(2,3,4,6-tetra-O-acetyl-β-D-glucopyranosyl) thiosemicarbazone (**n**)
IC$_{50}$: 340.5 ± 21.7 μM

Figure 176. The numbering and kinetic results of the hydroxyl group at the ortho, meta and para position.

The root mean square deviation (r.m.s.d) for CA atoms of (**l**) was 0.24 Å for the catalytic site while no binding occurred at the new allosteric site of GPb. The r.m.s.d for CA atoms of (**m**) was 0.20 Å for the catalytic site and 0.35 Å for the new allosteric site. The r.m.s.d for CA atoms of (**n**) was 0.17 Å for the catalytic site and 0.21 Å for the new allosteric site.

*Figure 177. 2Fo-Fc electron density maps of (**l**) bound at the catalytic site of GPb. The map is contoured at 1σ level and the refined model is displayed.*

Kinetic studies revealed that (**l**) had the best inhibitory effect on GPb.
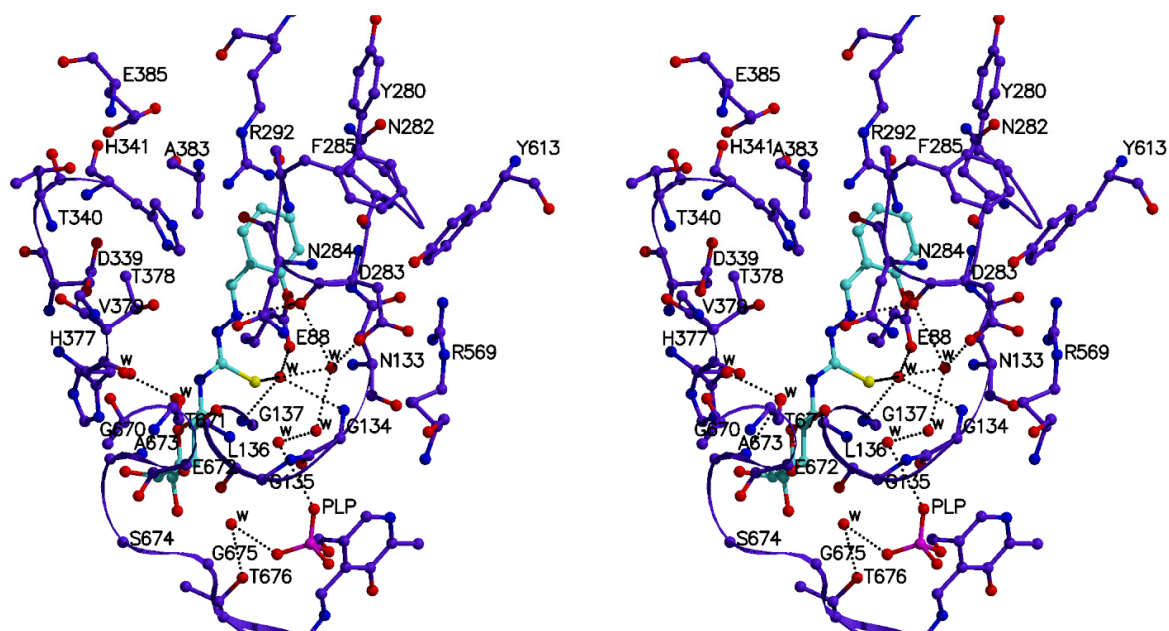
*Figure 178. Stereo diagram showing the network of interactions between (**l**) and residues of the catalytic site of GPb.*

*Figure 179. Stereo diagram showing the comparison between the GPb-(**l**) complex (cyan) and the GPb-N-acetyl-β-D-glucopyranosylamine complex (purple) in the vicinity of the catalytic site.*

Upon binding to the catalytic site of GPb, (**l**) forms 15 hydrogen bonds and 109 van der Waals interactions. A structural comparison with *N*-acetyl-β-D-glucopyranosylamine revealed profound conformational changes. The inhibitor shifts by ~ 119°. Water molecules were displaced (Wat105, Wat106, Wat355, Wat110 and Wat356) while Wat236 and Wat250 were shifted by ~ 1 Å. Asn282 was rotated by 78.27° [ND2-**CG-CB-**CA] while the backbone oxygen was shifted by 3.82 Å. Asp283 was rotated by 58.64° [OD1-**CG-CB-**CA] and in this case also the backbone oxygen was shifted by 2.91 Å. Asn284 undergoes a profound change of orientation and is rotated by 48.39° [OD1-**CG-CA-**CB]. The phenyl ring of the side chain of Phe285 changed direction and the whole amino acid was rotated by 27.40° [CG-**CB-CA-**C]. Phe286, His377, Arg292 and Glu385 undergo less profound conformational changes. It is interesting to note that the aromatic part of the inhibitor is positioned into the catalytic site, in a way that doesn't destabilize the amino acids of the adjacent 280s loop. It can therefore be assumed that the orientation it acquires is energetically favourable for the stabilization of the T-state of the enzyme.

Inhibitor atom	Protein atom	Distance (Å)	Angle (°)
O2	Tyr573 OH	3.1	146.2
	Glu672 OE1	3.1	176.9
	Wat236	3.0	-
	Wat239	3.1	-
O3	Glu672 OE1	2.7	118.5
	Ser674 N	3.1	170.2
	Gly675 N	3.2	140.8
O4	Gly675 N	2.7	130.9
	Wat110	2.6	-
O6	His377 ND1	2.7	158.5
	Asn484 OD1	2.8	137.2
O7	Asp283 O	2.6	117.5
N3	Asp283 O	2.9	146.3
S1	Wat70	3.3	-
	Wat240	3.3	-

*Figure 180. The network of hydrogen bond interactions between (**l**) and residues of the catalytic site of GPb.*

O2	**…Wat236**	…Lys574 NZ		
		…PLP O2P		
		…Wat52	…Gly135 N	
			…Wat55	…Arg569 N
				…PLP O2P
	…Wat239	…Thr671 O		
		…Ala673 N		
		…Wat86	…Val379 N	
			…Thr671 O	
O4	**…Wat110**	…Thr676 OG1		
		…PLP O3P		
S1	**…Wat70**	…Glu88 OE2		
		…Gly134 N		
		…Gly137 N		
	…Wat240	…Asp283 O		
		…Asp283 OD2		
		....Wat52		

*Figure 181. The water hydrogen bond network of (**l**) at the catalytic site of GPb.*

Inhibit atom	Protein atom	No. of contacts
C1	His377 O; Wat236	2
C2	His377 O; Glu672 OE1; Wat236, Wat239	4
C3	Glu672 OE1; Gly675 N; Wat110, Wat236	4
C4	Gly675 N; Wat110	2
C5	Gly135 C; Leu136 N; Wat110	5
C6	Gly135 C, O; Leu136 N; His377 ND1; Asn484 OD1; Wat110	6
C7	Leu136 CB; Asn284 ND2	2
C8	Asn283 O; Asn284 CA, O	3
C9	Asp283 C, O; Asn284 CA, O	4
C10	Glu88 OE1; Asp283 C, CA, N, O	5
C11	Glu88 OE1; Asn133 ND2; Asp283 C, CA, N, O; Wat181	7
C12	Asn282 CB; Asp283 N; Wat181	3
C13	Phe285 O; Arg292 NH2; Wat250	3
C14	Asn284 O; His341 CE1; NE2; Wat250	4
O2	Asn284 OD1; His377 O	2
O3	Glu672 C, CD, CG; Ala673 C, CA, CB, N; Ser674 C, CA; Gly675 CA; Wat239	11
O4	Asn484 OD1; Ser674 C, CA, CB, N; Gly675 CA, C, O; Thr676 N	9
O5	Leu136 CA, N; His377 CB, ND1	4
O6	Leu139 CD2; His377 CG, CE1; Asn484 CG; Val455 CB, CG1, CG2	7
O7	Glu88 OE1; Asn133 CB, CG, ND2; Asp283 C, CA; Wat70, Wat240	8
N1	His377 CB, O	2
N2	Asp283 O; Asn CG, ND2, OD1	4
N3	Asn284 ND2	1
S1	Gly135 N; Leu136 CB, N; Asp283 O; Wat52, Wat70, Wat240	7

Figure 182. The van der Waals network of interactions of (l) at the catalytic site of GPb.

The methoxy & methyl groups
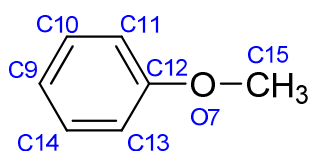
4-methoxybenzaldehyde-4-(2,3,4,6-tetra-O-acetyl-β-D-glucopyranosyl) thiosemicarbazone (q)
IC_{50}: 406.5 ± 40.6 μM
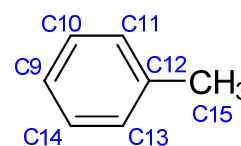
4-methylbenzaldehyde-4-(2,3,4,6-tetra-O-acetyl-β-D-glucopyranosyl) thiosemicarbazone (r)
IC_{50}: 192.4 ± 5.8 μM

Figure 183. The numbering and kinetic results of the methoxy & methyl groups at the para position.

The root mean square deviation (r.m.s.d) for CA atoms of (**q**) was 0.20 Å for the catalytic site and 0.23 Å for the new allosteric site. The r.m.s.d for CA atoms of (**r**) was 0.31 Å for

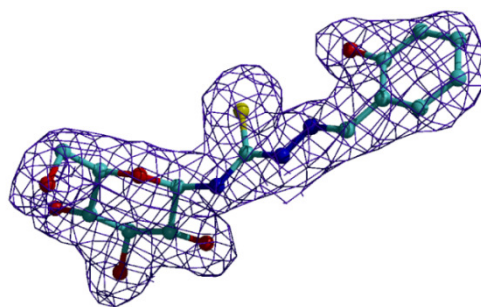the catalytic site and 0.27 Å for the new allosteric site. Kinetic studies revealed that (**r**) had the best inhibitory effect on GPb.
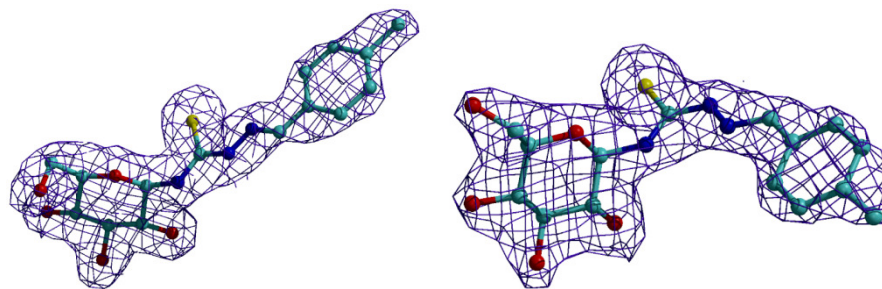
*Figure 184. 2Fo-Fc electron density maps of (**r**) bound at the catalytic site of GPb (left) and at the new allosteric site of GPb. The maps are contoured at 1σ level and the refined models are displayed.*

Upon binding to the catalytic site of GPb, (**r**) forms 18 hydrogen bonds and 101 van der Waals interactions. A structural comparison with *N*-acetyl-β-D-glucopyranosylamine revealed a rotation of the inhibitor by 13.51° [O5-**C1-N1**-C7]. Water molecules were displaced (Wat105, Wat106, Wat355, Wat109 and Wat110) while Wat34 was shifted by ~ 1 Å. The backbone oxygen of Asn282 was shifted by 3.41 Å while the whole amino acid was rotated by 80.66° [ND2-**CG-CB**-CA].
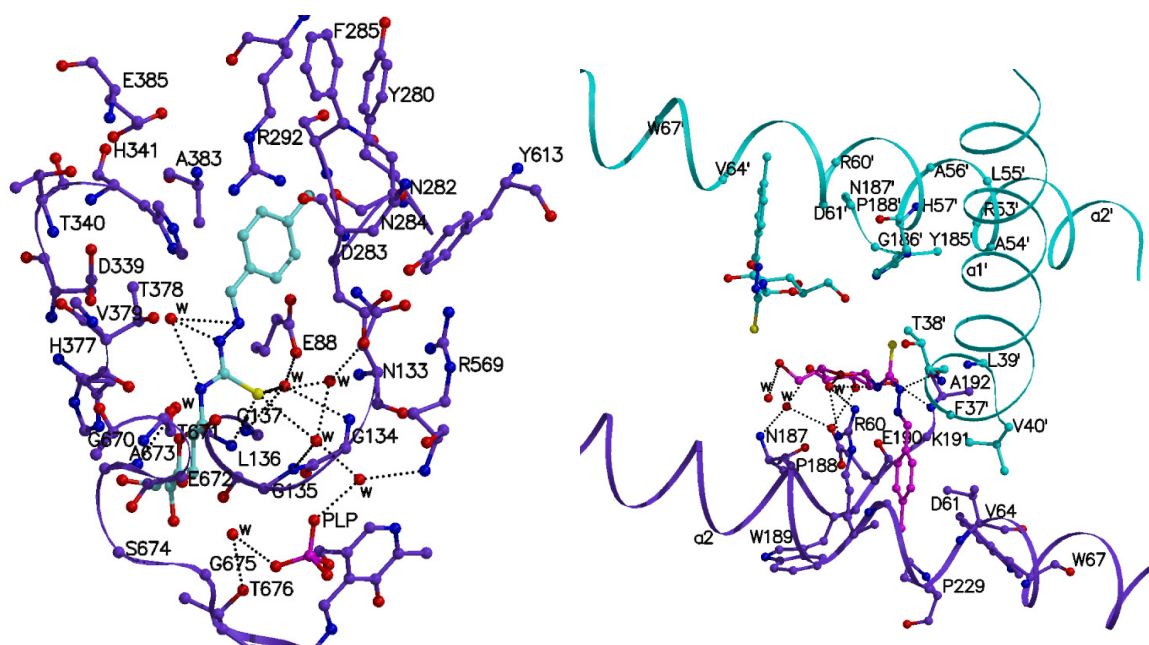
*Figure 185. Representation of the molecular interactions of (**r**) when bound at the catalytic site (left) and at the new allosteric site of GPb (right).*
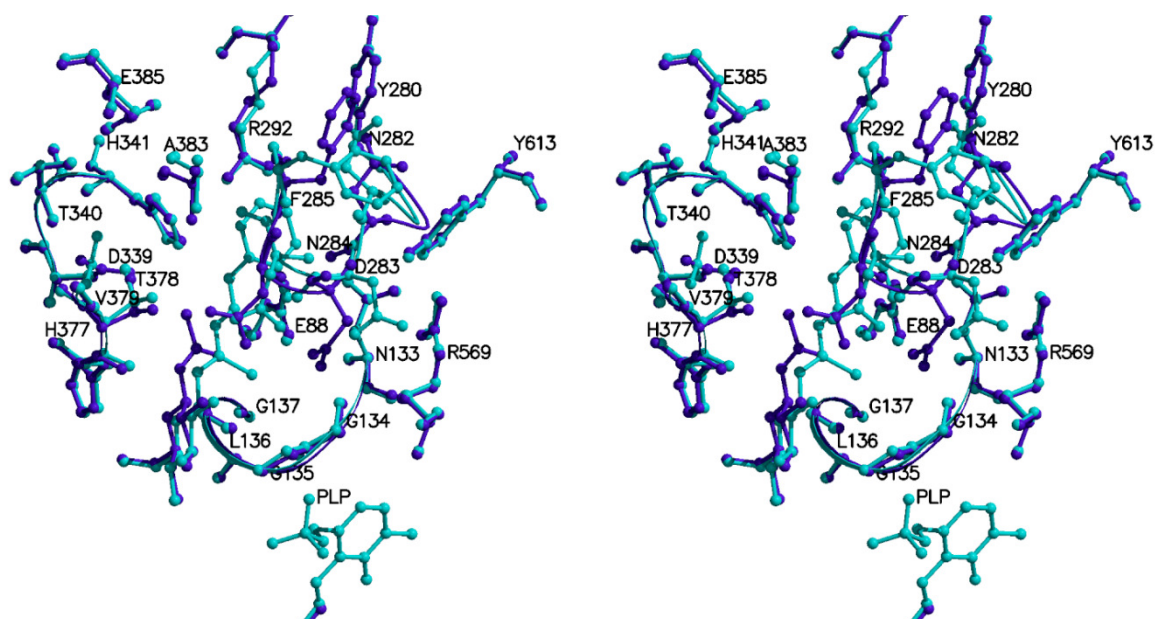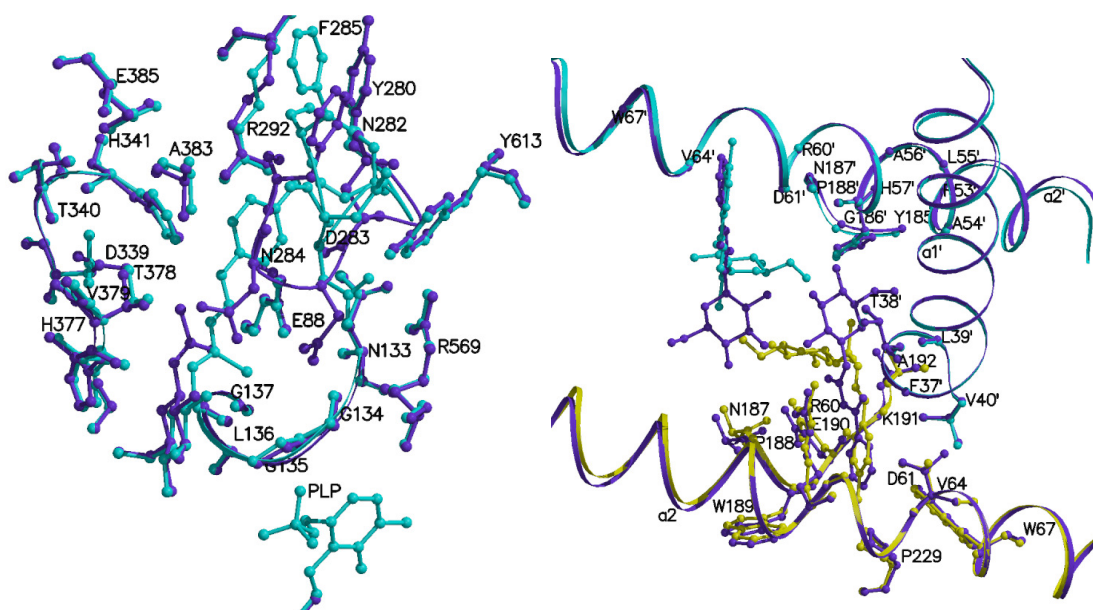
*Figure 186. Left: diagram showing the comparison between the GPb-(**r**) complex (cyan) and the GPb-N-acetyl-β-D-glucopyranosylamine complex (purple) in the vicinity of the catalytic site. Right: diagram showing the comparison of N´-benzoyl-β-D-glucopyranosyl urea-(**r**) complex in the vicinity of the new allosteric site. Purple: N´-benzoyl-β-D-glucopyranosyl urea-GPb complex; yellow: GPb-(**r**) complex (subunit 1); cyan: GPb-(**r**) complex (subunit 2).*

A significant conformational change was observed for Asn284. The amino acid changes entirely direction. The CA atom shifted by 3.90 Å, the C atom shifted by 2.94 Å, the N atom shifted by 3.01 Å and the O atom by 2.28 Å. Phe285 and Phe286 undergo less profound changes. Upon binding to the new allosteric site of GPb, (**r**) forms 7 hydrogen bonds and 81 van der Waals interactions. A structural comparison with *N´*-benzoyl-β-D-glucopyranosyl urea revealed that upon binding to the enzyme the inhibitor rotates by 10.48° around [O5**-C1-N1-**C7]. Water molecules are displaced (Wat136, Wat239 and Wat243) while Wat203 and Wat207 are shifted by ~ 1 Å. No other profound conformational changes were noted in the protein environment.

Inhibitor atom	Protein atom	Distance (Å)	Angle (°)	Inhibitor atom	Protein atom	Distance (Å)	Angle (°)
O2	Tyr573 OH	3.1	148.5	O2	Ala192 N	2.7	175.5
	Glu672 OE1	3.2	178.7	O3	Glu190 OE1	2.9	117.1
	Wat169	3.0	-	O4	Wat201	2.7	-
	Wat170	2.8	-	O5	Wat203	2.8	-
O3	Glu672 OE1	2.7	120.2	O6	Wat204	3.3	-
	Ser674 N	3.1	176.3	N1	Wat203	3.3	-
	Gly675 N	3.1	143.4	N2	Thr38´ O	2.7	154.8
O4	Gly675 N	2.7	128.6				
	Wat106	2.7	-				
O6	His377 ND1	2.6	161.7				
	Asn484 OD1	2.7	138.2				
N1	Wat36	3.2	-				
N2	Wat36	2.5	-				
N3	Wat36	3.2	-				
S1	Leu136 N	3.2	162.5				
	Wat26	3.3	-				
	Wat27	3.0	-				
	Wat28	3.3	-				

*Figure 187. The network of hydrogen bond interactions between (**r**) and residues of the catalytic site of GPb (left) and residues of the new allosteric site of GPb (right).*

O2	…Wat169	…Thr671 O		
		…Ala673 N		
	…Wat170	…Tyr573 OH		
		…Lys574 NZ		
		…Wat26	…Gly135 N	
			…Wat25	...Arg569 N
				…PLP O2P
			…Wat27	…Asp283 OD2
			…Wat170	…Tyr573 OH
				...Lys574 NZ
O4	…Wat106	…Thr676 OG1		
		…PLP O3P		
N1/N2/N3	…Wat36			
S1	...Wat26			
	…Wat27			
	…Wat28	…Glu88 OE2		
		...Gly134 N		
		…Gly137 N		

O4	…Wat201	…Asn187 N
		…Glu190 OE1
O5/N1	…Wat203	…Arg60 NH1
		…Arg60 NH2
O6	…Wat204	No interactions

*Figure 188. The water hydrogen bond network of (**r**) at the catalytic site (top) and at the new allosteric site of GPb (bottom).*

Inhibitor atom	Protein atom	No. of contacts	Inhibitor atom	Protein atom	No. of contacts
C1	His377 O; Wat170	2	C1	Glu190 O; Wat52	2
C2	His377 O; Glu672 OE1; Wat169, Wat170	4	C2	Glu190 O; Ala192 N	2
C3	Glu672 OE1; Gly675 N; Wat106, Wat170	4	C3	Glu190 OE1	1
C4	Gly675 N; Wat106	3	C4	Glu190 OE1; Wat201	2
C5	Gly135 C, CA; Leu136 N; Wat106	4	C5	Wat203	1
C6	Gly135 C, O; Leu136 CA, N; Leu139 CD2; His377 ND1; Asn484 OD1	7	C6	Asn187 O; Wat203, Wat204	3
C7	Leu136 CB; Wat36	2	C7	Lys191 CD, CE; Wat203 OH2; Thr38´ O	4
C8	Wat36	1	C8	Arg60 CZ, NH1, NH2, NE; Lys191 CD; Phe37´ O; Thr38´ O; Val40´ CG2	8
C9	Asp283 CA; His341 CE1	2	C9	Arg60 CZ, NH1, NH2, NE; Val40´ CG2	5
C10	Glu88 OE1; Asp283 CA, CB; Wat29	4	C10	Arg60 CZ, NH1; Pro188 O; Glu190 C, O	5
C11	Glu88 OE1; Asn133 ND2; Asp283 CA, CB; Wat29	5	C11	Trp67 CZ3; Pro188 O; Trp189 C, O	4
C12	Asn282 C, O; Arg292 NH2; Wat29	4	C12	Arg60 CD; Trp67 CZ3	2
C13	Asn282 O; His341 NE2; Wat35	3	C13	Arg60 CD, CG, NE, O; Val64 CG1	5
C14	His341 CE1; NE2; Wat35	3	C14	Arg60 CD, CZ, NE; Val64 CG1; Wat207; Phe37´ O; Val40´ CG2	7
C15	Tyr280 CB, O; Asn282 C, O, OD1; Arg292 CZ, NH1, NH2	8	C15	Arg60 CB; Leu63 CD1; Trp67 CZ3; Pro229 CD, CG	5
O2	His377 O; Wat170	2	O2	Glu190 O; Lys191 C, CA; Ala192 CA, CB	5
O3	Glu672 C, CD, CG; Ala673 C, CA, CB, N; Ser674 C, CA; Gly675 CA; Wat169	11	O3	Glu190 CD, CG; Tyr226 CD2, CE2; Wat201	5
O4	Asn484 OD1; Ser674 C, CA, CB, N, OG; Gly675 C, CA, O	9	O4	Glu190 OE1	1
O5	Leu135 C; Leu136 CA, CB, N; His377 CB, ND1, O	7	N1	Glu190 O; Lys191 CD; Wat203	3
O6	Leu139 CD2; His377 CG, CE1; Asn484 CG; Val455 CB, CG1, CG2	7	N2	Arg60 NH2; Lys191 CD, CE; Wat203; Thr38´ C	4
N1	His377 CB, O	2	N3	Arg60 CZ, NH1, NH2; Glu190 O; Lys191 CD; Thr38´O	6
N2	Leu136 CD1	1	S1	Thr38´O	1
S1	Gly135 N; Leu136 CB, N; Wat26, Wat27, Wat28	6			

*Figure 189. The van der Waals network of interactions of (**r**) at the catalytic site of GPb (left) and at the new allosteric site of GPb (right).*

The nitro group
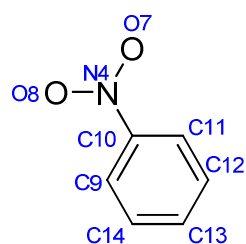
2-nitrobenzaldehyde-4-(2,3,4,6-tetra-
O-acetyl-β-D-glucopyranosyl)
thiosemicarbazone (*i*)
IC$_{50}$: 484.2 ± 23.3 µM
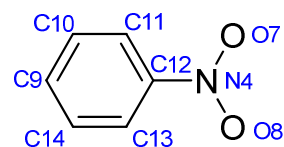
4-nitrobenzaldehyde-4-(2,3,4,6-tetra-
O-acetyl-β-D-glucopyranosyl)
thiosemicarbazone (*k*)
IC$_{50}$: 25.7 ± 0.9 µM

Figure 190. The numbering and kinetic results of the nitro group at the ortho and para positions.

The root mean square deviation (r.m.s.d) for CA atoms of (**i**) was 0.13 Å for the catalytic site while no binding occurred at the new allosteric site. The r.m.s.d for CA atoms of (**k**) was 0.18 Å for the catalytic site and 0.24 Å for the new allosteric site. Kinetic studies revealed that (**k**) had the best inhibitory effect on GPb. It is interesting to note the big difference in the IC$_{50}$ value between the ortho and the para position.
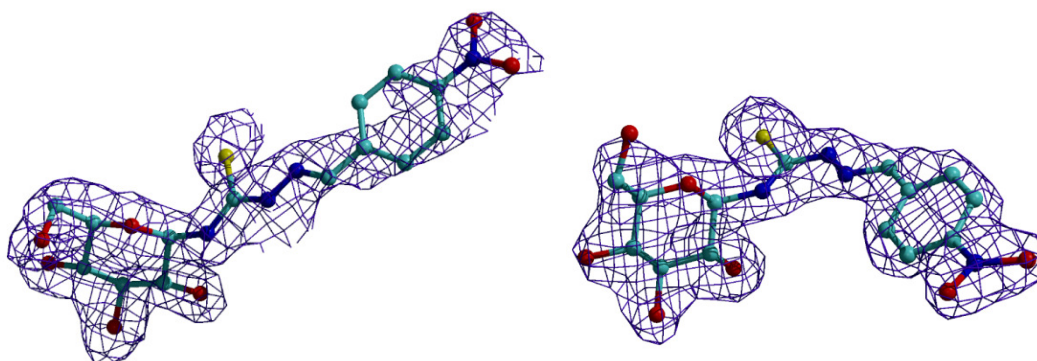
*Figure 191. 2Fo-Fc electron density maps of (**k**) bound at the catalytic site of GPb (left) and at the new allosteric site of GPb. The maps are contoured at 1σ level and the refined models are displayed.*
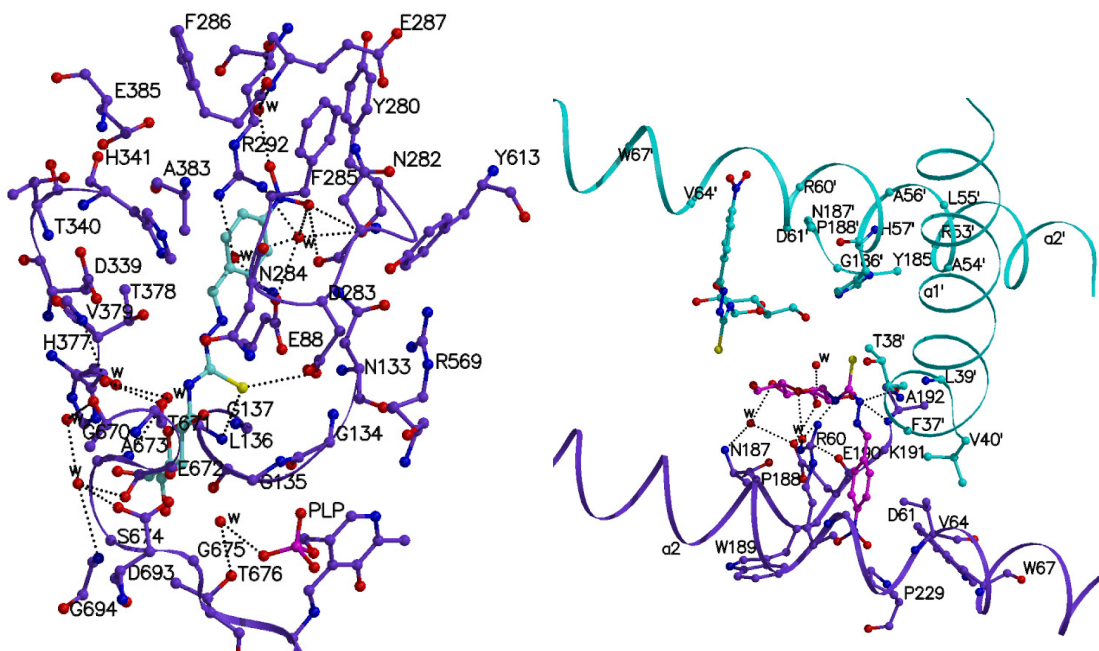
*Figure 192. Representation of the molecular interactions of (**k**) when bound at the catalytic site (left) and at the new allosteric site of GPb (right).*
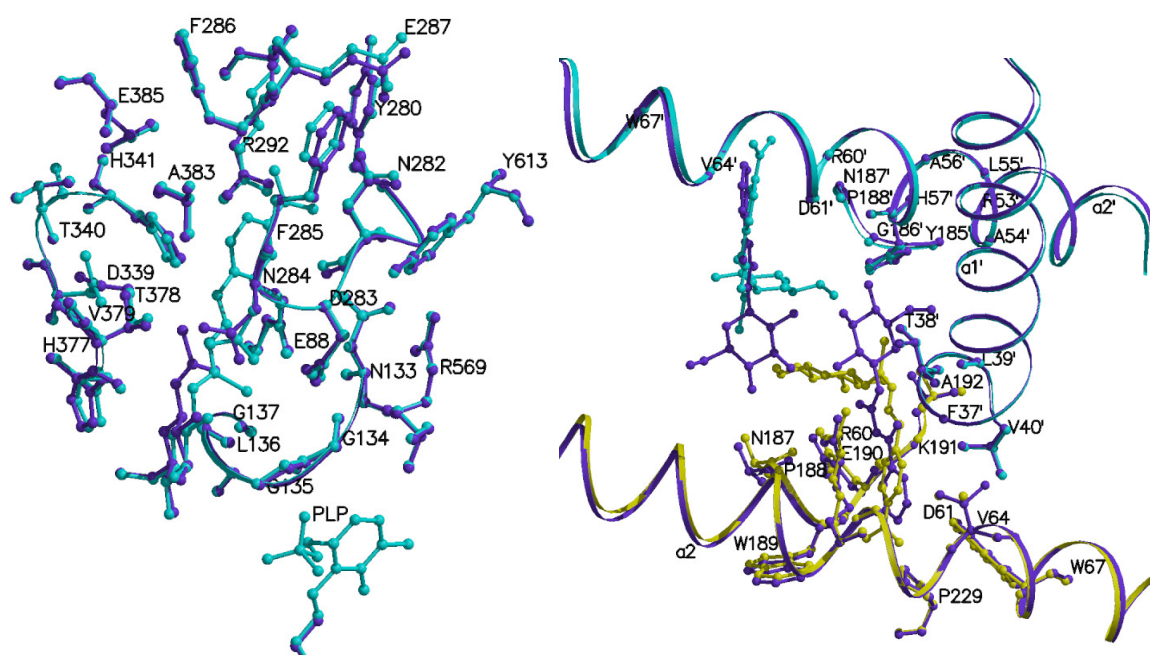
*Figure 193. Left: diagram showing the comparison between the GPb-(**k**) complex (cyan) and the GPb-N-acetyl-β-D-glucopyranosylamine complex (purple) in the vicinity of the catalytic site (left). Right: diagram showing the comparison of N´-benzoyl-β-D-glucopyranosyl urea-(**k**) complex in the vicinity of the new allosteric site. Purple: N´-benzoyl-β-D-glucopyranosyl urea-GPb complex; yellow: GPb-(**k**) complex (subunit 1); cyan GPb-(**k**) complex (subunit 2).*

Inhibitor atom	Protein atom	Distance (Å)	Angle (°)	Inhibitor atom	Protein atom	Distance (Å)	Angle (°)
O2	Asn284 ND2	3.3	139.1	O2	Ala192 N	2.8	173.2
	Asn284 OD1	3.2	99.0	O3	Glu190 OE1	2.9	119.0
	Tyr573 OH	3.0	147.9		Wat233	3.1	-
	Glu672 OE1	3.1	178.9	O4	Wat232	2.8	-
	Wat114	3.0	-	O5	Wat234	2.9	-
O3	Glu672 OE1	2.7	119.4	N1	Wat234	3.0	-
	Ser674 N	3.0	175.4	N2	Thr38´ O	2.8	155.8
	Gly675 N	3.0	142.5				
O4	Gly675 N	2.8	126.2				
	Wat135	2.6	-				
O6	His377 ND1	2.7	154.0				
	Asn484 OD1	2.7	137.9				
O7	Tyr280 O	3.0	103.7				
	Asn282 O	3.3	115.9				
	Wat26	2.7	-				
O8	Wat187	2.6	-				
S1	Leu136 N	3.3	157.3				
	Asp283 OD1	3.3	109.8				

*Figure 194. The network of hydrogen bond interactions between (**k**) and residues of the catalytic site of GPb (left) and residues of the new allosteric site of GPb (right).*

Upon binding to the catalytic site of GPb, (**k**) forms 18 hydrogen bonds and 129 van der Waals interactions. A structural comparison with *N*-acetyl-β-D-glucopyranosylamine revealed negligible conformational changes. This can be explained by the fact that the two oxygens form H-bonds with the surrounding environment while the nitro group has a delocalized system of π electrons stabilizing in this way the compound. Water molecules were displaced in order to fit the inhibitor into the binding pocket (Wat105, Wat106, Wat314, Wat355, Wat108, Wat109 and Wat110). Upon binding to the new allosteric site of GPb, (**k**) forms 7 hydrogen bonds and 79 van der Waals interactions. A structural comparison with *N*´-benzoyl-β-D-glucopyranosyl urea revealed negligible changes, as in the case of the catalytic site. Wat136 and Wat282 were displaced, while Wat24 and Wat234 were shifted by ~ 1.5 Å. The inhibitor shifted by ~ 58° upon binding.

O2	**…Wat114**	…Thr671 O			
		…Ala673 N			
		…Wat113	…Val379 N		
			…Thr671 O		
			…Wat112	…Gly670 O	
				…Wat115	…Glu672 O
					…Asp693 OD2
					…Gly694 N
O4	**…Wat135**	…Thr676 OG1			
		…PLP O3P			
O7	**…Wat26**	...Glu88 OE1			
		...Tyr280 O			
		…Arg292 NH1			
		…Wat25	…Glu88 OE1		
			…Arg292 NH2		
O8	**…Wat187**	…Glu287 N			
		…Glu287 O			

O3	**…Wat233**	…Tyr226 OH
O4	**…Wa232**	…Asn187 N
		…Glu190 OE1
O5/N1	**…Wa234**	…Arg60 NH1
		…Asn187 O
		…Glu190 O

*Figure 195. The water hydrogen bond network of (**k**) at the catalytic site (top) and at the new allosteric site of GPb (bottom).*

Inhibitor atom	Protein atom	No. of contacts	Inhibitor atom	Protein atom	No. of contacts
C1	His377 O	1	C1	Wat234	1
C2	His377 O; Glu672 OE1; Wat114	3	C2	Glu190 O; Ala192 N; Wat234	3
C3	Glu672 OE1; Gly675 N; Wat135	3	C3	Glu190 OE1; Wat233	2
C4	Asn484 OD1; Gly675 N; Wat135	3	C4	Glu190 OE1; Wat232	2
C5	Gly135 C; Leu136 N; Wat135	3	C5	Wat234	1
C6	Gly135 C, O; Leu136 CA, N; Leu139 CD2; His377 ND1; Asn484 OD1; Wat135	8	C7	Lys191 CD; Thr38´ O	2
C7	Leu136 CB; Asn284 CG, ND2, OD1	4	C8	Arg60 NH1, NH2, CZ; Lys191 CD; Phe37´ O; Thr38´ O; Val40´ CG2	7
C8	Asn284 CA, N	2	C9	Arg60 CZ, NH1, NH2, NE; Val40´ CG2	5
C9	Asn282 N, O; His341 CE1, NE2	4			
C10	Glu88 OE1; Asn282 O; His341 CE1; Wat25	4	C10	Arg60 CZ, NH1; Pro188 O; Glu190 C, O; Wat234 OH2	6
C11	Glu88 OE1; Asn133 ND2, Asn282 C, O; Wat25, Wat26	6	C11	Pro188 O; Trp189 C; Glu190 O	3
C12	Asn282 O; Phe285 O; Arg292 NH2; Wat25, Wat26	5	C12	Arg60 CD; Trp67 CZ3	2
C13	Asn282 O; Phe285 C, O	3	C13	Arg60 CD, CG, NE; Val64 CG1; Wat49 OH2	5
C14	Phe285 N, O; His341 NE2	3	C14	Arg60 CD, CZ, NE; Val64 CG1; Wat49 OH2; Phe37´ O; Val40´ CG2	7
O2	Asn284 CG; Wat114	2	O2	Glu190 O; Lys191 C, CA; Ala192 CA, CB	5
O3	Glu672 C, CD, CG; Ala673 C, CA, CB, N; Ser674 C, CA; Gly675 CA; Wat114	11	O3	Glu190 CD, CG; Tyr226 CD2, CE2	4
O4	Asn484 OD1; Ser674 C, CB; Gly675 CA, C, O; Thr676 N	8	O4	Wat233	1
O5	Leu136 CA, CB, N; His377 CB, ND1, O	6	O7	Pro188 O; Trp189 C, CA, O, CE3; Pro229 CD, CG	7
O6	Leu139 CD2; His377 CG, CE1; Asn484 CG; Val455 CB, CG1, CG2	7	O8	Arg60 O; Leu63 CB, CD1; Trp67 CE3, CZ3	5
O7	Tyr280 C, CA, CB; Asn282 C, CA, CB, N, ND2; Arg292 NH1	9	N1	Glu190 O	1
O8	Phe285 O; Arg292 CZ, NH, NE2	4	N2	Arg60 NH2; Lys191 CD, CE; Thr38´ C	4
N1	Asn284 CG, ND2, OD1; His377 CB, O	5	N3	Arg60 CZ, NH1, NH2; Lys191 CD; Wat234; Thr38´ O	6
N2	Leu136 CD1; Asn284 CG, N, ND2, OD1	5			
N3	Asn284 N, ND2	2			
N4	Asn282 CB, O; Phe285 O; Arg292 CB, NH1, NH2; Wat26, Wat187	8			
S1	Gly135 N; Leu136 CA, CB, N; Asp283 CG, OD1, OD2; Asn284 ND2; Wat23, Wat24	10			

*Figure 196. The van der Waals network of interactions of (**k**) at the catalytic site of GPb (left) and at the new allosteric site of GPb (right).*

The fluoride group
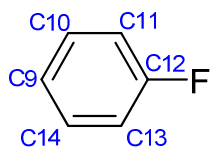
4-fluorobenzaldehyde-4-(β-D-glucopyranosyl)-
thiosemicarbazone (**a**)

IC$_{50}$: 5.7 ± 0.4 μM
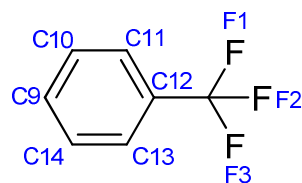
4-trifluoromethylbenzaldehyde-4-
(β-D-glucopyranosyl)-
thiosemicarbazone (**h**)

IC$_{50}$: 524.3 ± 11.4 μM

Figure 197. The numbering and the kinetic results of the fluoride group.

The root mean square deviation (r.m.s.d) for CA atoms of (**a**) was 0.18 Å for the catalytic site and for the new allosteric site was 0.29 Å. The r.m.s.d for CA atoms of (**h**) was 0.20 Å for the catalytic site and 0.15 Å for the new allosteric site. Kinetic studies revealed that (**a**) had the best inhibitory effect on GPb. It is interesting to note the profound difference in the IC$_{50}$ values between (**a**) and (**h**).
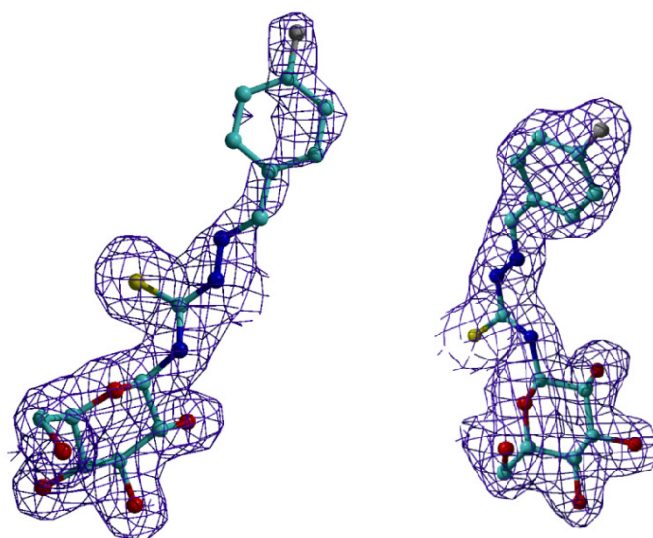
*Figure 198. 2Fo-Fc electron density maps of (**a**) bound at the catalytic site of GPb (left) and at the new allosteric site of GPb. The maps are contoured at 1σ level and the refined models are displayed.*

Upon binding to the catalytic site of GPb, (**a**) forms 13 hydrogen bonds and 102 van der Waals interactions with the surrounding environment and water molecules. A structural comparison with *N*-acetyl-β-D-glucopyranosylamine revealed a shift of the inhibitor by ~ 62° upon binding. A number of water molecules get displaced in order for the bulky inhibitor to fit into the binding site (Wat110, Wat355, Wat106, Wat109, Wat356 and Wat105). Phe285 rotated by 25.27° [CA-**CB-CG-**N]. No other profound conformational changes were noted. It is interesting to note that the aromatic part of the ligand fits into the catalytic site, in such a way that it doesn't destabilize Asp283 and Asn284 of the 280s loop. In order to stabilize its favourable position, it forms a hydrogen bond with the main chain oxygen atom of Asn282.
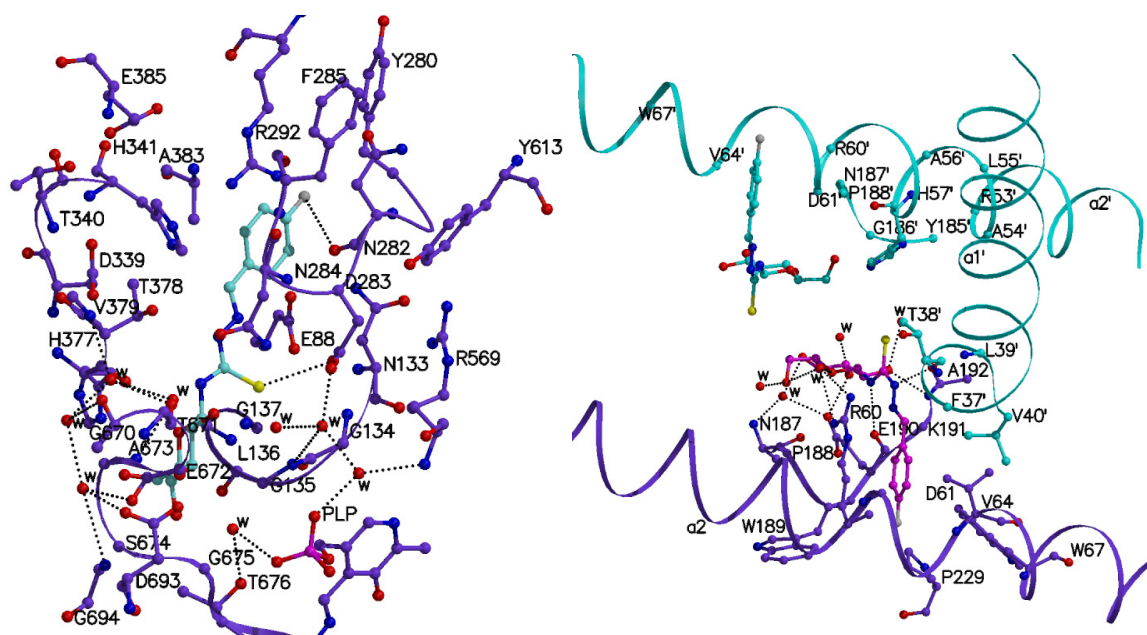
*Figure 199. Representation of the molecular interactions of (**a**) when bound at the catalytic site (left) and at the new allosteric site of GPb (right).*
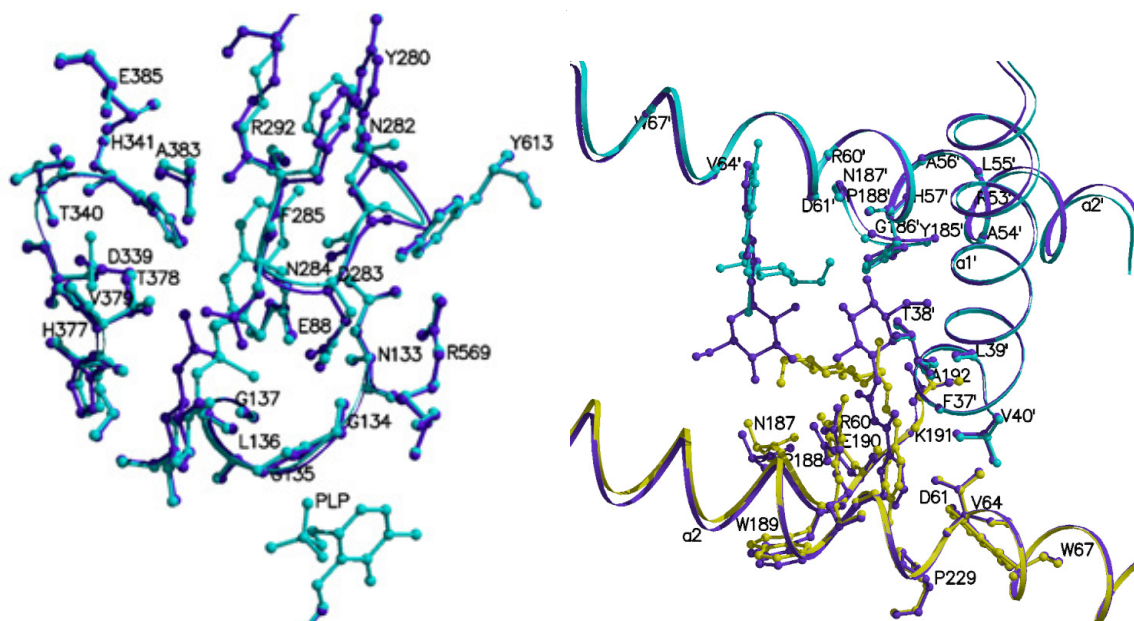
*Figure 200. Left: diagram showing the comparison between the GPb-(**a**) complex (cyan) and the GPb-N-acetyl-β-D-glucopyranosylamine complex (purple) in the vicinity of the catalytic site (left) Right: diagram showing the comparison of N´-benzoyl-β-D-glucopyranosyl urea-(**a**) complex in the vicinity of the new allosteric site. Purple: N´-benzoyl-β-D-glucopyranosyl urea-GPb complex; yellow: GPb-(**a**) complex (subunit 1); cyan: GPb-(**a**) complex (subunit 2).*

Upon binding to the new allosteric site of GPb, (**a**) forms 9 hydrogen bonds and 111 van der Waals interactions. A structural comparison with $N´$-benzoyl-β-D-glucopyranosyl urea revealed that the inhibitor shifted by ~ 133° upon binding, shifting the glucopyranose moiety. Water molecules were displaced (Wat136, Wat239 and Wat137), while Wat280 and Wat301 were shifted by 3.07 Å and 1.67 Å respectively. No significant changes were noted in the protein environment surrounding the inhibitor.

Inhibitor atom	Protein atom	Distance (Å)	Angle (º)	Inhibitor atom	Protein atom	Distance (Å)	Angle (º)
O2	Tyr573 OH	3.1	149.7	O2	Ala192 N	2.9	174.7
	Glu672 OE1	3.2	171.6		Wat298	2.8	-
	Wat234	2.7	-	O3	Glu190 OE1	2.8	121.9
	Wat237	2.9	-		Wat252	3.0	-
O3	Glu672 OE1	2.8	117.1	O4	Wat180	2.8	-
	Ser674 N	3.1	176.2	O5	Wat301	2.8	-
	Gly675 N	3.2	140.0	O6	Wat301	3.1	-
O4	Gly675 N	2.8	131.8	N1	Glu190 O	3.3	153.7
	Wat116	2.6	-	N2	Thr38´ O	2.8	153.6
O6	His377 ND1	2.7	153.6				
	Asn484 OD1	2.8	137.2				
S1	Asp283 OD1	3.3	111.3				
F1	Asn282 O	3.3	124.7				

*Figure 201. The network of hydrogen bond interactions between (**a**) and residues of the catalytic site of GPb (left) and residues of the new allosteric site of GPb (right).*

O2	…Wat234	…Tyr573 OH			
		…Lys574 NZ			
		…Wat54	…Gly135 N		
			…Asp283 OD2		
			….Wat57	…Arg569 N	
				…PLP O2P	
	…Wat237	…Thr671 O			
		...Ala673 N			
		…Wat91	…Val379 N		
			…Thr671 O		
			...Wat254	...Gly670 O	
				…Wat95	…Glu672 O
					…Asp693 OD2
					…Gly694 N
O4	**…Wat116**	…Thr676 OG1			
		…PLP O3P			

O3	**…Wat252**	…Tyr226 OH
O4	**…Wat180**	…Asn187 N
		…Glu190 OE1
O5	**…Wat301**	…Arg60 NH1
		…Arg60 NH2

*Figure 202. The water hydrogen bond network of (**a**) at the catalytic site (top) and at the new allosteric site of GPb (bottom).*

Inhibitor atom	Protein atom	No. of contacts	Inhibitor atom	Protein atom	No. of contacts
C1	Wat234	1	C1	Glu190 O; Wat298, Wat301	3
C2	His377 O; Glu672 OE1; Wat234, Wat237	4	C2	Glu190 O; Wat298	2
C3	Glu672 OE1; Gly675 N; Wat116, Wat234	4	C3	Glu190 OE1; Wat252, Wat298	3
C4	Gly675 N; Wat116	2	C4	Glu190 OE1; Wat180	2
C5	Gly135 C, CA; Leu136 N; Wat116	4	C5	Wat301	1
C6	Gly135 C,O; Leu136 N; His377 ND1; Asn484 OD1	5	C6	Wat246, Wat301	2
C7	Leu136 CB; Asn284 ND2	2	C7	Arg60 NH2; Lys191 CD; Wat301; Thr38´ O	4
C8	Asn284 N	1	C8	Arg60 CZ, NH1, NH2, NE; Phe37´ O; Thr38´ O; Val40´ CG2	7
C9	Asn282 O; Asn284 N; His341 CE1	3	C9	Arg60 CD, CZ, NH1, NE; Val40´ CG2	5
C10	Asn282 O; Phe285 O; His341 NE2	3	C10	Arg60 CD, NE; Val64 CG2; Wat300; Phe37´ O; Val40´ CG2	6
C11	Asn282 O; Phe285 O	2	C11	Arg60 CB, CD, CG, O; Val64 CG2	5
C12	Asn282 C, O; Arg292 NH2; Wat182	4	C12	Trp67 CZ3	1
C13	Glu88 OE1; Asn133 ND2; Asn282 C, O; Wat182	5	C13	Trp67 CZ3; Pro188 O; Trp189 C, O	4
C14	Glu88 OE1; Asn282 O; Wat182	3	C14	Pro188 O; Glu190 C, O	3
O2	Asn284 CG, OD1, ND2; His377 O	4	O2	Glu190 O; Lys191 C, CA; Ala192 CA, CB	5
O3	Glu672 C, CD, CG; Ala673 C, CA, CB, N; Ser674 C, CA; Wat237	10	O3	Glu190 CD, CG; Tyr226 CD2, CE2; Wat180	5
O4	Asn484 OD1; Ser674 C, CB; Gly675 C, CA, O; Thr676 CG2, N	8	O4	Wat252	1
O5	Leu136 CA, CB, N; His377 CB, ND1	4	O6	Asn187 C, O; Pro188 CA	3
O6	Leu139 CD2; His377 CE1, CG; Val455 CG1, CG2; Asn484 CG	6	F1	Leu63 CD1; Trp67 CZ3; Pro229 CD, CG	4
F1	Tyr280 CB, O; Asn282 CB, O; Arg292 CZ, NH1, NH2; Wat182	8	N1	Glu190 O; Wat301	2
N1	Asn284 OD1, ND2; His377 CB, O	4	N2	Arg60 CZ, NH1, NH2; Lys191 CD; Thr38´ C	5
N2	Leu136 CD1; Asn284 CG, ND2	3	N3	Arg60 CZ, NH1, NH2; Glu190 O; Lys191 CD; Thr38´ O	6
N3	Asn284 ND2, N	2	S1	Wat298, Wat301; Thr38´ O	3
S1	Gly135 N; Leu136 CB, N; Asp283 CG, OD1, OD2; Asn284 ND2; Wat54, Wat74, Wat234	10			

*Figure 203. The van der Waals network of interactions of (**a**) at the catalytic site of GPb (left) and at the new allosteric site of GPb (right).*

186
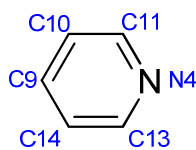
The pyridyl group

4-pyridinecarboxaldehyde-4-(β-D-glucopyranosyl) thiosemicarbazone (v)

IC$_{50}$: 200.0 ± 17.0 μM

Figure 204. The numbering and the kinetic results of the pyridyl group at the para position.

The root mean square deviation (r.m.s.d) for CA atoms of (**v**) was 0.20 Å for the catalytic site and for the new allosteric site was 0.34 Å.
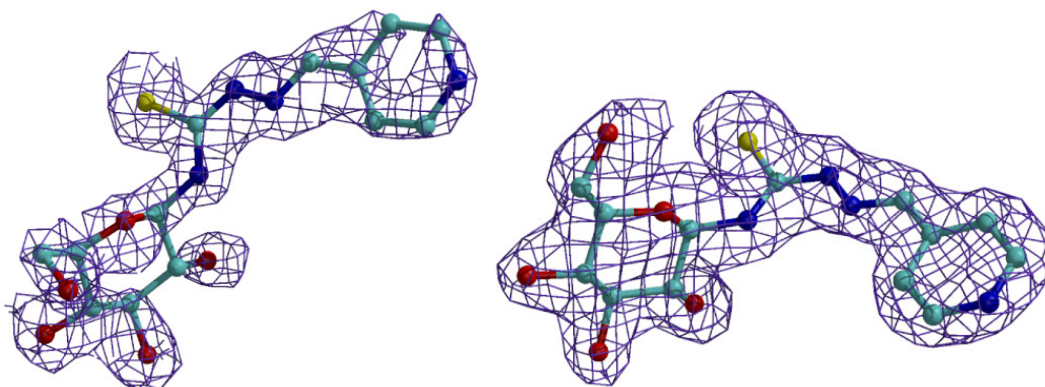
Figure 205. 2Fo-Fc electron density maps of (v) bound at the catalytic site of GPb (left) and at the new allosteric site of GPb. The maps are contoured at 1σ level and the refined models are displayed.

Upon binding to the catalytic site of GPb, (**v**) forms 18 hydrogen bonds and 113 van der Waals interactions. The aromatic part of the ligand fits into the subsite β-pocket of the site. A structural comparison with *N*-acetyl-β-D-glucopyranosylamine revealed insignificant changes in the protein environment. The inhibitor rotates by 28° [O5-**C1-N1-**C7]. In the water network, some water molecules were displaced (Wat105, Wat110, Wat355 and Wat314).
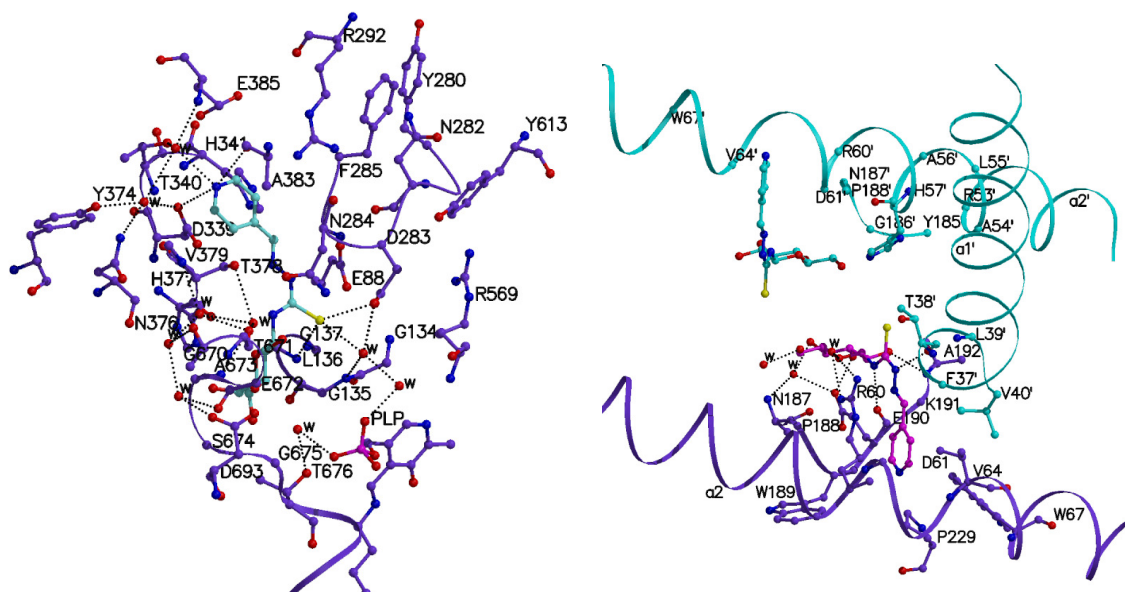
*Figure 206. Representation of the molecular interactions of (**v**) when bound at the catalytic site (left) and at the new allosteric site of GPb (right).*
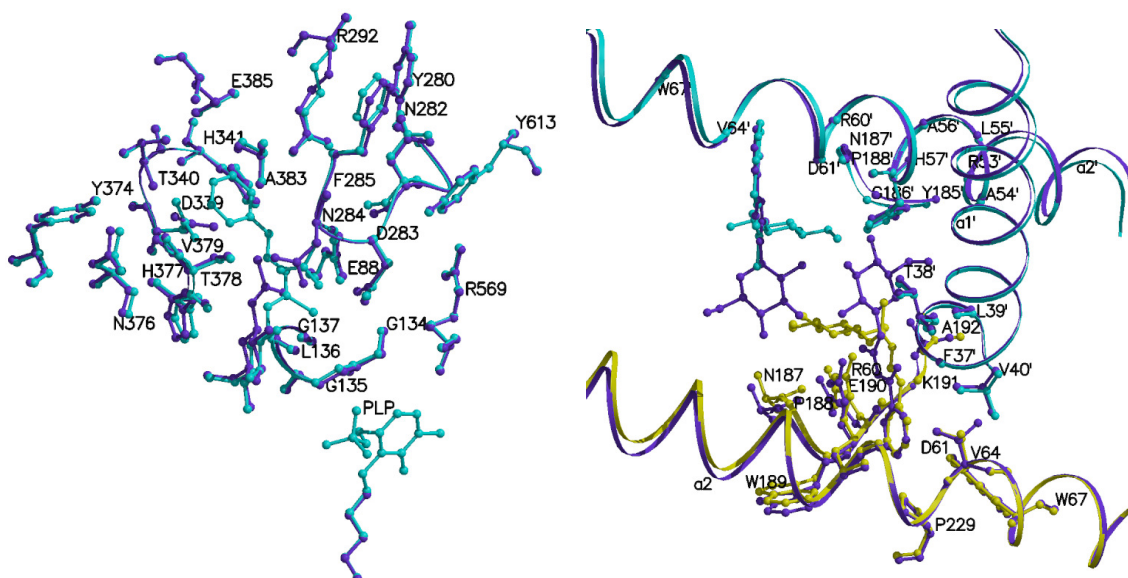
*Figure 207. Left: diagram showing the comparison between the GPb-(**v**) complex (cyan) and the GPb-N-acetyl-β-D-glucopyranosylamine complex (purple) in the vicinity of the catalytic site. Right: diagram showing the comparison of N´-benzoyl-β-D-glucopyranosyl urea-(**v**) complex in the vicinity of the new allosteric site. Purple: N´-benzoyl-β-D-glucopyranosyl urea-GPb complex; yellow: GPb-(**v**) complex (subunit 1); cyan: GPb-(**v**) complex (subunit 2).*

Upon binding to the new allosteric site of GPb, (**v**) forms 8 hydrogen bonds and 80 van der Waals interactions. As in the case of the catalytic site, insignificant conformational changes were observed in the protein environment, while some water molecules were displaced (Wat136, Wat239, Wat243 and Wat250).

Inhibitor atom	Protein atom	Distance (Å)	Angle (°)	Inhibitor atom	Protein atom	Distance (Å)	Angle (°)
O2	Asn284 ND2	3.3	139.6	**O2**	Ala192 N	2.9	171.5
	Asn284 OD1	3.3	99.8	**O3**	Glu190 OE1	2.7	121.6
	Tyr573 OH	3.0	149.8	**O4**	Wat124	2.7	-
	Glu672 OE1	3.2	178.3	**O5**	Wat126	2.8	-
	Wat57	3.0	-	**O6**	Wat125	2.6	-
O3	Glu672 OE1	2.7	122.0		Wat126	2.5	-
	Ser674 N	3.1	174.8	**N1**	Glu190 O	3.1	153.5
	Gly675 N	3.2	142.9	**N2**	Thr38´ O	2.8	155.1
O4	Gly675 N	2.8	128.7				
	Wat45	2.6	-				
O6	His377 ND1	2.7	146.0				
	Asn484 OD1	2.7	137.9				
N4	Asp339 OD2	3.0	105.4				
	Ala383	3.0	121.9				
	Wat59	3.0	-				
S1	Leu136 N	3.3	164.0				
	Asp283 OD1	3.0	117.3				
	Wat27	3.1	-				

*Figure 208. The network of (**v**) hydrogen bond interactions between and residues of the catalytic site of GPb (left) and residues of the new allosteric site of GPb (right).*

O2	**…Wat57**	…Thr671 O			
		…Ala673 N			
		…Thr378 OG1			
		…Wat56	...Val379 N		
			…Thr671 O		
			…Wat55	…Gly670 O	
				…Wat54	…Glu672 O
					…Asp693 OD2
N4	**…Wat59**	...Thr340 OG1			
		…Glu385 N			
		…Wat58	...Asp339 OD2		
			...Tyr374 OH		
			...Asn376 ND2		
S1	**…Wat27**	...Gly135 N			
		…Asp283 OD1			
		…Asp283 OD2			
		…Wat28	…Arg569 N		
			…PLP O3P		

O4	**…Wat124**	…Asn187 N
		…Glu190 OE1
O5	**…Wat126**	…Arg60 NH1
		…Arg60 NH2
O6	**…Wat125**	No interactions
	…Wat126	

Figure 209. The water hydrogen bond network of (v) at the catalytic site (top) and at the new allosteric site of GPb (bottom).

Inhibitor atom	Protein atom	No. of contacts	Inhibitor atom	Protein atom	No. of contacts
C2	His377 O; Glu672 OE1; Wat57	3	C1	Glu190 O; Wat126	2
C3	Glu672 OE1; Gly675 N; Wat45	3	C2	Glu190 O	1
C4	Asn484 OD1; Gly675 N; Wat45	3	C3	Glu190 OE1	1
C5	Gly135 C, CA; Leu136 N; Wat45	4	C4	Asn187 O; Glu190 OE1; Wat124	3
C6	Gly135 C, O; Leu136 N; His377 CE1, ND1; Asn484 OD1; Wat45	7	C5	Wat126	1
C7	Leu136 CB; Asn284 CG, ND2, OD1	4	C6	Asn187 O; Wat125, Wat126	3
C8	Leu136 CD1	1	C7	Lys191 CD; Wat126 OH2; Thr38´ O	3
C9	Asp339 CG, OD1; His341 NE2	3	C8	Arg60 CZ, NH1, NH2, NE; Thr38´ O; Val40´ CG2	6
C10	Asp339 CG, OD1, OD2; Thr378 CG2	4	C9	Arg60 CD, CG, CZ, NE; Val40´ CG2	5
C11	Asp339 CG, OD1, OD2; Thr378 CG2; Ala383 O; Wat58, Wat59	7	C10	Arg60 CD; Pro188 O; Glu190 C, O	4
C12	Asp339 CG, OD1, OD2; His341 CD2, NE2; Ala383 O; Wat59, Wat60	8	C11	Arg60 CD; Trp67 CZ3; Pro188 O; Trp189 C, O; Pro229 CD	6
C13	Asp339 OD1; His341 CD2, CE1, NE2; Ala383 O; Wat60	6	C12	Arg60 CD, CZ; Val64 CG1; Trp67 CE3, CZ3	5
O2	Asn284 CG; His377 O	2	C13	Arg60 CD, CG, NE; Val64 CG1; Wat127; Val40´ CG2	6
O3	Glu672 C, CD, CG; Ala673 C, CA, CB, N; Ser674 C, CA; Wat57	10	O2	Glu190 O; Lys191 C, CA; Ala192 CA, CB	5
O4	Asn484 OD1; Ser674 C, CB; Gly675 C, CA, O; Thr676 N	7	O3	Glu190 CD, CG; Tyr226 CD2, CE2; Wat124	5
O5	Leu135 C; Leu136 CA, CB, N; His377 CB, ND1	6	O5	Asn187 O; Glu190 O	2
O6	Leu139 CD2; His377 CG, CE1; Asn484 CG; Val455 CB, CG1, CG2	7	N1	Arg60 NH1; Lys191 CD; Wat126	3
N1	Asn284 ND2, OD1; His377 CB, O	4	N2	Arg60 CZ, NH1, NH2; Lys191 CD; Thr38´ C	5
N2	Leu136 CB, CD1; Asn284 CG, N, ND2, OD1; Wat25	7	N3	Arg60 CZ, NH1, NH2, NE; Glu190 O; Lys191 CD; Thr38´O	7
N3	Leu136 CD1; Asn284 CG, OD1	3	N4	Arg60 CD, CG; Trp67 CZ3; Pro229 CD, CG	5
N4	Asp339 CG, OD1; Ala383 C; Wat58	4	S1	Wat126; Thr38´O	2
S1	Gly135 CA, N; Leu136 N, CB; Asp283 CG, OD1, OD2; Asn284 ND2; Wat26, Wat27	10			

Figure 210. The van der Waals network of interactions of (v) at the catalytic site of GPb (left) and at the new allosteric site of GPb (right).

	p-bromo (g)	*m*-chloro (c)	*o*-hydroxyl (l)	*p*-methyl (r)
Experiment	T state GPb soaked with 10mM (**g**) in 20% DMSO for 7 hrs	T state GPb soaked with 20mM (**c**) in 20% DMSO for 16 hrs	T state GPb soaked with 20mM (**l**) in 20% DMSO for 21 hrs	T state GPb soaked with 20mM (**r**) in 20% DMSO for 3.5 hrs
Wavelength (Å)	0.97976	0.977	0.815	1.04498
Oscillation range (°)	0.8	0.8	0.8	0.8
No. of images (°)	55	80	34	80
Space Group	P4_32_12	P4_32_12	P4_32_12	P4_32_12
Unit cell dimensions	a=b=128.9 Å c=116.8 Å α=β=γ=90°	a=b=128.9 Å c=116.3 Å α=β=γ=90°	a=b=128.5 Å c=115.8 Å α=β=γ=90°	a=b=127.6 Å c=115.6 Å α=β=γ=90°
Resolution (Å)	30.0-2.23	30.0-1.95	30.0-2.07	35.6-2.10
No. of observations	780344	799860	177014	690901
No. of unique reflections (outermost)	47672 (2290)	70758 (3407)	48018 (2438)	49630 (6658)
R_m (outermost shell)[b]	0.071 (0.462)	0.053 (0.429)	0.084 (0.435)	0.092 (0.426)
Completeness (outermost shell) (%)	98.1 (96.6)	98.6 (96.6)	80.4 (83.1)	89.6 (83.7)
Outermost shell (Å)	2.27–2.23	1.98–1.95	2.11–2.07	2.21–2.10
$< I / \sigma (I) >$ (outermost shell)[c]	9.67 (3.55)	17.0 (4.3)	9.59 (3.72)	11.7 (3.1)
Redundancy (outermost shell)	3.6 (3.7)	5.3 (4.8)	2.5 (2.3)	3.3 (3.1)
B-values (Å^2) (Wilson plot)	36.5	27.6	31.3	29.0
Resolution range (Å)	91.29–2.23	29.54–1.95	27.99–2.07	90.17-2.10
No of reflections used (free)	45222 (2413)	67130 (3589)	45659 (3065)	47052 (2509)
Residues included	(12-254) (261–314) (324–836)	(12-254) (261–314) (324–836)	(12-254) (261–314) (324–836)	(12-254) (261–314) (324–836)
No of protein atoms	6595	6597	6600	6599
No of water molecules	157	297	286	263
No. of heteroatoms	24 (catalytic), 24 (new allosteric), 15 (PLP)	24 (catalytic), 24 (new allosteric), 15 (PLP)	24 (catalytic), 15 (PLP)	24 (catalytic), 24 (new allosteric), 15 (PLP)
Final R (R_{free}) (%)[d]	0.197 (0.234)	0.194 (0.222)	0.189 (0.225)	0.192 (0.227)
R (R_{free}) (outermost shell)	0.251 (0.320)	0.249 (0.270)	0.230 (0.304)	0.240 (0.274)
r.m.s.d. in bond lengths (Å)	0.008	0.007	0.007	0.007
r.m.s.d. in bond angles (°)	1.091	1.038	1.030	1.043
Average B (Å^2) for residues	(12-254) (261–314) (324–836)	(12-254) (261–314) (324–836)	(12-254) (261–314) (324–836)	(12-254) (261–314) (324–836)
Overall	42.1	31.5	33.4	34.4
CA, C, N, O	41.3	30.7	32.7	33.6
Side chain	42.9	32.4	34.0	35.1
Average B (Å^2) for heteroatoms	54.9 (catalytic), 50.0 (new allosteric), 32.9 (PLP)	34.0 (catalytic), 32.4 (new allosteric), 22.3 (PLP)	28.6 (catalytic), 25.1 (PLP)	31.4 (catalytic), 33.8 (new allosteric), 26.7 (PLP)
Average B (Å^2) for water molecules	38.8	36.9	38.8	36.6

	p-nitro (k)	*p*-fluoro (a)	*p*-pyridyl (v)
Experiment	T state GPb soaked with 6.7mM (**k**) in 20% DMSO for 3 hrs	T state GPb soaked with 20mM (**a**) in 20% DMSO for 13 hrs	T state GPb soaked with 20mM (**v**) in 20% DMSO for 7 hrs
Wavelength (Å)	1.04498	0.979	0.8081
Oscillation range (°)	0.8	0.8	0.8
No. of images (°)	106	80	90
Space Group	P4₃2₁2	P4₃2₁2	P4₃2₁2
Unit cell dimensions	$a=b=128.3$ Å $c=115.8$ Å $\alpha=\beta=\gamma=90°$	$a=b=128.9$ Å $c=116.3$ Å $\alpha=\beta=\gamma=90°$	$a=b=128.5$ Å, $c=115.9$ Å $\alpha=\beta=\gamma=90°$
Resolution (Å)	35.7-2.05	30.0-1.95	30.0-1.98
No. of observations	386948	791008	672692
No. of unique reflections (outermost)	60721 (8786)	67752 (4302)	66434 (3310)
R_m **(outermost shell)** [b]	0.093 (0.450)	0.060 (0.352)	0.057 (0.472)
Completeness (outermost shell) (%)	99.7 (100.0)	94.6 (96.7)	99.0 (97.7)
Outermost shell (Å)	2.16–2.05	1.98–1.95	2.11–2.07
$<I/\sigma(I)>$ **(outermost shell)** [c]	19.5 (5.6)	16.6 (6.19)	20.15 (5.13)
Redundancy (outermost shell)	6.4 (6.3)	5.5 (5.4)	6.1 (6.0)
B-values (Å²) (Wilson plot)	24.1	27.4	25.1
Resolution range (Å)	90.54–2.05	29.40–1.95	90.91–1.98
No. of reflections used (free)	57608 (3081)	64292 (3428)	62917 (3829)
Residues included	(12-254) (261–314) (324–836)	(12-254) (261–314) (324–836)	(12-254) (261–314) (324–836)
No. of protein atoms	6595	6597	6595
No. of water molecules	300	306	210
No. of heteroatoms	26 (catalytic), 26 (new allosteric), 15 (PLP)	24 (catalytic), 24 (new allosteric), 15 (PLP)	23 (catalytic), 23 (new allosteric), 15 (PLP)
Final R (R_{free}) (%) [d]	0.186 (0.213)	0.189 (0.217)	0.192 (0.224)
R (R_{free}) **(outermost shell)**	0.221 (0.269)	0.231 (0.279)	0.233 (0.291)
r.m.s.d. in bond lengths (Å)	0.007	0.007	0.007
r.m.s.d. in bond angles (°)	1.017	1.026	1.037
Average B (Å²) for residues	(12-254) (261–314) (324–836)	(12-254) (261–314) (324–836)	(12-254) (261–314) (324–836)
Overall	27.6	30.3	26.9
CA, C, N, O	26.7	29.5	26.0
Side chain	28.3	31.1	27.7
Average B (Å²) for heteroatoms	36.4 (catalytic), 32.0 (new allosteric), 17.6 (PLP)	28.7 (catalytic), 29.4 (new allosteric), 20.3 (PLP)	41.7 (catalytic), 41.7 (new allosteric), 17.3 (PLP)
Average B (Å²) for water molecules	32.2	36.7	30.6

a Native T state RMGPb crystals, grown in the tetragonal lattice, space group P4₃2₁2 were soaked with various concentrations of inhibitors in buffered solutions at pH 6.7 in the presence of DMSO. X-ray diffraction data were collected using synchrotron radiation sources at Daresbury Laboratory, UK and EMBL-Hamburg outstation at DESY, Germany and processed with the HKL package. Complex structure determination and analysis were performed according to standard protocols as implemented in the CCP4 package.

b $R_{symm} = \Sigma_h\Sigma_i|I(h) - I_i(h)/\Sigma_h\Sigma_iI_i(h)$ where $I_i(h)$ and $I(h)$ are the ith and the mean measurements of the intensity of reflection h. **c** $\sigma(I)$ is the standard deviation of I.

d $R_{cryst} = \Sigma_h|F_o - F_c|/\Sigma_hF_o$, where F_o and F_c are the observed and calculated structure factors amplitudes of reflection h, respectively. R_{free} is equal to R_{cryst} for a randomly selected 5% subset of reflections not used in the refinement. Values in parentheses are for the outermost shell.

Figure 211. Diffraction data and refinement statistics.

Conclusions

Comparing the binding of each compound with that of *N*-acetyl-β-D-glucopyranosylamine at the catalytic site, it is interesting to see that there is a pattern emerging based on the electronegativity of the directing groups. Between the three compounds with the –Cl substituent, the one in the ortho position causes a moderate shift of the 280s loop upon binding. The one in the meta position causes a significant shift in the 280s loop, while the one in the para position causes a major shift in the 280s loop. However, between the three compounds with the –OH substituent the opposite effect is observed. The substituent in the ortho position causes the biggest shift of the 280s loop and the strongest destabilization of the protein environment. In the case of the –Br substituent the effect of a significant shift of the 280s loop is the same in both the meta and para positions. In addition there is a similarity between the –F and –CF$_3$ substituents as well as the –O-CH$_3$ and –CH$_3$ substituents. All cause a significant shift of the 280s loop. Interestingly, the binding of the inhibitors with the –NO$_2$ substituents is different. There is a negligible shift of the 280s loop. This can be explained by the fact that the nitro group has an unstable delocalized system of π electrons and it is the most electron rich functional group. The substituent in the para position causes even less significant changes than in the ortho position. According to the *Hammett σ substituent constants*, the nitro group in the para position has the strongest mesomeric and electron withdrawing inductive effect. This is reflected by the Hammett substituent constant as well as the low IC$_{50}$ value in the para position compared to the much higher value in the ortho position. Binding to the new allosteric site of GPb does not promote extensive conformational changes except for small shifts in the atoms surrounding the inhibitor i.e. of residues 60, 64, 189 and 191, which undergo conformational changes in order to accommodate the ligand.

4. General conclusions

Diabetes is a rapidly growing disease throughout the world and is slowly being recognized as a global "epidemic". It has been noticed that over the past years an increase in obesity as well as a change in lifestyle, especially in the eastern world, have led to an exponential increase of diabetes cases. As the predicted numbers for the future are daunting, an immediate call for prevention and treatment is undoubtable. Various diabetes drugs work in different ways to lower blood sugar levels. A drug may work by stimulating the pancreas to produce and release more insulin; inhibiting the production and release of glucose from the liver, in this way requiring less insulin to transport sugar into the cells; by blocking the action of stomach enzymes that break down carbohydrates or make tissues more sensitive to insulin. On a molecular level, new drugs should target the lowering of blood plasma glucose, which leads to undesired hyperglycaemia. A reasonable aim would be the inhibition of glycogen degradation into glucose molecules. In a negative feedback mechanism, a particular pathway is deactivated by inhibiting the first step of the reaction. This study has focused on glycogen phosphorylase, an enzyme that catalyzes the first step of glycogen degradation.

A number of inhibitors of glycogen phosphorylase were studied kinetically and X-ray crystallographically. The majority of these compounds bound to the catalytic site of glycogen phosphorylase, as most were glucose analogues. Some also bound to the allosteric site, the new allosteric site and the inhibitor site of the enzyme. An interesting finding was the discovery of a novel binding site of the enzyme, located near the catalytic site. Although glycogen phosphorylase is a very well-known enzyme structurally, this finding showed that possibly more binding sites are yet to be discovered and exploited on glycogen phosphorylase. This could open up new pathways for structure based drug design of diabetes type 2. The combination of kinetic and X-ray crystallographic studies proved valuable to obtain information about the inhibitors and their mode of action. The diversity of various functional groups proved to affect inhibitor potency. The mode of binding of each inhibitor was affected by the presence/absence of hydrophilic groups as well as electron withdrawing groups. Stereochemistry also governed inhibitor binding, with the presence of α-glucose or β-glucose analogues having a profound effect on binding. More specifically, the β-pocket of the catalytic site is conformationally ordered in a way that favours β-glucose analogues. The reactivity of the alpha or beta naphthyl groups also had

an inhibitory and structural effect. The deletion or substitution of only one atom or functional group of a ligand can have a substantial effect on inhibition. The structural analysis of enzyme-ligand complexes allowed a detailed mapping of the molecular forces that govern inhibitor recognition by the enzyme and has added valuable assets to the structure-driven design approach of new inhibitors with better potency. It can also be concluded that the mode of action of the ligands concentrated on the stabilization of the amino acids of the 280s loop, stabilizing the T state of the enzyme and making the protein environment in this way energetically stable. The introduction of virtual screening and docking was a useful tool and must not be underestimated. It provided important information which was used to direct the kinetic and crystallographic experiments in the correct direction.

Drug design is a long and multi-step process. If compounds like the ones studied would get the approval for further pre-clinical studies, many issues would have to be addressed such as the risk of hypoglycaemia, unwanted side effects, toxicity, solubility, transport to the target site and permeability of the blood brain barrier. In addition to the demand of a treatment for diabetes type 2, the effectiveness of lifestyle intervention for the prevention of the disease must not be underestimated or neglected. Individuals, and especially children and young adults, must be vigilant about the dangers of obesity and consumption of unhealthy foods, and they must become aware of the necessity for physical activity and a balanced diet. Society must become more aware and schools for example could introduce a healthy diet in school lunch menus. These facts are crucial not only for the prevention of diabetes but are key components to a healthy lifestyle.

5. References

1. Kepler, J. (1611) *Strena seu de Nive Sexangula.*

2. Steno, N. (1669) *De solido intra solidum naturaliter contento dissertationis prodromus.*

3. Haüy, R.J. (1784) *Essai d'une théorie sur la structure des crystaux.*

4. Miller, W.H. (1839) *A treatise to Crystallography.*

5. Hessel, J.F.C. (1831). *Kristallometrie oder Kristallonomie und Kristallographie.*

6. Bravais, A. (1850) *Mémoire sur les systèmes formés par des points distribués regulièrement sur un plan ou dans l'espace.*

7. Shafranovskii, I., Belov, N.V. (1962) *50 Years of X-Ray Diffraction,* ed. Paul Ewald (Springer): 351–353.

8. Schönflies, A. (1891) *Kristallsysteme und Kristallstruktur.*

9. Barlow, W. (1883) Probable nature of the internal symmetry of crystals, *Nature* 29, 186–188.

10. Friedrich, W., Knipping P., von Laue, M. (1912) Interferenz-Erscheinungen bei Röntgenstrahlen, *Sitzungsberichte der Mathematisch-Physikalischen Classe der Königlich-Bayerischen Akademie der Wissenschaften zu München,* 303–322.

11. Dickinson, R.G., Raymond, A.L., (1923) The Crystal Structure of Hexamethylene-Tetramine, *Journal of the American Chemical Society* 45, 22–29.

12. Crowfoot, D., Bunn, C.W., Rogers-Low, B.W. & Turner-Jones, A. (1949) The X-ray crystallographic investigation of the structure of penicillin. In *The chemistry of penicillin*, edited by H.T. Clarke, J.R. Johnson & R. Robinson, pp. 310–367. Princeton University Press.

13. Beddell, C.R., Goodford, P.J., Norrington, F.E. (1976) Compounds designed to fit a site of known structure in human haemoglobin, *British Journal of Pharmacology*, 57, 201-209.

14. Klebe, G. (2000) Recent developments in structure-based drug design, *Journal of Molecular Medicine*, 78, 269-281.

15. Davis, A.M., Teague, S.J., Kleywegt, G.J. (2003) Application and limitations of x-ray crystallographic data in structure based Ligand and drug design, *Angewandte Chemie International Edition*, 42, 2718-2736.

16. Anderson, A.C. (2003) The process of structure based drug design, *Chemistry & Biology*, 10, 787-797.

17. Teague, S.J. (2003) Implications of protein flexibility for drug discovery, *Nature Reviews*, 2, 527-541.

18. Stryer, L., Berg, J.M., Tymoczko, J.L. (2002), *Biochemistry* (5th ed.), New York: W. H. Freeman.

19. Bollen, M., Keppens, S., Stalmans, W. (1998) Specific features of glycogen metabolism in the liver, *Biochemistry Journal*, 336, 19-31.

20. Mathis, D., Vence, L., Benoist, C. (2001) β-cell death during progression to diabetes, *Nature*, 414, 792-798.

21. Brownlee, M. (2001) Biochemistry and molecular cell biology of diabetic complications, *Nature*, 414, 813-820.

22. Kitagawa, T., Owada, M., Urakami, T., Yamanchi, K. (1998) Increased incidence of non-insulin dependent diabetes mellitus among Japanese school children correlates with an increased intake of animal protein and fat, *Clinical Pediatrics*, 37, 111-116.

23. Dabelea, D., Hanson, R.L., Bennett, P.H., Roumain, J., Knowler, W.C., Pettitt, D.J. (1998) Increasing prevalence of type II diabetes in American Indian children, *Diabetologia*, 41, 904-910.

24. Drake, A.J., Betts, P.R., Crowne E.C., Shield J.P. (2002) Diabetes type 2 in obese white children, *Archives of Disease in Childhood*, 86, 207-208.

25. Ramachandran, A., Snehalatha, C., Satyavani, K., Sivasankari, S., Vijay, V. (2003) Diabetes type 2 in Asian-Indian urban children, *Diabetes Care*, 26, 1022-1025.

26. Braun, B., Zimmerman, M., Kretcher, N., Spargo, R., Smith, R., Gracey, M. (1996) Risk factors for diabetes and cardiovascular disease in young Australian Aborigines, *Diabetes Care*, 19, 472-479.

27. Stumvoll, M., Goldstein, B.J., van Haeften, T.W. (2005) Diabetes type 2: principles and therapy, *The Lancet*, 365, 1333-1346.

28. Pierce, M., Keen, H., Bradley, C. (1995) Risk of diabetes in offspring of patients with non-insulin dependent diabetes, *Diabetic Medicine*, 12, 6-13.

29. Taylor, S.I. (1999) Deconstructing diabetes type 2, *Cell*, 97, 9-12.

30. Kahn, S.E. (2000) The importance of the β-cell in the pathogenesis of diabetes type 2 mellitus, *The American Journal of Medicine*, 108 (6A), 2S-8S.

31. Rhodes, C.J. (2005) Diabetes type 2-a matter of β-cell life and death? *Science*, 307, 380-383.

32. American Diabetes Association (2004) Diagnosis and classification of diabetes mellitus, *Diabetes Care*, 27 (1), S5-S10.

33. Brownlee, M. (2001) Biochemistry and molecular cell biology of diabetic complications, *Nature*, 414, 813-820.

34. Hodgkin, C.D. (1935) X-ray Single Crystal Photographs of Insulin, *Nature* 135, 591–592.

35. Yalow, R.S., Berson, S.A. (1960) Immunoassay of endogenous plasma insulin in man, *Journal of Clinical Investigation*, 39, 1157-1175.

36. Bagdade, J.D., Bierman, E.L., Porte, D. Jr. (1967) The significance of basal insulin levels in the evaluation of the insulin response to glucose in diabetic and non-diabetic subjects, *Journal of Clinical Investigation*, 46, 1549-1557.

37. Lawson, M.L., Gerstein, H.C., Tsui, E., Zinman B. (1999) Effect of intensive therapy on early macrovascular disease in young individuals with diabetes type 1: a systematic review and meta analysis, *Diabetes Care*, 22, B35-9.

38. Polonsky, K.S., O'Meara, N.M. (2001) in *Endocrinology* 4th edition (Decroot, L. J. & Jameson, L. J.), 697-711 (Saunders, Philadelphia).

39. Bell, G.I., Polonsky, S. (2001) Diabetes mellitus and genetically programmed defects in β-cell function, *Nature*, 414, 788-791.

40. Saltiel, A.R., Kahn, C.R. (2001) Insulin signalling and the regulation of glucose and lipid metabolism, *Nature*, 414, 799-806.

41. Petersen, K.F., Dufour S., Savage D.B., Bilz S., Solomon, Yonemitsu S., Cline G.W., Befroy D., Zemany L., Kahn B.B., Papademetris X., Rothman D.L., Shulman G.I. (2007) The role of skeletal muscle insulin resistance in the pathogenesis of the metabolic syndrome, *PNAS*, 104 (31) 12587-12594.

42. Maechler, P., Wollheim, C.B. (2001) Mitochondrial function in normal and diabetic β-cells, *Nature*, 414, 807-812.

43. Maassen, J.A. (2004) *Diabetes,* 53, S103.

44. Malaisse, W.J. et al. (1979) The stimulus secretion coupling of glucose induced insulin release, *Diabetologica*, 16, 331-341.

45. Lowell, B.B., Shulman, G.I. (2005) Mitochondrial dysfunction and diabetes type 2, *Science*, 307, 384-387.

46. Green, A., Hirsch, N.C., Pramming, S.K. (2003) The changing world demography of diabetes type 2, *Diabetes/Metabolism Research and Reviews*, 19, 3-7.

47. Zimmet, P., Alberti, K.G.M.M., Shaw, J. (2001) Global and societal implications of the diabetes epidemic, *Nature*, 414, 782-787.

48. Murray, C.L.J., Lopez, A.D. (1996) *Global Health Statistics*, volume II, Harvard School of Public Health: Boston, MA.

49. Wild, S., Roglic, G., Green, A., Sicree, R., King, H. (2004) Global prevalence of diabetes: estimates for the year 2000 and projections for 2030, *Diabetes Care*, 10, 2568-2569.

50. King, H., Aubert, R., Herman, W. (1998) Global burden of diabetes, 1995-2025: prevalence, numerical estimates and projections, *Diabetes Care*, 21, 1414-1431.

51. Dowse, G., Zimmet, P., Finch, C., Collins, V. (1991) Decline in incidence of epidemic glucose intolerance in Nauruans: implications of the thrifty genotype, *American Journal of Epidemiology*, 133, 1093-1104.

52. Rubinstein, H., Zimmet, P. (1993) Phosphate, Wealth, and Health in Nauru: A Study of Lifestyle Change (Brolga, Gundaroo).

53. Zimmet, P. in The Medical Challenge: Complex Traits (Fischer, E. & Moller, G.), 55-110 (Piper, Munich, 1997).

54. Zimmet, P. (1992) Kelly West Lecture 1991: Challenges in diabetes epidemiology-from West to the rest, *Diabetes Care*, 15, 232-252.

55. Coleman, D. (1979) Obesity genes: beneficial effects in heterozygous mice, *Science*, 203, 663-665.

56. Haines, H., Hackel, D., Schmidt-Nielsen, K. (1965) *American Journal of Physiology*, 208, 297-300.

57. Neel, J. (1962) Diabetes and the "thrifty" genotype: commentary, *American Journal of Human Genetics*, 14, 353-362.

58. Livanova, N.B., Chebotareva, N.A., Eronina, T.B., Kurganov, B.I. (2002) Pyridoxal-5´-phosphate and conformational cofactor of muscle glycogen phosphorylase b, *Biochemistry*, 67 (10) 1089-1098.

59. Cori, G.T., Green, A.A. (1943) Crystalline muscle phosphorylase: II. Prosthetic group, *Journal of Biological Chemistry*, 151, 31-38.

60. Newgard, C.B., Hwang, P.K., Fletterick, R.J. (1989) The family of glycogen phosphorylase: structure and function, *Critical Reviews in Biochemistry and Molecular Biology*, 24, 69-99.

61. Oikonomakos, N.G. (2002) Glycogen phosphorylase as a molecular target for diabetes type 2 therapy, *Current Protein and Peptide Science*, 3, 1-26.

62. Monod, J., Changeux, J.-P., Jacob, F. (1965) *Journal of Molecular Biology*, 12, 88-118.

63. Bollen, M., Stalmans, W. (1992) *Critical Reviews in Biochemistry and Molecular Biology*, 27, 227-281.

64. Johnson, L.N. (1992) Glycogen phosphorylase: control by phosphorylation and allosteric effectors, *The FASEB Journal*, 6, 2274-2282.

65. Baker, D.J., Timmons, J.A., Greenhaff, P.L. (2005) Glycogen phosphorylase inhibition in diabetes type 2 therapy. A systematic evaluation of metabolic and functional effects in rat skeletal muscle, *Diabetes*, 54, 2453-2459.

66. Barford, D., Hu, S.-H., Johnson, L.N. (1990) The structural mechanism of glycogen phosphorylase control by phosphorylation and AMP, *Journal of Molecular Biology*, 218, 233-260.

67. Johnson, L.N., Hajdu, J., Acharya, K.R., Stuart, D.I., McLaughlin, P.J., Oikonomakos, N.G., Barford, D. (1989) In *Allosteric Enzymes* (Herve, G., Ed.), 81-127, CRC Press, Boca Raton, FL.

68. Oikonomakos, N.G., Acharya, K.R., Johnson, L.N. (1992) In *Post-Translational modification of proteins* (Harding, J. J. and Crabbe, M.J.C., Eds), 81-151, CRC Press Boca Raton, FL.

69. Klein, W., Schinzel, R., Buehner, M., Helmreich, J.M. (1990) The role of pyridoxal 5´-phosphate in glycogen phosphorylase catalysis, *Biochemistry*, 29 (5), 1099-1107.

70. Martin J.L., Johnson, L.N., Withers, S.G. (1990) Comparison of the binding of glucose 1-phosphate derivatives to T state glycogen phosphorylase b, *Biochemistry*, 29, 10745-10757.

71. Martin, J.L., Veluraja, K., Ross, K., Johnson, L.N., Fleet, W.J., Ramsden, N.G., Bruce, I., Orchard, M.G., Oikonomakos, N.G., Papageorgiou, A.C., Leonidas, D. D., Tsitoura, H.S. (1991) Glucose analogue inhibitors of glycogen phosphorylase: the design of potential drugs for diabetes, *Biochemistry*, 30, 10101-10116.

72. Melpidou, A., Oikonomakos, N.G. (1983) Effect of glucose-6-P on the catalytic and structural properties of glycogen phosphorylase α, *FEBS Letters*, 154 (1), 105-110.

73. Oikonomakos, N.G., Schnier, J.B., Zografos, S.E., Skamnaki, V.T., Tsitsanou, K.E., Johnson, L.N. (2000) Flavopiridol inhibits glycogen phosphorylase by binding at the inhibitor site, *The Journal of Biological Chemistry*, 275 (44) 34566-34573.

74. Oikonomakos, N.G., Skamnaki, V.T., Tsitsanou, K.E., Gavalas, N.G., Johnson, L.N. (2000) A new allosteric site in glycogen phosphorylase b as a target for drug interactions, *Structure*, 8, 575-584.

75. Oikonomakos, N.G., Zographos, S.E., Skamnaki, V.T., Archontis, G. (2002) The 1.76 Å resolution crystal structure of glycogen phosphorylase B complexed with glucose, and CP320626, a potential antidiabetic drug, *Bioorganic & Medicinal Chemistry*, 10, 1313-1319.

76. Cheng, A.Y.Y., Fantus, I.G. (2005) Oral hyperglycaemic therapy for diabetes type 2 mellitus, *Canadian Medical Association Journal*, 172 (2), 213-226.

77. Sutherland, D.E., Gruessner, R.W., Dunn, D.L., (2001) Lessons learned from more than 1,000 pancreas transplants at a single institution. *Annals of Surgery*. 233:463-501.

78. Suzuki, K., Bonner-Weir, S., Trivedi, N., (1998) Function and survival of macroencapsulated syngeneic islets transplanted into streptozocin-diabetic mice, *Transplantation*, 66:21-28.

79. Lee, H.C., Kim, S.J., Kim, K.S., Shin, H.C., Yoon, J.W. (2000) Remission in models of diabetes type 1 by gene therapy using a single-chain insulin analogue, *Nature*, 408:483-488.

80. Agius, L. (2007) New hepatic targets for glycaemic control in diabetes, *Best Practice & Research Clinical Endocrinology & Metabolism*, 21 (4), 587-605.

81. Fischer, E.H., Krebs, E.G. (1958) The isolation and crystallization of rabbit skeletal muscle phosphorylase b, *The Journal of Biological Chemistry*, 231, 65-71.

82. Yunis, A., Fischer, E.H., Krebs, E.G. (1962) Comparative studies on glycogen phosphorylase, *The Journal of Biological Chemistry*, 237 (9), 2809-2815.

83. Gill, S.C., von Hippel, P.H. (1989) Calculation of protein extinction coefficients from amino acid sequence data, Analytical Biochemistry, 182, 319-326.

84. Saheki, S., Takeda, A., Shimazu, T. (1985) Assay of inorganic phosphate in the mild pH range, suitable for measurement of glycogen phosphorylase activity, *Analytical Biochemistry*, 148, 277-281.

85. Leatherbarrow, R.J. (1992) *Grafit version 3.01*, Erithacus Software, Staines, United Kingdom.

86. Segel, I. H. (1975) *Enzyme Kinetics*, Wiley.

87. Otwinowski, Z., Minor, W. (1997) Processing of x-ray data collected in oscillation mode, *Methods in Enzymology*, 276, 307-326.

88. Murshudov, G.N., Vagin, A.A., Dodson, E.J. (1997) Refinement of macromolecular structures by the maximum-likelihood method, *Acta Crystallographica D*, 53, 240-255.

89. Gregoriou, M., Noble, M.E.M., Watson, K.A., Garman, E.F., Krulle, T.M., Fuente, C., Fleet, G.W.J., Oikonomakos, N.G., Johnson, L.N. (1998) The structure of glycogen phosphorylase glucopyranose spiro-hydantoin complex at 1.8 Å resolution at 100 K: the role of water structure and its contribution to binding, *Protein Science*, 7, 915-927.

90. Jones, T.A., Zou, J.Y., Cowan, S.W., Kjeldgaard M. (1991) Improved methods for the building of protein models in electron density maps and the location of errors in these models, *Acta Crystallographica A*, 47, 110-119.

91. Emsley, P., Cowtan, K. (2004) Coot: model building tools for molecular graphics, *Acta Crystallographica D-Biological Crystallography*, 60, 2126-2132.

92. Laskowski, R.A., MacArthur, M.W., Moss, D.S., Thornton, J.M. (1993) PROCHECK: a program to check the stereochemical quality of protein structures, *Journal of Applied Crystallography*, 26, 283-291.

93. CCP4. The CCP4 (Collaborative Computational project Number 4) suite: programs for protein crystallography (1994) *Acta Crystallographica D*, 50, 740-763.

94. Kraulis, P. (1991) MOLSCRIPT: A program to produce both detailed and schematic plots of protein structures, *Journal of Applied Crystallography*, 24, 946-950.

95. Merritt, E.A., Bacon, D.J. (1997) Photorealistic molecular graphics, *Methods of Enzymology*, 277, 505-524.

96. Rhodes, G. (2006) *Crystallography made crystal clear: A guide for users of macromolecular models*, 3rd edition, Academic Press, Elsevier.

97. Oikonomakos, N.G., Kosmopoulou, M., Zographos, S.E., Leonidas, D.D., Chrysina, E.D., Somsák, L., Nagy, V., Praly, J.-P., Docsa, T., Tóth, B., Gergely, P. (2002) The binding of N´-acetyl and Benzoyl-N´-β-D-glucopyranosyl ureas to glycogen phosphorylase b: kinetic and crystallographic studies, *European Journal of Biochemistry*, 269, 1684-1696.

98. Sriram, D., Sreenivasan, H., Srinivasan, S., Priya, K., Vishnu Thrirtha, M., Loganathan, D. (1997) Beta-1-N-acetomido-D-glucopyranose, *Acta Crystallographica C*, 53, 1075-1077.

99. Anagnostou, E., Kosmopoulou, M.N., Chrysina, E.D., Leonidas, D.D., Hadjiloi, T., Tiraidis, C., Györgydeák, Z., Somsák, L., Docsa, T., Gergely, P., Oikonomakos, N.G. (2006) Crystallographic studies on two bioisosteric analogues. N-acetyl-β-D-glucopyranosylamine and N-trifluoracetyl-β-D-glucopyranosylamine, potent inhibitors of muscle glycogen phosphorylase, *Bioorganic Medicinal Chemistry*, 14, 181-189.

100. Watson, K.A., Mitchell, E.P., Johnson, L.N., Cruciani, G., Son, J.C., Bichard, C.J.F., Fleet, G.W.J., Oikonomakos, N.G., Kontou, M., Zographos, S.E. (1995) Glucose analogue inhibitors of glycogen phosphorylase: from crystallographic analysis to drug prediction using GRID force field and GOLPE variable selection, *Acta Crystallographica D*, 51, 458-472.

101. Eaton, V.J., Steele, D. (1973) Dihedral angle of biphenyl in solution and the molecular force field, *Journal of Chemical Society Faraday Transactions 2*, 69, 1601-1608.

102. Martin, J.L., Veluraja, K., Ross, K., Johnson, L.N., Fleet, G.W.J., Ramsden, N.G., Bruce, I., Orchard, M., Oikonomakos, N.G., Papageorgiou, A.C., Leonidas, D.D., Tsitura, H.S. (1991) Glucose analogue inhibitors of glycogen phosphorylase: the design of potential drugs for diabetes, *Biochemistry*, 30, 10101-10116.

103. Watson, K.A., Chrysina, E.D., Tsitsanou, K.E., Zographos, S.E., Archontis, G., Fleet, G.W.J., Oikonomakos, N.G. (2005) Kinetic and crystallographic studies of glucopyranose spiro-hydantoin and glucopyranosylamine analogues inhibitors of glycogen phosphorylase, *Proteins*, 61, 966-983.

104. Oikonomakos, N.G., Kontou, M., Zographos, S.E., Watson, K.A., Johnson, L.N., Bichard, C.J.W., Fleet, G.W.J., Acharya, K.R. (1995) N-acetyl-β-D-glucopyranosylamine: a potent T state inhibitor of glycogen phosphorylase. A comparison with α-D-glucose, *Protein Science*, 4, 2469-2477.

105. Chrysina, E.D., Oikonomakos, N.G., Zographos, S.E., Kosmopoulou, M.N., Bischler, N., Leonidas, D.D., Kovács, L., Docsa, T., Gergely, P., Somsák, L. (2003) Crystallographic studies on α- and β-D-glucopyranosyl formamide analogues, inhibitors of glycogen phosphorylase, *Biocatalysis and Biotransformation*, 21, 233-242.

106. Chrysina, E.D., Kosmopoulou, M.N., Kardakaris, R, Bischler, N., Leonidas, D.D., Kannan, T., Loganathan, D., Oikonomakos, N.G. (2005) Binding of β-D-glucopyranosyl bismethoxyphosphoramidate to glycogen phosphorylase b: kinetic and crystallographic studies, *Bioorganic Medicinal Chemistry*, 13, 765-772.

107. Petsalakis, E.I., Chrysina, E.D., Tiraidis, C., Hadjiloi, T., Leonidas, D.D., Oikonomakos, N.G., Aich, U., Varghese, B., Loganathan, D. (2006) Crystallographic studies on N-azidoacetyl-β-D-glucopyranosylamine, an inhibitor of glycogen phosphorylase: comparison with N-acetyl-β-D-glucopyranosylamine, *Bioorganic Medicinal Chemistry*, 14, 5316-5324.

108. Bichard, C.J.F., Mitchell, E.P., Wormald, M.R., Watson, K.A., Johnson, L.N., Zographos, S.E., Koutra, D.D., Oikonomakos, N.G., Fleet, G.W.J. (1995) Potent inhibition of glycogen phosphorylase by a spiro-hydantoin of glucopyranose: first pyranose analogues of hydantoin, *Tetrahedron Letters*, 36, 2145-2148.

109. Krüle, T.M., Watson, K.A., Gregoriou, M., Johnson, L.N., Crook, S., Watkin, D.J., Griffiths, R.C., Nasj, R.J., Tsitsanou, K.E., Zographos, S.E., Oikonomakos, N.G., Fleet, G.W.J. (1995) Specific inhibition of glycogen phosphorylase by a spirodiketopiperazine at the anomeric position of glucopyranose, *Tetrahedron Letters*, 36, 8291-8294.

110. Brandstetter, T.W., Fuente, C., Kim, Y-h., Johnson, L.N., Crook, S.Q., Lilley, P.M., Watkin, D.J., Tsitsanou, K.E., Zographos, S.E., Chrysina, E.D., Oikonomakos, N.G., Fleet, C.W.J. (1996) Glucofuranose analogues of hydantoin, *Tetrahedron*, 52, 10721-10736.

111. Krüle, T.M., delaFuente, C., Watson, K.A. Gregoriou, M., Johnson, L.N., Tsitsanou, K.E., Zographos. S.E., Oikonomakos, N.G., Fleet, G.W.J. (1997) Stereospecific synthesis of spiro-hydantoin of beta-glucopyranose: inhibitors of glycogen phosphorylase, *Synlett*, 211-213.

112. Oikonomakos, N.G., Skamnaki, V.T., Ösz, E., Szilágyi, L., Somsák, L., Docsa, T., Tóth, B., Gergely, P. (2002) Kinetic and crystallographic studies of glucopyranosylidene spiro-hydantoin binding to glycogen phosphorylase b, *Bioorganic Medicinal Chemistry*, 10, 261-268.

113. Chrysina, E.D., Kosmopoulou, M.N., Tiraidis, C., Kardakaris, R., Bischler, N., Leonidas, D.D., Hadady, Z., Somsák, L., Docsa, T., Gergely, P., Oikonomakos, N.G. (2005) Kinetic and crystallographic studies on 2-(β-D-glucopyranosyl)-5-methyl-1,3,4-oxadiazole, -benzothiazole and -benzimidazole, inhibitors of muscle glycogen phosphorylase b. Evidence of a new binding site, *Protein science*, 14, 873-888.

114. Dzubak, P., Hajduch, M., Vydta, D., Hustova, A., Kvasnica, M., Biedermann. D., Markova, L., Urban, M., Sarek, J. (2006) Pharmacological activities of natural triterpenoids and their therapeutic implications, *Natural Products Reports*, 23, 394-411.

115. Liu, J. (1995) Pharmacology of oleanolic and ursolic acid, *Journal of Ethnopharmacology*, 49, 57-68.

116. Pisha, E., Chai, H., Lee, I.S., Chanwedera, T.E., Farnsworth, N.R., Cordell, G.A., Beecher, C.W.W., Fong, H.H.S., Kinghorn, A.D., Brown, D.M., Wani, M.C., Wall, M.E., Hieken, T.J., Dasgupta, T.K., Pezzuto, J.M. (1995) Discovery of betulinic acid as a selective inhibitor of human melanoma that functions by induction of apoptosis, *Nature Medicine*, 1, 1046-1051.

117. Dimeglumine, B. (2007) Bevirimat anti-HIV agent viral maturation inhibitor, *Drugs Future*, 32, 7-11.

118. Liby, K.T., Yore, M.M., Sporn, M.B. Triterpenoids and rexinoids as multifunctional agents for the prevention and treatment of cancer, *Nature Reviews Cancer*, 7, 357-369.

119. Fukushima, M., Matsuyama, F., Ueda, N., Egawa, K., Takemoto, J., Kajimoto, Y., Yonaha, N., Miura, T., Kanedo, T., Nishi, Y., Mitsui, R., Fugita, Y., Yamada, Y., Seino, Y. (2006) Effect of corosolic acid on post challenge plasma glucose levels, *Diabetes Research and Clinical Practice*, 73, 174-177.

120. Rush, W.R., Murray, G.R., Graham, D.J.M. (1993) The comparative steady-state bioavailability of the active ingredients of madecassol, *European Journal of Drug Metabolism & Pharmacokinetics*, 18, 323-326.

121. Zographos, S.E., Oikonomakos, N.G., Tsitsanou, K.E., Leonidas, D.D., Chrysina, E.D., Skamnaki, V.T., Bischoff, H., Goldmann, S., Schram, M., Watson, K.A., Johnson, L.N. (1997) The structure of glycogen phosphorylase b with an alkyl-dihydropyridine-dicarboxylic acid compound, a novel and potent inhibitor, *Structure*, 5, 1413-1425.

122. Oikonomakos, N.G., Tsitsanou, K.E., Zographos, S.E., Skamnaki, V.T., Goldmann, S., Bischoff, H. (1999) Allosteric inhibition of glycogen phosphorylase a by the potential antidiabetic drug 3-isopropyl 4-(2-chlorophenyl)-1,4-dihydro-1-ethyl-2-methyl-pyridine-3,5,6-tricarboxylate, *Protein Science*, 8, 1930-1945.

123. Tiraidis, C., Alexacou, K.-M., Zographos, S.E., Leonidas, D.D., Gimisis, T., Oikonomakos, N.G. (2007) FR258900, a potential anti-hyperglycaemic drug, binds at the allosteric site of glycogen phosphorylase, *Protein Science*, 16, 1773-1782.

124. Lvdia Moreira Lima and Eliezer J. Barreiro (2005) Bioisosterism: A useful strategy for molecular modification and drug design, *Current Medicinal Chemistry*, 12, 23-49.

125. Horne, W. S., Yadav, M. K., Stout, C. D., Ghadiri, M. R. (2004) Heterocyclic peptide backbone modifications in an α-helical coiled coil, *Journal of American Chemical Society*, 126, 15366-15367.

126. Appendino, G., Bacchiega, S., Minassi, A., Cascio, M.G., De Petrocellis, L., Di Marzo, V. (2007) The 1,2,3-Triazole Ring as a Peptido- and Olefinomimetic Element: Discovery of Click Vanilloids and Cannabinoids, *Angewandte Chemie International Edition*, 46 (48), 9312-9315.

127. Angell, Y.L., Burgess, K. (2007) Peptidomimetics *via* copper-catalyzed azide-alkyne cycloadditions, *Chemical Society Reviews*, 36, 1674-1689.

128. Whitford, D. (2008) *Proteins, Structure and Function*, John Wiley & Sons, Ltd.

129. Vincent, A. (2000) *Molecular Symmetry and Group Theory*, John Wiley & Sons, Ltd., 2nd edition.

130. Warren, L. DeLano, *The PyMol Molecular Graphics System*, DeLano Scientific LLC, San Carlos, CA, USA.

131. Yonetani, T., Tsuneshige, A. (2003) The global allostery model of haemoglobin: an allosteric mechanism involving homotropic and heterotrophic mechanisms, *Comptes Rendus Biologies*, 326, 523-532.

132. McMurray, J. (2000) *Organic Chemistry*, 5th edition, Brooks/Cole.

133. Tsitsanou, K.E., Oikonomakos, N.G., Zographos, S.E., Skamnaki, V.T., Gregoriou, M., Watson, K.A., Johnson, L.N., Fleet, G.W.J. (1999) Effects of commonly used cryoprotectants on glycogen phosphorylase activity and structure, *Protein Science*, 8, 741-749.

134. Weber, P.C. (1997) Overview of protein crystallization methods, *Methods in Enzymology*, 276, 13-22. 135.

135. Kyra-Melinda Alexacou, Joseph M. Hayes, Costas Tiraidis, Spyros E. Zographos, Demetres D. Leonidas, Evangelia D. Chrysina, Georgios Archontis, Nikos G. Oikonomakos, Jashuva V. Paul, Babu Varghese, Duraikkannu Loganathan (2008) Crystallographic and computational studies on 4-phenyl-*N*-[β-D-glucopyranosyl]-1*H*-1,2,3-triazole-1-acetamide, an inhibitor of glycogen phosphorylase: Comparison with α-D-glucose, *N*-acetyl-β-D-glucopyranosylamine and *N*-benzoyl-*N´*-β-D-glucopyranosyl urea binding, *Proteins: structure, function and bioinformatics*, 71 (3), 1307-1323.

136. Wen, X., Sun, H., Liu, J., Cheng, K., Zhang, P., Zhang, L., Hao, J., Zhang, L., Peizhou, N., Zographos, S.E., Leonidas, D.D., Alexacou, K.-M., Gimisis, T., Hayes, J.M., Oikonomakos, N.G. (2008) Naturally occurring pentacyclic triterpenes as inhibitors of glycogen phosphorylase: synthesis, structure-activity relationships, and X-ray crystallographic studies, *Journal of Medicinal Chemistry*, 51, 3540-3554.

137. Evangelia D. Chrysina, Éva Bokor, Kyra-Melinda Alexacou, Maria-Despoina Charavgi, George N. Oikonomakos, Spyros E. Zographos, Demetres D. Leonidas, Nikos G. Oikonomakos, László Somsák (2009) Amide–1,2,3-triazole bioisosterism: the glycogen phosphorylase case, *Tetrahedron Asymmetry,* 20, 733-740.

6. List of publications

1. Tiraidis, C., Alexacou, K.-M., Zographos, S.E., Leonidas, D.D., Gimisis, T., and Oikonomakos, N.G. (2007) FR258900, a potential anti-hyperglycaemic drug, binds at the allosteric site of glycogen phosphorylase. *Protein Science,* 16 (8), 1773-1782.

2. Kyra-Melinda Alexacou, Joseph M. Hayes, Costas Tiraidis, Spyros E. Zographos, Demetres D. Leonidas, Evangelia D. Chrysina, Georgios Archontis, Nikos G. Oikonomakos, Jashuva V. Paul, Babu Varghese, Duraikkannu Loganathan (2008) Crystallographic and computational studies on 4-phenyl-*N*-[β-D-glucopyranosyl]-1*H*-1,2,3-triazole-1-acetamide, an inhibitor of glycogen phosphorylase: Comparison with α-D-glucose, *N*-acetyl-β-D-glucopyranosylamine and *N*-benzoyl-*N´*-β-D-glucopyranosyl urea binding, *Proteins: structure, function and bioinformatics*, 71 (3), 1307-1323.

3. Xiaoan Wen, Hongbin Sun, Jun Liu, Keguang Cheng, Pu Zhang, Liying Zhang, Jia Hao, Luyong Zhang, Peizhou Ni, Spyros E. Zographos, Demetres D. Leonidas, Kyra-Melinda Alexacou, Thanasis Gimisis, Joseph M. Hayes, Nikos G. Oikonomakos (2008) Naturally Occurring Pentacyclic Triterpenes as Inhibitors of Glycogen Phosphorylase: Synthesis, Structure-Activity Relationships and X-ray Crystallographic Studies, *Journal of Medicinal Chemistry*, 51 (12), 3540-3554.

4. Zographos, S.E., Leonidas, D.D., Alexacou, K.-M., Gimisis, T., Hayes, J.M., Oikonomakos, N.G, Wen, X., Sun, H., Liu, J., Cheng, K., Zhang, P., Zhang, L., Hao, J., Zhang, L., and Ni, P. (2008) Pentacyclic triterpenes, inhibitors of glycogen phosphorylase, as potential drugs for type 2 diabetes: X-ray crystallographic studies, *Planta Medica*, 74, 1146-1147.

5. Somsák, L., Czifrák, K., Tóth, M., Bokor, É., Chrysina, E.D., Alexacou, K.-M., Hayes, J.M., Tiraidis, C. Lazoura, E., Leonidas, D.D., Zographos, S.E., Oikonomakos, N.G. (2008). New inhibitors of glycogen phosphorylase as potential antidiabetic agents, *Current Medicinal Chemistry*, 15, 2933-2983.

6. Evangelia D. Chrysina, Éva Bokor, Kyra-Melinda Alexacou, Maria-Despoina Charavgi, George N. Oikonomakos, Spyros E. Zographos, Demetres D. Leonidas, Nikos G. Oikonomakos, László Somsák (2009) Amide–1,2,3-triazole bioisosterism: the glycogen phosphorylase case, *Tetrahedron Asymmetry*, 20, 733-740.

7. Mahmoud Benltifa, Joseph M. Hayes, Sébastien Vidal, David Gueyrard, Peter G. Goekjian, Jean-Pierre Praly, Gregory Kizilis, Costas Tiraidis, Kyra-Melinda Alexacou, Evangelia, D. Chrysina, Spyros E. Zographos, Demetres D. Leonidas, Georgios Archontis, Nikos G. Oikonomakos (2009) Glucose-based Spiro-isoxazolines: A New Family of Potent Glycogen Phosphorylase Inhibitors, **Bioorganic & Medicinal Chemistry**, 17, 7368-80.

8. Nóra Felfödi, Marietta Tóth, Evangelia D. Chrysina, Maria-Despoina Charavgi, Kyra-Melinda Alexacou, László Somsák (2010) Synthesis of new glycosyl biuret and urea derivatives as potential glycoenzyme inhibitors, **Carbohydrate Research**, 345, 208-213.

9. Kyra-Melinda Alexacou, Alia-Cristina Deleanu, Evangelia D. Chrysina, Marianna-Despoina Charavgi, Ioannis D. Kostas, Spyridon E. Zografos, Nikos G. Oikonomakos and Demetres D. Leonidas, The binding of β-D-glucopyranosyl-thiosemicarbazone derivatives to glycogen phosphorylase: a new class of inhibitors, **Bioorganic & Medicinal Chemistry**, *manuscript in preparation.*

10. Alexacou, K-M., Charavgi, M-D., Tiraidis, C., MacKerell, A.D. Jr., Zhong, S., Zographos, S.E., Leonidas, D.D., Oikonomakos, N.G., Chrysina, E.D. Computer aided and structure based inhibitor design of glycogen phosphorylase as potential lead compounds for type 2 therapeutics, *manuscript in preparation.*

7. Poster Presentations

1. C. Tiraidis, K.-M. Alexacou, S.E. Zographos, D.D. Leonidas, N.G. Oikonomakos, M. Benltifa, S.Vidal, D. Gueyrard, P.G. Goekjian, J.-P. Praly, Oxadiazoles-C-aryl-glucosides and spiro-isoxazolines: new classes of compounds, inhibitors of glycogenolysis, as potential drugs for diabetes type 2, **3rd Conference of the Hellenic Crystallographic Association, Patra, Greece, 22-24 September 2006.**

2. K.-M. Alexacou, C.Tiraidis, S.E. Zographos, D.D. Leonidas, N.G. Oikonomakos, M. Benltifa, S.Vidal, D. Gueyrard, P.G. Goekjian, J.-P. Praly, Oxadiazoles-c-aryl-glucosides and spiro-isoxazolines as potential lead compounds for the design of diabetes type 2 therapeutic agents, **58th Meeting of the Hellenic Society of Biochemistry & Molecular Biology, Patra, Greece, 9-11 November 2006.**

3. Kyra-Melinda Alexacou, Costas Tiraidis, Spyros E. Zographos, Demetres D. Leonidas, Thanasis Gimisis, Nikos G. Oikonomakos, FR258900, a potential anti-hyperglycaemic drug, binds at the allosteric site of glycogen phosphorylase: kinetic and crystallographic studies, **2nd Hellenic Symposium, Organic Synthesis-From Chemistry to Biology, Medicine and Material Science, Athens, Greece, 19-21 April 2007.**

4. Kyra-Melinda Alexacou, Zhang Yun Zhi, Jean-Pierre Praly, Spyros E. Zographos, Demetres D. Leonidas, Evangelia D. Chrysina, Nikos G. Oikonomakos, Kinetic and crystallographic studies of a new class of *C*-glucosyl derivatives of hydroquinone, inhibitors of glycogen phosphorylase, as potential lead compounds for diabetes type 2 therapeutics, **13th Hellenic Symposium of medicinal Chemistry, Athens, 14-15 March 2008.**

5. Alia-Cristina Deleanu, Ioannis D. Kostas, Ioannis Liratzis, Kyra-Melinda Alexacou, Demetres D. Leonidas, Spyros E. Zographos, Nikos G. Oikonomakos, β-D-Glucopyranosyl-modified thiosemicarbazones as inhibitors of glycogen phosphorylase, **13th Hellenic Symposium of medicinal Chemistry, Athens, 14-15 March 2008.**

6. Kyra-Melinda Alexacou, Katalin Czifrák, László Somsák, Spyros E. Zographos, Demetres D. Leonidas, Nikos G. Oikonomakos, X-ray crystallographic and kinetic studies on a group of Glucopyranosylidene-spiro-iminothiazolone compounds. On the way to rational drug design for the treatment of diabetes type 2, **Select Biosciences: Protein Crystallography Europe, Amsterdam, Netherlands, 18-20 June 2008.**

7. Spyros E. Zographos, Demetres D. Leonidas, Kyra-Melinda Alexacou, Thanasis Gimisis, Joseph M. Hayes, Nikos G. Oikonomakos, Xiaoan Wen, Hongbin Sun, Jun Liu, Keguang Cheng, Pu Zhang, Liying Zhang, Jia Hao, Luyong Zhang, Peizhou Ni, Pentacyclic triterpenes, inhibitors of glycogen phosphorylase, as potential drugs for diabetes type 2: X-ray crystallographic studies, **7th Joint Meeting of AFERP, ASP, GA, PSE & SIF, Athens, 3-8 August 2008.**

8. L. Somsák, V. Nagy, N. Felföldi, B. Kónya, K. Telepó, T. Docsa, P. Gergely, E. D. Chrysina, K.-M. Alexacou, S. E. Zographos, D. D. Leonidas, N. G. Oikonomakos, Design, synthesis, and structure activity relationships of glycogen phosphorylase inhibitors. Glucose derivatives against diabetes type 2 mellitus, **4th Central European Conference: Chemistry towards Biology, Dobogókö, Hungary, 8-11 September 2008**.

9. Alia C. Deleanu, Ioannis D. Kostas, Ioannis Liratzis, Kyra-Melinda Alexacou, Demetres D. Leonidas, Spyros E. Zographos, Nikos G. Oikonomakos, β-D-Glucopyranosyl-modified thiosemicarbazones as inhibitors of glycogen phosphorylase, **4th Central European Conference: Chemistry towards Biology, Dobogókö, Hungary, 8-11 September 2008**.

10. Marianna A. Charavgi, Kyra-Melinda Alexacou, Costas Tiraidis, Alexander D. MacKerell, Jr., Shijun Zhong, Spyros E. Zographos, Demetres D. Leonidas, Nikos G. Oikonomakos, Virtual database screening, kinetic and crystallographic studies of new classes of glycogen phosphorylase inhibitors as potential lead compounds for type 2 diabetes therapeutics, **4th Conference of the Hellenic Crystallographic Association, Athens, 22-24 September 2008**.

11. Kyra-Melinda Alexacou, Éva Bokor, László Somsák, Spyros E. Zographos, Evangelia D. Chrysina, Demetres D. Leonidas, Organic synthesis, kinetic and X-ray crystallographic studies of 1-(β-D-glucopyranosyl)-4-hydroxymethyl-1,2,3-triazole. A potential target for glycogen phosphorylase drug design and diabetes type 2 therapeutics, **3rd Hellenic Symposium, Organic Synthesis-From Chemistry to Biology, Medicine and Material Science, Athens, 15-17 October 2009.**

8. Curriculum vitae

<div align="center">

Kyriaki-Melinda Alexacou

Nationality:

Address:

Phone:

Mobile:

Email:

</div>

Education

- **MSc**, University of Sussex, UK, 2006

  Subject: Genetic Manipulation & Molecular Cell Biology (*with distinction*)

  Dissertation: "Genetic and proteomic studies of *Streptococcus uberis* wild type 0140J and insertional mutant adcI"

- **BSc**, Queen Mary, University of London, UK, 2004

  Subject: Biochemistry (*Honours, 2nd upper class)*

  Dissertation: "Spectroscopic investigations of copper binding to the prion protein (90-126). Can hydroxyl radicals be linked to mad cow disease?"

- **GCE A-levels**, Hellenic-American Educational Foundation, Athens, Greece, 1999-2001

  Subjects: Chemistry, Biology, Mathematics

- **1st Experimental Lyceum "Gennadio"**, Athens, Greece, 1993-1999

  Subjects: philosophy, history, civics, English, French, physical education, modern Greek and literature, mathematics, physics, chemistry and biology (overall average grade "excellent" 18 8/12 and excellent conduct)

- **Hill Elementary School**, Athens, Greece, 1985-1993

Educational & research skills

- **Since December 2006**: Registered user of the European Synchrotron Radiation Sources for X-ray crystallographic data collection of the Synchrotron Radiation Source, Daresbury Laboratory, Daresbury, UK and EMBL, Hamburg-Outstation, DESY

- **October 2004**: Radiation Safety for Laboratory Workers course, University of Sussex, UK

Qualifications

- Microsoft office, internet, Linux, WinCOOT, CCP4i, Molecular Graphics, PyMOL

- Fluent in Greek, English, French

- Advanced piano level

- **January 1998:** Certificat Pratique De Langue Française

- **December 1996:** Certificate of Proficiency in English

- **September 1996:** Certificat De Langue Française

- **December 1994:** First Certificate in English

- **Summer 1993:** Intermediate Certificate in English

Fellowships & memberships

- **Since 2006**: EU Marie Curie Fellow (EST Program, contract No MEST-CT-020575)

- **Since 2009:** Member of the American Chemical Society

Awards

- **January 2000:** Award for excellent progress and outstanding behaviour and manners during the academic year 1998-1999, 1st Experimental Lyceum "Gennadio", Athens, GR.

- **October 1999:** "Excellence Honours" award for the academic year 1998-1999, overall grade of 18 $^{8/12}$, 1st Experimental Lyceum "Gennadio", Athens, GR

- **October 1998:** "Excellence Honours" award for the academic year 1997-1998, overall grade of 18 $^{11/13}$, 1st Experimental Lyceum "Gennadio", Athens, GR

- **July 1994:** Silver medal award for long jump, "Sport Camp" summer camp, GR

- **October 1994:** "Excellence Honours" award for the academic year 1993-1994, overall grade of 18 $^{6/12}$, 1st Experimental Lyceum "Gennadio", Athens, GR

References

Dr. Demetres D. Leonidas

Associate Professor of Biochemistry

Department of Biochemistry & Biotechnology

University of Thessaly

26 Ploutonos st. 41221

Larisa, Greece

"He who has gone, so we but cherish his memory, abides with us,

more potent, nay, more present than the living man"

Antoine de Saint-Exupéry (1900-1944)

Nikos G. Oikonomakos (1945-2008)